

---

# The benefit of interpretable data-driven methods for wake steering applications

Balthazar Sengers

---

Bei der Fakultät für Mathematik und Naturwissenschaften  
der Carl von Ossietzky Universität Oldenburg  
zur Erlangung des Grades und Titels eines

**Doktors der Naturwissenschaften (Dr. rer. nat.)**

angenommene Dissertation

**von Balthazar Arnoldus Maria Sengers**

geboren in 's-Hertogenbosch, Niederlande



Gutachter: Prof. Dr. Martin Kühn  
Zweitgutachter: Dr. Mahdi Abkar  
Tag der Disputation: 22.08.2023

# Abstract

Wake steering by intentional yaw misalignment has been demonstrated in numerical, wind tunnel and field experiments to increase the total power production of wind farms. The industry is, however, still hesitant to adopt this strategy due to large uncertainties associated with it. A better understanding of how atmospheric conditions affect wake steering is deemed essential for its deployment on a larger scale. This work demonstrates the role interpretable data-driven approaches can play in achieving this objective.

The first part of this work focuses on a more accurate representation of the turbine wake in engineering models, which are typically used to define yaw misalignment set points used by yaw controllers in wake steering experiments. An interpretable data-driven wake model is developed, which uses a set of only linear equations to estimate wake characteristics from inflow and turbine variables. Besides standard parameters such as wind speed deficit and wake center position, this model is also able to reproduce the curled wake shape associated with wake steering.

This newly proposed data-driven model is compared to a selection of commonly used analytical wake models in their ability to estimate the characteristics of a single wake. First trained on a subset of large eddy simulation data and later on lidar measurements from an onshore field campaign, the models are evaluated on their performance on unseen testing data. In both experiments, the data-driven model consistently outperforms its analytical counterparts when estimating the available power of a virtual downstream turbine. Especially when the turbine is misaligned, hence when wake steering is applied, or when the atmospheric boundary layer is stably stratified, hence when wake steering is most effective, the data-driven model exhibits a higher accuracy. In particular, not only the wind speed deficit, but also the wake position and shape are better reproduced. Moreover, the data-driven model allows for a flexible choice of input parameters, and allows for the direct use of disturbed measurement (i.e. SCADA data) at minimum loss of accuracy.

The second part of this work focuses on situations detrimental for wake steering. Using an engineering model based on the data-driven wake model described above, rapid wind direction changes are identified as conditions harmful to the successful application of wake steering. Feeding preview wind direction information to the yaw controller of the upstream turbine is shown to increase the power production of a turbine pair. The optimum preview time is demonstrated to be independent of the wind direction change rate. A large eddy simulation study confirms that these harmful conditions can be mitigated using preview wind direction information, demonstrating that power losses are converted into power gains, and existing power gains are further increased.

Acknowledging that these results cannot directly be generalized to scenarios outside

of the studied conditions, this work demonstrates that wake steering applications can benefit from exploiting data-driven methods. Moreover, this work illustrates that this can be achieved with simple, interpretable methods.



# Zusammenfassung

Sowohl numerische Untersuchungen als auch Windkanal- und Feldexperimente haben gezeigt, dass sich durch bewusstes Schrägstellen von Windenergieanlagen zum Wind deren Nachläufe ablenken lassen und sich die Gesamtleistung eines Windparks dadurch erhöhen lässt. Die Industrie ist jedoch derzeit noch zurückhaltend in der Anwendung dieser Strategie, da diese auch von großen Unsicherheiten behaftet ist. Daher ist ein besseres Verständnis darüber, wie sich atmosphärische Umgebungsbedingungen auf die Nachlaufsteuerung auswirken für die großskalige Anwendung von großer Relevanz. In dieser Arbeit wird die Rolle von interpretierbaren, datengetriebenen Ansätzen zum Erreichen dieses Ziels demonstriert.

Der erste Teil dieser Arbeit widmet sich einer genaueren Repräsentation von Nachläufen in Industriemodellen, die typischerweise zur Bestimmung von Sollwerten für die Gierregelung verwendet und dann wiederum in Experimenten zur Nachlauflenkung eingesetzt werden. Dazu wird ein interpretierbares, datengetriebenes Nachlaufmodell aus einem Satz von einfachen linearen Gleichungen entwickelt, um die Nachlaufcharakteristiken basierend auf Einströmgrößen und Turbinengrößen abzuschätzen. Neben der Bestimmung von Standardparametern, wie dem Windgeschwindigkeitsdefizit und der Position des Nachlaufzentrums, eignet sich dieses Modell auch dafür die durch die Nachlaufregelung verursachte, gebogene Form des Nachlaufs zu reproduzieren.

Die Ergebnisse des hier entwickelten, datengetriebenen Modells werden mit den Ergebnissen von üblicherweise verwendeten, analytischen Nachlaufmodellen für einzelne Nachläufe verglichen. Die Modelle werden evaluiert, in dem sie erst basierend auf einer Teilmenge eines Datensatzes aus Large-Eddy-Simulationsdaten und später auf Lidar-Messungen aus einer Feldkampagne trainiert und anschließend gegen ein unverwendeten Testdatensatz validiert werden. In beiden Experimenten schneidet das datengetriebene Modell durchweg besser bei der Abschätzung der verfügbaren Leistung einer virtuellen stromabwärts gelegenen Turbine als die getesteten analytischen Modelle ab. Insbesondere wenn die Turbinen gegiert sind und somit der Nachlauf abgelenkt wird, oder wenn die Schichtung in der atmosphärischen Grenzschicht stabil ist und die Ablenkungsstrategie am effektivsten ist, zeigt das datengetriebene Modell eine höhere Genauigkeit. Explizit wird nicht nur das Windgeschwindigkeitsdefizit, sondern auch die Nachlaufposition und -form besser reproduziert. Darüber hinaus erlaubt das datengetriebene Modell eine flexible Wahl von Eingabeparametern und sogar die direkte Nutzung von beeinflussten Daten (z.B. SCADA-Daten), bei minimalem Verlust an Genauigkeit.

Der zweite Teil dieser Arbeit beschäftigt sich mit Situationen, welche problematisch für das Anwenden der Nachlaufablenkung sein können. Durch Verwendung

eines auf dem hier entwickelten, datengetriebenen Nachlaufmodell basierenden Industriemodell wird aufgezeigt, dass schnelle Änderungen der Windrichtung eine erfolgreiche Anwendung der Nachlaufsteuerung erschweren. Es hat sich gezeigt, dass es durch Einspeisung von Windrichtungsinformationen in den Regler einer stromaufwärts gelegenen Turbine, bevor diese von der Windenergieanlage selber erfahren werden, zu einer Steigerung der Leistungserzeugung eines Turbinenpaares kommt. Es wird aufgezeigt, dass die optimale Vorschauzeit unabhängig von der Windrichtungsänderungsrate ist. Eine Large-Eddy-Simulations-Studie bestätigt, dass die Verwendung einer Vorhersage der Windrichtung den für die Nachlaufablenkung schädlichen Bedingungen entgegenwirken kann. Ertragsverluste werden in -gewinne überführt und bereits bestehende Ertragsgewinne werden weiter erhöht.

Zwar ist eine Generalisierung der Ergebnisse auf Szenarien außerhalb der in der Arbeit betrachteten Bedingungen nicht unmittelbar möglich. Dennoch zeigt diese Arbeit, dass Anwendungen der Nachlaufablenkung durch das Ausnutzen von datengetriebenen Methoden profitieren können. Darüber hinaus illustriert diese Arbeit, dass ein solcher Nutzen bereits mit einfachen, interpretierbaren Methoden erreicht werden kann.

# Contents

|                                                                                    |             |
|------------------------------------------------------------------------------------|-------------|
| <b>Abstract</b>                                                                    | <b>iii</b>  |
| <b>Zusammenfassung</b>                                                             | <b>v</b>    |
| <b>List of Figures</b>                                                             | <b>x</b>    |
| <b>List of Tables</b>                                                              | <b>xvii</b> |
| <b>List of Abbreviations</b>                                                       | <b>xix</b>  |
| <b>List of Symbols</b>                                                             | <b>xx</b>   |
| <b>1 Introduction</b>                                                              | <b>1</b>    |
| 1.1 Climate change . . . . .                                                       | 1           |
| 1.2 Renewable energy . . . . .                                                     | 2           |
| 1.3 Atmospheric variability . . . . .                                              | 4           |
| 1.4 Turbine wake . . . . .                                                         | 5           |
| 1.5 Wind farm control . . . . .                                                    | 6           |
| 1.6 Data-driven solutions . . . . .                                                | 8           |
| 1.7 Objective and research questions . . . . .                                     | 9           |
| 1.8 Structure of the thesis . . . . .                                              | 9           |
| <b>2 Methods</b>                                                                   | <b>12</b>   |
| 2.1 Large-eddy simulations . . . . .                                               | 12          |
| 2.1.1 Governing Equations . . . . .                                                | 13          |
| 2.1.2 Boundary conditions . . . . .                                                | 15          |
| 2.1.3 Wind direction change . . . . .                                              | 16          |
| 2.1.4 Wind turbine model . . . . .                                                 | 18          |
| 2.2 Machine learning models . . . . .                                              | 20          |
| 2.2.1 Multi-task lasso algorithm . . . . .                                         | 21          |
| 2.2.2 Mean shift clustering algorithm . . . . .                                    | 22          |
| 2.3 Lidar . . . . .                                                                | 23          |
| 2.3.1 Measurement trajectories . . . . .                                           | 24          |
| 2.3.2 Lidar Simulator . . . . .                                                    | 25          |
| <b>3 A new method to characterize the curled wake shape under yaw misalignment</b> | <b>27</b>   |
| 3.1 Introduction . . . . .                                                         | 28          |
| 3.2 Methodology . . . . .                                                          | 29          |

|          |                                                                                                                             |           |
|----------|-----------------------------------------------------------------------------------------------------------------------------|-----------|
| 3.2.1    | Large-eddy simulations . . . . .                                                                                            | 29        |
| 3.2.2    | Wake tracking algorithms . . . . .                                                                                          | 31        |
| 3.3      | Results and discussion . . . . .                                                                                            | 32        |
| 3.3.1    | Evaluation of the proposed Multiple 1D Gaussian method . . . . .                                                            | 32        |
| 3.3.2    | Future applications . . . . .                                                                                               | 36        |
| 3.4      | Conclusions . . . . .                                                                                                       | 37        |
| <b>4</b> | <b>A physically interpretable data-driven surrogate model for wake steering</b>                                             | <b>38</b> |
| 4.1      | Introduction . . . . .                                                                                                      | 39        |
| 4.2      | Large-eddy simulations . . . . .                                                                                            | 40        |
| 4.2.1    | Precursor simulations . . . . .                                                                                             | 41        |
| 4.2.2    | Main simulations . . . . .                                                                                                  | 42        |
| 4.3      | Development of the Data-driven wAKE steeRING surrogaTe model . . . . .                                                      | 43        |
| 4.3.1    | Defining key wake steering parameters . . . . .                                                                             | 44        |
| 4.3.2    | Input parameters . . . . .                                                                                                  | 45        |
| 4.3.3    | Regression model . . . . .                                                                                                  | 47        |
| 4.3.4    | Wake composition: reversed multiple 1D Gaussian . . . . .                                                                   | 47        |
| 4.3.5    | Feature selection . . . . .                                                                                                 | 48        |
| 4.3.6    | Benchmark models . . . . .                                                                                                  | 49        |
| 4.4      | Results . . . . .                                                                                                           | 49        |
| 4.4.1    | Performance on training data . . . . .                                                                                      | 49        |
| 4.4.2    | Performance on testing data . . . . .                                                                                       | 51        |
| 4.4.3    | Operation without derating . . . . .                                                                                        | 52        |
| 4.5      | Discussion . . . . .                                                                                                        | 54        |
| 4.5.1    | Generalizability . . . . .                                                                                                  | 54        |
| 4.5.2    | Interpretability . . . . .                                                                                                  | 54        |
| 4.5.3    | Speed test . . . . .                                                                                                        | 55        |
| 4.6      | Conclusions . . . . .                                                                                                       | 56        |
| <b>5</b> | <b>Validation of an interpretable data-driven wake model using lidar measurements from a field wake steering experiment</b> | <b>57</b> |
| 5.1      | Introduction . . . . .                                                                                                      | 58        |
| 5.2      | Measurement campaign . . . . .                                                                                              | 60        |
| 5.2.1    | Measurement site . . . . .                                                                                                  | 60        |
| 5.2.2    | Yaw control experiment . . . . .                                                                                            | 61        |
| 5.2.3    | Nacelle lidar . . . . .                                                                                                     | 62        |
| 5.2.4    | Ground-based lidar (VAD) . . . . .                                                                                          | 65        |
| 5.2.5    | Met mast . . . . .                                                                                                          | 66        |
| 5.2.6    | Wind turbine operational data . . . . .                                                                                     | 66        |
| 5.2.7    | GPS . . . . .                                                                                                               | 66        |
| 5.2.8    | Selection of data for model evaluation . . . . .                                                                            | 66        |
| 5.3      | Methods . . . . .                                                                                                           | 68        |
| 5.3.1    | Multiple 1D Gaussian method . . . . .                                                                                       | 68        |
| 5.3.2    | Reference power . . . . .                                                                                                   | 69        |
| 5.3.3    | Training and testing data . . . . .                                                                                         | 69        |
| 5.3.4    | Data-driven wAKE steeRING surrogaTe model (DART) . . . . .                                                                  | 70        |
| 5.3.5    | Analytical wake model . . . . .                                                                                             | 73        |

|          |                                                                                                      |            |
|----------|------------------------------------------------------------------------------------------------------|------------|
| 5.4      | Results . . . . .                                                                                    | 74         |
| 5.4.1    | Observed wake characteristics . . . . .                                                              | 74         |
| 5.4.2    | Performance of wake models . . . . .                                                                 | 77         |
| 5.5      | Discussion . . . . .                                                                                 | 82         |
| 5.5.1    | Campaign . . . . .                                                                                   | 82         |
| 5.5.2    | Data-driven model . . . . .                                                                          | 84         |
| 5.5.3    | Implications for future work . . . . .                                                               | 85         |
| 5.6      | Conclusions . . . . .                                                                                | 86         |
| <b>6</b> | <b>Increased power gains from wake steering control using preview<br/>wind direction information</b> | <b>87</b>  |
| 6.1      | Introduction . . . . .                                                                               | 88         |
| 6.2      | Turbine yaw controller . . . . .                                                                     | 89         |
| 6.2.1    | Greedy . . . . .                                                                                     | 89         |
| 6.2.2    | Wake steering . . . . .                                                                              | 89         |
| 6.3      | Simulation environment . . . . .                                                                     | 91         |
| 6.3.1    | Engineering model . . . . .                                                                          | 91         |
| 6.3.2    | Large-eddy simulations . . . . .                                                                     | 93         |
| 6.4      | Results . . . . .                                                                                    | 96         |
| 6.4.1    | Engineering model . . . . .                                                                          | 96         |
| 6.4.2    | Large-eddy simulations . . . . .                                                                     | 99         |
| 6.4.3    | Comparison of large-eddy simulation and engineering model<br>results . . . . .                       | 104        |
| 6.5      | Discussion . . . . .                                                                                 | 105        |
| 6.5.1    | Comparison to existing literature . . . . .                                                          | 105        |
| 6.5.2    | Generalizability . . . . .                                                                           | 106        |
| 6.5.3    | Large-eddy simulation considerations . . . . .                                                       | 106        |
| 6.5.4    | Forecasting wind direction changes . . . . .                                                         | 106        |
| 6.5.5    | Yaw controller . . . . .                                                                             | 107        |
| 6.5.6    | Effect of preview control on yawing action and loads . . . . .                                       | 108        |
| 6.6      | Conclusions . . . . .                                                                                | 108        |
| <b>7</b> | <b>Conclusions and outlook</b>                                                                       | <b>110</b> |
| 7.1      | Conclusions . . . . .                                                                                | 110        |
| 7.2      | Outlook . . . . .                                                                                    | 112        |
|          | <b>Bibliography</b>                                                                                  | <b>114</b> |
|          | <b>Publications</b>                                                                                  | <b>133</b> |
|          | <b>Acknowledgments</b>                                                                               | <b>136</b> |
|          | <b>Curriculum Vitae</b>                                                                              | <b>137</b> |

# List of Figures

|     |                                                                                                                                                                                                                                                                                                                                                                                                                                                                                                                 |    |
|-----|-----------------------------------------------------------------------------------------------------------------------------------------------------------------------------------------------------------------------------------------------------------------------------------------------------------------------------------------------------------------------------------------------------------------------------------------------------------------------------------------------------------------|----|
| 1.1 | Global energy consumption per source <b>(a)</b> . Global renewable energy mix <b>(b)</b> . Data from BP (2022) via Our World in Data (Ritchie et al., 2022). . . . .                                                                                                                                                                                                                                                                                                                                            | 2  |
| 1.2 | Increase of energy consumption (2021 vs 1991) and percentage of wind and solar in energy mix for selection of countries, grouped by continent / region. Black cross indicates the global average. Data from BP (2022) via Our World in Data (Ritchie et al., 2022). . . . .                                                                                                                                                                                                                                     | 3  |
| 1.3 | Projected 2050 scenarios of energy consumption in the EU. Source: European Commission (2020b). . . . .                                                                                                                                                                                                                                                                                                                                                                                                          | 3  |
| 1.4 | 30-year mean wind speed at 100 m above surface over Europe, calculated from the New European Wind Atlas (NEWA). Source: Fraunhofer IWES (2019). . . . .                                                                                                                                                                                                                                                                                                                                                         | 5  |
| 1.5 | Number of publications mentioning the keywords "Turbine" and "Wind Farm Control" (black), "Axial Induction Control" (red) and "Wake Steering" (blue) in the title or abstract. Source: Digital Science (2018-) . . . . .                                                                                                                                                                                                                                                                                        | 7  |
| 1.6 | Structure of the thesis. "Ch" is short for Chapter, "RQ" is short for Research Question. . . . .                                                                                                                                                                                                                                                                                                                                                                                                                | 10 |
| 2.1 | Example of flow field of a turbulent jet modeled with RANS <b>(a)</b> , LES <b>(b)</b> and DNS <b>(c)</b> . Reused from Rodriguez (2019). . . . .                                                                                                                                                                                                                                                                                                                                                               | 12 |
| 2.2 | Illustrative sketches of domains in the simulation chain. <b>(a)</b> Precursor run with cyclic boundary conditions to generate turbulence and subsequent main run with one turbine using the turbulence recycling method. Figure inspired by IMUK (2022). <b>(b)</b> Same precursor run with one wind direction, subsequent theta run to change the wind direction and save planes to use as inflow in a main run with two turbines to simulate a wind direction change propagating through the domain. . . . . | 17 |
| 2.3 | Illustrative sketches of four wind turbine models: <b>(a)</b> Actuator Disc Model, <b>(b)</b> Actuator Disc Model with Rotation, <b>(c)</b> Actuator Line Model and <b>(d)</b> Actuator Sector Model. Red arrows indicate thrust, blue arrows torque. . . . .                                                                                                                                                                                                                                                   | 18 |
| 2.4 | <b>(a)</b> Visualization of relations within Artificial Inteligence. Reused from Miraftabzadeh et al. (2019). <b>(b)</b> Visualization of the classes within Machine learning. Reused from Kim and Tagkopoulos (2019). <b>(c)</b> Scikit-learn cheat sheet. Reused from scikit-learn (2022) . . . . .                                                                                                                                                                                                           | 20 |
| 2.5 | Non-zero elements (black) of $B$ for the output variable for the original lasso <b>(a)</b> and multi-task lasso <b>(b)</b> . . . . .                                                                                                                                                                                                                                                                                                                                                                            | 22 |

|     |                                                                                                                                                                                                                                                                                                                                                                                                                                                                                       |    |
|-----|---------------------------------------------------------------------------------------------------------------------------------------------------------------------------------------------------------------------------------------------------------------------------------------------------------------------------------------------------------------------------------------------------------------------------------------------------------------------------------------|----|
| 2.6 | (a) Schematic illustrating of the fundamental principle behind the Mean Shift clustering algorithm. Reused from Sok and Adams (2010). (b) Results from the Mean Shift clustering algorithm on three exemplary data set. Adapted from You et al. (2022). . . . .                                                                                                                                                                                                                       | 23 |
| 2.7 | Example of backscattered frequency distribution illustrating a doppler shift. Reused from Werner (2005). . . . .                                                                                                                                                                                                                                                                                                                                                                      | 24 |
| 2.8 | Sketches of pulsed lidar scanning trajectories. (a) PPI (blue) and RHI (purple) scans. Reused from Beck and Kühn (2019). (b) VAD scan. Adapted from Sathe and Mann (2013). . . . .                                                                                                                                                                                                                                                                                                    | 25 |
| 2.9 | LiXim trajectory with five PPI scans. Red markers indicate measurement points, black solid lines the path, starting at the lower right position. The blue shaded area illustrates the turbine wake. . . . .                                                                                                                                                                                                                                                                           | 26 |
| 3.1 | (a) Exemplary figure (SBL30, 5 rotor diameters downstream) illustrating the concept of the $f_{M1D}$ method, where the thick black lines illustrate two horizontal cross-sections. (b) and (c) demonstrate the fitting procedure at these two heights. . . . .                                                                                                                                                                                                                        | 31 |
| 3.2 | Exemplary figures (SBL30, 5 rotor diameters downstream) demonstrating (a) the positions of the wake center line, (b) the determination of the vertical wake center position based on the magnitudes of the wake center line and (c) the definition of wake curl $a$ [-] and tilt $\arctan b$ [°] based on wake center line. Information from the set of crosswise fitted Gaussian distributions is indicated with black crosses and red lines illustrate the fitted relation. . . . . | 32 |
| 3.3 | Vertical cross-section (looking downstream) of the SBL00 LES wake deficit wind field 5 rotor diameters downstream of the simulated turbine and the wake center positions identified by all methods (a). Reconstructed wind fields based on $f_{1D}$ (b), $f_{2D}$ (c) and $f_{M1D}$ (d). . . . .                                                                                                                                                                                      | 33 |
| 3.4 | Same as Figure 3.3, but for SBL30. . . . .                                                                                                                                                                                                                                                                                                                                                                                                                                            | 33 |
| 3.5 | Percentage Error of available power of a downstream turbine computed with a wind field based on $f_{1D}$ (black), $f_{2D}$ (blue), $f_{M1D}$ (red) relative to when computed with the LES wind field (calculated with $(P_{f_{xx}} - P_{LES})/P_{LES} * 100\%$ ). The boxplots include all six simulations described in Section 3.2.1. . . . .                                                                                                                                        | 34 |
| 3.6 | Wake center trajectories for NBL (a,c) and SBL (b,d) representing horizontal (a,b) and vertical (c,d) deflection for yaw angles of 0 (black), 30 (blue) and -30 (red) degrees. . . . .                                                                                                                                                                                                                                                                                                | 35 |
| 3.7 | Evolution of the wake curliness downstream of the turbine for two stratifications and three yaw angles. . . . .                                                                                                                                                                                                                                                                                                                                                                       | 36 |
| 3.8 | Preliminary result showing the potential of the development of a physically based empirical wake deflection parameterization. Contours indicate the SBL30 LES wind field at hub height, the black line indicate the wake center trajectory and the red line the wake center trajectory predicted with a simple statistical model. . . . .                                                                                                                                             | 37 |

|      |                                                                                                                                                                                                                                                                                                                                                                                                                                                                                                                                                                                                                                                                                                                                                      |    |
|------|------------------------------------------------------------------------------------------------------------------------------------------------------------------------------------------------------------------------------------------------------------------------------------------------------------------------------------------------------------------------------------------------------------------------------------------------------------------------------------------------------------------------------------------------------------------------------------------------------------------------------------------------------------------------------------------------------------------------------------------------------|----|
| 4.1  | Summary of inflow parameters (60 min averages), given as mean (dots) and standard deviation (whiskers) over the 15 main simulations performed in each BL (5 yaw angles times 3 pitch angles). Considered are wind speed ( $u_h$ ) and turbulence intensity at hub height (TI), wind shear ( $\alpha$ ) and veer ( $\delta\alpha$ ) over the rotor area, and the Obukhov stability parameter ( $zL^{-1}$ ) at $z = 2.5$ m. Equations for these variables can be found in Table 4.3. . . . .                                                                                                                                                                                                                                                           | 42 |
| 4.2  | Overview of the effect of yaw angle $\phi$ and pitch angle $\beta$ on thrust coefficient $C_T$ . Whiskers indicate the standard deviation between all eight BLs. . . . .                                                                                                                                                                                                                                                                                                                                                                                                                                                                                                                                                                             | 43 |
| 4.3  | Flowchart describing the training <b>(a)</b> and execution <b>(b)</b> procedure of DART. The section in which the process is described is indicated in parentheses. The coefficient matrix generated in <b>(a)</b> is used in <b>(b)</b> . . . . .                                                                                                                                                                                                                                                                                                                                                                                                                                                                                                   | 44 |
| 4.4  | Exemplary figures (BL1, $\phi = +30^\circ$ , $x = 5$ D) illustrating the key wake steering parameters. <b>(a)</b> Normalized wake deficit cross-section (contour) of original LES data. <b>(b)</b> The local normalized wake center deficits <b>A</b> , <b>(c)</b> local wake center positions $\mu$ , and <b>(d)</b> local wake widths $\sigma$ . Black crosses indicate LES, solid red lines the relation fitted in according to the multiple 1D Gaussian method (Sect. 4.3.1) and dashed red lines the assumed continuation in the reversed multiple 1D Gaussian composition method (Sect. 4.3.4). <b>(e)</b> Cross-section (contour) of the normalized wake deficit after applying the reversed multiple 1D Gaussian composition method. . . . . | 45 |
| 4.5  | Correlation matrix of the dimensionless input parameters in LES. Colors indicate a positive (red) or negative (blue) correlation. . . . .                                                                                                                                                                                                                                                                                                                                                                                                                                                                                                                                                                                                            | 46 |
| 4.6  | Accuracy of the wake composition procedure expressed as a percentage error in available power of a virtual downstream turbine. At each downstream distance, data from all 120 simulations are considered. The subplot in the top right zooms in to $4 D \leq x \leq 10 D$ . Axis labels correspond to those of the main plot. . . . .                                                                                                                                                                                                                                                                                                                                                                                                                | 48 |
| 4.7  | Performance of all models on training data displayed as percentage error in available power. In black GAUS, in blue GCH, in green DART-8 and in red DART-3. The boxes on the far right (labeled 4–10) include all simulations and all distances. The shaded areas indicate a significant improvement (green), insignificant difference (yellow) or significant decline (red) in the accuracy of DART compared to the benchmark models. . . . .                                                                                                                                                                                                                                                                                                       | 50 |
| 4.8  | Performance of GAUS (black), GCH (blue) and DART-3 (red) using a leave-one-out cross-validation technique. Performance is displayed as a percentage error in available power. Each box includes data from 15 main simulations and $4 D \leq x \leq 10 D$ . The shaded areas again indicate a significant improvement (green), insignificant difference (yellow) or significant decline (red) in the accuracy of DART-3 compared to the benchmark models. . . . .                                                                                                                                                                                                                                                                                     | 52 |
| 4.9  | Same as Fig. 4.8, but only for cases with $\beta = 0^\circ$ , i.e., without derating the turbine. . . . .                                                                                                                                                                                                                                                                                                                                                                                                                                                                                                                                                                                                                                            | 53 |
| 4.10 | Same as Fig. 4.9, but for partial-wake operation, i.e., with a virtual downstream turbine moved 0.5 D to the left. . . . .                                                                                                                                                                                                                                                                                                                                                                                                                                                                                                                                                                                                                           | 53 |



|      |                                                                                                                                                                                                                                                                                                                                                                                                                                                                                                                                                                                                                                                                   |    |
|------|-------------------------------------------------------------------------------------------------------------------------------------------------------------------------------------------------------------------------------------------------------------------------------------------------------------------------------------------------------------------------------------------------------------------------------------------------------------------------------------------------------------------------------------------------------------------------------------------------------------------------------------------------------------------|----|
| 4.11 | Case study of a turbine in a weakly stable boundary layer (BL3, $\phi = +30^\circ$ , $\beta = 0^\circ$ ). Cross-section of normalized wake deficit (contours) of the LES <b>(a)</b> , DART-3 <b>(b)</b> and GAUS <b>(c)</b> at $x = 6$ D downstream. <b>(d)</b> Wake center trajectory at $4\text{ D} \leq x \leq 10\text{ D}$ . . . . .                                                                                                                                                                                                                                                                                                                          | 54 |
| 4.12 | Regression coefficients of DART-3 estimating $\mu_y$ at $x = 6$ D using scaled input parameters. Since all input parameters are dimensionless, the corresponding coefficients are also dimensionless. Variable $y_0$ indicates the intercept or systematic offset. . . . .                                                                                                                                                                                                                                                                                                                                                                                        | 55 |
| 5.1  | Layout of the measurement site with the local topography, relative to mean sea level, indicated in the background. Black markers indicate turbines, where T1 is equipped with the nacelle lidar. White markers indicate the meteorological mast (MM) and ground-based lidar (VAD). Shaded areas indicate the wind direction sector with $\phi_t > 0^\circ$ (red) and $\phi_t < 0^\circ$ (yellow) and where wake measurements are assumed to be disturbed by the downstream turbines (grey). The thick solid black line indicates the measured locations used for analysis. (Source for topographic map including color bar: topographic-map.com, 2022.) . . . . . | 61 |
| 5.2  | Results of the virtual lidar tests. Bars indicate the mean and whiskers the standard deviation of the absolute percentage error (APE) of available power $P_{\text{av}}$ over six simulations. The number of PPI scans is indicated on the $x$ axis. “all” indicates the use of all numerical data, hence the error introduced by the composition method. The opaqueness represents the lidar’s angular speed $\omega_{\text{lidar}}$ . . . . .                                                                                                                                                                                                                   | 63 |
| 5.3  | Examples of multiple PPI scan filtering in LOS–CNR diagrams in which black markers indicate original data and red markers data kept after filtering. <b>(a)</b> A textbook case with few outliers that indicate hard targets and <b>(b)</b> a more problematic case in which there are many corrupted measurements. Here yellow markers indicate a second cluster from which all measurements were omitted. Black crosses indicate the two cluster centers. . . . .                                                                                                                                                                                               | 64 |
| 5.4  | Data availability of the 10 min averaged cases as a function of achieved yaw angle ( $\phi$ ). Colors indicate the targeted $\phi_t = -15^\circ$ (yellow), $\phi_t = 0^\circ$ (blue) and $\phi_t = +15^\circ$ (red). Solid vertical lines and accompanying text mark the median of the achieved yaw angles. . . . .                                                                                                                                                                                                                                                                                                                                               | 68 |
| 5.5  | Distribution of 10 min averaged inflow variables measured at the met mast for all 382 cases: hub height wind speed ( $U_h$ ), turbulence intensity (TI), shear ( $\alpha$ ) and veer ( $\delta\alpha$ ). . . . .                                                                                                                                                                                                                                                                                                                                                                                                                                                  | 68 |
| 5.6  | Correlation matrix of available input variables. In addition to the inflow variables shown in Fig. 5.5, yaw misalignment $\phi$ , rotor speed $\omega$ and power $P$ are considered input variables. . . . .                                                                                                                                                                                                                                                                                                                                                                                                                                                      | 72 |
| 5.7  | Performance of DART-3 on the training data. The set of input variables is $\{\phi, \alpha, P\}$ . <b>(a)</b> Histogram of PE of $P_{\text{av}}$ for one resample. Fitted normal distributions are indicated with solid lines, and MPE and MAPE are given in the top right. Histograms of MPEs <b>(b)</b> and MAPEs <b>(c)</b> over all 96 resamples. . . . .                                                                                                                                                                                                                                                                                                      | 72 |

|      |                                                                                                                                                                                                                                                                                                                                                                                                                                                                                                                                                                           |    |
|------|---------------------------------------------------------------------------------------------------------------------------------------------------------------------------------------------------------------------------------------------------------------------------------------------------------------------------------------------------------------------------------------------------------------------------------------------------------------------------------------------------------------------------------------------------------------------------|----|
| 5.8  | Correlation matrix of the input variables and wake characteristics. $A_z$ is the amplitude of the wake deficit normalized by $U_h$ , $\mu_y$ and $\mu_z$ the lateral and vertical wake center displacement, “curl” and “tilt” the wake curl and tilt, $\sigma_y$ and $\sigma_z$ the width and height of the wake, and $s_a$ and $s_b$ the quadratic and linear wake width parameter. . . . .                                                                                                                                                                              | 75 |
| 5.9  | Scatterplot of <b>(a)</b> $\mu_y$ and <b>(b)</b> curl as a function of yaw angle $\phi$ . Red markers indicate field measurements, and blue triangles indicate LES data. Fitted linear functions are indicated with lines. The quality of these fits is indicated by the correlation coefficient $R$ , corresponding to Fig. 5.8. White plus signs indicate the case studied in Fig. 5.10. . . . .                                                                                                                                                                        | 76 |
| 5.10 | Exemplary case illustrating the wake curl generated by a misaligned turbine ( $\phi = 12.8^\circ$ , $U_h = 9.4 \text{ m s}^{-1}$ , $\alpha = 0.33$ , $\delta\alpha = -0.8^\circ$ , $\text{TI} = 10.4\%$ ). <b>(a)</b> The wake deficit of the 10 min averaged lidar data of 17 consecutive PPI scans (colors) and local wake center positions (black plus signs) with corresponding fitted polynomial (dashed black line) indicating the wake curl. <b>(b)</b> The wake reconstructed by utilizing the composition method. The color bar applies to both figures. . . . . | 76 |
| 5.11 | Like Fig. 5.7 but for the testing data for GCH (black/grey), DART-3 (red), DART-4 (blue) and DART-7 (yellow). Histogram <b>(a)</b> for one resample and <b>(b)</b> for MPEs and <b>(c)</b> for MAPEs of all 96 resamples. Fitted normal distributions are indicated with lines, and statistics are given in the top right. . . . .                                                                                                                                                                                                                                        | 77 |
| 5.12 | Performance of GCH (grey), DART-4 (blue) and DART-7 (yellow) as a function of $\phi$ <b>(a–c)</b> and $\alpha$ <b>(d–f)</b> . Histogram of data availability per bin <b>(a, d)</b> and corresponding MPE <b>(b, e)</b> and MAPE <b>(c, f)</b> per bin. . . . .                                                                                                                                                                                                                                                                                                            | 78 |
| 5.13 | Accuracy of GCH <b>(a–c)</b> , DART-4 <b>(d–f)</b> and DART-7 <b>(g–i)</b> in estimating wake characteristics $A_z$ <b>(a, d, f)</b> , $\mu_y$ <b>(b, e, h)</b> and curl <b>(c, f, i)</b> . The models’ estimates are given on the $x$ axis and the observations on the $y$ axis. Solid lines indicate linear orthogonal distance regression fits and dashed lines the identity lines. . . . .                                                                                                                                                                            | 79 |
| 5.14 | MPE <b>(a)</b> and MAPE <b>(b)</b> as a function of training data set size. Markers indicate the means ( $\overline{\text{MPE}}$ and $\overline{\text{MAPE}}$ ), lines indicate the median and shaded areas indicate the standard deviation, corresponding to the fitted normal distributions in Fig. 5.11. . . . .                                                                                                                                                                                                                                                       | 80 |
| 5.15 | Same as Fig. 5.11b–c but with DART-4S (light blue). . . . .                                                                                                                                                                                                                                                                                                                                                                                                                                                                                                               | 82 |
| 5.16 | Results of the tests of Table 5.3. $\overline{\text{MPE}}$ and $\overline{\text{MAPE}}$ of Test 0 correspond to the values found in Fig. 5.11. . . . .                                                                                                                                                                                                                                                                                                                                                                                                                    | 84 |
| 6.1  | Target yaw misalignment $\phi_t$ as a function of the 60s averaged wind direction $\bar{\delta}$ for a changing wind direction standard deviation of $\sigma_\delta$ with a wind veer $\bar{\delta\alpha} = 4^\circ$ <b>(a)</b> and for a changing $\bar{\delta\alpha}$ with $\sigma_\delta = 4^\circ$ <b>(b)</b> . A turbine spacing of 6D is assumed and $\bar{\delta} = 0^\circ$ indicates the wind direction where the turbine pair is aligned. . . . .                                                                                                               | 91 |

|      |                                                                                                                                                                                                                                                                                                                                                                                                                                                                                 |     |
|------|---------------------------------------------------------------------------------------------------------------------------------------------------------------------------------------------------------------------------------------------------------------------------------------------------------------------------------------------------------------------------------------------------------------------------------------------------------------------------------|-----|
| 6.2  | Examples of the engineering model's results for a wind direction change rate of $\theta = 80^\circ \text{ h}^{-1}$ . Gray lines indicate the wind direction of an <b>(a)</b> smooth and <b>(b)</b> turbulent time series. Black and yellow indicate greedy SC and PC; blue and red indicate wake steering SC and PC, respectively. A turbine spacing of 6 D is assumed, and $\bar{\delta} = 0^\circ$ indicates the wind direction in which the turbine pair is aligned. . . . . | 93  |
| 6.3  | Examples of wind fields illustrating a wind direction change propagating through the domain. Wind field <b>(b)</b> is taken 140 s after wind field <b>(a)</b> . The background color indicates the wind speed and the arrows indicate the wind direction. The solid black lines indicate the turbines, both of which are operating in greedy control without preview information. The yellow markers indicate the location of the virtual met mast. . . . .                     | 95  |
| 6.4  | Turbine pair power gain $\Delta P$ of greedy control (yellow) and wake steering control (red) with PC relative to greedy SC as a function of preview time for wind direction change rates of $\theta = 80^\circ \text{ h}^{-1}$ <b>(a)</b> and $\theta = 160^\circ \text{ h}^{-1}$ <b>(b)</b> . Lines indicate the mean and shaded areas indicate the 95 % confidence interval over 50 turbulent time series. . . . .                                                           | 96  |
| 6.5  | Optimal preview time <b>(a)</b> and corresponding power gain relative to greedy SC <b>(b)</b> as a function of $\theta$ . Yellow indicates greedy PC, blue indicates wake steering SC, and red indicates wake steering PC. Lines indicate the mean and shaded areas indicate the 95 % confidence interval over 50 turbulent time series. . . . .                                                                                                                                | 97  |
| 6.6  | Histogram of optimum preview time <b>(a)</b> and corresponding power gain <b>(b)</b> when using wind direction measurements from a met mast. Lines indicate the median optimum preview time <b>(a)</b> and corresponding mean power gain <b>(b)</b> . Colors correspond to those used in Fig. 6.5. . . . .                                                                                                                                                                      | 98  |
| 6.7  | <b>(a)</b> Histogram of met mast data binned in mean of absolute differences (MAD). <b>(b)</b> Power gain of steering SC relative to greedy SC (blue) and power gain of steering PC relative to greedy SC (red). Power gains averaged over all 815 cases are noted in the top right corner. . . . .                                                                                                                                                                             | 99  |
| 6.8  | Simulated wind direction cases. Raw (gray) and low-pass-filtered (black) signals at the upstream turbine are shown, as well as the forced (dashed red) signal. <b>(a)</b> Case 1: a slowly varying wind direction change. <b>(b)</b> Case 2: a fast-varying wind direction change. . . . .                                                                                                                                                                                      | 100 |
| 6.9  | LES results for Case 1 <b>(a–b)</b> and Case 2 <b>(c–d)</b> . The left column shows the wind direction $\delta$ (gray, see Fig. 6.8) and orientations of the upstream turbine $\gamma$ (colors). The right column shows the raw (transparent) and low-pass-filtered (opaque) power gain $\Delta P$ relative to greedy SC. The gain averaged over the simulation $\overline{\Delta P}$ is indicated in the legend. . . . .                                                       | 101 |
| 6.10 | Seed analysis of low-frequency fluctuations. Averaged power gains $\overline{\Delta P}$ of six seeds for slowly varying $\text{MAD} < 40^\circ \text{ h}^{-1}$ <b>(a)</b> and fast-varying $\text{MAD} > 140^\circ \text{ h}^{-1}$ <b>(b)</b> wind direction changes. The average of all seeds is indicated on the far right. . . . .                                                                                                                                           | 103 |

|      |                                                                                                                                                                                                                                                                                                                                                                                          |     |
|------|------------------------------------------------------------------------------------------------------------------------------------------------------------------------------------------------------------------------------------------------------------------------------------------------------------------------------------------------------------------------------------------|-----|
| 6.11 | Same as Fig. 6.10, but for the seed analysis of high-frequency fluctuations. . . . .                                                                                                                                                                                                                                                                                                     | 104 |
| 6.12 | Comparison of the engineering model and LES in estimating the power gain $\overline{\Delta P}$ . The Pearson correlation coefficient ( $R$ ), mean absolute error (MAE) and orthogonal distance regression fit are indicated. <b>(a)</b> All results, <b>(b)</b> the results split by control strategy and <b>(c)</b> the results split by variability of the wind direction signal. . . | 105 |
| 6.13 | Same as Fig. 6.9, but for a case where $\delta = 0^\circ$ is crossed several times.                                                                                                                                                                                                                                                                                                      | 109 |
| 6.14 | Same as Fig. 6.11, but for a case where $\delta = 0^\circ$ is crossed several times.                                                                                                                                                                                                                                                                                                     | 109 |

# List of Tables

|     |                                                                                                                                                                                                                                                                                                                                                                                                                                                                                                                                                                                                                                        |    |
|-----|----------------------------------------------------------------------------------------------------------------------------------------------------------------------------------------------------------------------------------------------------------------------------------------------------------------------------------------------------------------------------------------------------------------------------------------------------------------------------------------------------------------------------------------------------------------------------------------------------------------------------------------|----|
| 3.1 | Summary of simulation parameters for precursor and main simulations. The length ( $t$ ) and size ( $L_x, L_y, L_z$ ) of the precursor simulations (normalized by the rotor diameter ( $D = 126$ m)) is determined empirically until convergence to a stationary state occurs. The size of the domain of the main simulations is extended only in streamwise direction. The geostrophic wind ( $u_g, v_g$ ) is constant in precursor and corresponding main simulations. . . . .                                                                                                                                                        | 29 |
| 3.2 | Summary of the most relevant inflow parameters, given as mean and standard deviation over the three main simulations. Results consist of rotor effective wind speed ( $U_{eff}$ ), turbulence intensity at hub height ( $TI_h$ ), wind shear ( $\alpha$ ) and veer ( $\delta\alpha$ ) over the rotor area and the Obukhov Length ( $L$ ). . . . .                                                                                                                                                                                                                                                                                      | 30 |
| 4.1 | Summary of simulation parameters and classification into neutral (NBL), near-neutral (NNBL), weakly stable (WSBL) and stable (SBL) boundary layers. The size ( $L_{x,p}, L_y, L_z$ ) of the domains is normalized by the rotor diameter ( $D = 126$ m). All parameters are identical in precursor and main simulations, except for the domain size, which is extended in the streamwise direction ( $L_{x,m}$ ); $t_p$ is the simulated time of the precursor run, $u_g$ and $v_g$ the geostrophic wind, $\partial\theta\partial t^{-1}$ the heating rate, $H$ the sensible heat flux, and $z_0$ the surface roughness length. . . . . | 41 |
| 4.2 | Defined dimensionless key wake steering parameters. The normalized wake deficit is computed as described in Sect. 4.2.2. All length parameters are nondimensionalized by the rotor diameter $D$ . . . . .                                                                                                                                                                                                                                                                                                                                                                                                                              | 45 |
| 4.3 | Set of dimensionless input parameters: $dir$ is the wind direction [ $^\circ$ ], $z$ is the height above the surface [m], $\bar{u}_h$ and $\sigma_{u_h}$ are the mean and standard deviation of the wind speed at hub height [ $\text{m s}^{-1}$ ], $u_{eff}$ is rotor effective wind speed [ $\text{m s}^{-1}$ ], $T$ is thrust [N], $Q$ is torque [N m], and $\omega$ is rotor speed [ $\text{rad s}^{-1}$ ]. Subscript $_{ut}$ indicates upper-tip and $_{lt}$ lower-tip height. . . . .                                                                                                                                            | 46 |
| 4.4 | Model training (DART) or tuning (GAUS and GCH) time using all 120 simulations and seven ( $4D \leq x \leq 10D$ ) downstream distances. Iteration times are expressed as the mean over the first 100 iterations. DART's total is a simple multiplication of iteration and combinations. . . . .                                                                                                                                                                                                                                                                                                                                         | 51 |
| 4.5 | Model run time [ms] when simulating seven ( $4D \leq x \leq 10D$ ) and one ( $x = 6D$ ) downstream distances expressed as mean $\pm$ standard deviation over 40 iterations. . . . .                                                                                                                                                                                                                                                                                                                                                                                                                                                    | 56 |

|     |                                                                                                                                                                                                    |    |
|-----|----------------------------------------------------------------------------------------------------------------------------------------------------------------------------------------------------|----|
| 5.1 | Dimensionless variables describing the wake characteristics obtained with the multiple 1D Gaussian method. Reused from Sengers et al. (2022) with permission. . . . .                              | 69 |
| 5.2 | Overview of all possible combinations of input variables in DART-3 and their respective $\overline{\text{MAPE}}$ values. Boldface indicates the combination resulting in the lowest error. . . . . | 73 |
| 5.3 | Overview of all tests carried out for the uncertainty analysis. . . . .                                                                                                                            | 84 |

# List of Abbreviations

|                          |                                                              |
|--------------------------|--------------------------------------------------------------|
| ADMR                     | Actuator Disc Model with Rotation                            |
| AEP                      | Annual Energy Production                                     |
| APE                      | Absolute Percentage Error                                    |
| BL                       | Boundary Layer                                               |
| CNR                      | Carrier-to-noise ratio                                       |
| DART                     | Data-driven wake steering surrogate model                    |
| FLORIS                   | Flow Redirection and Induction in Steady-state               |
| GAUS                     | Gaussian wake model                                          |
| GCH                      | Gaussian-Curl Hybrid model                                   |
| LES                      | Large-eddy simulation                                        |
| LOS                      | Line-of-sight velocity                                       |
| LUT                      | Look-up table                                                |
| MAD                      | Mean of absolute differences                                 |
| MAE                      | Mean absolute error                                          |
| MAPE                     | Mean absolute percentage error                               |
| $\overline{\text{MAPE}}$ | Mean of the mean absolute percentage errors of all resamples |
| MM                       | Meteorological mast                                          |
| MPE                      | Mean percentage error                                        |
| $\overline{\text{MPE}}$  | Mean of the mean percentage errors of all resamples          |
| NBL                      | Neutral Boundary Layer                                       |
| NNBL                     | Near Neutral Boundary Layer                                  |
| PALM                     | Parallelized Large-eddy simulation Model                     |
| PC                       | Preview control                                              |
| PE                       | Percentage error                                             |
| PPI                      | Plan position indicator                                      |
| $R$                      | Pearson correlation coefficient                              |
| SBL                      | Stable Boundary Layer                                        |
| SC                       | Standard control                                             |
| SCADA                    | Standard supervisory control and data acquisition            |
| VAD                      | Velocity-azimuth display                                     |
| WRC                      | Wake Redirection Control                                     |
| WSBL                     | Weakly Stable Boundary Layer                                 |

# List of Symbols

Some inconsistencies in the use of symbols between the chapters are present. Since these are published works, it was decided to keep the symbols as published in the respective papers. Besides, this list does not include symbols used only in Chapter 2 (Methods), as this chapter introduces many symbols that are only used locally.

|                                                                  |                                                                                      |
|------------------------------------------------------------------|--------------------------------------------------------------------------------------|
| $\partial\Theta \partial t^{-1}, \partial\theta \partial t^{-1}$ | Heating rate                                                                         |
| $\alpha$                                                         | Vertical wind shear                                                                  |
| $\alpha_{\text{floris}}, \alpha_{\text{GCH}},$                   | Tuning parameter GAUS & GCH                                                          |
| $\beta$                                                          | Blade pitch angle                                                                    |
| $\beta_{\text{floris}}, \beta_{\text{GCH}}$                      | Tuning parameter GAUS & GCH                                                          |
| $\gamma$                                                         | Turbine orientation                                                                  |
| $\Delta$                                                         | Grid size. When followed by another symbol, it indicates a difference                |
| $\delta$                                                         | Wind direction                                                                       |
| $\delta_{\text{h}}$                                              | Wind direction at hub height. When indicating measurement data, it is measured at MM |
| $\delta_{\text{lp}}$                                             | Low-pass filtered wind direction                                                     |
| $\delta_{\text{lt}}$                                             | Wind direction at lower tip height                                                   |
| $\delta_{\text{S}}$                                              | Wind direction at hub height, measured at nacelle (SCADA)                            |
| $\delta\alpha$                                                   | Vertical wind veer                                                                   |
| $\theta$                                                         | Wind direction change rate                                                           |
| $\theta_{\text{VAD}}$                                            | Azimuth angle VAD lidar                                                              |
| $\mu_y$                                                          | Lateral wake center displacement                                                     |
| $\mu_z$                                                          | Vertical wake center displacement                                                    |
| $\rho$                                                           | Air density                                                                          |
| $\sigma$                                                         | Standard deviation of Gaussian fit, indicates width of wake                          |
| $\sigma_{\delta}$                                                | Wind direction standard deviation, uncertainty parameter                             |
| $\sigma_{u_{\text{h}}}$                                          | Standard deviation of the wind speed at hub height                                   |
| $\sigma_y$                                                       | Width of wake at center height                                                       |
| $\sigma_z$                                                       | Vertical extent                                                                      |
| $\phi$                                                           | Yaw misalignment angle                                                               |
| $\phi_{\text{e}}$                                                | Effective yaw misalignment angle                                                     |
| $\phi_{\text{PPI}}$                                              | Elevation angle PPI scans                                                            |
| $\phi_{\text{S}}$                                                | Yaw misalignment angle, measured at nacelle (SCADA)                                  |
| $\phi_{\text{t}}$                                                | Target yaw misalignment angle                                                        |
| $\phi_{\text{VAD}}$                                              | Elevation angle VAD lidar                                                            |
| $\omega$                                                         | Rotor speed                                                                          |
| $\omega_{\text{lidar}}$                                          | Angular speed of lidar scan                                                          |



|                                                     |                                                                                                                |
|-----------------------------------------------------|----------------------------------------------------------------------------------------------------------------|
| $A_z$                                               | Amplitude of wake deficit normalized with $U_h$                                                                |
| $C_T$                                               | Thrust coefficient                                                                                             |
| $C_Q$                                               | Torque coefficient                                                                                             |
| $C_P$                                               | Power coefficient                                                                                              |
| curl                                                | Wake curl                                                                                                      |
| $D, D$                                              | Rotor diameter                                                                                                 |
| $H$                                                 | Sensible heat flux                                                                                             |
| $k_{a,\text{floris}}, k_{a,\text{GCH}}$             | Tuning parameter GAUS & GCH                                                                                    |
| $k_{b,\text{floris}}, k_{b,\text{GCH}}$             | Tuning parameter GAUS & GCH                                                                                    |
| $L$                                                 | Obukhov length                                                                                                 |
| $L_x, L_y, L_z$                                     | Domain size in x, y, z direction                                                                               |
| $P$                                                 | Power                                                                                                          |
| $P_{\text{av}}$                                     | Available power                                                                                                |
| $s_a$                                               | Quadratic wake width parameter                                                                                 |
| $s_b$                                               | Linear wake width parameter                                                                                    |
| $t$                                                 | Time                                                                                                           |
| TI                                                  | Turbulence intensity                                                                                           |
| $TI_h, TI_h$                                        | Turbulence intensity at hub height                                                                             |
| $TI_S$                                              | Turbulence intensity, measured at nacelle                                                                      |
| TSR                                                 | Tip Speed Ratio                                                                                                |
| tilt                                                | Wake tilt                                                                                                      |
| $U$                                                 | Horizontal wind speed                                                                                          |
| $u$                                                 | Streamwise component of horizontal wind speed. Used interchangeably with $U$ when wind direction is irrelevant |
| $U_\infty, u_\infty$                                | Undisturbed inflow wind speed                                                                                  |
| $U_{\text{def}}, U_{\text{def}}, u_{\text{def}}$    | Wake deficit                                                                                                   |
| $U_{\text{eff}}, U_{\text{eq}}$                     | Rotor effective or equivalent wind speed, used interchangeably                                                 |
| $U_h, u_h$                                          | Wind speed at hub height. When indicating measurement data, it is measured at MM                               |
| $U_{\text{lt } i}$                                  | Wind speed at lower tip height                                                                                 |
| $U_S$                                               | Wind speed at hub height, measured at nacelle (SCADA)                                                          |
| $U_{\text{wake}}, U_{\text{wake}}, u_{\text{wake}}$ | Wind speed in the wake                                                                                         |
| $u_g, v_g$                                          | Components of the geostrophic wind                                                                             |
| $z_0$                                               | Surface roughness length                                                                                       |
| $z L^{-1}$                                          | Obukhov stability parameter                                                                                    |

# Chapter 1

## Introduction

### 1.1 Climate change

In the 1700s mankind discovered that fossil fuels could be used to power machinery, starting an age of economic prosperity in the form of the industrial revolution (Lucas Jr., 2004). The use of heavy machinery in factories and the invention of the steam engine are some of the most classical examples. The second industrial revolution, about a century later, brought steel production that allowed a quick expansion of the rail network (Agarwal and Agarwal, 2017). It also brought electrification, greatly increasing the productivity of factories by shifting from steam to electric powered machinery, which further increased the economic growth (Devine Jr., 1983). The development of the electricity grid, first initiated by the Edison Electric Illuminating Company of New York (Hargadon and Douglas, 2001), paved the way for household electrification.

Although current generations still benefit from the technological progress made during these revolutions, it also initiated the biggest threat to life on earth to date: climate change. As early as the late 1800s, scientists (Phillips, 1882; Arrhenius, 1896) have been warning that burning fossil fuels, specifically the emission of carbon dioxide that goes with it, affects the earth's climate. In the following decades, some scientists would try to raise attention for this threat (e.g., Callendar, 1938; Plass, 1956), but governments and the general public were just not interested. In a 1965 report produced by the US government's President's Science Advisory Committee (Revelle et al., 1965), CO<sub>2</sub> emissions were finally recognized as a potential hazard. Coauthor of this report was Prof. Keeling, who established the CO<sub>2</sub> monitoring site at the Mauna Loa Observatory, Hawaii, producing what is now known as the 'Keeling Curve' (Harris, 2010). After this report, an uptake in scientific and news articles related to climate change could be observed (Harrison, 1982). The growing interest eventually led to the formation of the Intergovernmental Panel on Climate Change (IPCC) in 1988, who bundle relevant literature on climate change in assessment reports (IPCC, 2022). The first big step towards policies mitigating the effects of climate change came during the 1992 United Nations Framework Convention on Climate Change that led to the Kyoto protocol, in which states committed to reduce greenhouse gas emissions. The Paris Agreement followed in 2015, with the agreement to keep the global temperature rise below 2 °C, and was signed by 193 parties (United Nations, 2022).

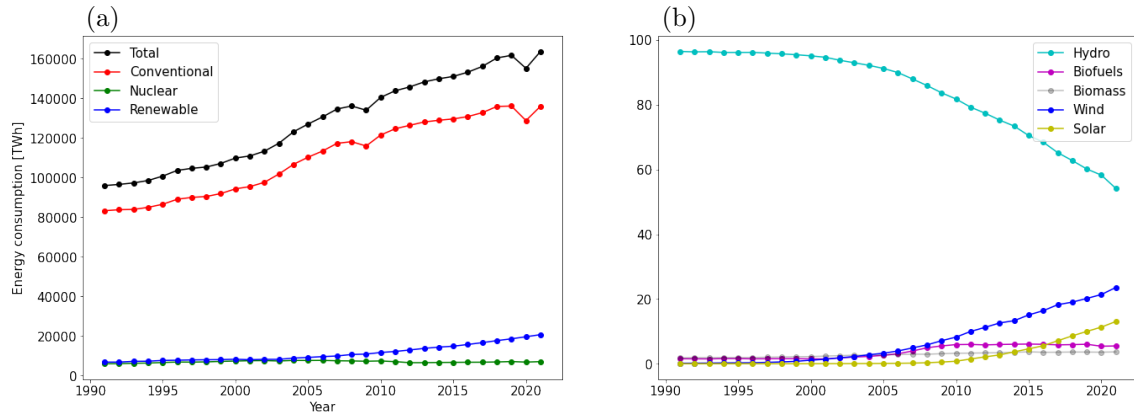


Figure 1.1: Global energy consumption per source (a). Global renewable energy mix (b). Data from BP (2022) via Our World in Data (Ritchie et al., 2022).

## 1.2 Renewable energy

The reduction of energy consumption and the transition from conventional to renewable sources of energy are considered two key aspects to meet the Paris Agreement. Although these objectives were established several decades before and countries have formally committed to these goals, information on energy consumption developments sketches a more pessimistic story. Figure 1.1a shows that the total energy demand has increased by 70 % in the last three decades, with no signs of slowing down. The vast majority of energy is still provided by conventional sources (coal, gas and oil), with renewable sources only satisfying 12.6 % of the total energy demand. Figure 1.1b indicates what source make up the renewable energy mix, illustrating that historically hydropower was the dominant source. In recent years, wind and solar have gained momentum, now taking up 37 % of the total energy gained from renewable energy resources, or 4.6 % of the total energy demand.

Although almost all countries have signed the Paris Agreement, the difference in realization of climate goals differs enormously, as clearly illustrated in Figure 1.2. European countries appear to be the most committed, typically showing a small reduction of energy consumption over the last 30 years and the largest percentages of wind and solar in the energy mix. On the other side of the spectrum are countries in Asia and the Middle East, with energy consumption increases of several hundred percents. Asian countries typically have a relatively high installed capacity of renewables, whereas countries in the Middle East rely mainly on conventional sources. It should be noted here that the effect of outsourcing, mainly by European and North American countries, has not been included in these numbers. Allocating the energy needed to produce and transport goods to the countries in which they are eventually used, would alter this figure drastically.

One of the biggest climate policies currently in place is the EU green deal, initiated in December 2019 and updated several times since. With the green deal, Europe aims to reduce greenhouse gas emissions by 55 % by 2030 (compared to 1990 levels), followed by being the first climate-neutral continent by 2050 (European Commission, 2021). Developments in many fields are targeted, including mobility, biodiversity and clean energy, totaling to an investment of €1 trillion until 2030 (European

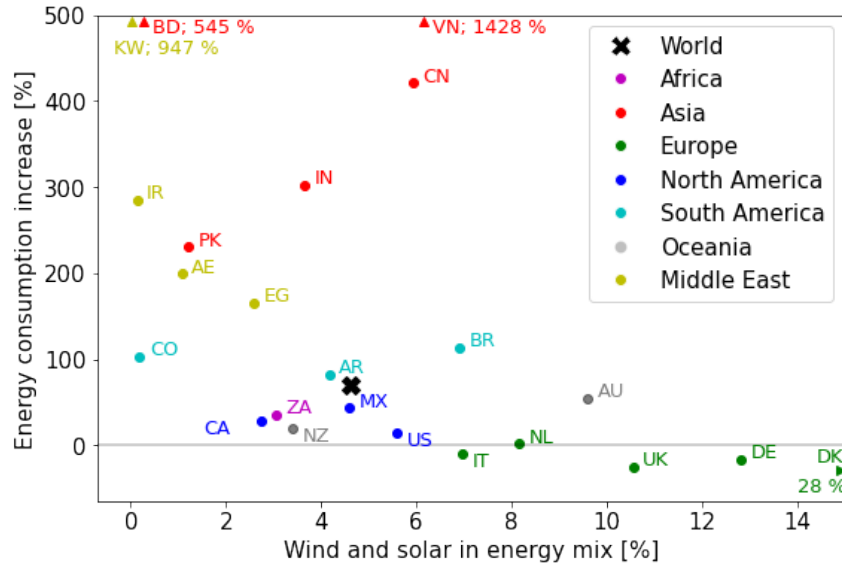


Figure 1.2: Increase of energy consumption (2021 vs 1991) and percentage of wind and solar in energy mix for selection of countries, grouped by continent / region. Black cross indicates the global average. Data from BP (2022) via Our World in Data (Ritchie et al., 2022).

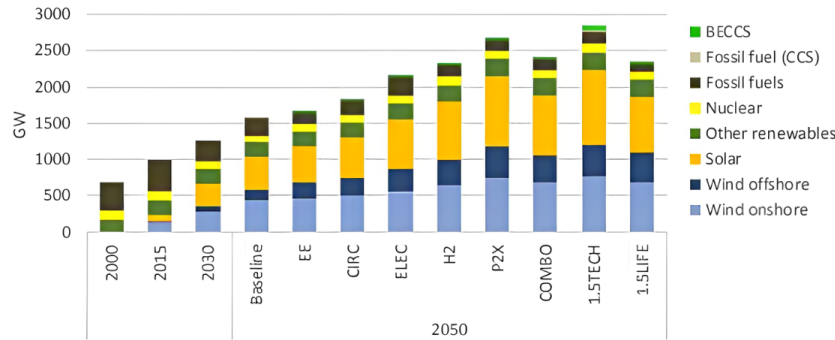


Figure 1.3: Projected 2050 scenarios of energy consumption in the EU. Source: European Commission (2020b).

Commission, 2020a). Since energy production and use accounted for more than 75 % of the emissions (European Commission, 2021), the energy transition is one of the main pillars for successfully reaching these climate goals.

Various scenarios of the targeted energy mix in 2050 are illustrated in Fig. 1.3. All scenarios assume an approximately equal contribution of solar and wind, where their installed capacity should make up at least 75 % of the power demand. The 2020 Offshore wind and ocean energy strategy had already set the concrete goal of an installed offshore capacity of 300 GW in 2050 (European Commission, 2020c). The REPowerEU plan (European Commission, 2022), a resultant of the EU's desire to be independent of Russian gas after their invasion of Ukraine, mentions 600 GW of solar photovoltaic newly installed by 2030. REPowerEU states that a total of €300 billion will be invested to reach the goal of 45 % of renewables in the energy mix by 2030.

The US government launched the Federal Sustainability Plan in late 2021, aiming to reach net-zero emission by 2050 from all federal operations (The White House,

2021a). Although a strong sign, this plan does not extend to the private sector. The White House (2021b) announced the goal to install 30 GW of offshore wind by 2030, and 110 GW by 2050. The Department Of Energy (2021) outlines the potential of solar energy, with an estimated capacity of 550 GW in 2030 and 1600 GW in 2050. One large difference with the EU is that the US mainly relies on private investments to build new solar and wind farms.

### 1.3 Atmospheric variability

One of the most challenging aspect of power generation from wind and solar sources is their dependency on the weather. Whereas conventional forms of energy production can be tuned to match the region’s demand at any given time, wind and solar are subject to the variability of the atmospheric boundary layer. Focusing on wind energy in the rest of this thesis, power output fluctuations are heavily correlated to variations of the wind speed. This exists on a range of spatial and temporal scales.

The location of the wind farm has a huge impact on its Annual Energy Production (AEP). The earth’s surface exerts a friction force on the atmospheric flow, effectively slowing down the wind close to the surface. The magnitude of this friction depends on the surface roughness, which is smaller offshore and larger where the terrain is rough (e.g. forest). The effect of terrain can clearly be seen by looking at the wind speed climatology (long term averages), such as Figure 1.4. Far offshore the mean wind speed is highest, whereas the wind speed decreases rapidly over land. Also the effect of topography is clearly visible: the local differences in the Alps are huge, indicating mountain tops and valleys, whereas the average wind speed in northern Italy is very low due to blockage.

Meteorological conditions affect the wind farm’s power yield on a range of temporal scales. On the largest scale there is intra-annual variability, such as the effect climate change is expected to have on the wind energy resource. Zha et al. (2021) modeled that global warming causes the near-surface wind speed in the Northern Hemisphere to decrease, but that it increases in the Southern Hemisphere. Pryor and Barthelmie (2010); Pryor et al. (2012) reported on an increased occurrence of extreme wind. Tobin et al. (2016) modeled that the effect on the AEP on a global scale is small, but locally can be affected by up to 15 %. Besides climate change, the El Niño-Southern Oscillation, a change in wind direction over the Pacific Ocean that brings drastic changes in temperature and rainfall in Asia and the Americas, is also thought to affect the wind resource. Watts et al. (2016) modeled that the wind speed in Chile is reduced by several percent during El Niño events. On the contrary, Mohammadi and Goudarzi (2018) report on an increased probability of higher wind speeds in California during El Niño events based on 50 years of data.

Seasonality is typically better understood and well researched, but its impact differs greatly with location. The monsoon winds are a common phenomenon around the equator, bringing in a change in dominant wind direction between seasons. Abolude et al. (2017) report on large seasonal differences between regions in Asia depending on the wind direction. The region around India and Bangladesh sees a four-fold increase in power availability in summer months compared to the rest of the year due to a strong wind coming from the Indian Ocean. The South Chinese sea experiences this maximum during winter months due to wind from the North East.

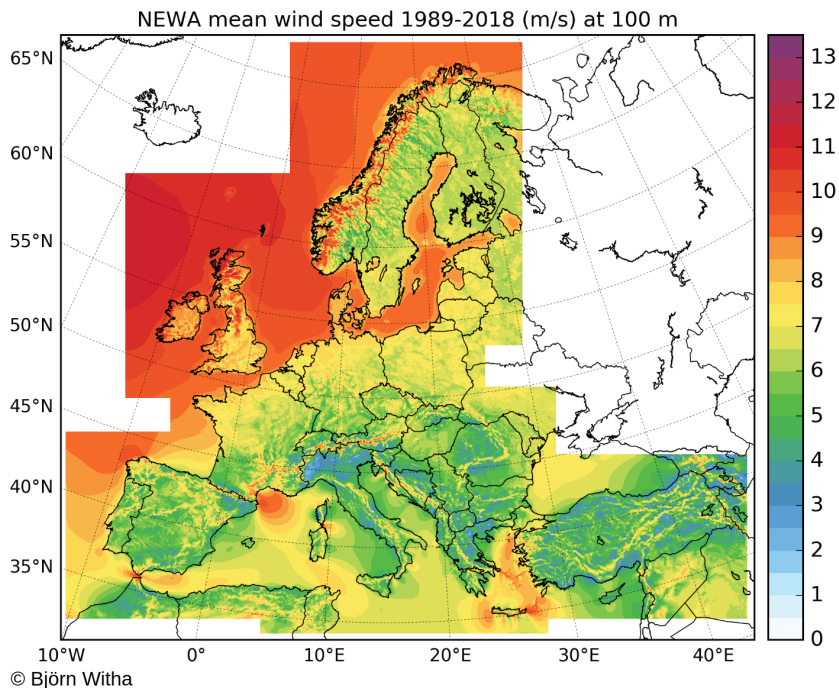


Figure 1.4: 30-year mean wind speed at 100 m above surface over Europe, calculated from the New European Wind Atlas (NEWA). Source: Fraunhofer IWES (2019).

Both can be explained by the wind coming from the open sea, rather than from land, corresponding to Fig. 1.4. Also at higher latitudes seasonal differences can be observed. Nyenah et al. (2022) report on a capacity factor 2.5 times as high in winter as in summer in North East Germany. The U.S. Energy Information Administration (2015) shows large seasonal differences in the US alone, with wind capacity peaking in summer on the west coast, but in winter in the rest of the country.

On a shorter time scale, the occurrence of mesoscale weather systems impact the power generation. High pressure systems are often associated with calm weather and low wind speeds. These systems can sustain for several days, resulting in low generated power. On the contrary, low pressure systems are typically associated with stormy weather and higher wind speeds, resulting in a high power generation. Besides, these cyclones also have far-stretching weather fronts surrounding them, typically associated with rapid changes in wind direction and speed, called wind ramps (Lacerda et al., 2017). Especially when the wind speeds are close to the cut-out limit, these ramp events can be critical to forecast to ensure grid stability (Valdecabres et al., 2020).

## 1.4 Turbine wake

By extracting energy from the atmospheric flow, wind turbines leave a downstream region of decreased wind speed and increased turbulence (Lissaman, 1979). This region is typically named the turbine wake, and results in power losses and increased loads of a downstream turbine. Wake effects are estimated to lead to wind farm power losses of up to 50-60 % for certain wind directions (e.g., Nilsson et al., 2014; Grassi et al., 2014). Its effective AEP is highly dependent on wind farm layout and

turbine spacing, as illustrated in van der Laan et al. (2022). In their study, AEP losses of about 10 % were estimated for an 8x8 wind farm with a turbine spacing of 8 rotor diameters, which increased to almost 25 % when the spacing was halved. The characteristics of the wake are dependent on many variables. The wake deficit (wind speed difference compared to the undisturbed inflow) depends on the turbine characteristics. The thrust force the turbine exerts on the flow has the largest impact as it determines how much energy is extracted. Each turbine type has its own characteristic  $C_T$ -curve describing the optimum thrust force coefficient as a function of wind speed. The  $C_T$  is decreased by sub-optimal blade pitch angles or tip speed ratio (Kim et al., 2018) and a misalignment of the turbine with the incoming wind direction (Bartl et al., 2018a). Next to wind speed, there are other atmospheric variables that affect the wake’s characteristics. As a higher turbulence intensity results in enhanced mixing, it is directly linked to wake recovery and wake expansion (Bastankhah and Porté-Agel, 2014; Niayifar and Porté-Agel, 2016). Vertical wind shear, the difference in wind speed between two heights due to friction at the surface, affects the transport of momentum. Due to the rotation of the wake, lower momentum parcels closer to the surface are transported upwards and vice versa. This increases mixing and results in a small wake displacement (Fleming et al., 2014a; Gebraad et al., 2016). The difference in wind direction between two heights following the Ekman spiral, named vertical wind veer, affects the shape of the wake. In the Northern Hemisphere, the top half of the wake is deflected to the right, whereas the bottom half is deflected to the left, creating an elliptic wake shape as demonstrated in Abkar et al. (2018). Lastly, atmospheric stability is often considered in wake studies. It is driven by a temperature difference between the surface and air layers, resulting in either the generation of turbulence (convective or unstable boundary layer) or destruction of turbulence (stable boundary layer). Both divert the wind speed profile from a pure logarithmic function as typically assumed. The effects of stability on the wake characteristics are mainly indirect, as it influences both the turbulence intensity and shear (Gryning et al., 2007; Abkar and Porté-Agel, 2015).

## 1.5 Wind farm control

In standard operation of a wind farm, each turbine aims to maximize its own power generation, called greedy control. Due to the negative effects turbine wakes have on downstream turbines (Sect. 1.4), the idea of wind farm control has received an increasing amount of attention in recent years, as illustrated by increase in the number of publications in Fig. 1.5. The fundamental idea of this control strategy is to maximize the power generation of the wind farm as a whole, rather than on an individual turbine level. Typically, the upstream turbine is deliberately operated sub-optimally, causing a power loss but also a reduced wake deficit that reaches a downstream turbine. The weaker wake will benefit the downstream turbine and result in an increased power generation. When performed successfully, the combined power of the two turbines will be larger than for the greedy control strategy.

Relying on the nonlinear relation of wind speed and power, Axial Induction Control (AIC) reduces the turbine’s axial induction factor by increasing the blade pitch angle. This results in a derating of the turbine (Steinbuch et al., 1988) and consequently a weaker wake. The effectiveness of AIC is under debate, with some studies showing

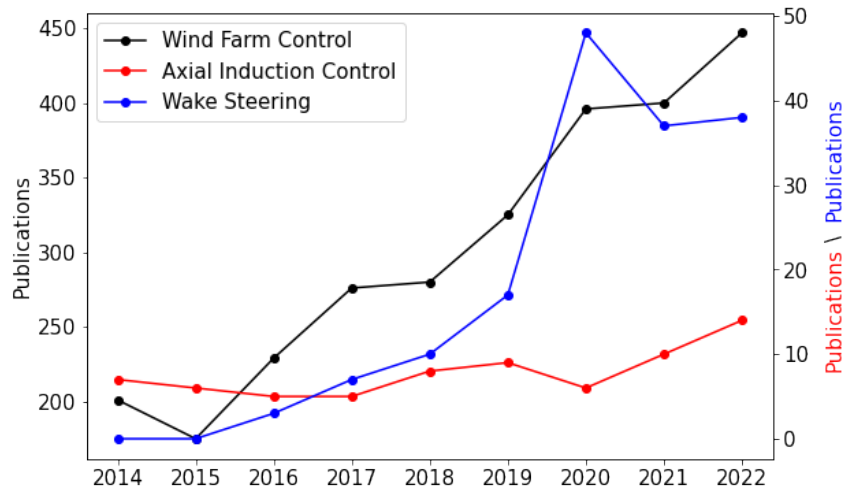


Figure 1.5: Number of publications mentioning the keywords "Turbine" and "Wind Farm Control" (black), "Axial Induction Control" (red) and "Wake Steering" (blue) in the title or abstract. Source: Digital Science (2018-)

promising results (e.g., Corten and Schaak, 2003; Vali et al., 2016), while others find no or negligible benefits (e.g., Annoni et al., 2016; van der Hoek et al., 2019).

Another wind farm control strategy, named wake steering, intentionally misaligns the turbine with the mean wind direction. This introduces a lateral component of the thrust force, which deflects the wake off of its normal trajectory (Dahlberg and Medici, 2003; Wagenaar et al., 2012). Wake steering is commonly accepted as a promising wind farm control strategy, as is evident from the fast growing list of publications (Fig. 1.5). The overview in Kheirabadi and Nagamune (2019) illustrates that the vast majority of studies finds a power gain when using wake steering.

Other, less well explored wind farm control strategies worth mentioning are turbine repositioning (Fleming et al., 2015) and wake steering via nacelle tilt or via individual blade pitch control (Fleming et al., 2014a).

The scope of this thesis is limited to wind farm control by wake steering. A few noteworthy studies are discussed next. For a turbine pair in steady state conditions, Fleming et al. (2015) illustrated a power gain of 4.6 % using a high-fidelity simulation tool, which was increased to 12.5 % in Fleming et al. (2018) for a larger wind farm. In the first wind tunnel study, Adaramola and Krogstad (2011) found a gain of 12 % for a turbine pair in steady state conditions. For the implementation of wake steering in the free field, where conditions are more dynamic, set points of optimal yaw misalignment angles need to be defined for a range of atmospheric conditions. For this reason, low-fidelity wake models, or engineering models, have been developed. These wake models are often simplified flow models that heavily rely on assumptions to make them several orders of magnitude more computationally efficient than high-fidelity flow models. Wake models are employed to find the optimum yaw misalignment angle under a range of atmospheric conditions, such as various wind speeds and wind directions. Typically, a lookup-table (LUT) is generated, containing the target yaw angle for each combination of inflow variables. This LUT will then be used by the turbine's yaw controller to implement wake steering. Using this approach, Fleming et al. (2017b) first demonstrated a power



gain of up to 12 % achieved with wake steering in a commercial wind farm, paving the way for many field experiments in the years following.

Currently, the main reasons for the lack of adaptation of wake steering by the industry are the large uncertainties and lack of validation (van Wingerden et al., 2020; Boccolini et al., 2021). As illustrated by the overview in Kheirabadi and Nagamune (2019), the expected gains from wake steering varies enormously between studies. Additionally, there have been reports on erroneous steering, observing power losses compared to greedy control, which is destructive for the faith in this strategy by the industry. A better understanding of the impact of atmospheric conditions on the characteristics of the wake, as discussed in Sect. 1.4, and a good reproduction of these effects in wake models is deemed paramount for the industrial adoption of wake steering.

## 1.6 Data-driven solutions

More data supporting the benefit of wake steering need to be gathered to convince the industry. These data will be used to demonstrate power gains achievable with wake steering, as well as to validate and further develop models of all fidelities. This section highlights developments that are believed to facilitate this in the coming years.

Nowadays, society is going through the fourth industrial revolution, characterized by rapid technological developments, such as robotics (e.g., autonomous vehicles), gene editing, and advancements in computing technologies (Schwab, 2016). The latter can affect the wind energy industry in many ways. Moore’s law (Moore, 1965, 1975) postulates that the number of transistors on microchips doubles every two years, resulting in faster and more affordable computers. Furthermore, quantum computing holds high expectations, possibly benefiting the wind energy community in the future. These advancements allow more users to work with numerical models and to further develop more complex and more computational expensive models, like large-eddy simulations (LES). This all contributes to enhancing our fundamental understanding of the atmospheric and wind farm flow physics, which was identified as one of the grand challenges in wind energy science (Veers et al., 2019). Specifically, this can then also be used to deepen our understanding of how atmospheric conditions affect wake steering.

Beside the increase in computational power, the emergence of the Internet of Things (IoT) technology offers new opportunities. IoT refers to the communication of sensors over the internet and is associated with cloud computing and big data. Typical examples are smart home appliances and health monitoring devices (Rose, 2015). Karad and Thakur (2021) argued that IoT is approaching the field of wind energy and that it will be especially beneficial in turbine monitoring and control, maintenance, and prediction systems. Wind farm control, specifically wake steering, can benefit from IoT by enabling the use of data from more sensors than the anemometer and vane installed on the nacelle roof. Using more (undisturbed) data can be used to reduce the measurement error (Sinner et al., 2020; van der Hoek et al., 2021), provide preview information (Rott et al., 2020; Theuer et al., 2020), or give feedback in a closed-loop setup (Howland et al., 2020, 2022).

Lastly, flow modeling is being transformed by the rapid development of artificial intelligence or machine learning (Brunton et al., 2020). Whereas analytical and

statistical models have been the norm for the last decades, wind farm flow modeling is shifting towards data-driven methods (Zehtabiyani-Rezaie et al., 2022). Machine learning methods can, for instance, provide a feasible alternative for low-fidelity wake models, which as discussed in Sect. 1.4 are normally heavily simplified to ensure low computational costs. Although data-driven models can be expensive to train, their execution time is comparable to that of low-fidelity models. Some studies (e.g., Ti et al., 2020; Asmuth and Korb, 2022) have already shown the high accuracy of data-driven wake models using Neural Networks. Drawback of these models are their complexity and low degree of interpretability (black box). Furthermore, these models have a high need for data, but with the ongoing developments in computational power and IoT, this last argument might soon become obsolete. Many industries are adopting these new technological opportunities and the wind energy industry seems to be following. It is fitting that solving climate change issues induced by the first industrial revolution could be facilitated by developments of the fourth industrial revolution.

## 1.7 Objective and research questions

Based on the current state of wake steering research and emerging computing technologies, the main objective of this thesis is defined as follows:

*Demonstrate the benefit of interpretable data-driven approaches  
for wake steering applications*

The keyword "interpretable" here refers to the desire to be explainable or understandable. The first part of this thesis is tasked with the design of a wake model that is purely data-driven and retains a high degree of interpretability. In the second part of this thesis, this wake model is applied to study how the wake steering concept can be further improved. Each of the following research questions is answered in the subsequent chapters:

1. How can characteristics of a steady state wake be described with a set of quantifiable parameters?
2. How can these wake parameters be estimated from inflow and turbine variables?
3. What variables and how much data need to be obtained in the field to estimate these wake parameters?
4. What conditions are detrimental for wake steering and can these be mitigated by using preview wind direction information?

## 1.8 Structure of the thesis

This section describes the structure of the thesis according the flow chart in Fig. 1.6. Chapter 1 has placed this work in the wider context of climate change and energy transition, and has provided a general understanding of wake effects and how they can be mitigated with the wake steering control strategy. It ended on a short description of emerging computing technologies and how wake steering can

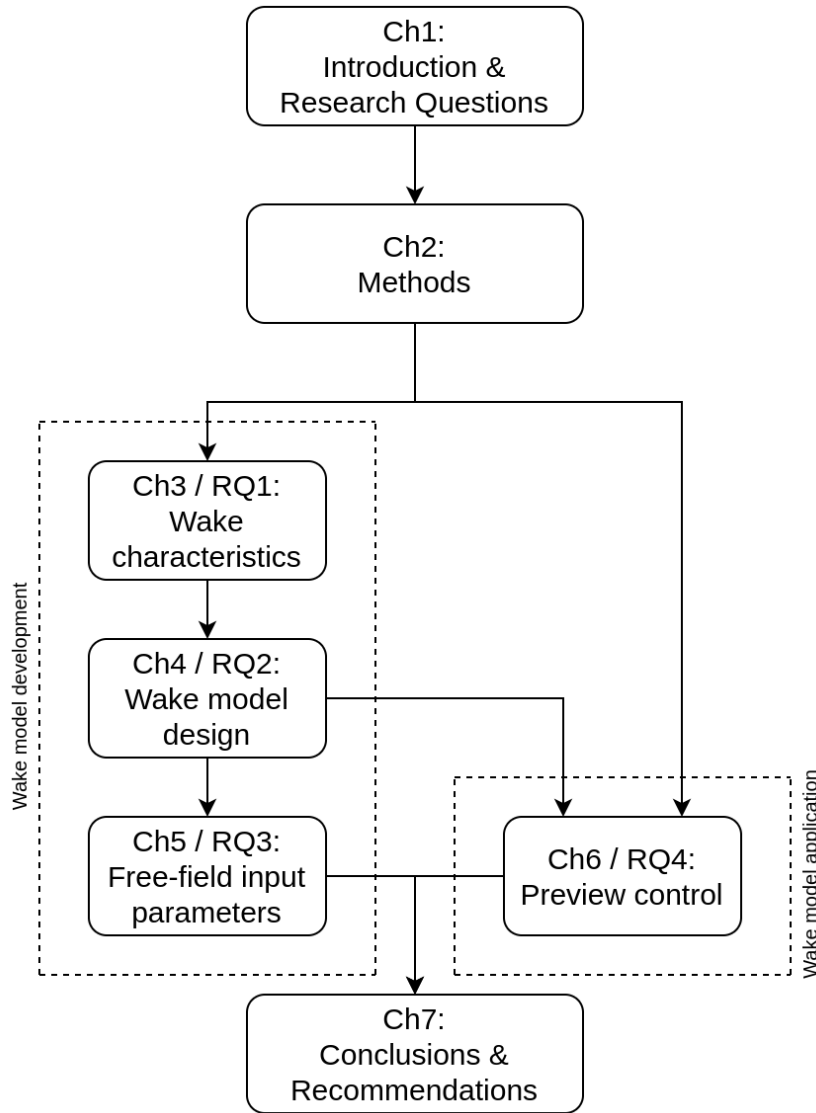


Figure 1.6: Structure of the thesis. "Ch" is short for Chapter, "RQ" is short for Research Question.

benefit from them, resulting in the thesis objectives and related research questions. Chapter 2 provides background information of the methods used in this thesis. This consists of fundamentals of the main numerical model and measurement device used to obtain data. Additionally, a notion on used Machine Learning methods is included.

In Chapter 3, representing the conference paper Sengers et al. (2020), the first step towards data-drive wake modeling is made by developing a method to describe the wake characteristics as a set of quantifiable parameters. Small additions to the method presented in this Chapter are mentioned in Sect. 4.3.1. The wake behind a single turbine in a neutral and stable boundary layer is simulated in LES. The wake characteristics of turbines with and without intentional misalignment are described using the new method. This method is then compared to conventional wake tracking methods and its results are used to discuss the wake behavior as function of stability and yaw angle.

In Chapter 4, representing the journal paper Sengers et al. (2022), the interpretable

data-driven wake model is designed. Making use of only linear equations, the wake model estimates wake characteristics from standard inflow (e.g., shear, veer, TI) and turbine (e.g., yaw angle, thrust force coefficient) variables. Turbine wakes in eight conditions, representing different atmospheric stabilities, and several yaw angles are simulated in LES. The wake model is trained on a subset of the data and its performance is tested on the remainder.

In Chapter 5, representing the journal paper Sengers et al. (2023b), the wake model is applied to field data. Information on the wake is provided by a nacelle-mounted long-range lidar, while inflow data is collected by sensors mounted on a met mast and the nacelle. Many variables are collected during this extensive campaign, allowing for an analysis of the wake model's accuracy as function of the variables used as input parameters. This includes a setup in which only standard measurements (SCADA data) is used.

In Chapter 6, representing the submitted journal paper Sengers et al. (2023a), a theoretical study of the effectiveness of wake steering for different wind direction time series is performed. A simple engineering model based on the previously developed wake model analyses many time series, after which a few interesting ones are reproduced in LES. It is hypothesized that scenarios problematic for wake steering can be mitigated by the use of preview wind direction information. Investigating whether this is true makes up the main objective of this chapter.

Lastly, Chapter 7 summarizes the main findings, draws conclusions from them, and provides recommendations for future research.

# Chapter 2

## Methods

This chapter describes the main methods used in this thesis. First, in Sect. 2.1 the large-eddy simulation model PALM, which played a large role in this work, is described. This includes a general description of the governing principles, as well as aspects specific to this work. Section 2.2 then briefly introduces Machine Learning, including a more detailed description of the algorithms used here. Lastly, Sect. 2.3 briefly discusses lidar devices used for wind applications, as well as a summary of how these devices were used in this work.

### 2.1 Large-eddy simulations

Within computational fluid dynamics (CFD), three branches of models are typically distinguished. The highest fidelity comprises of Direct Numerical Simulations (DNS), which run at a grid size of a few millimeters to directly solve the governing equations and explicitly solve all turbulence. These simulations are currently still restricted to low Reynolds number flows due to their huge computational demand. Large-eddy simulations (LES) provide a more computationally feasible method by only explicitly resolving the largest turbulence scales and parameterizing the smaller

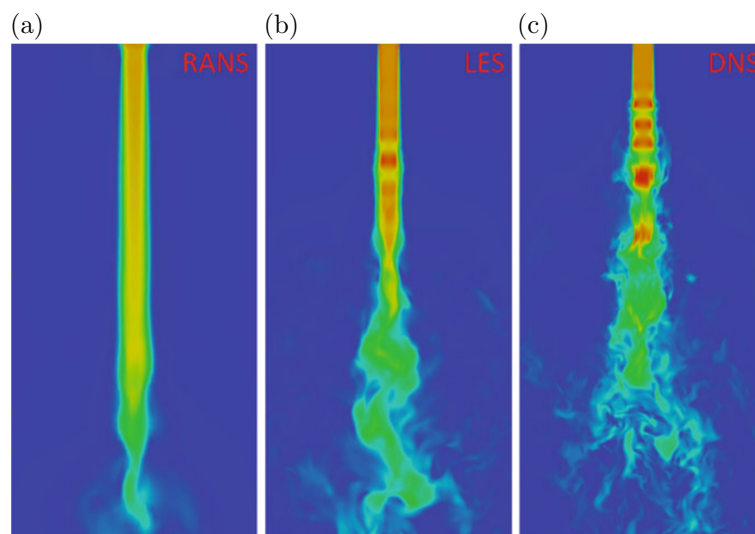


Figure 2.1: Example of flow field of a turbulent jet modeled with RANS (a), LES (b) and DNS (c). Reused from Rodriguez (2019).

scales. Lastly, Reynolds Averaged Navier-Stokes (RANS) models only solve the mean state and parameterize all turbulence. They are therefore heavily reliant on the quality of the turbulence model. An example comparing RANS, LES and DNS is displayed in Fig. 2.1, clearly illustrating that a higher degree of details is modeled when more turbulence is explicitly resolved.

In this thesis, the PARallelized Large-eddy simulation Model (PALM; (Maronga et al., 2020)) is used to model the flow field around a wind turbine. The PALM code is optimized for massive parallel computing and has been used in atmospheric and oceanic boundary layer studies. Its governing equations and most relevant settings are discussed in the following sections.

### 2.1.1 Governing Equations

The atmospheric flow can be described by a set of prognostic equations. Most relevant for this thesis are the equations for conservation of mass (Eq. 2.1) and momentum (Eq. 2.2) (Stull, 1988):

$$\frac{\partial \rho}{\partial t} + \frac{\partial(u_j \rho)}{\partial x_j} = 0 \quad (2.1)$$

$$\underbrace{\frac{\partial u_i}{\partial t}}_{\text{Rate of change}} + \underbrace{u_j \frac{\partial u_i}{\partial x_j}}_{\text{Advection}} = \underbrace{-\delta_{i3}g}_{\text{Gravity}} - \underbrace{2\epsilon_{ijk}\Omega_j u_k}_{\text{Coriolis}} - \underbrace{\frac{1}{\rho} \frac{\partial p}{\partial x_i}}_{\text{Pressure gradient}} + \underbrace{\frac{1}{\rho} \frac{\partial \tau_{ij}}{\partial x_j}}_{\text{Viscous}} \quad (2.2)$$

in which  $\rho$  is the air density,  $u_i$  the wind components,  $g$  the acceleration due to gravity,  $\Omega_j$  the angular velocity of the earth's rotation,  $p$  the atmospheric pressure and  $\tau_{ij}$  is the stress tensor.  $x$  indicates a spatial dimension, and  $\delta_{i3}$  and  $\epsilon_{ijk}$  the Kronecker-Delta and Levi-Civita symbol, respectively.

PALM solves the volume-averaged form of these equations following Schumann (1975), which can be derived by making the following assumptions and manipulations:

- Pressure consists of a mean and perturbations:  $p = \bar{p} + p^*$ . Here,  $p^*$  represents the resolved perturbations ( $\pi^*$ ) minus the perturbations handled by the subgrid-scale model ( $\frac{2}{3}\rho e$ ):

$$-\frac{1}{\rho} \frac{\partial p}{\partial x_i} = -\frac{1}{\rho} \frac{\partial \bar{p}}{\partial x_i} - \frac{1}{\rho} \frac{\partial \pi^*}{\partial x_i} + \frac{\partial^2 e}{\partial x_i^2}$$

with  $e = \frac{1}{2} \overline{u'_i u'_i}$  the subgrid-scale turbulent kinetic energy.

- Boussinesq approximation: Density fluctuations are only considered in the buoyancy term. For all other terms, the density is presumed constant ( $\rho_0$ ). Using the hydrostatic law  $d\bar{p} = -\rho_0 g dz$  and using term  $-\delta_{i3}g$  from Eq. 2.2 gives:

$$-g - \frac{1}{\rho} \frac{\partial \bar{p}}{\partial z} = -g + g \frac{\rho_0}{\rho} = g \left( \frac{\rho_0 - \rho}{\rho} \right)$$

Assuming an ideal gas in hydrostatic equilibrium  $p = \rho R \theta$ , density and (potential) temperature are inversely related, hence:

$$g \left( \frac{\rho_0 - \rho}{\rho} \right) = g \left( \frac{\theta - \theta_0}{\theta_0} \right)$$

which in terms of volume averaging can be rewritten as:

$$g \left( \frac{\theta - \theta_0}{\theta_0} \right) = g \frac{\bar{\theta} - \langle \theta \rangle}{\langle \theta \rangle}$$

where  $\bar{\theta}$  indicates a box average and  $\langle \theta \rangle$  a domain average.

- Geostrophic equilibrium: the pressure gradient force is balanced by the Coriolis force:

$$-\frac{1}{\rho_0} \frac{\partial \bar{p}}{\partial x} = -f_3 v_g$$

$$-\frac{1}{\rho_0} \frac{\partial \bar{p}}{\partial y} = f_3 u_g$$

where  $f_3 = 2\omega \sin \phi$  is the Coriolis parameter with  $\omega = 2\pi/86400\text{s}$  and  $\phi$  the latitude. Together with the Boussinesq approximation, the mean of the pressure term can finally be rewritten as:

$$-\delta_{i3}g - \frac{1}{\rho_0} \frac{\partial \bar{p}}{\partial x_i} = \epsilon_{i3j} f_3 u_{g,j} + \delta_{i3}g \frac{\bar{\theta} - \langle \theta \rangle}{\langle \theta \rangle}$$

- The Coriolis term can be rewritten as

$$-2\epsilon_{ijk} \Omega_j \bar{u}_k = -\epsilon_{ij3} f_j \bar{u}_k$$

where  $f_j$  is the Coriolis parameter.

- Reynolds decomposition of the advection term reads:

$$\overline{u_j \frac{\partial u_i}{\partial x_j}} = \frac{\partial \bar{u}_i \bar{u}_j}{\partial x_j} = \frac{\partial \bar{u}_i \bar{u}_j}{\partial x_j} + \frac{\partial \overline{u_i' u_j'}}{\partial x_j}$$

- Molecular friction can be neglected as its effect is small compared to other forces. The stress tensor is therefore negligible:

$$\frac{1}{\rho} \frac{\partial \tau_{ij}}{\partial x_j} \approx 0$$

With these assumptions and manipulations, Eq. 2.1 and 2.2 can be rewritten as:

$$\frac{\partial \bar{u}_j}{\partial x_j} = 0 \tag{2.3}$$

$$\frac{\partial \bar{u}_i}{\partial t} = -\frac{\partial \bar{u}_i \bar{u}_j}{\partial x_j} + \delta_{i3}g \frac{\bar{\theta} - \langle \theta \rangle}{\langle \theta \rangle} - \epsilon_{ij3} f_j \bar{u}_k + \epsilon_{i3j} f_3 \bar{u}_{g,j} - \frac{1}{\rho_0} \frac{\partial \bar{\pi}^*}{\partial x_i} - \frac{\partial}{\partial x_j} \left( \overline{u_i' u_j'} - \frac{2}{3} e \delta_{ij} \right) \tag{2.4}$$

which is the form of these equations as used in Maronga et al. (2020).

A time integration of the prognostic variables is done by a third-order Runge-Kutta scheme. It calculates the solution in three intermediate steps, resulting in a higher accuracy. Williamson (1980) proposed a fifth-order scheme to calculate the advection term, which uses this time scheme. Wicker and Skamarock (2002) found that this

combination is a good trade-off between accuracy and simplicity.

A pressure solver using a Poisson equation is used to ensure a divergence-free flow. During time integration, the perturbation pressure term  $-\frac{1}{\rho_0} \frac{\partial \pi^*}{\partial x_i}$  is excluded from Eq. 2.4, yielding local velocities (divergence) that need to be compensated for by adjusting the pressure term. In this thesis, this compensation term is found using an iterative multigrid scheme, effectively smoothing out any local disturbances over a larger volume.

A subgrid-scale model is needed to provide turbulent closure, as the terms  $\overline{u'_i u'_i}$  and  $\overline{u'_i u'_j}$  cannot explicitly be resolved. In this thesis, the default 1.5-order turbulent closure parameterization is used, which was developed by Deardorff (1980) and modified by Moeng and Wyngaard (1988) and Saiki et al. (2000). The covariance term, representing the energy transported by subgrid-scale eddies, is assumed to relate the local gradients of their mean quantities, formulated as follows:

$$\overline{u'_i u'_j} - \frac{2}{3} e \delta_{ij} = -K_m \left( \frac{\partial \overline{u_i}}{\partial x_j} + \frac{\partial \overline{u_j}}{\partial x_i} \right) \quad (2.5)$$

in which  $K_m$  is the eddy-transfer coefficient of momentum. Analogous formulations can be derived for temperature, moisture and other scalar variables. The value for  $K_m$  is parameterized as a function of the height of the point that is being calculated, the grid spacing, stratification (atmospheric stability) and the subgrid-scale turbulent kinetic energy calculated with its prognostic equation.

### 2.1.2 Boundary conditions

#### Surface

The Monin-Obukhov similarity theory (MOST) is applied between the surface and the first grid level. It assumes that in this layer the horizontally-averaged fluxes are constant, but in PALM it is assumed that MOST can also be applied locally. In the surface layer, the vertical gradient of the mean horizontal wind speed ( $\overline{u_{\text{hor}}} = \sqrt{\overline{u^2} + \overline{v^2}}$ ) can be described by

$$\frac{\partial \overline{u_{\text{hor}}}}{\partial z} = \frac{u_*}{\kappa z} \Phi \left( \frac{z}{L} \right) \quad (2.6)$$

in which  $u_*$  is the friction velocity,  $\kappa = 0.41$  the Von Kármán constant and  $\Phi$  the similarity function for momentum. This term is a function of the stability parameter Obukhov length  $L$  and is empirically determined using the Businger-Dyer relations:

$$\Phi = \begin{cases} 1 + 5 \frac{z}{L} & \text{for } \frac{z}{L} \geq 0 \\ (1 - 16 \frac{z}{L})^{-\frac{1}{4}} & \text{for } \frac{z}{L} < 0 \end{cases} \quad (2.7)$$

In PALM, the friction velocity  $u_*$  is computed with the following equation:

$$u_* = \left[ (\overline{u'w'_0})^2 + (\overline{v'w'_0})^2 \right]^{\frac{1}{4}} \quad (2.8)$$

in which  $\overline{u'w'_0}$  and  $\overline{v'w'_0}$  indicate the surface momentum fluxes.  $u_*$  is calculated considering a layer between  $z_0$  and  $0.5\Delta z$ , the latter indicating the height halfway between the surface and the lower grid cell. Using Eq. 2.8 in Eq. 2.6 finally derives expressions for the momentum fluxes as function of the wind speed gradients and



Obukhov length. The derivation described here has focused on the momentum flux, but analogous derivation can be made for temperature and humidity. Lastly, in a neutral boundary layer the potential temperature of the surface is the same as that at the lowest grid level (Neumann boundary condition). Non-neutral boundary layers can be simulated by either prescribing a surface heat flux or a surface temperature change rate (Dirichlet boundary condition).

### **Lateral**

LES typically uses cyclic boundary conditions in both lateral and longitudinal direction, which means that the flow that leaves the domain gets reintroduced on the other side. However, this would result in simulating an infinite row of turbines rather than just a single turbine or turbine pair. PALM has the option to use non-cyclic boundary conditions in one direction. To avoid very large model domains that would be needed for the flow to become turbulent, a turbulence recycling method (Lund et al., 1998; Kataoka and Mizuno, 2002) can be used, visualized in Fig. 2.2a. A precursor simulation of a smaller, empty (no turbines) domain with cyclic boundary conditions is performed, in which random perturbations are added to an initially laminar flow to generate a flow field with realistic turbulent features. When a stationary state is reached, information on average and turbulent quantities is saved to be used in a subsequent main run containing turbines. The boundary conditions of this main run is cyclic in crosswise direction, but non-cyclic in streamwise direction. The flow field is initialized with the information from the prerun. Afterwards, mean profiles obtained in the precursor run are described at the inlet (dirichlet boundary condition), while turbulent fluctuations are taken from a recycling plane some distance downstream and added to the mean profiles at the inlet. A Sommerfeld radiation equation is solved at the outlet to ensure that disturbances reaching the outlet do not affect the flow upstream. It considers a theoretical flow field at an infinite distance and uses that solution at the outlet, ensuring that only "outgoing" waves pass through the outlet (Schot, 1992).

Lastly, very long turbulent structures (superstructures) are typically not fully captured as this would result in large domain lengths and consequently expensive simulations. In smaller domains, these structures persist due to a lack of space to break up, resulting in 'streaks' of high or low velocities. To prevent this, PALM uses the shifted boundary conditions approach proposed by Munters et al. (2016a), which shifts the plane in crosswise direction before reintroducing it in the domain. Although originally developed for cyclic boundary conditions, PALM also allows this for non-cyclic boundary conditions with turbulence recycling.

### **2.1.3 Wind direction change**

In Chapter 6, dynamic wind direction changes are simulated in PALM. This can be done by nesting LES into a mesoscale model, such as the Weather Research and Forecasting (WRF) model (e.g., Udina et al., 2020), but this affects the turbulent characteristics of the LES since WRF resolves structures on a larger scale (Mirocha et al., 2013). As an alternative, Munters et al. (2016b) proposed a method to rotate the domain, mimicking wind direction changes. Although promising, this method is computationally expensive due to MPI communication.

This thesis adopts the method proposed by Stieren et al. (2021), which treats the

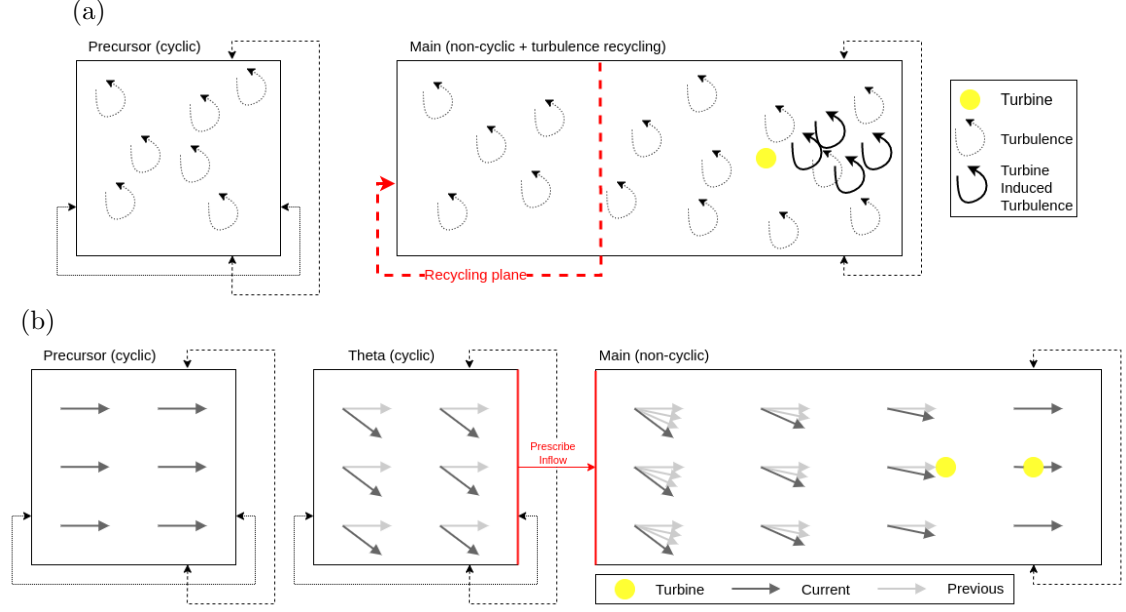


Figure 2.2: Illustrative sketches of domains in the simulation chain. **(a)** Precursor run with cyclic boundary conditions to generate turbulence and subsequent main run with one turbine using the turbulence recycling method. Figure inspired by IMUK (2022). **(b)** Same precursor run with one wind direction, subsequent theta run to change the wind direction and save planes to use as inflow in a main run with two turbines to simulate a wind direction change propagating through the domain.

domain as a non-inertial rotating reference frame. Dynamic wind direction changes are included by adding an artificial Coriolis term  $F_\theta$  to the momentum equations of Eq. 2.4. This term reads:

$$F_\theta = -\theta(t)u_j\epsilon_{ij3} \quad (2.9)$$

in which  $\theta(t)$  is the wind direction change rate as function of time in radians per second. One should be aware that a rotation in the meteorological frame is in opposite direction of the mathematical frame. This artificial forcing is applied to every cell in the domain. In addition, the driving geostrophic wind is rotated with the same rate. The centrifugal and Euler force are neglected in this engineering approach. Although physical not fully correct, Stieren et al. (2021) demonstrated that the observed wind direction compares well with the forced signal.

This method has two disadvantages for the wind turbine modeling. First, cyclic boundary conditions are needed. As discussed in the previous section, this is undesirable for wind farm modeling. Second, the whole wind field rotates in the same direction at the same time, which means that a wake is artificially deflected before reaching the positions of a downstream turbine. To circumvent these issues, in this thesis a second precursor run (called a theta run) is performed, see the simulation chain depicted in Fig. 2.2b. It is a continuation of the initial precursor run, hence an empty domain without turbines, in which the desired wind direction change is performed. At one position in the domain, the quantities are saved and subsequently used as at the inlet of the main run with non-cyclic boundary conditions. Note that with this methodology, no turbulence recycling method is performed as the full inflow conditions are provided by the theta run. This ensures that the wind direction change propagates through the domain.

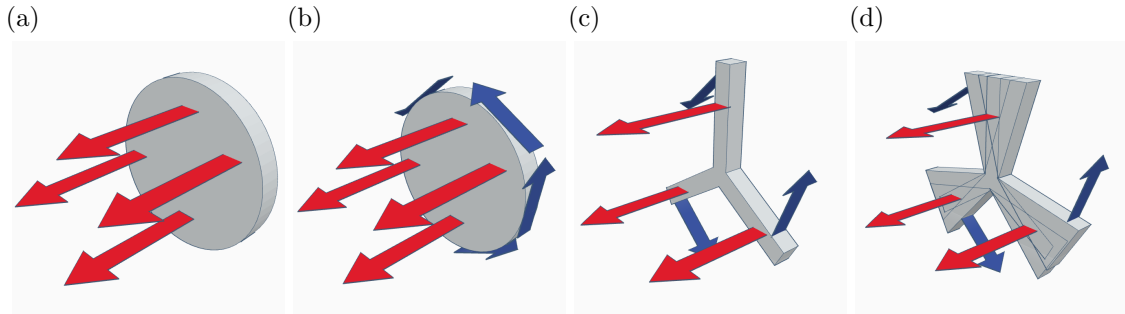


Figure 2.3: Illustrative sketches of four wind turbine models: (a) Actuator Disc Model, (b) Actuator Disc Model with Rotation, (c) Actuator Line Model and (d) Actuator Sector Model. Red arrows indicate thrust, blue arrows torque.

Besides large memory costs, the main disadvantage of this method is that it introduces an unwanted vertical velocity. Obeying Eq. 2.3, the non-zero mean gradient  $\partial\bar{u}/\partial x$  introduced by the wind direction change propagating through the domain needs to be compensated. As the boundary conditions are cyclic in lateral direction, it cannot be compensated by  $\partial\bar{v}/\partial y$  and therefore needs to be compensated by  $\partial\bar{w}/\partial z$ . Line-averaged velocities of  $\bar{w} = |0.2| \text{ m s}^{-1}$  have been observed, which over time alter the vertical profiles of wind speed and direction. Although undesirable, the profiles are not deemed to become non-physical. For this reason, it is argued that this issue has a negligible effect on the results presented in Chapter 6.

#### 2.1.4 Wind turbine model

To include the impact a wind turbine has on the flow, models of a range of fidelities can be used. The simplest way would be to increase the surface roughness, as is for instance done in Barrie and Kirk-Davidoff (2010). While this might give reasonable results in mesoscale models, it does not give an accurate representation in microscale models. Four turbine models are discussed in the following.

##### Actuator Disc Model

Modeling the rotor as a porous disc, named an Actuator Disc Model (ADM, Fig. 2.3a) has been adopted in many studies (e.g., Calaf et al., 2010; Steinfeld et al., 2010) because of its simplicity. It has not been used in this thesis, but is described here to provide background information. In this model, a thrust force ( $F_T$ ) is calculated:

$$F_T = \frac{1}{2}\rho_0 C_T A U^2 \quad (2.10)$$

in which  $\rho_0$  is the air density,  $C_T$  the turbine's thrust coefficient, determined from its  $C_T$ -curve,  $A$  is the rotor area and  $U$  the undisturbed wind speed.  $F_T$  is uniformly applied to the whole rotor area, adding a sink term to the momentum equation of Eq. 2.4. While it reproduces the most relevant characteristics of the far wake quite well (Witha et al., 2014), it fails to represent the more complex dynamics of the near wake.

##### Actuator Disc Model with Rotation

To overcome these issues, an Actuator Disc Model with Rotation (ADM, Fig. 2.3b)

has been developed. The model used here is based on the description of Wu and Porté-Agel (2011). The rotor area is no longer considered as one plane, but divided up into smaller segments. Rather than a thrust force, for each segment a lift ( $F_L$ ) and drag ( $F_D$ ) force is calculated:

$$F_L = \frac{1}{2}\rho_0 U_{rel}^2 C_L \frac{N_B c}{2\pi r} \quad (2.11)$$

$$F_D = \frac{1}{2}\rho_0 U_{rel}^2 C_D \frac{N_B c}{2\pi r} \quad (2.12)$$

where  $U_{rel}$  is the relative wind speed calculated from the wind speed components of the local flow field and the blade velocity,  $C_L$  and  $C_D$  the segment's lift and drag coefficients,  $N_B$  the number of blades,  $c$  the chord length and  $r$  the distance between the segment and rotor center. Afterwards, these forces are projected onto axial and tangential planes and smeared on PALM's grid using a polynomial function that approaches a Gaussian kernel. By calculating the lift and drag forces, in addition to thrust a torque is added to the flow.

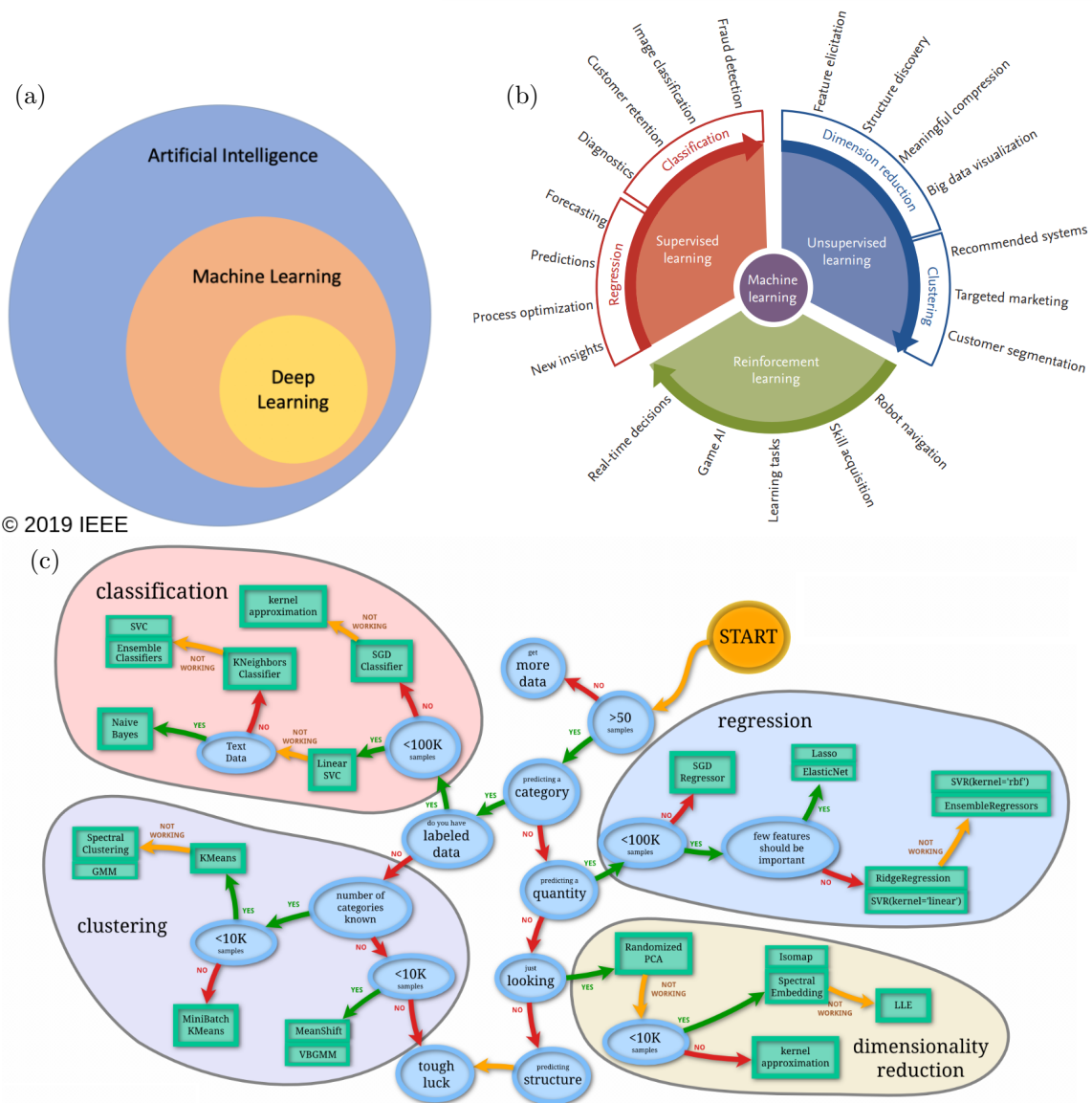
Witha et al. (2014) has shown that the details of the near wake can be better captured with ADMR. The implemented model has also provided good results in studies by Dörenkämper et al. (2015) and Vollmer et al. (2016) and is therefore used in the majority of the simulation performed in this thesis.

### Actuator Line Model

A higher fidelity representation of a wind turbine rotor than ADMR is a Actuator Line Model (ALM, Fig. 2.3c), in which the turbine blades are represented by rotating lines. As in ADMR, the blades are divided in segments for which lift and drag forces are calculated and smeared onto the flow field. Contrary to ADMR, these forces are only calculated at the positions of the turbine blades, represented by lines (Churchfield et al., 2017). Due to its high fidelity, ALM is typically considered to be the most accurate turbine models. This benefit is most visible in simulations with a high spatial resolution and dynamic areas such as the near wake. Additionally, due to the detailed computation of forces on the turbine blades, it can be used to study fatigue loads. The main disadvantage of ALM is that a blade must not pass through more than one grid cell per simulation time step, resulting in simulations with a very high temporal resolution and consequently high computational costs.

### Actuator Sector Model

To overcome this issue, an Actuator Sector Model (ASM, Fig. 2.3d) can be used. In the implementation developed by Krüger et al. (2022), PALM is coupled with the aeroelastic code FAST containing the turbine model. While FAST still uses the ALM model and runs with a very fine time step, the flow field is updated less frequently. After each PALM time step, the wind field is frozen and sent to FAST, which performs calculations at a smaller time step until it catches up. The forces of the line in the center of the simulated sector are then smeared onto the flow field. This methodology allows PALM to retain its coarser temporal resolution while still retaining the higher accuracy of an ALM. The ASM is used in Chapter 5 to reproduce the wake observed in free-field measurements as accurately as possible.



© 2019 IEEE

Figure 2.4: (a) Visualization of relations within Artificial Intelligence. Reused from Miraftebadeh et al. (2019). (b) Visualization of the classes within Machine learning. Reused from Kim and Tagkopoulos (2019). (c) Scikit-learn cheat sheet. Reused from scikit-learn (2022)

## 2.2 Machine learning models

Machine learning (ML) algorithms can be considered one of the emerging computational technologies, as discussed in Chapter 1. It comprises of methods designed to make predictions and are employed when conventional methods (statistical or analytical approaches) fall short. Machine learning is considered part of artificial intelligence (AI), as can be seen in Fig. 2.4a. Examples of AI that are not ML are chatbots or smart appliances. Part of ML is deep learning, which comprises of neural networks with multiple processing layers able to extract abstract relations from the data. These models are typically very complex, impossible to interpret (black box models) and have a high data need. Although neural networks have shown to be successful in wind energy applications (Marugán et al., 2018), for most

problems they are more complex than necessary or need more data than can feasibly be acquired and ML methods are more attractive. ML methods can be split up in three classes, see Fig. 2.4b.

Supervised learning remains closest to conventional statistics. By providing training data containing both inputs and their related outputs, the ML algorithm aims to find relations that it later can use to predict the output variables when only inputs are known. When the data is numerical, regression models such as the well established Ordinary Least Squares method can be used to for instance estimate the relation between temperature and ice cream sold. For categorical data, classification algorithms can be used to for instance determine the likelihood of an email being spam.

With unsupervised learning, the algorithm is tasked to find a structure in its input data. It can be used to cluster data together, each cluster containing data points that are more similar to each other than to data in other clusters. This can for instance be used to group customers together to develop tailored marketing strategies for each cluster. Another application of unsupervised learning is dimension reduction, such as the widely used Proper Orthogonal Decomposition (POD) method. Related variables can be grouped together, reducing the number of dimensions and therefore increasing the interpretability of the data.

Lastly, in reinforced learning the algorithm learns by doing and receiving feedback. The algorithm aims to maximize its rewards, which are awarded based on the decisions made, for instance when playing chess against an opponent.

Many ML algorithms have been developed making it difficult to decide on a method when first being presented with a problem. The python package *scikit-learn* (Pedregosa et al., 2011) provides many ML algorithms, as well as a flow-chart to help the user’s decision making, see Fig. 2.4c. It contains an incomplete overview of the supervised and unsupervised algorithms available in the package. Two ML algorithms are used in this thesis: a variation of the Lasso regression algorithm and the MeanShift clustering algorithm. Both were selected using this flow chart and will be described in the following.

### 2.2.1 Multi-task lasso algorithm

The multi-task lasso algorithm is used in Chapter 4 to estimate wake parameters (e.g. wake center displacement) from a set of input variables (e.g. shear, thrust coefficient). Its technical details are discussed here. The original lasso implementation from Tibshirani (1996) seeks to find the coefficients  $\mathbf{B}$  based on the following cost function:

$$\operatorname{argmin}_B \sum_n (\mathbf{y}_n - \sum_p \mathbf{x}_{np} \mathbf{B}_p)^2 + \lambda \sum_p |\mathbf{B}_p|, \quad (2.13)$$

in which  $\mathbf{y}$  represents the output,  $\mathbf{x}$  the input,  $n$  is the sample size and  $p$  the input parameter. It uses the regularization parameter  $\lambda$ , leading to sparse coefficients for the coefficient vector  $\vec{B}$ . The multi-task setting from Obozinski et al. (2006) extends the lasso regression to estimate  $d$  (in this thesis the distance downstream) outputs simultaneously, penalizing the blocks of coefficients over the tasks. The loss function

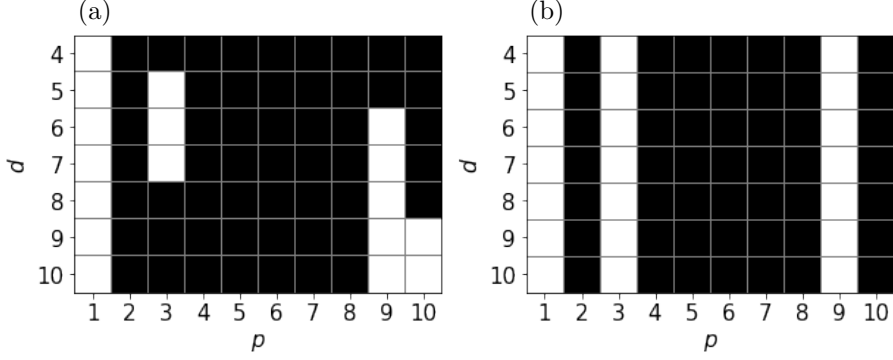


Figure 2.5: Non-zero elements (black) of  $B$  for the output variable for the original lasso (a) and multi-task lasso (b).

is therefore extended and finds the coefficient matrix  $\mathbf{B}$  based on

$$\operatorname{argmin}_B \sum_d \sum_n (\mathbf{y}_{nd} - \sum_p \mathbf{x}_{np} \mathbf{B}_{pd})^2 + \lambda \sum_p \sqrt{\sum_d (\mathbf{B}_{pd})^2}. \quad (2.14)$$

In contrast to Eq. (2.13), the multi-task lasso implementation penalizes not only the single coefficients, but also the blocks of coefficients over all tasks represented by the Euclidean norm. Note that if  $d = 1$ , Eq. (2.14) reduces to the standard lasso estimate of Eq. (2.13).

An exemplary result is illustrated in Fig. 2.5. Whereas the original lasso model selects a new set of variables for each distance, the multi-task lasso always takes the same set. This makes physically more sense and leads to fewer variables in total, therefore reducing the risk of overfitting. The model is optimized using the cyclical descent algorithm implemented in Pedregosa et al. (2011).

## 2.2.2 Mean shift clustering algorithm

The mean shift clustering algorithm is used in Chapter 5 in the procedure to filter data from the nacelle-mounted lidar. Hard targets are typically characterized by low LOS and high CNR values, making it relatively easy to filter out. However, occasionally a large part of the scanned points was characterized with these features and the distinction between good and bad data was not immediately clear. The mean shift clustering algorithm was used to identify clusters containing good or bad data, after which clusters were either kept or disregarded. The technical details of the algorithm are discussed here.

The mean shift clustering algorithm (Fukunaga and Hostetler, 1975) is an iterative method that determines a center of mass (the mean,  $x_i$ ) for all point in a region of interest:

$$m(x_i) = \frac{\sum_{x_j \in N(x_i)} K(x_j - x_i) x_j}{\sum_{x_j \in N(x_i)} K(x_j - x_i)} \quad (2.15)$$

in which  $N(x_i)$  are the samples in the region of interest and  $K(x_j - x_i)$  a Gaussian kernel of the distance to the current estimate. The center of this region is then shifted to the location of the center of mass:

$$x_i^{t+1} = m(x_i^t) \quad (2.16)$$

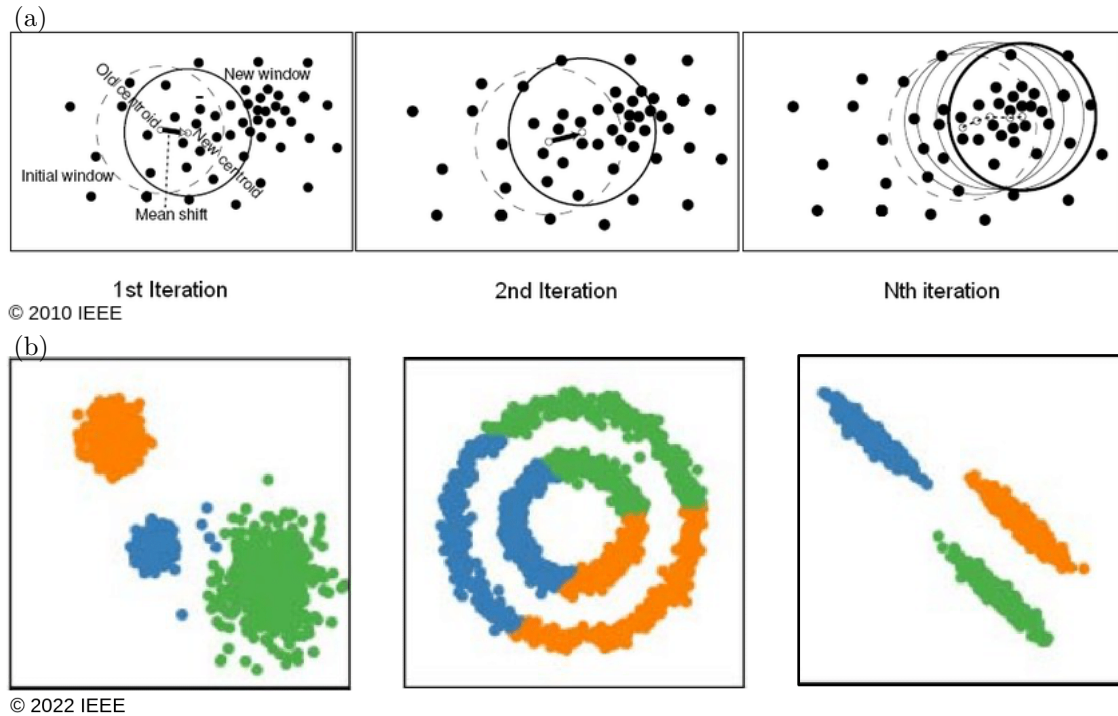


Figure 2.6: (a) Schematic illustrating of the fundamental principle behind the Mean Shift clustering algorithm. Reused from Sok and Adams (2010). (b) Results from the Mean Shift clustering algorithm on three exemplary data set. Adapted from You et al. (2022).

and this procedure is repeated until convergence takes place (Fig. 2.6a). Instead of setting the number of clusters, as in for instance K-means clustering, in the mean shift algorithm the size of the region of interest (called bandwidth) needs to be determined manually. After identifying the number of clusters and their centroids, each data point is allocated to a cluster based on its Euclidean distance to the centroid. Figure 2.6b demonstrates the outcome of Mean Shift clustering on three exemplary data sets, illustrating that it performs well when there are no underlying structures present in the data set.

## 2.3 Lidar

Besides in situ measurements like cup anemometers and wind vanes, remote sensing devices can be used to measure the atmospheric flow. The industry mainly uses remote sensing technologies for wind resource assessments in the planning stage, and wind turbine performance (power curve) testing after installation. The application of remote sensing devices in research is wider spread and includes for instance sampling the inflow for loads and (preview) control studies, or to investigate the atmospheric flow in complex terrain (Clifton et al., 2018). Additionally, remote sensing can be used to sample the turbine wake in for instance wake steering experiments (e.g., Fleming et al., 2017a; Bromm et al., 2018).

Two devices are available for these purposes: radars (radio detection and ranging) and lidars (light detection and ranging). Radars emit radio waves which are reflected by humid particles, whereas lidars emit laser beams which are reflected by aerosols. While radars have a larger measurement range than lidars (around 30 km and 10



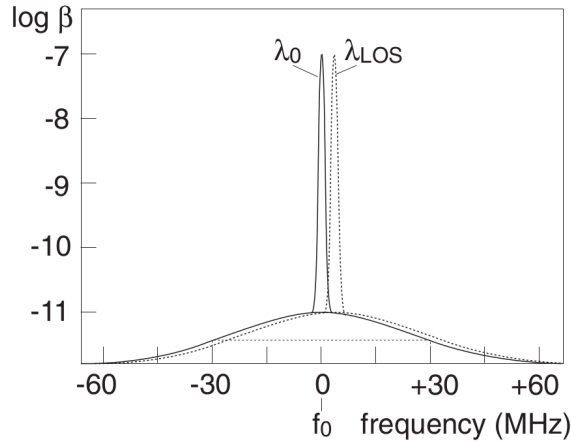


Figure 2.7: Example of backscattered frequency distribution illustrating a doppler shift. Reused from Werner (2005).

km, respectively), their practicality is limited due to their size and costs (Würth et al., 2019).

Focusing on lidars, the emitted laser beam has a certain frequency. When being reflected by an aerosol, this frequency will slightly be altered because of the velocity of this particle. The backscattered frequencies captured by the device will show a shifted distribution, called a Doppler shift, as illustrated in Fig. 2.7. This shift can subsequently be used to determine the line-of-sight (LOS) velocity (Werner, 2005). One can distinguish continuous wave and pulsed lidar (Peña et al., 2013). Continuous wave lidars emit one wave signal with a very high temporal frequency. These lidars can only sample one distance at the time and due to their optical properties the measurement range is limited to about 150 m. They are therefore used to obtain measurements with a high spatial and temporal resolution in the short-range. Pulsed lidar, on the other hand, emit a sequence of short pulses to sample the flow field at a range of distances simultaneously. The LOS can be determined for each distance considering the time difference between emission of the pulse and retrieval of the backscatter. The measurement range is limited by the carrier-to-noise ratio (CNR) decreasing with distance. The spatial and temporal resolution of pulsed lidars is much lower than for continuous wave lidars, and the scanning trajectories are typically much simpler.

In this work, a lidar is used to sample the wake of a turbine during a wake steering field experiment in Chapter 5. The targeted distance is about 600 m downstream of the turbine, hence a long-range pulsed lidar was used.

### 2.3.1 Measurement trajectories

The scanner head of a pulsed lidar can rotate around either the vertical or horizontal axis, but not around both simultaneously. This limits the complexity of its scanning strategies to simple trajectories. A plan position indicator (PPI) scan follows a trajectory with a constant elevation (vertical) angle and a changing azimuth (horizontal) angle. On the contrary, a range height indicator (RHI) scan follows a trajectory with a constant azimuth angle and a changing elevation angle. A schematic example of these scans can be found in Fig. 2.8a. As explained in

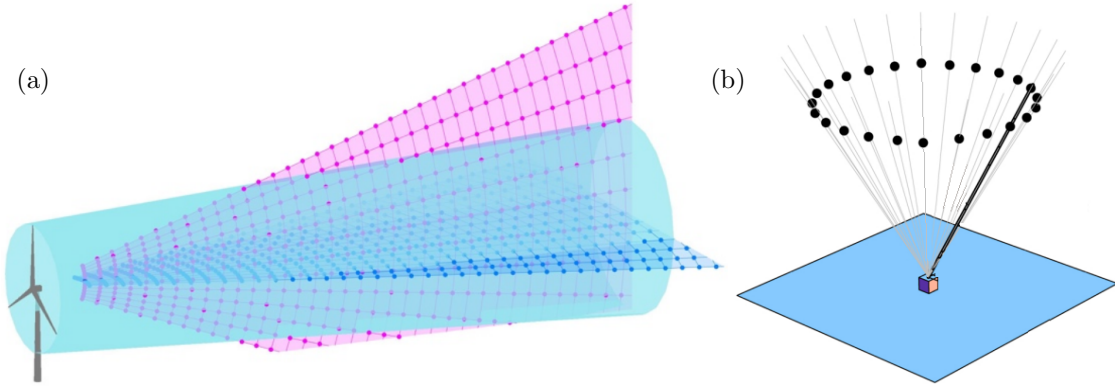


Figure 2.8: Sketches of pulsed lidar scanning trajectories. **(a)** PPI (blue) and RHI (purple) scans. Reused from Beck and Kühn (2019). **(b)** VAD scan. Adapted from Sathe and Mann (2013).

the previous section, the measurement obtained with these scans consist of only line-of-sight velocities. Assuming a homogeneous inflow, the azimuth and elevation angles can be used to approximate the horizontal wind speed from the line-of-sight velocities, using the following equation:

$$\text{LOS} = u \cos(\phi_{\text{lidar}}) \cos(\theta_{\text{lidar}}) \quad (2.17)$$

in which  $\phi_{\text{lidar}}$  is the elevation angle and  $\theta_{\text{lidar}}$  the azimuth angle. Here it is assumed that  $\phi_{\text{lidar}} = 0^\circ$  is a perfectly horizontal scan and  $\theta_{\text{lidar}} = 0^\circ$  a perfect alignment with the mean wind direction. These scanning trajectories are not suited to obtain wind direction measurements.

When a pulsed lidar is used to obtain vertical profiles of the wind speed and direction, a velocity-azimuth display (VAD) is used. The lidar, typically situated at the surface, is performing a conical scan at one elevation angle, as illustrated in Fig. 2.8b. To determine the wind speed components and subsequently the horizontal wind speed and direction, the LOS measurements can be fitted with the following sinusoid:

$$\text{LOS} = u \cos(\theta_{\text{lidar}}) \sin\left(\frac{\pi}{2} - \phi_{\text{lidar}}\right) + v \sin(\theta_{\text{lidar}}) \sin\left(\frac{\pi}{2} - \phi_{\text{lidar}}\right) + w \cos\left(\frac{\pi}{2} - \phi_{\text{lidar}}\right) \quad (2.18)$$

in which  $\theta_{\text{lidar}} = 0^\circ$  indicates north. The wind speed components can subsequently be used to obtain horizontal wind speed and direction estimates, which represent a spatial average over the area covered by the cone.

### 2.3.2 Lidar Simulator

To determine an appropriate scanning strategy for a study's objectives, it is desirable to investigate the impact of the scanning trajectories on the measurement error before deployment of the lidar. This can be done numerically by using large-eddy simulation data as input to a code emulating the lidar's characteristics. Using volumetric PALM results, the Lidar Scanner Simulator (LiXim, Trabucchi (2019)) is employed in this thesis to obtain synthetic lidar data. The lidar's hardware characteristics can be modified to match the device available for deployment, which makes the simulator suited for studies with either continuous wave (Kidambi Sekar et al., 2022) or pulsed lidars (van Dooren et al., 2016; Ortensi et al., 2022).

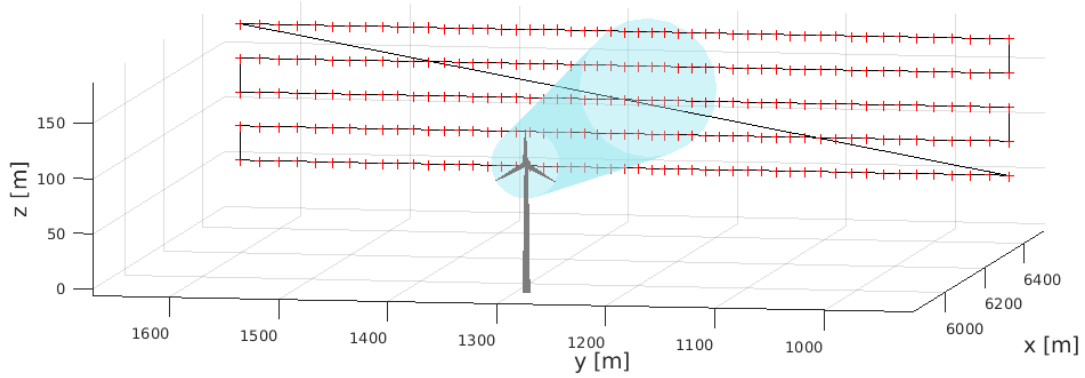


Figure 2.9: LiXim trajectory with five PPI scans. Red markers indicate measurement points, black solid lines the path, starting at the lower right position. The blue shaded area illustrates the turbine wake.

LiXim obtains the line-of-sight velocity by temporally and spatially interpolating the LES data for the probe volume of a predefined measurement point. Rather than estimating just one value, the probe volume is divided in segments for which a LOS value is calculated. Weighted with a normal distribution, an average LOS for the probe volume will be obtained.

The desired scanning trajectory can be emulated in LiXim. An example with five consecutive PPI scans as later used in Chapter 5 is displayed in Fig. 2.9.

## Chapter 3

# A new method to characterize the curled wake shape under yaw misalignment

The content of this chapter is identical to the following conference proceedings: Sengers, B. A. M., Steinfeld, G., Heinemann, D., and Kühn, M.: A new method to characterize the curled wake shape under yaw misalignment, *Journal of Physics: Conference Series*, 1618, 062050, <https://doi.org/10.1088/1742-6596/1618/6/062050>, 2020.

©Author(s) 2020. This work is distributed under the Creative Commons Attribution 3.0 License. Reprinted with permission.

**Abstract** Wake Redirection Control due to intentional yaw misalignment is a promising method to enhance power yield at wind farm level. A turbine misaligned with the inflow wind produces a curled wake shape, which is currently not accounted for in wake tracking algorithms. This study proposes a new 2D wake description specifically designed to account for the non-elliptic shape of the redirected wake. The performance of this new method is evaluated by employing a large-eddy simulation model at different atmospheric stratifications. A comparison with traditionally used approaches indicates an improvement in describing wake shape and center position, and consequently a significantly higher accuracy in the power estimation of a virtual downstream turbine. A brief outlook suggests that this wake tracking algorithm is suited to study the effect of the most influential atmospheric and operational parameters on wake propagation under yaw misalignment and the development of a physically based empirical wake parameterization.

### 3.1 Introduction

As the wind energy industry is maturing, awareness of the negative effects of turbine wakes on power production in wind farms is increasing. Lately, focus is shifting from optimal control of individual turbines to optimization on a farm level. Wake Redirection Control (WRC) by intentional yaw misalignment (Dahlberg and Medici, 2003; Wagenaar et al., 2012) is currently regarded as one of the most promising methods to enhance power yield at a farm level. By misaligning the turbine with the incoming flow, a crosswise thrust force component is introduced, redirecting the wake away from a downstream turbine. In recent years, the potential of WRC has been demonstrated by numerical simulations (Gebraad et al., 2015; Vollmer et al., 2016; Fleming et al., 2018; Martínez-Tossas et al., 2019; Hulsman et al., 2020), wind tunnel experiments (Dahlberg and Medici, 2003; Campagnolo et al., 2016; Wang et al., 2016) and free-field measurements (Fleming et al., 2017b; Bromm et al., 2018; Fleming et al., 2019; Howland et al., 2019) with reported power yield increases of up to 15% depending on studied inflow conditions, used yaw controller and turbine spacing. Additionally, Howland et al. (2019); Gebraad et al. (2017) reported a potential increase in Annual Energy Production (AEP) on farm level.

The magnitude of the crosswise thrust force component introduced by yaw misalignment is not uniform over the rotor area, but varies in the vertical with a maximum near hub height. As first reported by Howland et al. (2016), this results in asymmetric curling of the wake to a kidney-like shape. This has implications for determining the wake position downstream of the turbine, as assuming a self-similar Gaussian distribution of the wake deficit is inaccurate. This in turn affects the quality of power and load assessments.

In turbine wake studies, including those applying WRC by intentional yaw misalignment, it is common practice to consider the wake center trajectory to be representative for the propagation of the wake downstream of the turbine. However, there is no consensus in the literature how to define this wake center. The location of the maximum wind speed deficit and the Center of Mass (CoM) are two of the simplest, yet most frequently used methods in this respect. Both are, however, sensitive to turbulence, which might be undesirable when studying steady state situations. In Vollmer et al. (2016), the wake center is determined using three methods: (1) by fitting a simple one-dimensional Gaussian at hub height, (2) by fitting a more convoluted two-dimensional bivariate Gaussian to the wind field and (3) by determining the location of the minimal potential available power of a virtual downstream turbine. Methods 2 and 3 are currently considered state-of-the-art methods to identify the wake center. They found dissimilarities between the three methods, especially under large turbine yaw angles, as none of the methods is able to accurately account for the curled wake shape.

To contribute to the growing interest in WRC by intentional yaw misalignment, this study proposes a new method to identify frequently studied wake characteristics, specifically designed to account for the non-elliptic shape of the redirected wake. Next to a new definition for the wake center, metrics to determine wake area and curliness are proposed. The performance of the proposed method is evaluated in comparison with traditional methods, in its ability to describe the location of the wake center and the wake as a whole. Potential applications include studying the dependency of wake characteristics on atmospheric and operational parameters and

the development of a physically based empirical wake parameterization or wake meandering model.

## 3.2 Methodology

An overview of the LES model PALM and the simulation set-up is described in the following section, followed by an overview of traditional and the proposed wake tracking algorithms.

### 3.2.1 Large-eddy simulations

#### General

The performance of the discussed methods is evaluated by employing the PArallelized Large-eddy simulation Model (PALM, Maronga et al. (2020)), which uses a non-hydrostatic incompressible Boussinesq approximation of the Navier-Stokes equations on a regularly spaced grid using right-handed Cartesian coordinates. Information exchange between the surface and the lowest grid cell is achieved by applying the Monin-Obukhov Similarity Theory. In this study, model revision 3455 with default numerical schemes is used. All simulations have a spatial resolution of  $\Delta = 5$  m in the boundary layer, while the vertical resolution above the boundary layer height increases with 6% per cell to save computational resources. The Coriolis parameter corresponds to  $55^\circ\text{N}$  and the surface roughness is constant at  $z_0 = 0.1$  m, representing low crops. The simulation chain includes a precursor without and a main simulation with one turbine.

#### Precursor simulations

Precursor simulations generate realistic turbulent inflow conditions by adding random perturbations to an initially laminar flow. Two inflow conditions representing a Neutral Boundary Layer (NBL) and a Stable Boundary Layer (SBL), respectively, are generated, both having approximately the same mean wind speed and direction at hub height to allow for a fair comparison of the downstream wind field. A Convective Boundary Layer is omitted in this study, as WRC is found not to be beneficial under this condition (Vollmer et al., 2016). The simulations use cyclic horizontal boundary conditions and the total simulation time is determined empirically until convergence to a stationary state occurs. The NBL does not

Table 3.1: Summary of simulation parameters for precursor and main simulations. The length ( $t$ ) and size ( $L_x$ ,  $L_y$ ,  $L_z$ ) of the precursor simulations (normalized by the rotor diameter ( $D = 126$  m)) is determined empirically until convergence to a stationary state occurs. The size of the domain of the main simulations is extended only in streamwise direction. The geostrophic wind ( $u_g$ ,  $v_g$ ) is constant in precursor and corresponding main simulations.

|           |     | $t$ | $L_x$   | $L_y$   | $L_z$   | $u_g$  | $v_g$  |
|-----------|-----|-----|---------|---------|---------|--------|--------|
|           |     | [h] | [ $D$ ] | [ $D$ ] | [ $D$ ] | [m/s]  | [m/s]  |
| Precursor | NBL | 28  | 40.6    | 20.3    | 6.3     | 10.115 | -3.969 |
|           | SBL | 20  | 11.4    | 7.6     | 3.8     | 9.500  | -5.170 |
| Main      | NBL | 1   | 61.0    | 20.3    | 6.3     | 10.115 | -3.969 |
|           | SBL | 1   | 30.5    | 7.6     | 3.8     | 9.500  | -5.170 |

Table 3.2: Summary of the most relevant inflow parameters, given as mean and standard deviation over the three main simulations. Results consist of rotor effective wind speed ( $U_{eff}$ ), turbulence intensity at hub height ( $TI_h$ ), wind shear ( $\alpha$ ) and veer ( $\delta\alpha$ ) over the rotor area and the Obukhov Length ( $L$ ).

|     | $U_{eff}$<br>[m/s] | $TI_h$<br>[%]   | $\alpha$<br>[-]  | $\delta\alpha$<br>[°] | $L$<br>[m]     |
|-----|--------------------|-----------------|------------------|-----------------------|----------------|
| NBL | $8.28\pm 0.05$     | $10.30\pm 0.17$ | $0.166\pm 0.002$ | $2.03\pm 0.27$        | $\infty$       |
| SBL | $8.11\pm 0.02$     | $5.68\pm 0.01$  | $0.322\pm 0.001$ | $9.61\pm 0.04$        | $145.0\pm 0.2$ |

prescribe a thermal forcing at the surface, while the SBL simulation specifies a constant cooling rate of  $\partial\Theta/\partial t = 0.25$  K/h, following Beare and Macvean (2004). A cooling rate was described rather than a negative surface heat flux, as recommended by Basu et al. (2008). The details of the precursor simulations are summarized in Table 3.1.

### Main simulations

The main simulations subsequently use the information generated in the precursor simulations by utilizing a turbulence recycle method, which adds a turbulent signal to a fixed mean inflow, as upstream boundary conditions. The downstream boundary condition ensures an undisturbed outflow by utilizing a radiation boundary condition. Table 3.1 summarizes the used simulation parameters. Total simulation time includes 20 minutes of spin-up time and a subsequent 60 minutes used for analysis. The size of the domain is only extended in streamwise direction and the recycle area has the same size as the precursor domain. One turbine is simulated, located in the center of the domain in crossstream direction and 6 rotor diameters downstream of the recycling area in streamwise direction. A 5MW NREL turbine, with a hub height of 90 m and a rotor diameter  $D$  of 126 m (Jonkman et al., 2009), is simulated with an Actuator Disc Model with Rotation (ADMR) (Dörenkämper et al., 2015). Turbine yaw angles ( $\phi$ ) of  $-30^\circ$ ,  $0^\circ$ , and  $30^\circ$  are simulated for both inflow conditions, resulting in six simulations in total. A positive yaw angle is here defined as a clockwise rotation of the turbine, looking from above. Main simulations will hereafter be referred to as an abbreviation of its stability and yaw angle, e.g. NBL00; SBL30. The most relevant inflow parameters are displayed in Table 3.2, showing comparable wind speed for all simulations and dissimilar atmospheric conditions related to a Neutral and Stable Boundary Layer. The small spread of the parameters between the three simulations in the same boundary layer, indicated by the standard deviation, can be neglected.

For the downstream wind field, the following will solely study the wake deficit, simply defined as  $U_{def} = U_{wake} - U_\infty$ , where  $U_\infty$  represents the undisturbed inflow and  $U_{wake}$  the observed wind speed in the wake. To this end, frozen turbulence is assumed, meaning the advection velocity is assumed constant in streamwise direction. To reduce the impact of small-scale turbulence, the analyzed wind fields comprise of 60-minute averages.

### 3.2.2 Wake tracking algorithms

#### Traditional methods

As a reference, this study adopts the three wake center definitions used in Vollmer et al. (2016). Two of these utilize the principle that a wake deficit can be described by a Gaussian distribution. The simple one-dimensional Gaussian ( $f_{1D}$ ) only considers a horizontal slice of the wind field at hub height, whereas the bivariate Gaussian ( $f_{2D}$ ) assumes an elliptically shaped wake, thereby including information in two dimensions. Both identify the wake center as the location of the curve's minimum, found with a least squares fitting procedure. Additionally, the 95% confidence interval ( $1.96\sigma$ ) can be used as a measure for the wake width, as proposed in Doubrawa et al. (2016). The pragmatic Available Power method ( $f_{AP}$ ) defines the wake center as the location of the minimal available power produced by a virtual turbine, making it dependent on the defined rotor area. This approach does not provide a metric for the wake width, but could be combined with other definitions such as 99% of the incoming wind speed as proposed in Bastankhah and Porté-Agel (2016). This concept is however very sensitive to turbulence and will therefore not be considered in this study.

#### Multiple 1D Gaussian method

The proposed method also applies the fundamental idea of describing a wake with a Gaussian distribution. It seeks to combine the strengths of  $f_{1D}$  (simple and robust) and  $f_{2D}$  (two dimensional). The Multiple 1D Gaussian ( $f_{M1D}$ ) method fits a simple one-dimensional Gaussian distribution in crosswise direction at every vertical level where information is available, essentially identifying a center, width and magnitude at each altitude. This is illustrated in Figure 3.1 for hub height and upper tip height. To avoid including turbulent cells in the wake, a limit is introduced where the minimum of every fit needs to be larger than the deficit of the wake edge ( $1.96\sigma$ ) at hub height. This is particularly relevant when the wake deficit is small (e.g. far downstream and at higher altitudes).

The black crosses in Figure 3.2a illustrate the wake center positions as identified by the set of one-dimensional Gaussian distributions fitted in crosswise direction. By fitting another one-dimensional Gaussian through the magnitudes of this set of distributions (Figure 3.2b), one obtains the vertical position of the wake center.

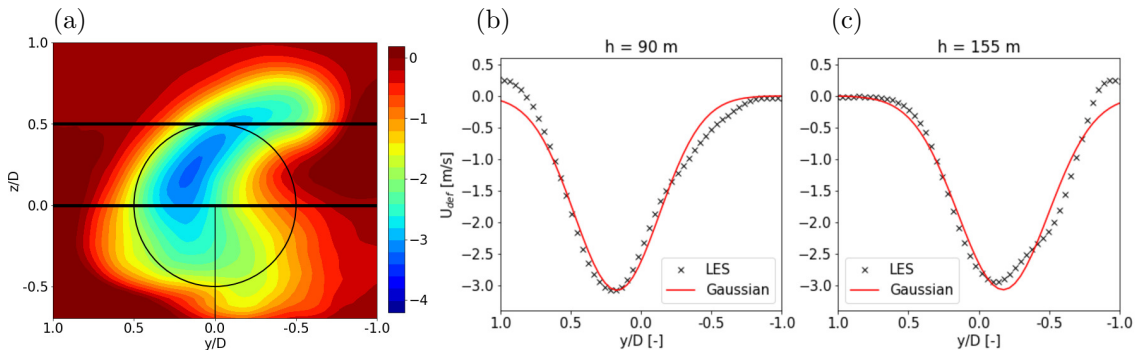


Figure 3.1: **(a)** Exemplary figure (SBL30, 5 rotor diameters downstream) illustrating the concept of the  $f_{M1D}$  method, where the thick black lines illustrate two horizontal cross-sections. **(b)** and **(c)** demonstrate the fitting procedure at these two heights.



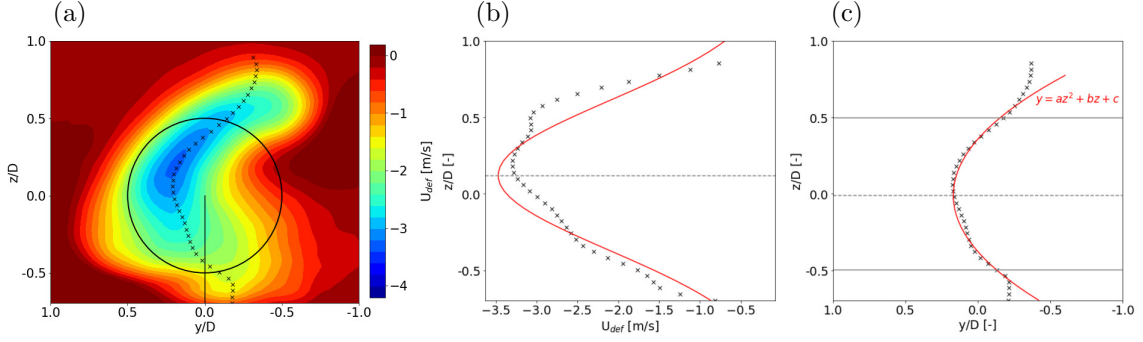


Figure 3.2: Exemplary figures (SBL30, 5 rotor diameters downstream) demonstrating (a) the positions of the wake center line, (b) the determination of the vertical wake center position based on the magnitudes of the wake center line and (c) the definition of wake curl  $a$  [-] and tilt  $\arctan b$  [°] based on wake center line. Information from the set of crosswise fitted Gaussian distributions is indicated with black crosses and red lines illustrate the fitted relation.

The center positions of this set of distributions can in turn be used to express the curliness and tilt of the wake (Figure 3.2c). A simple second-degree polynomial ( $y = az^2 + bz + c$ ) is fitted to these positions between lower and upper tip height, where  $a$  represents the curliness and  $\arctan b$  the tilt of the wake. Comparing the dashed gray lines in Figures 3.2b and c, one can see that the maximum deficit and maximum curl do not necessarily occur at the same altitude. The wake area can simply be deduced from the 95% confidence intervals of the set of one-dimensional Gaussian distributions.

### 3.3 Results and discussion

This section will first present an evaluation of the proposed method, followed by a short overview of its future applications.

#### 3.3.1 Evaluation of the proposed Multiple 1D Gaussian method

Figure 3.3a presents the vertical cross-section of the wake deficit five rotor diameters downstream of a simulated turbine in SBL00. Distances are normalized by the rotor diameter and centered around the turbine's hub. The wake is elliptically shaped and stretched in crosswise direction due to strong wind veer in the SBL (Table 3.2). This strong veer also introduces a small wake deflection even in the absence of yaw misalignment. All four methods identify the wake center at very similar positions, where  $f_{1D}$  by definition excludes any vertical movement. A simplified wind field can be reconstructed from the Gaussian-based methods, using information from the fitted distributions. For this purpose,  $f_{1D}$  uses the same distribution in horizontal and vertical direction, describing a circular wake. These reconstructed wind fields are shown in Figures 3.3b-d. The circular shape described by  $f_{1D}$  severely underestimates the maximum wake deficit. Both  $f_{2D}$  and  $f_{M1D}$  are able to capture the elliptical shape, where the former describes the wake as a perfect ellipse and the latter allows slight deviations and therefore includes more detail.  $f_{2D}$  identifies the wake center as the location with the maximum deficit, which is not necessarily true for  $f_{M1D}$ . Although not designed for an elliptically shaped wake,  $f_{M1D}$  presents the

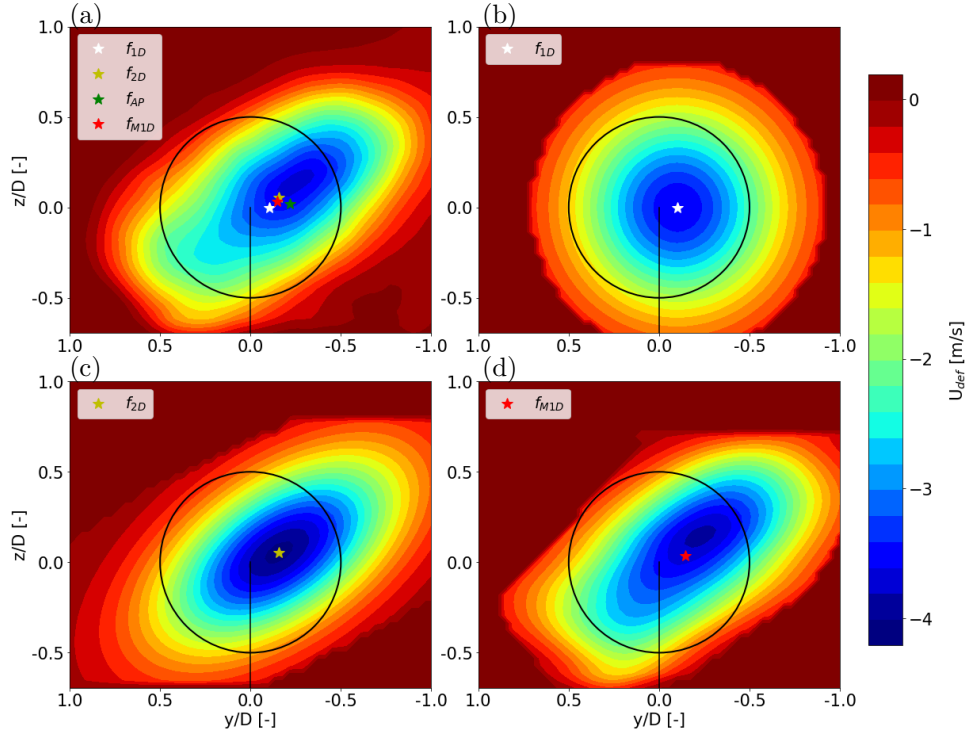


Figure 3.3: Vertical cross-section (looking downstream) of the SBL00 LES wake deficit wind field 5 rotor diameters downstream of the simulated turbine and the wake center positions identified by all methods (a). Reconstructed wind fields based on  $f_{1D}$  (b),  $f_{2D}$  (c) and  $f_{M1D}$  (d).

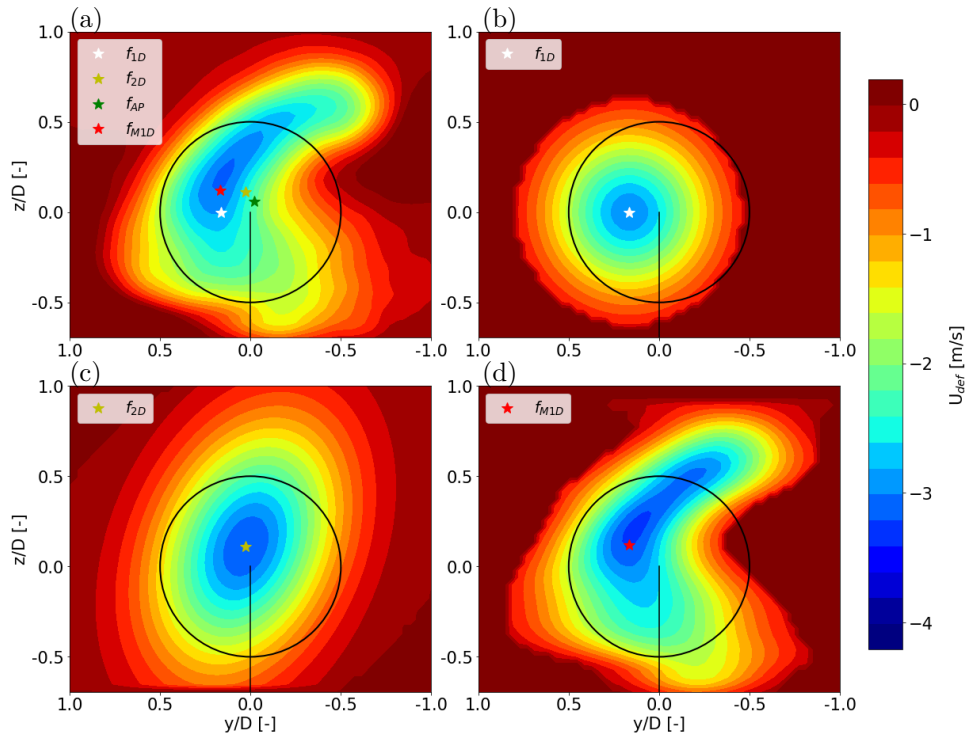


Figure 3.4: Same as Figure 3.3, but for SBL30.

most accurate description of the wind field.

Figure 3.4 presents these results for a redirected wake (SBL30). Figure 3.4a shows that the  $f_{2D}$  and  $f_{AP}$  methods identify a wake center on the inner side of the curled wake, identifying practically no crosswise displacement. This is due to these methods' assumptions of a circularly or elliptically shaped wake, which is not satisfied in this example. The  $f_{1D}$  method better captures the lateral displacement, but excludes any vertical movement. The  $f_{M1D}$  method does not have this limitation and locates the wake center closest to the location of the maximum deficit. The reconstructed wind fields in Figures 3.4b-d clearly show that the curled shape is only captured in  $f_{M1D}$ , demonstrating a superiority of the proposed method. Interesting to note is that  $f_{1D}$  largely underestimates the total wake area, since it does not account for any vertical expansion.

The LES and reconstructed wind fields can be used to estimate the available power of a virtual turbine located downstream of the wake-producing turbine in mean wind direction. The available power is estimated by the cubed rotor effective wind speed. Figure 3.5 presents the percentage error of the available power computed with the reconstructed wind field relative to when computed with the LES wind field. The boxes include all six simulations described in Section 3.2.1. One observes that all methods perform better in the far wake, since there the wake deficit can be more accurately described by a Gaussian distribution. By contrast, the near wake region shows a high momentum zone in the central part of the near wake, introduced by a low thrust force around the turbine's hub. Further,  $f_{2D}$  holds more accurate results than  $f_{1D}$ , but  $f_{M1D}$  consistently outperforms both methods. Especially in the far wake ( $x/D \geq 4$ ), only  $f_{M1D}$  has no systematic bias and it has the smallest spread of all methods. This also indicates that  $f_{M1D}$  is competitive in estimating the available power, the main strength of the  $f_{AP}$  method. This result stresses the improvement of  $f_{M1D}$  over the other methods.

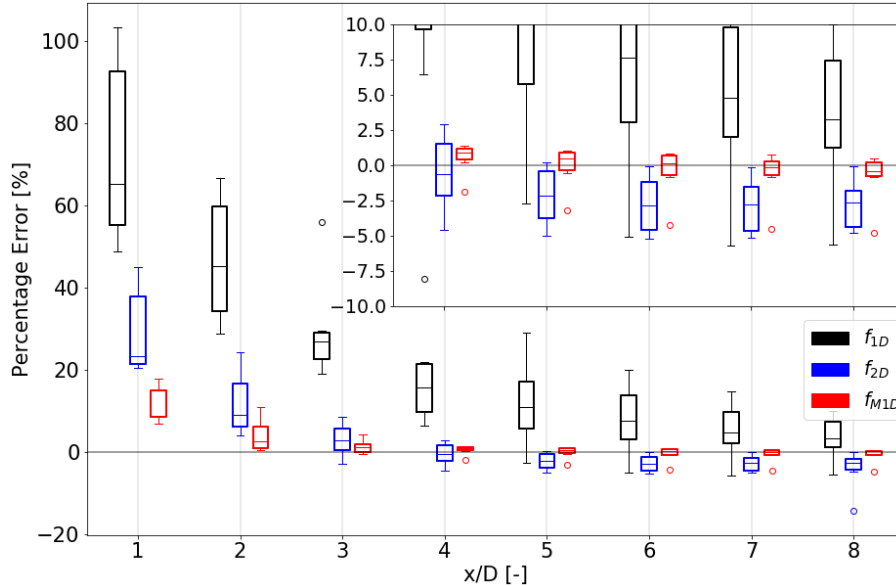


Figure 3.5: Percentage Error of available power of a downstream turbine computed with a wind field based on  $f_{1D}$  (black),  $f_{2D}$  (blue),  $f_{M1D}$  (red) relative to when computed with the LES wind field (calculated with  $(P_{f_{xx}} - P_{LES})/P_{LES} * 100\%$ ). The boxplots include all six simulations described in Section 3.2.1.

Figure 3.6 shows the horizontal wake center trajectories for the NBL (a) and SBL (b) at three yaw angles as determined by the four discussed methods. A  $0^\circ$  yaw angle results in no lateral displacement in the NBL and a small displacement in the SBL, as already observed in Figure 3.3. The differences between the four methods are rather small. There are more noticeable differences between the methods when there is a yaw misalignment.  $f_{2D}$  and  $f_{AP}$  typically show the smallest lateral deflection, whereas  $f_{M1D}$  is very comparable to  $f_{1D}$  and generally finds the largest lateral deflection. The wake displacement is asymmetric, which is due to wind veer and therefore best visible in the SBL. This corresponds to the findings of Fleming et al. (2015), who reported on more effective wake deflection under negative yaw angles compared to positive ones. It should be noted that the deviating trajectory of  $f_{2D}$  in SBL-30 is due to the detachment of the downstream wake in two separate cells as mentioned in Vollmer et al. (2016), which is currently not accounted for in any of the wake center definitions.

Figure 3.6c-d shows the vertical wake center trajectories in the NBL (c) and SBL (d). It should be noted that the vertical displacement is about an order of magnitude smaller than the horizontal displacement. By definition,  $f_{1D}$  excludes any vertical displacement. An initial vertical displacement in the near wake is observed for all simulations. Interestingly, the wake center moves back to hub height in the far wake for non-yawed turbines, but not in the case of yaw misalignment. This suggests that

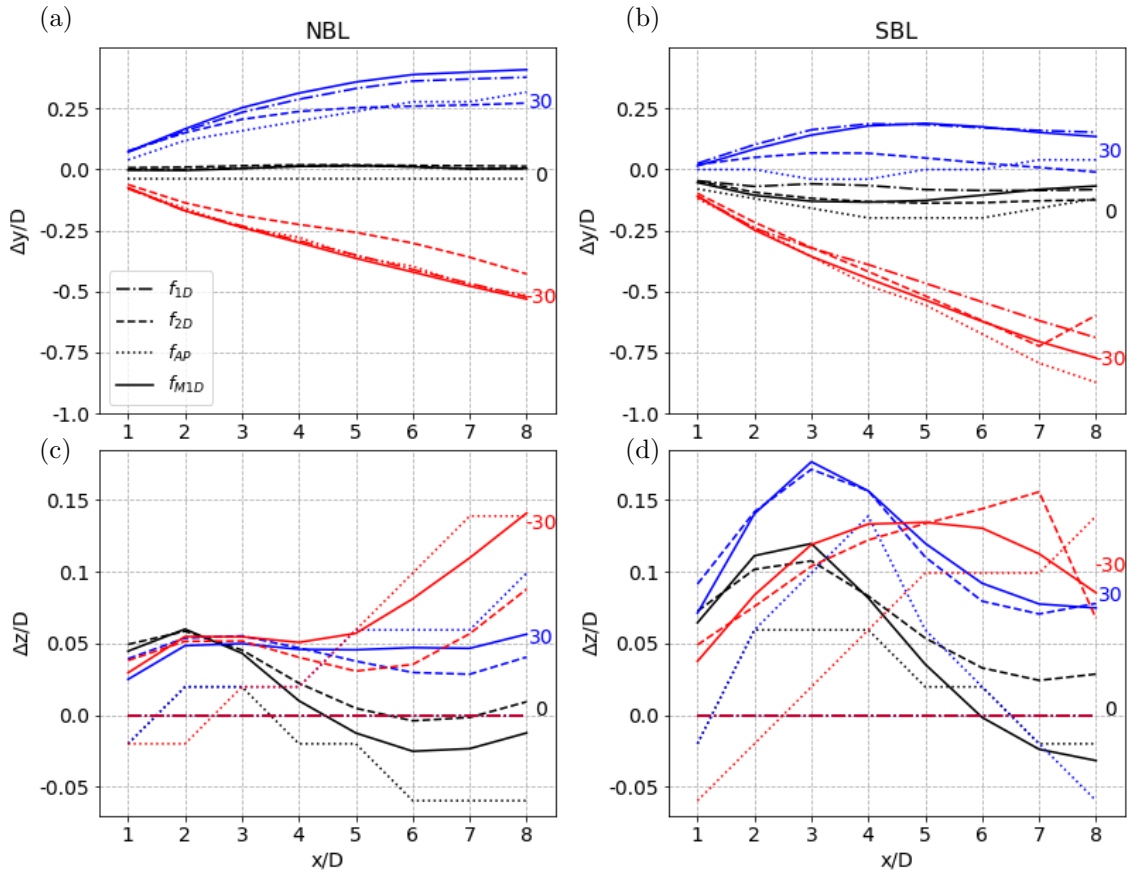


Figure 3.6: Wake center trajectories for NBL (a,c) and SBL (b,d) representing horizontal (a,b) and vertical (c,d) deflection for yaw angles of  $0$  (black),  $30$  (blue) and  $-30$  (red) degrees.

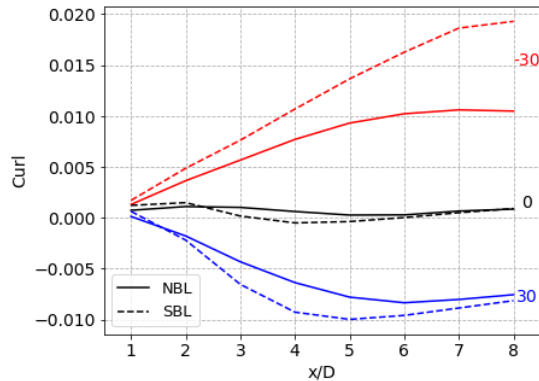


Figure 3.7: Evolution of the wake curliness downstream of the turbine for two stratifications and three yaw angles.

yaw misalignment unintentionally also results in a slight vertical deflection. For this reason, to accurately describe the characteristics of the redirected wake, one should take the vertical displacement into account. In general,  $f_{M1D}$  is most similar to  $f_{2D}$ , which is currently the standard to study vertical wake center displacement. These results demonstrate that  $f_{M1D}$  indeed combines the strengths of  $f_{1D}$  (best in horizontal) and  $f_{2D}$  (best in vertical).

### 3.3.2 Future applications

A potential application of the newly proposed wake tracking algorithm is to study the wake curliness as determined by the method described in Section 3.2.2. Figure 3.7 shows that a non-yawed turbine does not produce a curled wake and therefore has a curliness parameter around zero. The misaligned turbines indicate that the curl is mainly generated in the near wake and remains relatively constant further downstream. Exception to this is SBL-30, showing an ever increasing curliness parameter. This is again due to the detachment of the wake in two separate cells, which is currently not accounted for. These preliminary results suggest that atmospheric conditions affect the wake curliness as the curl parameter is larger in a SBL than in a NBL, for instance due to less mixing.

Figure 3.8 shows a first result of the development of a physically based empirical wake deflection parameterization. The black line indicates the wake center trajectory as determined directly from the LES using  $f_{M1D}$ , while the red line indicates a predicted trajectory based on simple inflow and operational parameters (shear, veer, torque and yaw angle) by employing a simple Ordinary Least Squares fitting model. The testing data set merely encompasses SBL30, whereas the training data set includes five different inflow conditions (not SBL) combined with five yaw angles. These preliminary results suggest that it is possible to determine the wake trajectory of a redirected wake solely based on atmospheric and operational parameters.

In the future, this work will be elaborated on by including vertical wake center displacement and wake shape parameters, as well as the magnitude and distribution of the wake deficit. Additionally, the aspired wake parameterization should be applicable to a wide range of locations and atmospheric conditions, and will be validated with field measurements.

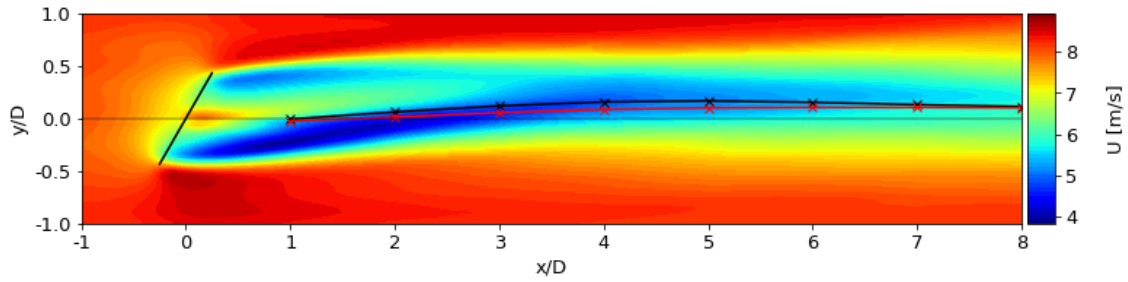


Figure 3.8: Preliminary result showing the potential of the development of a physically based empirical wake deflection parameterization. Contours indicate the SBL30 LES wind field at hub height, the black line indicate the wake center trajectory and the red line the wake center trajectory predicted with a simple statistical model.

### 3.4 Conclusions

This study proposes a new 2D wake description specifically designed to account for shape deformations introduced by intentional yaw misalignment. This parameterized wake tracking algorithm describes frequently studied wake characteristics, such as the wake shape and center position.

Utilizing a large-eddy simulation model at different atmospheric stratifications, a comparison with traditionally used approaches demonstrates a significantly more accurate wake description of the newly proposed method. This does not only include a better estimation of the wake center position, but also a better description of the shape of the redirected wake by introducing a curliness parameter. Consequently, it provides a significantly higher accuracy in the power estimation of a virtual downstream turbine compared to traditional approaches.

A drawback of the newly proposed method is its sensitivity to turbulence, especially when the wake deficit is small (e.g. far downstream and at higher altitudes).

A brief outlook suggests that this wake tracking algorithm is suited to study the effect of the most influential atmospheric and operational parameters on wake propagation under yaw misalignment and the development of a physically based empirical wake parameterization.

## Chapter 4

# A physically interpretable data-driven surrogate model for wake steering

The content of this chapter is identical to the following journal article:

Sengers, B. A. M., Zech, M., Jacobs, P., Steinfeld, G., and Kühn, M.: A physically interpretable data-driven surrogate model for wake steering, *Wind Energy Science*, 7, 1455-1470, <https://doi.org/10.5194/wes-7-1455-2022>, 2022.

©Author(s) 2022. This work is distributed under the Creative Commons Attribution 4.0 License. Reprinted with permission.

**Abstract** Wake steering models for control purposes are typically based on analytical wake descriptions tuned to match experimental or numerical data. This study explores whether a data-driven surrogate model with a high degree of physical interpretation can accurately describe the redirected wake. A linear model trained with large-eddy simulation data estimates wake parameters such as deficit, center location and curliness from measurable inflow and turbine variables. These wake parameters are then used to generate vertical cross-sections of the wake at desired downstream locations. In a validation considering eight boundary layers ranging from neutral to stable conditions, the far wake's trajectory, curl and available power are accurately estimated. A significant improvement in accuracy is shown in a benchmark study against two analytical wake models, especially under derated operating conditions and stable atmospheric stratifications. Even though the results are not directly generalizable to all atmospheric conditions, locations or turbine types, the outcome of this study is encouraging.

## 4.1 Introduction

Wind turbine wakes cause considerable power losses and increased loads at downstream machines. Control strategies to mitigate these negative effects are gaining support in the wind energy community. In particular wake steering, or wake redirection through intentional yaw misalignment (Dahlberg and Medici, 2003; Wagenaar et al., 2012), is regarded as a promising control strategy. A yaw misalignment introduces a lateral thrust force component, which redirects the downstream wake and generates two counter-rotating vortices around upper- and lower-tip height that curl the wake into a kidney shape (Howland et al., 2016). Numerical simulations (e.g., Gebraad et al., 2016; Fleming et al., 2018; Hulsman et al., 2020), wind tunnel experiments (e.g., Campagnolo et al., 2016; Bartl et al., 2018b; Bastankhah and Porté-Agel, 2019) and free-field campaigns (e.g., Fleming et al., 2017b, 2019, 2020; Bromm et al., 2018) have demonstrated the potential of an increased wind farm power production when utilizing the wake steering concept. The efficacy of wake steering is strongly dependent on turbine operation and atmospheric inflow characteristics, such as the turbine thrust coefficient (Jimenez et al., 2010), atmospheric stability (Vollmer et al., 2016), wind shear (Schottler et al., 2017) and turbulence intensity (Bastankhah and Porté-Agel, 2016).

Wake steering controllers regulating the turbine yaw angle are often based on simple wake models that can describe the downstream wake under different inflow conditions. These models, such as those available in the FLORIS framework (NREL, 2020), are typically based on a simplified analytical description of the momentum conservation equations for stationary inflow conditions. When combined with a dynamic controller, wind direction variability can be included (Rott et al., 2018; Simley et al., 2020). The performance of these wake steering controllers, and therefore the accuracy of the underlying wake models, is essential for a successful application of wake steering as a control strategy in a real wind farm.

Frequently used in recent years is the wake model based on Gaussian self-similarity (Bastankhah and Porté-Agel, 2014, 2016; Abkar and Porté-Agel, 2015; Niayifar and Porté-Agel, 2016). Combining wake deficit and wake deflection models, the Gaussian (GAUS) model uses turbulence intensity as an atmospheric inflow parameter. It was validated against field measurements in Annoni et al. (2018) and used as a controller in a field campaign in Fleming et al. (2019). A disadvantage of this model is the negligence of the counter-rotating vortices generated with yaw misalignment and consequently the absence of wake curling. In addition, it does not account for the initial wake deflection caused by the torque-induced wake rotation in sheared inflow (Zahle and Sørensen, 2008). The curl model (Martínez-Tossas et al., 2019) accounts for these phenomena by explicitly including vortices in a model based on linearized Reynolds-averaged Navier–Stokes equations. Having a strong physical basis, it is able to include a wide range of atmospheric conditions and allows flexibility in the wake shape generation. A disadvantage is the high computational expense compared to GAUS. For this reason, King et al. (2021) proposed to include the vortex description of the curl model into GAUS in the Gaussian-Curl Hybrid (GCH) model. This incorporates the initial wake deflection and even secondary wake steering, the deflection of the wake of a downstream turbine by the vortices generated by the yawed upstream turbine (Fleming et al., 2018), but not the curling of the wake itself. In addition, the model includes a wake recovery term representing added



entrainment by the vortices generated due to yaw misalignment. Fleming et al. (2020) showed promising results when using GCH as controller input in a free-field campaign.

These analytical models contain parameters that can be tuned to match numerical or experimental data. In addition, data can be used to formulate parameterized error terms (Schreiber et al., 2020). However, completely data-driven wake models remain rare, and those that exist generally use complex machine learning models with a low interpretability (e.g., Göçmen and Giebel, 2018; Ti et al., 2020). This is remarkable since simple data-driven models are proven to be able to describe complex physical phenomena (Brunton et al., 2016) and are already widely used for prediction purposes, including wind power (Stathopoulos et al., 2013; Messner and Pinson, 2019) and power curve predictions (Marčiukaitis et al., 2017). Although analytical models are presumably more robust, especially when the data set is small, the maximum achievable accuracy is also limited as it is not feasible to develop one model for all scenarios. An analytical model will not be able to capture features for which equations were not in place; hence constant updates to the model code are necessary (e.g., Abkar et al., 2018; Bastankhah et al., 2022). With the community demanding that wake models include increasingly more complex features (e.g., the wake curl), data-driven models become interesting as they can directly capture these features when enough data are available.

The objective of this study is to explore the potential of a Data-driven wAKE steeRING surrogate model (DART) that retains a high degree of physical interpretation. It is investigated whether the curled wake can accurately be described by a set of measurable inflow and turbine variables, and how the use of these variables can be optimized in an interpretable model. Next, the potential of this surrogate model is systematically assessed by evaluating its performance with large-eddy simulation (LES) results for a reference wind speed under a range of atmospheric conditions and subsequently benchmarking it against two analytical wake models (GAUS and GCH). Lastly, the surrogate model’s generalizability to all atmospheric conditions, locations and turbine types is discussed.

## 4.2 Large-eddy simulations

In this study data are generated with revision 3475 of the PARallelized Large-eddy simulation Model (PALM; Maronga et al., 2020), which uses a non-hydrostatic incompressible Boussinesq approximation of the Navier–Stokes equations and the Monin–Obukhov similarity theory to describe surface fluxes. In the boundary layer, the grid on a right-handed Cartesian coordinate system is regularly spaced with  $\Delta = 5$  m, while above the boundary layer height the vertical grid size increases with 6% per cell to save computational costs. The Coriolis parameter corresponds to that at  $55^\circ$  N. Default numerical schemes are used, the main ones being a third-order Runge–Kutta scheme for time integration, a fifth-order Wicker–Skamarock advection scheme for the momentum equations, Deardorff’s 1.5-order turbulence closure parameterization for subgrid-scale turbulence and an iterative multigrid scheme for the horizontal boundary conditions. The simulation chain consists of a precursor simulation to generate realistic inflow conditions and a subsequent main simulation that contains one turbine.

Table 4.1: Summary of simulation parameters and classification into neutral (NBL), near-neutral (NNBL), weakly stable (WSBL) and stable (SBL) boundary layers. The size ( $L_{x,p}, L_y, L_z$ ) of the domains is normalized by the rotor diameter ( $D = 126$  m). All parameters are identical in precursor and main simulations, except for the domain size, which is extended in the streamwise direction ( $L_{x,m}$ );  $t_p$  is the simulated time of the precursor run,  $u_g$  and  $v_g$  the geostrophic wind,  $\partial\theta\partial t^{-1}$  the heating rate,  $H$  the sensible heat flux, and  $z_0$  the surface roughness length.

|     |      | $t_p$ | $L_{x,p}$ | $L_{x,m}$ | $L_y$ | $L_z$ | $u_g$                | $v_g$                | $\partial\theta\partial t^{-1}$ | $H$                    | $z_0$ |
|-----|------|-------|-----------|-----------|-------|-------|----------------------|----------------------|---------------------------------|------------------------|-------|
|     |      | [h]   | [D]       | [D]       | [D]   | [D]   | [m s <sup>-1</sup> ] | [m s <sup>-1</sup> ] | [K h <sup>-1</sup> ]            | [K m s <sup>-1</sup> ] | [m]   |
| BL1 | NBL  | 28    | 40.6      | 61.0      | 20.3  | 14.0  | 10.115               | -3.969               | -                               | -                      | 0.1   |
| BL2 | NBL  | 28    | 40.6      | 61.0      | 20.3  | 14.0  | 10.595               | -5.572               | -                               | -                      | 0.5   |
| BL3 | WSBL | 25    | 27.9      | 50.0      | 14.0  | 8.4   | 9.952                | -5.115               | -0.125                          | -                      | 0.1   |
| BL4 | WSBL | 45    | 27.9      | 50.0      | 14.0  | 8.4   | 10.607               | -6.447               | -0.125                          | -                      | 0.5   |
| BL5 | SBL  | 20    | 11.4      | 30.5      | 7.6   | 4.6   | 9.500                | -5.170               | -0.250                          | -                      | 0.1   |
| BL6 | SBL  | 20    | 11.4      | 30.5      | 7.6   | 4.6   | 10.565               | -6.585               | -0.250                          | -                      | 0.5   |
| BL7 | NBL  | 40    | 40.6      | 61.0      | 20.3  | 14.0  | 9.609                | -3.193               | -                               | -                      | 0.03  |
| BL8 | NNBL | 40    | 40.6      | 61.0      | 20.3  | 14.0  | 9.831                | -3.488               | -                               | -0.001                 | 0.1   |

#### 4.2.1 Precursor simulations

Inflow conditions with realistic turbulent features are generated from an initially laminar flow by adding random perturbations in a precursor simulation with cyclic horizontal boundary conditions. To study the potential of DART under different inflow conditions, eight boundary layers (BLs) ranging from a neutral to a strongly stable BL are used as reference inflow conditions, all having approximately the same wind direction and wind speed at hub height. As reported by Vollmer et al. (2016), wake steering is ineffective in a convective boundary layer, which is therefore not considered in this study. Due to the large computational expense it was not possible to increase the number of simulations. Although these eight BLs do not capture the great variability in the free field, it is considered sufficient to provide a proof of concept for data-driven models.

The total domain size and simulation time vary between the BLs, are determined empirically until convergence to a stationary state occurs and are dependent on the size of the largest eddies that explicitly need to be resolved. The details of the precursor simulations are summarized in Table 4.1.

BL1 and BL2 portray neutral conditions with roughness lengths representing low crops ( $z_0 = 0.1$  m) and parkland ( $z_0 = 0.5$  m), which are typical landscapes found in northern Germany. Following Basu et al. (2008), constant cooling rates at the surface are prescribed to generate stable BLs, where BL3 and BL4 represent weakly stable ( $\partial\theta\partial t^{-1} = -0.125$  K h<sup>-1</sup>) and BL5 and BL6 strongly stable conditions ( $\partial\theta\partial t^{-1} = -0.25$  K h<sup>-1</sup>; following Beare and Macvean, 2004). Two additional (near-)neutral BLs are generated, one representing grassland ( $z_0 = 0.03$  m) and one having a very small negative sensible heat flux ( $H = -0.001$  K m s<sup>-1</sup>), which is in the acceptable range defined in Basu et al. (2008).

Stationary inflow conditions are taken at 2.5 rotor diameters ( $D$ ) upstream of the turbines simulated in the main simulations (Sect. 4.2.2) and averaged over a line of size  $2D$  in the crosswise direction and a period of 60 min. These inflow conditions are assumed to be undisturbed, hence far enough from the turbine that induction does not play a role. Typical inflow parameters are displayed in Fig. 4.1, indicating that the wind speed is comparable for all simulations but that the atmospheric

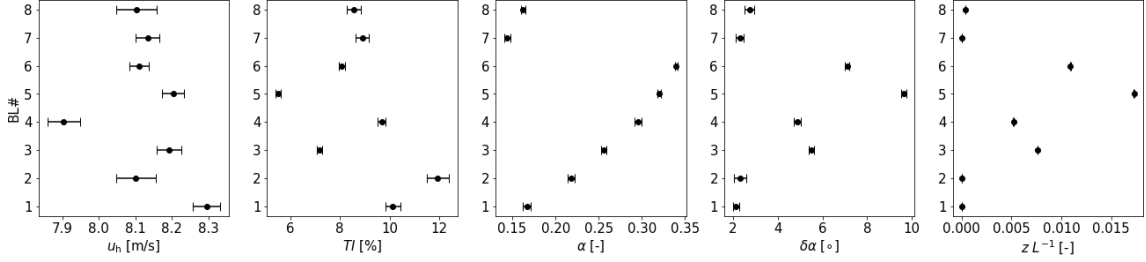


Figure 4.1: Summary of inflow parameters (60 min averages), given as mean (dots) and standard deviation (whiskers) over the 15 main simulations performed in each BL (5 yaw angles times 3 pitch angles). Considered are wind speed ( $u_h$ ) and turbulence intensity at hub height (TI), wind shear ( $\alpha$ ) and veer ( $\delta\alpha$ ) over the rotor area, and the Obukhov stability parameter ( $zL^{-1}$ ) at  $z = 2.5$  m. Equations for these variables can be found in Table 4.3.

conditions vary. A more stable boundary layer, indicated by a larger Obukhov stability parameter ( $zL^{-1}$ ), typically has a higher shear ( $\alpha$ ) and veer ( $\partial\alpha$ ) and lower turbulence intensity (TI). The spread of the parameters between the main simulations (see Sect. 4.2.2) in the same boundary layer, indicated by the standard deviation as whiskers in Fig. 4.1, is small enough to be neglected.

#### 4.2.2 Main simulations

After generating stationary inflow conditions with a precursor, simulations with one turbine are performed. Information on turbulence characteristics from the precursor simulation is fed to the main simulation by adding a turbulent signal to a fixed mean inflow (turbulence recycling method) far upstream of the turbine. A radiation boundary condition ensures undisturbed outflow downstream of the simulated turbine. The size of the recycling area is equal to the domain size of the precursor simulation, and the domain size of the main simulation is only extended in streamwise direction by placing a turbine at  $x = 6D$  downstream of the recycling area. Wake data until  $x = 10D$  are used for analysis, but the domain is extended to  $x = 13D$  to eliminate blockage effects. The total simulation time is 80 min: the first 20 min are considered spin-up time, and the last 60 min are used for analysis. The simulated turbine is an actuator disc model with rotation (ADMR) representing a 5 MW NREL turbine, having a hub height of 90 m and a rotor diameter  $D$  of 126 m (Jonkman et al., 2009), as implemented in Dörenkämper et al. (2015). Turbine yaw angles ( $\phi$ ) of  $-30$ ,  $-15$ ,  $0$ ,  $15$  and  $30^\circ$  are simulated, where a positive yaw angle is defined here as a clockwise rotation of the turbine when looking from above. Pitch angles ( $\beta$ ) of  $0$ ,  $2.5$  and  $5^\circ$  are simulated to study the effect of the thrust force on downstream wake characteristics. This adds up to a total of 120 main simulations with one turbine, i.e., 15 turbine settings (5 yaw angles times 3 pitch angles) for each of the 8 inflow conditions. The effect of  $\phi$  and  $\beta$  on the thrust coefficient  $C_T$  is illustrated in Fig. 4.2, illustrating that the effect of the turbine yaw angle of the thrust coefficient is approximately symmetric around zero.

It should be noted that smaller step sizes for yaw and pitch angles would be preferred as these step sizes could be too coarse when utilizing a regression-based model (Sect. 4.3.3). This can lead to deviating estimates when interpolating to values far away from these set points (e.g., for  $\phi = 7.5^\circ$ ). Increasing the step size would, however, lead to more simulations, which was computationally not feasible and not

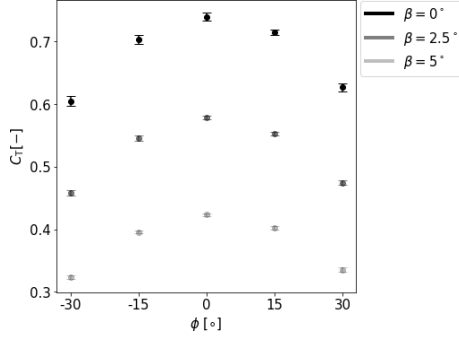


Figure 4.2: Overview of the effect of yaw angle  $\phi$  and pitch angle  $\beta$  on thrust coefficient  $C_T$ . Whiskers indicate the standard deviation between all eight BLs.

deemed necessary to show proof of concept.

The wake is described using the normalized wake deficit, defined as  $u_{nd} = \frac{u_{wake} - u_\infty}{u_{\infty,h}}$ , where  $u_{wake}$  represents the observed wind speed in the wake,  $u_\infty$  the undisturbed inflow 2.5 D upstream at the same height and  $u_{\infty,h}$  the undisturbed inflow at hub height. It is assumed that the advection velocity is constant in streamwise direction (assumption of frozen turbulence) and that the wake behaves as a passive tracer in the ambient wind (Larsen et al., 2008).

### 4.3 Development of the Data-driven wake steering surrogate model

This section describes the development of the Data-driven wake steering surrogate model (DART). It should be noted that many different kinds of data-driven models exist. For the purpose of this exploratory study, the focus was to develop a simple regression model that performs well on small data sets without the risk of overfitting. Figure 4.3 displays a flowchart of the training and execution (including testing) procedure. The respective sections in which each step is explained are indicated in parentheses. DART is trained with the LES data representing reference inflow conditions (BLs) described in Sect. 4.2. From the wake data, key wake steering variables are deducted by executing the multiple 1D Gaussian method explained in Sect. 4.3.1. Additionally, input variables are extracted at 2.5 D upstream, and several operations are performed (Sect. 4.3.2) to determine the final input parameters. A multi-task lasso regression (Sect. 4.3.3) is subsequently performed to generate a coefficient matrix.

This matrix can be used in the execution (testing) of the model to estimate the key wake steering parameters for new inflow conditions. The same operations as in the training procedure are done on the input variables to obtain the input parameters, after which the linear model (Sect. 4.3.3) is solved to estimate the key wake steering parameters. A reversed version of the multiple 1D Gaussian model can then be executed (Sect. 4.3.4) to obtain gridded wake data. During model development, this wake estimation can be compared to the original LES data. One can experiment with different input variables and operations to determine what set of input parameters gives the most accurate solution (Sect. 4.3.5). This last step has not been included in Fig. 4.3 to reduce clutter.

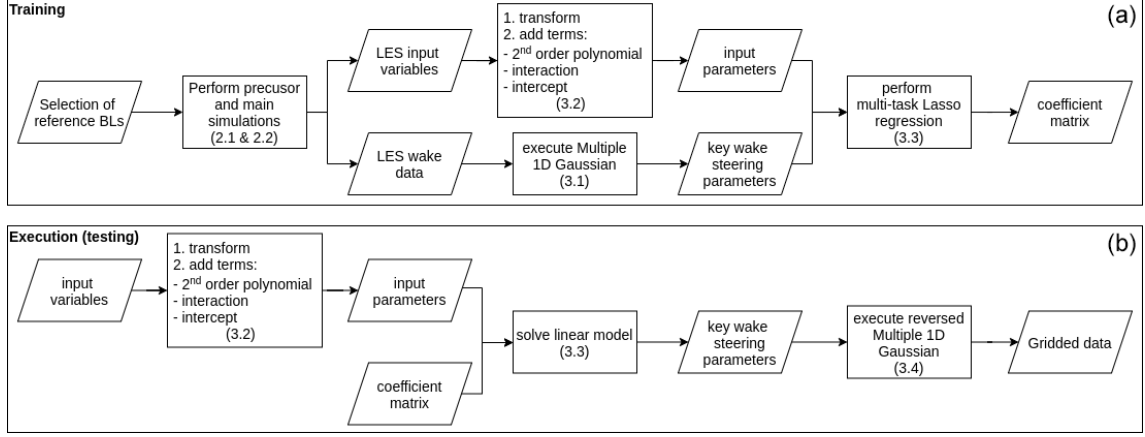


Figure 4.3: Flowchart describing the training (a) and execution (b) procedure of DART. The section in which the process is described is indicated in parentheses. The coefficient matrix generated in (a) is used in (b).

### 4.3.1 Defining key wake steering parameters

A data-driven model will not be able to produce a full multidimensional flow field but rather estimate parameters describing the wake at desired downstream positions. Since curled wakes are considered, key wake steering parameters in this study are retrieved with the multiple 1D Gaussian method (Sengers et al., 2020). In the example below, the wake of a turbine with a  $+30^\circ$  yaw angle in BL1 at  $x = 5D$  is considered (Fig. 4.4a). This method fits a simple 1D Gaussian at every vertical level ( $k = 1 \dots K$ ) where information is available to obtain a set of local normalized wake center deficits ( $\mathbf{A} = A_1 \dots A_K$ ), wake center positions ( $\boldsymbol{\mu} = \mu_1 \dots \mu_K$ ) and wake widths ( $\boldsymbol{\sigma} = \sigma_1 \dots \sigma_K$ ). Subsequently, another Gaussian can be fitted through the local wake center deficits in the vertical (Fig. 4.4b) to find the overall normalized wake center deficit ( $A_z$ ) and vertical position with respect to hub height ( $\mu_z$ ), as well as the vertical extension of the wake ( $\sigma_z$ ). The local wake center position and width at vertical level  $k$  that corresponds to  $\mu_z$  are subsequently considered to be lateral wake center position ( $\mu_y$ ) relative to the turbine location and wake width ( $\sigma_y$ ). Next, by fitting a second-order polynomial through the local wake center positions between upper- and lower-tip height (Fig. 4.4c), one obtains a measure for the curl (coefficient of quadratic term) and tilt (coefficient of linear term) of the wake. An expression for the wake width as a function of height is found by repeating this step for the local wake widths (Fig. 4.4d) to obtain coefficients  $s_a$  and  $s_b$ . After this procedure, the wake can be described by the set of dimensionless parameters displayed in Table 4.2.

Note that this method cannot accurately capture the splitting of the wake in two separate cells, which might occur under strong veer as discussed in Vollmer et al. (2016). Such cases will result in inaccurate values for the key wake steering parameters and should be filtered out before applying the regression model described in Sect. 4.3.3.

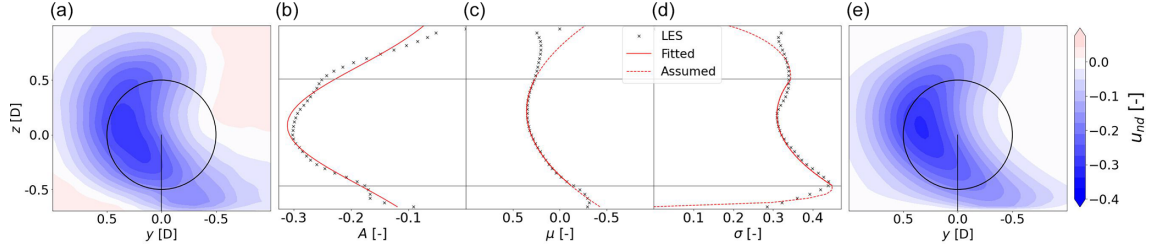


Figure 4.4: Exemplary figures (BL1,  $\phi = +30^\circ$ ,  $x = 5D$ ) illustrating the key wake steering parameters. (a) Normalized wake deficit cross-section (contour) of original LES data. (b) The local normalized wake center deficits  $\mathbf{A}$ , (c) local wake center positions  $\boldsymbol{\mu}$ , and (d) local wake widths  $\boldsymbol{\sigma}$ . Black crosses indicate LES, solid red lines the relation fitted in according to the multiple 1D Gaussian method (Sect. 4.3.1) and dashed red lines the assumed continuation in the reversed multiple 1D Gaussian composition method (Sect. 4.3.4). (e) Cross-section (contour) of the normalized wake deficit after applying the reversed multiple 1D Gaussian composition method.

Table 4.2: Defined dimensionless key wake steering parameters. The normalized wake deficit is computed as described in Sect. 4.2.2. All length parameters are nondimensionalized by the rotor diameter  $D$ .

| Scalar parameter                         | Symbol     |
|------------------------------------------|------------|
| Amplitude of the normalized wake deficit | $A_z$      |
| Lateral wake center displacement         | $\mu_y$    |
| Vertical wake center displacement        | $\mu_z$    |
| Width of the wake center height          | $\sigma_y$ |
| Vertical extent                          | $\sigma_z$ |
| Curl                                     | curl       |
| Tilt                                     | tilt       |
| Quadratic wake width parameter           | $s_a$      |
| Linear wake width parameter              | $s_b$      |

### 4.3.2 Input parameters

A regression model (Sect. 4.3.3) is used to estimate the key wake steering parameters in Table 4.2. A set of measurable inflow and turbine variables are used as input parameters, which are made dimensionless to make the model more universally applicable, at least within the variability found between the simulations in this study. This set of parameters is presented in Table 4.3.

Although these input parameters might all have their own isolated effect on the wake propagation, they are heavily correlated in LES as shown in Fig. 4.5. One can identify several highly correlated input clusters, representing (1) yaw ( $\phi$ ), (2) atmospheric inflow ( $\delta\alpha$ ,  $\alpha$ ,  $zL^{-1}$ , TI) and (3) turbine variables ( $C_T$ ,  $C_Q$ , TSR). Note that wind speed is not included since it is approximately constant in all simulations and correlated with both inflow and turbine parameters. A high correlation between variables indicates that they contain much of the same information. Providing the same information to a model multiple times is futile as it will not improve the accuracy. For this reason, it is hypothesized that reasonable accuracy can be achieved with the regression model as long as one variable from each input cluster is included. This would reduce the number of model parameters and would give the user freedom to choose parameters based on preference and availability. However, since the input variables are not perfectly correlated, the information they contain is slightly different, and including both

Table 4.3: Set of dimensionless input parameters:  $\text{dir}$  is the wind direction [ $^\circ$ ],  $z$  is the height above the surface [m],  $\bar{u}_h$  and  $\sigma_{u_h}$  are the mean and standard deviation of the wind speed at hub height [ $\text{m s}^{-1}$ ],  $u_{\text{eff}}$  is rotor effective wind speed [ $\text{m s}^{-1}$ ],  $T$  is thrust [N],  $Q$  is torque [N m], and  $\omega$  is rotor speed [ $\text{rad s}^{-1}$ ]. Subscript  $_{\text{ut}}$  indicates upper-tip and  $_{\text{lt}}$  lower-tip height.

| Variable                    | Symbol         | Calculated                                                                          |
|-----------------------------|----------------|-------------------------------------------------------------------------------------|
| Turbine yaw angle           | $\phi$         | $\phi$                                                                              |
| Veer                        | $\delta\alpha$ | $\text{dir}_{\text{ut}} - \text{dir}_{\text{lt}}$                                   |
| Shear                       | $\alpha$       | $\ln \frac{u_{\text{ut}}}{u_{\text{lt}}} / \ln \frac{z_{\text{ut}}}{z_{\text{lt}}}$ |
| Obukhov stability parameter | $zL^{-1}$      | $2.5/L$                                                                             |
| Turbulence intensity        | TI             | $\sigma_{u_h}/\bar{u}_h$                                                            |
| Thrust coefficient          | $C_T$          | $T/(0.5 \rho u_{\text{eff}}^2 \pi (D/2)^2)$                                         |
| Torque coefficient          | $C_Q$          | $Q/(0.5 \rho \pi u_{\text{eff}}^2 (D/2)^3)$                                         |
| Tip speed ratio             | TSR            | $\omega(D/2)/u_h$                                                                   |

variables can increase the model's accuracy. For this reason, two versions of the surrogate model having a different number of variables are experimented with; see Sect. 4.3.5. Although a high correlation between input variables is usually undesirable in regression problems due to multicollinearity, Sect. 4.3.3 explains that this is not an issue due to the regression model used in this study.

This regression model is linear, so to include nonlinear relations the input variables can be transformed using reciprocal ( $f(x) = x^{-1}$ ), exponential ( $f(x) = e^x$ ), logarithmic ( $f(x) = \ln(x)$ ) or square root ( $f(x) = \sqrt{x}$ ) transformations. All these transformations have been tested in the procedure described in Sect. 4.3.5. In addition to the transformed variables, second-order polynomial and interaction terms are added, as well as an intercept (unity), extending the set of input parameters.

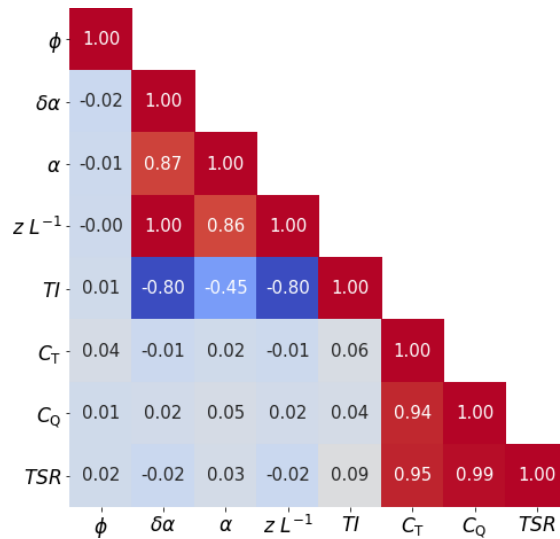


Figure 4.5: Correlation matrix of the dimensionless input parameters in LES. Colors indicate a positive (red) or negative (blue) correlation.

### 4.3.3 Regression model

Since the LES data set has a relatively small sample size, a linear model is chosen as they perform well on small sample sizes, reduce the risk of overfitting compared to more complex machine learning models and are highly interpretable (Hastie et al., 2009).

The regression is formulated as a linear model in matrix form

$$\underset{(n \times d)}{\mathbf{Y}} = \underset{(n \times p)}{\mathbf{X}} \times \underset{(p \times d)}{\mathbf{B}}, \quad (4.1)$$

which estimates the output variable  $\mathbf{Y}$  based on the design matrix  $\mathbf{X}$  and coefficient matrix  $\mathbf{B}$ . Matrix dimensions indicated in Eq. (4.1) represent the sample size  $n$ , number of downstream distances  $d$  and number of input parameters  $p$ . Note that  $p$  contains the transformed variables and their second-order and interaction terms as well as intercepts. Since these parameters are highly correlated and not all relevant, the coefficients are determined based on a lasso regression method as introduced by Tibshirani (1996). This guarantees a shrinkage of the number of variables through a regularization parameter found by cross-validation. Relevant input parameters are isolated from irrelevant parameters by multiplying the latter with a coefficient of zero, effectively eliminating them from Eq. (4.1). Multicollinearity is therefore not an issue in lasso, contrary to ordinary least squares, as typically only one parameter is chosen from a set of highly correlated input parameters. This reduces the number of input parameters, increasing the interpretability of the model. Additionally, it is desired that the same set of input parameters is used to estimate the output variable at all downstream distances. This is guaranteed in the multi-task lasso method introduced by Obozinski et al. (2006), which is implemented in the multi-task lasso algorithm from the *scikit-learn* Python library (Pedregosa et al., 2011). See Sect. 2.2.1 for further explanation.

Whereas fitting the regression coefficients is more complex than ordinary least squares fitting, the estimations of the key wake steering variables in the testing or execution phase are generated through simple matrix multiplication as shown in Eq. (4.1). The algorithm is therefore highly interpretable, easy to implement and computational inexpensive.

### 4.3.4 Wake composition: reversed multiple 1D Gaussian

The coefficient matrix  $\mathbf{B}$  can be used to estimate the key wake steering parameters in Table 4.2 from inflow variables. This information is used to compose a vertical cross-section of the wake deficit using the reverse of the multiple 1D Gaussian method described in Sect. 4.3.1. The amplitude of the normalized wake deficit  $\hat{\mathbf{A}}$  at each height ( $k = 1 \dots K$ ) can be computed by simply filling out the Gaussian function using  $A_z, \mu_z, \sigma_z$ . Similarly, local wake center positions  $\hat{\boldsymbol{\mu}}$  and local wake widths  $\hat{\boldsymbol{\sigma}}$  can be found by filling out a second-order polynomial. Additional assumptions outside of the rotor area are that the curl continues (dashed red line in Fig. 4.4c), and the wake width can be described by an ellipse between lower tip and surface and between upper tip and wake top (dashed red line in Fig. 4.4d). Finally, a simple 1D Gaussian can be filled out at every vertical level using the information from  $\hat{\mathbf{A}}, \hat{\boldsymbol{\mu}}, \hat{\boldsymbol{\sigma}}$ , resulting in a two-dimensional grid filled with  $u_{\text{nd}}$  values (Fig. 4.4e). Comparing this composed wake to the original LES in Fig. 4.4a, one can see that this simple



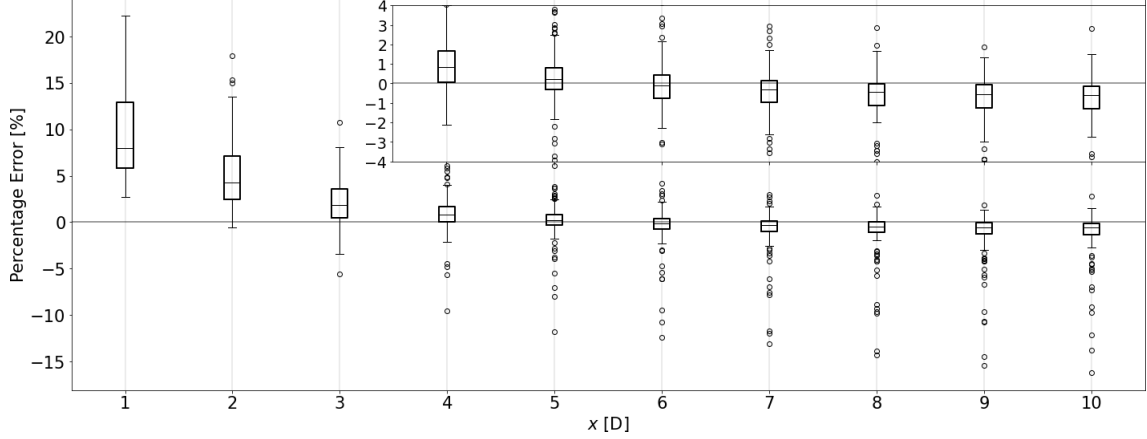


Figure 4.6: Accuracy of the wake composition procedure expressed as a percentage error in available power of a virtual downstream turbine. At each downstream distance, data from all 120 simulations are considered. The subplot in the top right zooms in to  $4D \leq x \leq 10D$ . Axis labels correspond to those of the main plot.

description still contains much of the original information. The shape of the wake is conserved, as well as the displacement of the wake center. The maximum deficit of the composed wake center appears to be slightly larger than in LES. Additionally, in the composition the maximum wake deficit is always in the center (definition of a Gaussian), which is not necessarily true in LES or reality.

#### 4.3.4.1 Wake composition validation

The procedure described in Sect. 4.3.4 is repeated for all 120 simulations, and  $1D \leq x \leq 10D$  at every  $D$ . The metric used here to evaluate the accuracy of this method is the percentage error in available power in the rotor area of the composed wake relative to when computed with the original LES wind field ( $PE [\%] = (P_{\text{comp}} - P_{\text{LES}})/P_{\text{LES}} \cdot 100$ ). A few things can be noted by studying the results shown in Fig. 4.6. The composition shows a large systematic positive bias in the near wake ( $x \leq 3D$ ). This is due to the so-called double-bell shape of the near wake, with a speed-up region around hub height. When attempting to fit this with a simple 1D Gaussian, the deficit in the rotor area is underestimated, resulting in a positive percentage error. For this reason, the near wake is excluded from analysis in the remainder of this work. Further downstream ( $x \geq 8D$ ) a small negative systematic bias can be identified, which is due to the “top-hat” shape of the wake deficit as a result of temporal averaging. This is not captured by a Gaussian function and will on average result in an overestimation of the wake deficit amplitude. The large (negative) outliers typically indicate cases where the wake does not have a Gaussian shape, such as the separation in two cells under strong veer. The median error in the region  $4D \leq x \leq 10D$  is, however, smaller than 1%.

#### 4.3.5 Feature selection

Numerous combinations of input parameters are possible. This includes choosing from the variables presented in Table 4.3, as well as which of the five transformations proposed in Sect. 4.3.2 to use. In order to find the most accurate solution, all

combinations are tested. The combination that provides the minimum absolute percentage error in available power over all training data, i.e., all considered simulations and downstream distances ( $4D \leq x \leq 10D$ ), is sought. When using all eight variables presented in Table 4.3, denoted DART-8, only the variable transformations need to be decided. The number of possible combinations is proportional to the number of transformations to the power of the number of variables. All five transformations are tested on all variables except for  $\phi$ , for which the logarithmic and square root transformations have been omitted because negative values occur. This results in a total of  $3^1 \cdot 5^7 = 234375$  possible combinations. Not only is using all variables computationally expensive, as is discussed in Sect. 4.4.1, operationally it is also unlikely that all variables are routinely obtained due to high costs. As hypothesized in Sect. 4.3.2, using one variable from each input cluster is already expected to produce accurate results. To test this, a version of DART with only three variables, denoted DART-3, is considered. Allowing each variable to be chosen and transformed, the total number of possible combinations is a multiplication of the possible combinations of each input cluster. In total,  $(1 \cdot 3) \cdot (4 \cdot 5) \cdot (3 \cdot 5) = 900$  possible combinations are tested to find the optimal set of input parameters. It should be noted that other feature selection procedures could be considered to reduce the computational expense needed for training, but enhancing the training procedure was considered outside of the scope of the current work.

#### 4.3.6 Benchmark models

DART is benchmarked against the Gaussian (GAUS) and the Gaussian-Curl Hybrid (GCH) models present in version 2.2.2 of the FLORIS framework (NREL, 2020). Although secondary steering is not studied here, the GCH is still included because of its incorporation of initial wake deflection and the added wake recovery term. Both models share the same tuning parameters for the far-wake onset ( $\alpha_{\text{floris}}, \beta_{\text{floris}}$ ) and wake recovery rate ( $k_{a,\text{floris}}, k_{b,\text{floris}}$ ). Analogous to the training of DART discussed in Sect. 4.3.5, the values of the tuning parameters are determined by minimizing the APE of available power over all considered simulations and downstream distances ( $4D \leq x \leq 10D$ ). Information on inflow (e.g.,  $u_h$ , TI) is taken from the LES data. The models are trained independently of each other and will therefore have different values for the tuning parameters.

The data used for the tuning include simulations with yaw and pitch angles. FLORIS adjusts the thrust coefficient numerically for yaw angles, but not for pitch angles. For this reason, the thrust coefficient lookup table was adjusted by the ratio  $C_{T,\text{pitch}}/C_{T,\text{nopitch}}$  found in LES (Fig. 4.2).

## 4.4 Results

### 4.4.1 Performance on training data

This section displays the performance of the Data-driven wAKE steeRing surrogate model (DART) and the benchmark models when using all 120 simulations for training or tuning. In Sect. 4.4.2 and 4.4.3 a validation of the model with testing data is shown.

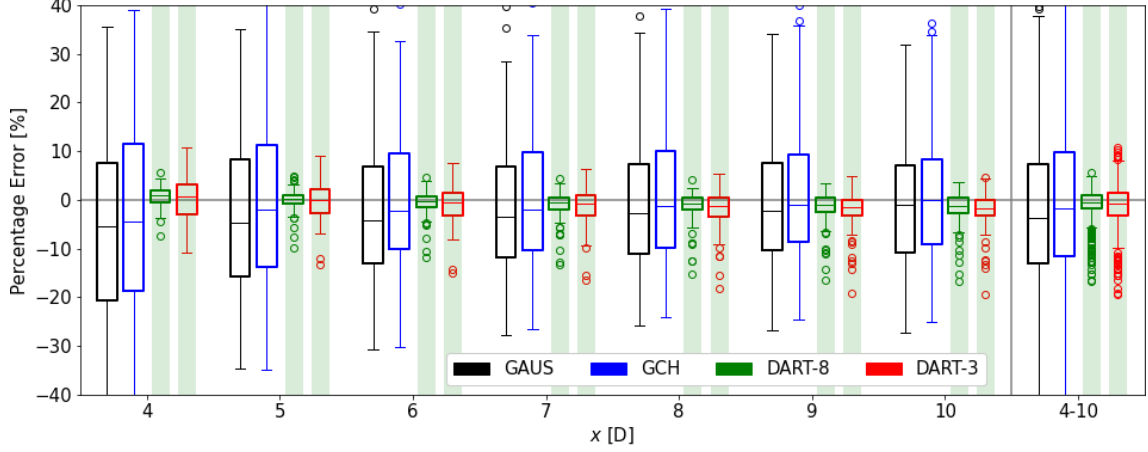


Figure 4.7: Performance of all models on training data displayed as percentage error in available power. In black GAUS, in blue GCH, in green DART-8 and in red DART-3. The boxes on the far right (labeled 4–10) include all simulations and all distances. The shaded areas indicate a significant improvement (green), insignificant difference (yellow) or significant decline (red) in the accuracy of DART compared to the benchmark models.

Following the feature selection procedure as described in Sect. 4.3.5, the optimal combination of input parameters of DART-8 was found to be the set  $(\phi, \delta\alpha, \alpha^{-1}, \ln(zL^{-1}), \text{TI}^{-1}, C_T^{-1}, \sqrt{C_Q}, \text{TSR}^{-1})$  and for DART-3  $(\phi, \delta\alpha^{-1}, \ln(C_T))$ . Figure 4.7 compares the performance of these versions to that of the benchmark models as a function of downstream distance. The shaded areas indicate a significant improvement (green), insignificant difference (yellow) or significant decline (red) in the DART accuracy compared to the best-performing benchmark model. Statistical significance is determined using an independent Welch  $t$  test on the absolute percentage error with a probability value  $< 0.05$ . This test assumes a normal distribution but can deal with unequal variances between data sets. From Fig. 4.7 it is clear that both DART-8 and DART-3 consistently provide significantly more accurate results than GAUS and GCH. Most striking is the variability in the benchmark models that is an order of magnitude larger than that of DART. The reason for this is systematically evaluated in Sect. 4.4.2 and 4.4.3. The systematic error, indicated by the median, is however very similar for all models. Comparing the two benchmark models, it is clear that GCH consistently estimates a higher power than GAUS due to the added wake recovery term. The accuracy of DART-8 is higher than that of DART-3, especially closer to the turbine. This is attributed to the stronger wake deficit closer to the turbine as the wake center deficit  $A_z$  exhibits a larger range of possible values closer to the turbine. For instance in the training data at  $x = 4 \text{ D}$ , the range is  $-0.6 \leq A_z \leq -0.21$ , whereas at  $x = 10 \text{ D}$  the range is  $-0.27 \leq A_z \leq -0.09$ . Estimations with the same relative error therefore bear a larger absolute error closer to the turbine. Having access to more information, DART-8 consistently has a smaller relative error when estimating  $A_z$  than DART-3, which has a larger effect on the available power estimates closer to the turbine.

The order of magnitude of computational costs needed to train the models on a single node is displayed in Table 4.4. Computational expenses needed to generate the LES database are not considered. The benchmark models tune their parameters in approximately 7.5 h (GAUS) and 8.25 h (GCH). DART’s training procedure is split up in different stages. The column “Iteration” refers to the regression fitting to

Table 4.4: Model training (DART) or tuning (GAUS and GCH) time using all 120 simulations and seven ( $4D \leq x \leq 10D$ ) downstream distances. Iteration times are expressed as the mean over the first 100 iterations. DART’s total is a simple multiplication of iteration and combinations.

|        | Iteration<br>[s] | Combinations<br>[-] | Total<br>[h] |
|--------|------------------|---------------------|--------------|
| GAUS   | –                | –                   | 7.5          |
| GCH    | –                | –                   | 8.25         |
| DART-8 | 148              | 234 375             | 9635         |
| DART-3 | 45               | 900                 | 11.25        |

obtain the coefficient matrix  $\mathbf{B}$  (Sect. 4.3.3) and the calculation of the absolute percentage error in available power at  $4D \leq x \leq 10D$  (Sect. 4.3.5). This can be carried out in seconds, in which fewer variables result in faster fitting. The column “Combinations” indicates the number of possible combinations that need to be tested (Sect. 4.3.5). The total training time is then simply the number of combinations to be tested times the execution time of one iteration. Because of its large number of possible combinations, DART-8’s total training time would be over a year on a single node, which is not operationally feasible. To generate the results in Fig. 4.7, the training process was heavily parallelized. With 900 possible combinations DART-3 can be trained in approximately 11.25 h, which is only slightly more than the benchmark models. As mentioned in Sect. 4.3.5, the training procedure could be enhanced, but this was considered outside of the scope of the current work. Even though Fig. 4.7 shows a small accuracy gain of DART-8 over DART-3, the computational costs to train DART-8 are much larger, and measuring all these variables in the free field is impractical. For these reasons, it is decided to only consider DART-3 in the remainder of this study.

#### 4.4.2 Performance on testing data

A simple leave-one-out cross-validation technique is used to discuss the performance of DART compared to the benchmark models. The models are trained or tuned with seven out of the eight BLs (Fig. 4.1) and tested on the remaining one, representing a new inflow condition. Eight evaluations can therefore be performed, i.e., each BL being tested once. Note that for each evaluation a set of optimal parameters and transformations are determined, which can differ from DART-3 in Fig. 4.7. Similarly, GAUS and GCH are tuned again, resulting in new values for their tuning parameters. Since the models show similar behavior in relation to the downstream distance as discussed in Sect. 4.4.1, here only the collective result over  $4D \leq x \leq 10D$  is discussed.

Figure 4.8 presents the results of this validation procedure. For all BLs, DART-3 shows a significant improvement over GAUS and GCH. The systematic biases (indicated by the medians) are similar for all models on the order of a few percent, but the variability is greatly reduced in DART-3. The main reason for this is that the benchmark models do not include a pitch angle parameter  $\beta$ . Although the  $C_T$  tables in the models are corrected in this study, the tunable parameters do not account for this. To clarify, LES finds a decreasing wake size (in both horizontal and vertical extent) with increasing  $\beta$ . This is accurately captured by DART-3, but GAUS and GCH produce a wake of similar size independent of  $\beta$  or  $C_T$ . The

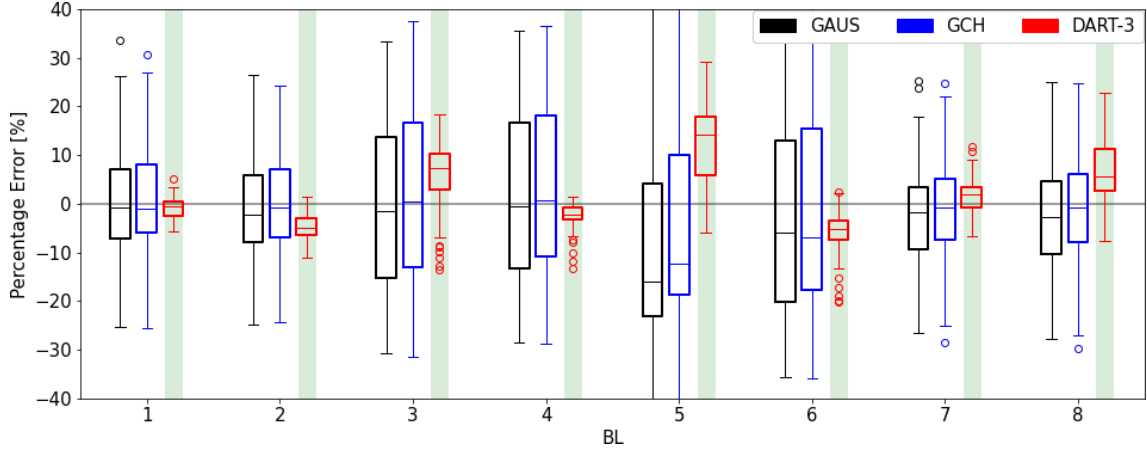


Figure 4.8: Performance of GAUS (black), GCH (blue) and DART-3 (red) using a leave-one-out cross-validation technique. Performance is displayed as a percentage error in available power. Each box includes data from 15 main simulations and  $4D \leq x \leq 10D$ . The shaded areas again indicate a significant improvement (green), insignificant difference (yellow) or significant decline (red) in the accuracy of DART-3 compared to the benchmark models.

inclusion of this effect is a notable improvement of DART that is important for control strategies such as axial induction control (e.g., Corten and Schaak, 2003; van der Hoek et al., 2019).

Furthermore, BL5 contains the worst results for all models. Figure 4.1 indicates that this is an extreme case as it has the highest Obukhov stability parameter and veer along with the lowest turbulence intensity. This is problematic for the models since it is an inflow condition unlike anything it was trained for. This indicates a limited generalizability of all models, and caution is needed when applying them under conditions that differ greatly from those used for training. This is further discussed in Sect. 4.5.1.

#### 4.4.3 Operation without derating

For a fair comparison between DART-3 and the benchmark models, this section only considers simulations representing operation without derating the turbine ( $\beta = 0^\circ$ ). The training (selection of parameters for DART-3) and tuning (tuning parameters of GAUS and GCH) have been repeated, and the results of the leave-one-out cross-validation technique are displayed in Fig. 4.9. The variability in the benchmark models in (near-)neutral conditions (BL 1, 2, 7 and 8) decreases considerably, but DART-3 still produces significantly more accurate results. In (weakly) stable boundary layers (BLs 3 to 6) GAUS and GCH still show a large variability and occasionally a large systematic bias, which is not true for DART-3. These results suggest that DART-3 outperforms the benchmark models, especially under stable stratifications, those conditions where wake steering is deemed most effective. Furthermore, the model performance is assessed for partial-wake operation. Figure 4.10 compares the models when the downstream turbine is moved 0.5D to the left (from the upstream observer’s point of view). Generally, the variability is greatly reduced since the deficit is smaller. The benchmark models display a systematic negative bias in all BLs, which is not true for DART-3. Only in BL8 does DART-3 not show a significant improvement over the benchmark models,

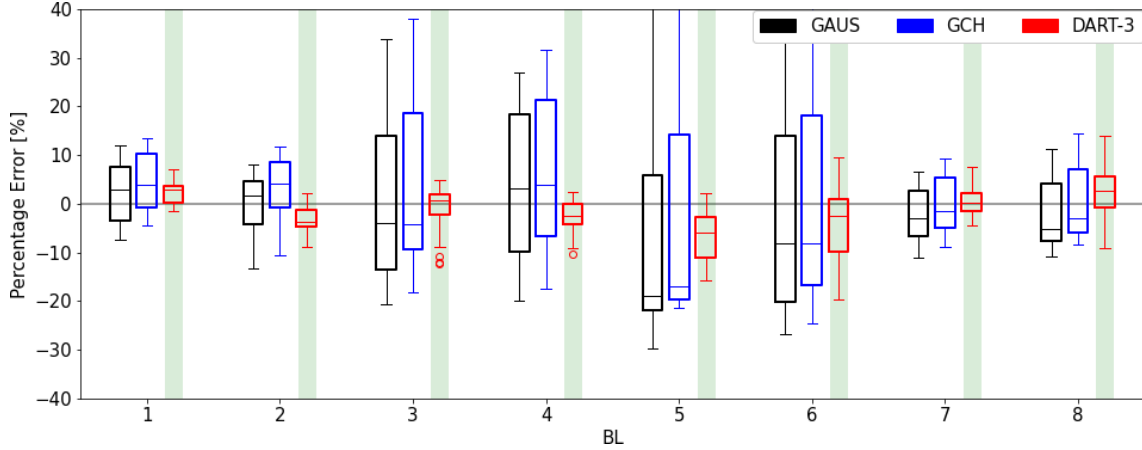


Figure 4.9: Same as Fig. 4.8, but only for cases with  $\beta = 0^\circ$ , i.e., without derating the turbine.

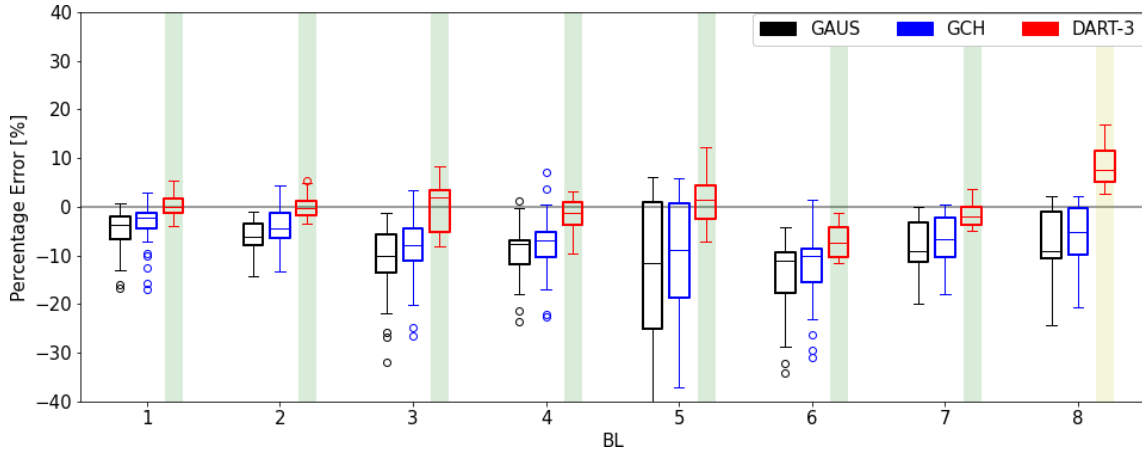


Figure 4.10: Same as Fig. 4.9, but for partial-wake operation, i.e., with a virtual downstream turbine moved  $0.5D$  to the left.

but no satisfying explanation has been found as to why exactly this BL displays this behavior.

A case study is displayed in Fig. 4.11a that presents the LES wake in a weakly stable boundary layer (BL3) for a turbine with  $\phi = +30^\circ$ . The wake has a clearly defined curl and a wake center left of the hub. The DART-3 wind field in Fig. 4.11b shows that the wake shape and center position are well presented. The GAUS model (Fig. 4.11c), however, produces a circular wake shape and a larger wake deflection to the left. The percentage errors indicated in the top of the figure show that DART-3 has a high accuracy for both virtual turbines, but GAUS has large biases due to the misplacement of the wake center. Under stable conditions the wind veer is relatively high, adding a crosswise force pointing towards to right above hub height. This force effectively opposes the lateral thrust force component introduced by yaw misalignment pointing to the left, reducing the deflection of the wake. The opposite is true for negative yaw angles, where wake deflection is enhanced by veer. This asymmetry has already been pointed out in Fleming et al. (2015), Vollmer et al. (2016) and Sengers et al. (2020). This effect is implicitly included in DART-3, but not in the benchmark models. Figure 4.11d illustrates that these models show an ever further deflecting wake, whereas DART-3 settles

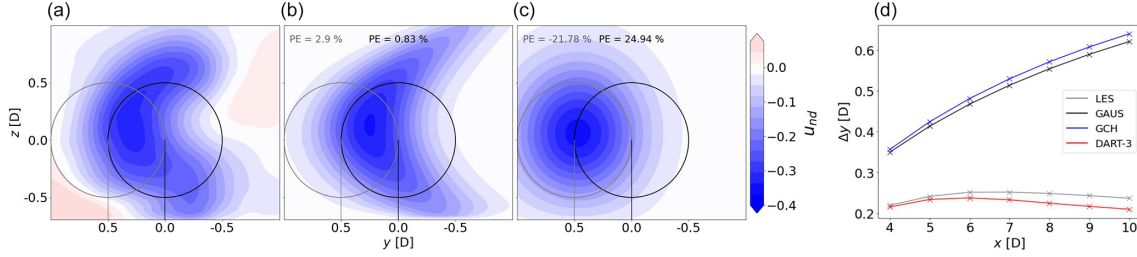


Figure 4.11: Case study of a turbine in a weakly stable boundary layer (BL3,  $\phi = +30^\circ$ ,  $\beta = 0^\circ$ ). Cross-section of normalized wake deficit (contours) of the LES (a), DART-3 (b) and GAUS (c) at  $x = 6D$  downstream. (d) Wake center trajectory at  $4D \leq x \leq 10D$ .

at a smaller lateral displacement close to LES. This explains not only the negative bias of the benchmark models in Fig. 4.10, but also their larger spread observed in Fig. 4.9. This result strengthens the previous indication that DART-3 is superior under stable stratifications.

## 4.5 Discussion

### 4.5.1 Generalizability

Although the results presented in Sect. 4.4 are encouraging and are believed to show proof of concept, they are not directly generalizable. A data-driven surrogate model is sensitive to the data used for training, and encountering situations that vary greatly from those used for training can result in large errors. This includes very dissimilar atmospheric conditions, as already illustrated by the strongly stable BL5 in Fig. 4.8, but extends to other locations (e.g., topography, wind farm layout) and turbine types. Generating a numerical database with more atmospheric conditions, tailored to each location and turbine type, is not possible due to the high computational expense of these high-fidelity models. This limits a large-scale implementation of data-driven surrogate models trained with numerical data. Potentially, field measurements could be used, either in isolation or in combination with numerical data. Wake data could possibly be obtained from long-range lidars (Brugger et al., 2020) or strain measurements from the turbine’s blades (Bottasso et al., 2018). Exploration of these possibilities is deemed an important task for future research.

In this exploratory study, the development of DART was limited to the far wake and a two-turbine setup. If desired, further development of the model is needed to include the near wake, which can for instance be done by including the super-Gaussian description (e.g., Shapiro et al., 2019; Blondel and Cathelain, 2020). An extension to wind farm level could be achieved by for instance applying the superposition principle as done in GAUS and GCH, although the accuracy of DART under disturbed inflow needs attention.

### 4.5.2 Interpretability

As mentioned in Sect. 4.1, analytical models such as GAUS and GCH are presumed to be more robust than purely data-driven models. However, when properly trained, the accuracy of DART is expected to be significantly higher than that

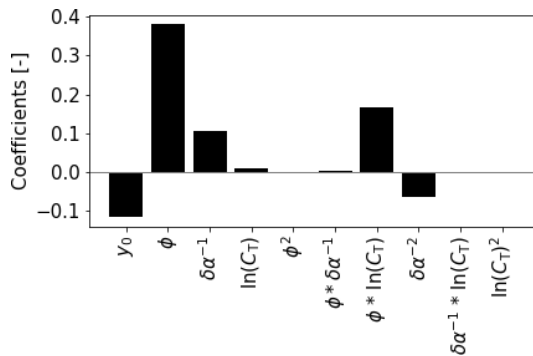


Figure 4.12: Regression coefficients of DART-3 estimating  $\mu_y$  at  $x = 6D$  using scaled input parameters. Since all input parameters are dimensionless, the corresponding coefficients are also dimensionless. Variable  $y_0$  indicates the intercept or systematic offset.

of analytical models as it is specifically tailored to certain scenarios. This can easily be understood by looking at the number of fitted or tuned parameters. Since DART includes second-order polynomial and interaction terms, adding more input variables exponentially increases the size of coefficient matrix  $\mathbf{B}$  (Eq. 4.1). This means that for DART-3, having only 3 input variables,  $\mathbf{B}$  contains 10 coefficients, but with 8 input variables DART-8's  $\mathbf{B}$  already contains 45 coefficients. When comparing this to the four tuning parameters of the benchmark models, one can understand why the latter are more robust but also are expected to have a lower maximum achievable accuracy.

To demonstrate DART's interpretability, Fig. 4.12 illustrates DART-3's fitted regression coefficients for all 10 input parameters for  $\mu_y$  at  $x = 6D$ . Since the order of magnitude of the input parameters can vary greatly, for this example the input parameters were scaled between  $-1$  and  $1$  before regression fitting. Consequently, the fitted coefficients indicate how important each input parameter is in estimating the output variable. For the lateral wake center displacement it can easily be seen that  $\phi$  is the dominant parameter, which intuitively makes sense. Other important parameters are the interaction term  $\phi \cdot \ln(C_T)$  (turbine variable cluster),  $y_0$  (intercept),  $\delta\alpha^{-1}$  and  $\delta\alpha^{-2}$  (atmospheric inflow cluster), while other parameters only slightly affect the wake center displacement.

Alternative to the interpretable lasso model, more complex black-box models (e.g., neural networks) could be considered as they are expected to have a higher accuracy when abundant data are available. Simpler models are, however, always preferred because they are less prone to overfitting, which is especially true for small sample sizes as used in this study. In addition, a model's interpretability typically diminishes with increasing complexity.

### 4.5.3 Speed test

A simple evaluation of computational costs has been carried out to ensure that DART is sufficiently computationally efficient. The speed test comprises producing cross-sections downstream of the turbine and therefore excludes the computational resources needed to generate the LES data and to train or tune the models. This test was executed on a laptop running Ubuntu 20.04.1 with eight 1.80 GHz Intel i7-8550U CPU's and 8 GB RAM, having a minimum number of processes running in



Table 4.5: Model run time [ms] when simulating seven ( $4D \leq x \leq 10D$ ) and one ( $x = 6D$ ) downstream distances expressed as mean  $\pm$  standard deviation over 40 iterations.

| $x$ [D] | 4-10       | 6          |
|---------|------------|------------|
| GAUS    | $58 \pm 2$ | $19 \pm 1$ |
| GCH     | $88 \pm 2$ | $32 \pm 1$ |
| DART-3  | $81 \pm 4$ | $13 \pm 3$ |

the background. All files containing relevant information, such as inflow variables, were stored locally at the same location. Run times are given as an average and standard deviation over 40 iterations, representing all simulations with  $\beta = 0^\circ$ , such that no adjustment of the benchmark’s thrust coefficient lookup table is needed. Table 4.5 shows that when producing results for the whole region considered in this study ( $4D \leq x \leq 10D$ ), the run time of DART is comparable to GCH and slightly higher than GAUS. When simulating only one downstream distance, for instance exactly where a turbine is located, DART performs similarly to GAUS. These results suggest that DART is quick enough to be used for controlling purposes.

## 4.6 Conclusions

This study explores the potential of a Data-driven wAKE steeRING surrogate model (DART) that retains a high degree of physical interpretation. After training with large-eddy simulation data, a model consisting of only linear equations is able to accurately describe the far wake in terms of trajectory, curl and available power. As input parameters, it uses measurable inflow and turbine variables that are commonly studied in the literature. The highest accuracy is obtained when including all available input variables, but the model’s training time becomes very large. When using only three measurable input variables, the surrogate model displays a slight accuracy loss, but the training time is greatly reduced. In a benchmark against the Gaussian and Gaussian-Curl Hybrid models, the data-driven model with three input variables typically shows a significantly higher accuracy. In particular it performs better under derated operating conditions and stable atmospheric stratifications since it implicitly includes the effect of turbine derating on wake size, as well as the effect of veer on the wake center position. These results are not directly generalizable to all atmospheric conditions, other locations or new turbine types, which presents a challenge for a large-scale implementation of data-driven surrogate models. The results shown in this study are, however, believed to show proof of concept for physically interpretable data-driven surrogate models for wake steering purposes.

## Chapter 5

# Validation of an interpretable data-driven wake model using lidar measurements from a field wake steering experiment

The content of this chapter is identical to the following journal article:

Sengers, B. A. M., Steinfeld, G., Hulsman, P., and Kühn, M.: Validation of an interpretable data-driven wake model using lidar measurements from a field wake steering experiment, *Wind Energy Science*, 8, 747-770, <https://doi.org/10.5194/wes-8-747-2023>, 2023.

©Author(s) 2023. This work is distributed under the Creative Commons Attribution 4.0 License. Reprinted with permission.

**Abstract** Data-driven wake models have recently shown a high accuracy in reproducing wake characteristics from numerical data sets. This study used wake measurements from a lidar-equipped commercial wind turbine and inflow measurements from a nearby meteorological mast to validate an interpretable data-driven surrogate wake model. The trained data-driven model was then compared to a state-of-the-art analytical wake model. A multi-plane lidar measurement strategy captured the occurrence of the wake curl during yaw misalignment, which had not yet conclusively been observed in the field. The comparison between the wake models showed that the available power estimations of a virtual turbine situated four rotor diameters downstream were significantly more accurate with the data-driven model than with the analytical model. The mean absolute percentage error was reduced by 19 % to 36 %, depending on the input variables used. Especially under turbine yaw misalignment and high vertical shear, the data-driven model performed better. Further analysis suggested that the accuracy of the data-driven model is hardly affected when using only supervisory control and data acquisition (SCADA) data as input. Although the results are only obtained for a single turbine type, downstream distance and range of yaw misalignments, the outcome of this study is believed to demonstrate the potential of data-driven wake models.

## 5.1 Introduction

With the wind energy industry maturing, more focus is being put on maximizing the power yield of existing assets. This involves moving away from the traditional, and currently still standard, greedy control of individual turbines to an optimization on the wind farm level. In recent years, especially the wake steering concept has received considerable attention in the literature; in this concept the turbine is intentionally misaligned with the inflow wind, introducing a lateral component of the thrust force that deflects the wake away from a downstream turbine. Many aspects of this strategy have been studied over the years, including the underlying physics (e.g., Howland et al., 2016; Bastankhah and Porté-Agel, 2016) and its characteristics under different atmospheric conditions (e.g., Vollmer et al., 2016; Schottler et al., 2017). Additionally, the implementation of this concept in the field with so-called yaw controllers has received attention. Such controllers typically include a representation of the wake in the form of engineering wake models used to solve the optimization problem, as well as the design of the yaw controller itself (e.g., wind direction robustness – Rott et al., 2018; Simley et al., 2020; hysteresis – Kanev, 2020; and open- versus closed-loop – Doekemeijer et al., 2020; Howland et al., 2020).

Although a large body of knowledge about the wake steering concept has been obtained, the industry appears to be hesitant to adapt due to the large uncertainties and lack of validation (van Wingerden et al., 2020; Boccolini et al., 2021). One limitation is the number of field experiments carried out. Due to the considerable expense and inaccessibility of test turbines, most research groups revert to high-fidelity simulations or wind tunnel experiments. Although they provide a higher degree of reproducibility and more flexibility in choosing the studied scenarios, these experiments take place in controlled environments and do not fully represent the complexity of the field. Wake models and yaw controllers are consequently developed based on data from idealized conditions. Their accuracy in field situations is questionable due to limited validation, slowing down the adoption by industry. This uncertainty is amplified by findings that the application of wake steering can lead to power losses under certain conditions (e.g., Fleming et al., 2020; Doekemeijer et al., 2021).

Several field campaigns have been conducted in recent years to study wake steering control. In their pioneering work, Wagenaar et al. (2012) used a scaled wind farm to demonstrate the concept. Using rear-facing nacelle-mounted lidars, asymmetries in wake deflection depending on the sign of the yaw angle were observed for the near wake (Trujillo et al., 2016) and far wake (Bromm et al., 2018). This asymmetry is also found using numerical tools (e.g., Fleming et al., 2015) and attributed to shear-induced initial wake deflection (Gebraad et al., 2016) or the Coriolis force (Archer and Vassel-Be-Hagh, 2019). One prominent aspect associated with wake steering is the development of the wake curl as observed in numerical and wind tunnel experiments (e.g., Howland et al., 2016; Vollmer et al., 2016; Hulsman et al., 2022b). Fleming et al. (2017a) included a short notion that a curled shape could be observed in the field, while Brugger et al. (2020) did not find a curled wake in their field experiment. They argued that the effect of wind veer was too large for the counter-rotating vortices to generate a curled wake, with wind veer reported to tilt the wake in one direction (Herges et al., 2017; Brugger et al., 2019).

Using fixed yaw misalignment angles, Howland et al. (2019) found statistically

significant gains of up to 47% for low wind speeds and a certain wind direction in a small wind farm consisting of six turbines. Ahmad et al. (2019) reported that wake steering is mainly beneficial in partial wake situations. Fleming et al. (2021) found an asymmetry of the downstream turbine power generation, where gains from correct steering (wake steered away from turbine) are larger than the losses from erroneous steering (wake steered into turbine). They attributed this effect to the added wake recovery induced by the counter-rotating vortices that also generate the wake curl.

Additionally, several controller test studies have been carried out in which instead of a fixed yaw angle, an optimal yaw angle is employed based on the inflow conditions. This optimal yaw angle is determined with low-fidelity wake models which generate discretized lookup tables (LUTs). In a series of papers from the National Renewable Energy Laboratory (NREL), different versions of the FLOW Redirection and Induction in Steady State (FLORIS; NREL, 2022) framework have been used to generate these LUTs. In a field campaign at an offshore wind farm with a turbine spacing of seven to eight rotor diameters, Fleming et al. (2017b) reported a 10% power gain for certain wind directions. Fleming et al. (2019, 2020) showed results of a field test with closely spaced turbines with two different versions of FLORIS, both resulting in a power gain for most conditions but clear power losses for some wind directions. Lastly, Doekemeijer et al. (2021) found large power gains of up to 35% for one wind direction sector with a two-turbine setup in complex terrain, but also here large losses were found for other wind directions.

These studies are pivotal in demonstrating the potential of wake steering but also indicate that there is a large variability in its demonstrated effectiveness. Next to atmospheric inflow conditions, this can be attributed to turbine type, turbine spacing and terrain. Additionally, the choice of yaw controller and accuracy of the wake model used to develop the LUTs are believed to have an effect.

After the pioneering wake deficit models of Jensen (1983) and Ainslie (1988), Jimenez et al. (2010) first came up with a wake deflection model under yaw misalignment. Nowadays, most analytical wake models are based on the Gaussian model (Bastankhah and Porté-Agel, 2014, 2016; Niayifar and Porté-Agel, 2016). Combined with the curl wake model (Martínez-Tossas et al., 2019), the Gaussian-curl hybrid (GCH) model (King et al., 2021) prescribes the effect of counter-rotating vortices generated by turbine yaw misalignment, such as yaw-induced wake recovery, asymmetric deflection and secondary steering. Lastly, Bastankhah et al. (2022) presented an analytical way to describe the development of the wake curl with downstream distance, and Bay et al. (2023) tackled “deep array” effects, in which many wakes interact deep inside a large wind farm, with the cumulative-curl model. In addition to these analytical models, data-driven wake (surrogate) models have received some attention in recent years. Most use complex neural networks (e.g., Ti et al., 2020; Renganathan et al., 2022; Purohit et al., 2022; Asmuth and Korb, 2022) and have shown highly accurate results. However, these models need lots of training data and have an extremely low interpretability (black-box models). In an attempt to overcome this, Sengers et al. (2022) presented an interpretable Data-driven wAKE steeRING surrogate model (DART). Using only linear equations, DART uses inflow and turbine variables to estimate wake parameters such as deficit, center location and curl. It has a reduced number of parameters and is therefore highly interpretable and needs fewer training data. In a comparison using large-eddy simulation (LES)

results, Sengers et al. (2022) demonstrated that DART outperformed the Gaussian and GCH models, especially under stable atmospheric conditions.

As mentioned before, studies validating wake models with field measurements are rare, especially when yaw misalignments are included, resulting in uncertainties about their accuracy. Moreover, comparisons between analytical and data-driven models in their abilities to reproduce the characteristics of wakes observed in the field are done sporadically. However, validations with measurements and comparisons between models are necessary to assess their performance and provide direction for future work.

The objective of this paper is to use nacelle-based lidar measurements of the wake of a commercial turbine to validate the DART model and compare its accuracy with that of the GCH model. To achieve the objective, this study comprises three components: (1) to design a scanning strategy able to capture wake characteristics such as deficit, center position and curl to accurately reconstruct a vertical cross-section of the wake; (2) to assess the performance of the wake models by their ability to estimate the available power of a virtual downstream turbine observed by the lidar; and (3) to investigate DART’s performance as a function of data set size and input variables, including an analysis of whether the model could operate on supervisory control and data acquisition (SCADA) data alone.

## 5.2 Measurement campaign

This section introduces the field experiment carried out within this study. Section 5.2.1 describes the measurement site and general setup. Section 5.2.2 describes the yaw control experiment. Section 5.2.3 through 5.2.7 then discuss the devices, their measurement strategies and data processing. Especially in Sect. 5.2.3 more details are provided, including results from a preliminary study to determine the scanning strategy of the nacelle lidar, since the measurements from this device are essential for this study. Lastly, Sect. 5.2.8 describes how the data from all devices are used to select 10 min averaged cases considered in the rest of the study.

### 5.2.1 Measurement site

Measurements were carried out in the period of February through April 2021 as a part of a yaw control field campaign at a slightly hilly onshore site in northeastern Germany located approximately 13.5 km from the Baltic Sea; see also Hulsman et al. (2022a). The layout of the site, including the positioning of the measurement equipment, is shown in Fig. 5.1. The nacelle of turbine T1 was equipped with a downstream-facing Leosphere WindCube 200S (serial no. WLS200S-024) pulsed lidar (Sect. 5.2.3). T1 was a commercial 3.5 MW eno126 turbine with a hub height of 117 m and a rotor diameter  $D$  of 126 m. The nacelle was further equipped with a Thies Clima wind vane and cup anemometer (Sect. 5.2.6), as well as a Trimble SPS three-antenna GNSS (hereafter called GPS) to measure orientation, tilt and roll (Sect. 5.2.7). A second pulsed lidar of the same type (serial no. WLS200S-023) was installed west of the turbine to measure inflow profiles (Sect. 5.2.4). North of this turbine, a meteorological mast (MM; Sect. 5.2.5) was erected and equipped with Thies Clima cup anemometers and wind vanes.

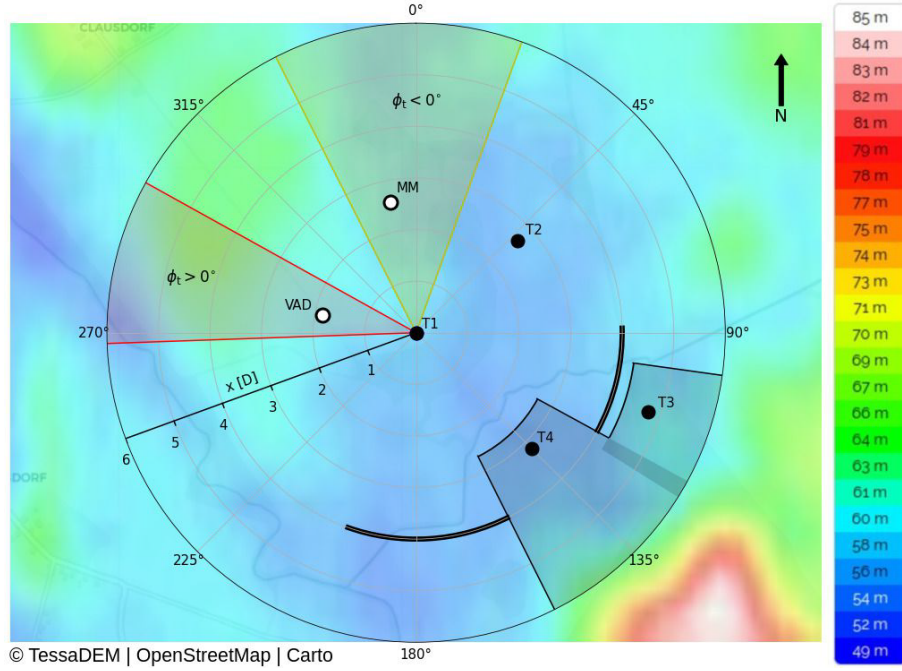


Figure 5.1: Layout of the measurement site with the local topography, relative to mean sea level, indicated in the background. Black markers indicate turbines, where T1 is equipped with the nacelle lidar. White markers indicate the meteorological mast (MM) and ground-based lidar (VAD). Shaded areas indicate the wind direction sector with  $\phi_t > 0^\circ$  (red) and  $\phi_t < 0^\circ$  (yellow) and where wake measurements are assumed to be disturbed by the downstream turbines (grey). The thick solid black line indicates the measured locations used for analysis. (Source for topographic map including color bar: topographic-map.com, 2022.)

Lastly, Fig. 5.1 shows that a small 6 m high hill  $5D$  upstream of T1 and a larger 27 m high hill  $8D$  downstream of T1 were exactly in the wind direction sector that was not used due to the presence of the downstream turbines (see Sect. 5.2.2). Two villages with low buildings were located about 1 km from T1, directly upstream for wind directions around  $\delta = 265^\circ$  and  $\delta = 320^\circ$  mainly outside of the studied wind direction sectors. The dominant vegetation in the area is of an agricultural nature, with patches of trees and bushes between the fields. These trees could affect the measurements for  $\delta \approx 350^\circ$ , as noted in Hulsman et al. (2022a) using data from the same site. This influence was accepted, as omitting this sector would result in large data losses.

### 5.2.2 Yaw control experiment

As these measurements were part of a larger field campaign, only the wind direction sector  $\delta = [268^\circ, 360^\circ] \cup [0^\circ, 20^\circ]$  could be used for experiments for this study. Unfortunately, in this sector two smaller turbines (T3 and T4) were located downstream of the lidar-equipped turbine. For the objectives of this study, measurements at  $4D$  downstream were targeted. This was to avoid the near wake, as the two investigated wake models fail to represent the non-Gaussian shape of the wake deficit, and to ensure that the wake curl had developed. The wind speed reduction due to the induction zone of T3 at  $4.8D$  (hub height of 103 m and a diameter of 93 m) was estimated to be on the order of 2% (estimated with the

vortex sheet theory – Medici et al., 2011) at the targeted distance of  $4D$ . Although not ideal, no alternative was possible due to the restrictions of the measurement site, and it was decided to neglect the effects of this induction zone.

Part of the wind direction sector could not be used due to the positioning of T4 at  $3.2D$  downstream. To make sure that the wake was not steered into T4, in the sector  $\delta = [268^\circ, 316^\circ]$  the turbine toggled between target yaw misalignment angles of  $\phi_t = 0^\circ$  (duration of 30 min) and  $\phi_t = +15^\circ$  (duration of 60 min, clockwise rotation looking from above), steering the wake to the left. Correspondingly, in the sector  $\delta = [316^\circ, 360^\circ] \cup [0^\circ, 20^\circ]$  the turbine toggled between  $\phi_t = 0^\circ$  (30 min) and  $\phi_t = -15^\circ$  (60 min, counterclockwise rotation looking from above), steering the wake to the right. The downside of this approach was that directly comparing positive and negative yaw angles under similar atmospheric conditions was not possible. Additionally, more data were collected in the first sector as this wind direction was more dominant.

Fixed yaw offsets were applied as this involved minimal changes to the yaw controller. Besides, a distribution of yaw misalignments was expected to be obtained due to the imperfect tracking of the wind direction by the yaw controller.

### 5.2.3 Nacelle lidar

This subsection describes the measurements performed with the nacelle-mounted lidar. Section 5.2.3.1 describes the design of the scanning strategy, including results of a numerical evaluation to determine what trajectory should be implemented in the field. Section 5.2.3.2 describes the processing, including filtering, of these data.

#### 5.2.3.1 Design scanning strategy

A pulsed lidar can be mounted onto the nacelle to sample the turbine’s wake. When operated with a single plan position indicator (PPI) scan with an elevation angle of  $\phi_{\text{PPI}} = 0^\circ$ , the line-of-sight velocities on a horizontal plane at hub height are obtained. Although quick, this trajectory only provides data at one height in the wake. Attempts have been made to capture information in the vertical plane, such as in Beck and Kühn (2019), who proposed a scanning pattern of alternating PPI and range height indicator (RHI) scans to obtain information in both dimensions. However, wake shape deformations due to wind veer (tilted) or yaw misalignment (curled) cannot be captured with this scanning strategy. Brugger et al. (2019, 2020) used nine PPI scans at different elevation angles, allowing the description of non-circular wake shapes in a vertical plane.

In this paper, their strategy was adopted and evaluated numerically to gain insights into how the number of PPI scans and their angular speed (following Carbaño Fuertes and Porté-Agel, 2018) affect the ability to capture the characteristics of 10 min averaged wake. This exercise used large-eddy simulation (LES) results, allowing for a systematic uncertainty analysis of the proposed scanning patterns.

The Parallelized Large-Eddy Simulation Model (PALM; Maronga et al., 2020) coupled with the aeroelastic code FAST (Jonkman and Buhl Jr., 2005; Krüger et al., 2022) representing the NREL 5 MW turbine (Jonkman et al., 2009) provides the numerical wind fields. Precursor simulations generated realistic inflow conditions, after which the main simulations with one turbine were performed. The aeroelastic code for the turbine installed in the field, as used in Sect. 5.4.1, was not yet available

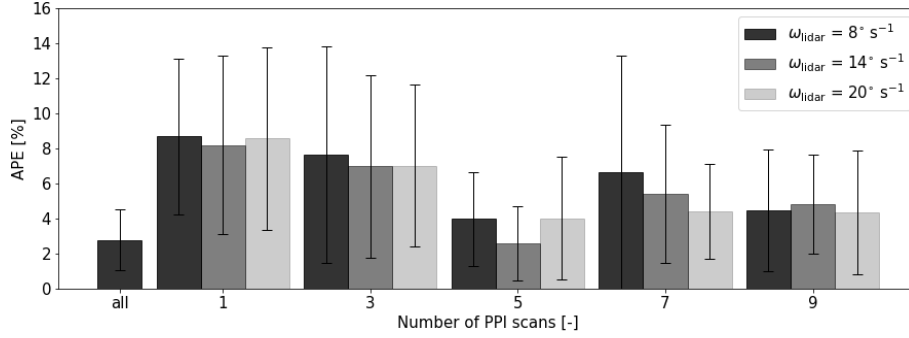


Figure 5.2: Results of the virtual lidar tests. Bars indicate the mean and whiskers the standard deviation of the absolute percentage error (APE) of available power  $P_{\text{av}}$  over six simulations. The number of PPI scans is indicated on the  $x$  axis. “all” indicates the use of all numerical data, hence the error introduced by the composition method. The opaqueness represents the lidar’s angular speed  $\omega_{\text{lidar}}$ .

during the planning stage of this campaign. Both turbine T1 and the NREL 5 MW turbine have the same rotor diameter (126 m) but differ in hub height (117 vs. 90 m) and aeroelastic properties. It was, however, assumed that at  $4D$  the characteristics of the wakes produced by these turbines are sufficiently similar.

A single turbine with yaw angles of  $\phi = \{-15, 0, 15^\circ\}$  in a neutral ( $\text{TI} = 10.3\%$ ,  $\alpha = 0.17$ ; see the Appendix for definitions of abbreviations and symbols used throughout) and a stable ( $\text{TI} = 5.7\%$  and  $\alpha = 0.32$ ) boundary layer with a hub height wind speed  $U_h \approx 8 \text{ m s}^{-1}$  was simulated. The simulation length was 25 min, of which the first 15 min was omitted as spin-up and the remaining 10 min was used for analysis. Synthetic lidar data targeting  $4D$  downstream were subsequently generated by employing the lidar simulator LiXim (Trabucchi, 2019) with an accumulation time of 0.1 s and an opening angle of  $70^\circ$ . Temporal averages were taken for all points in the scanning cycle. The wake composition method, later described in Sect. 5.3.1, was used to reconstruct vertical cross-sections of the wake, from which the available power  $P_{\text{av}}$  could be determined. This estimate is compared to the reference (subscript ref) 10 min averaged LES data. Used as a metric is the absolute percentage error (APE) over the six (two boundary layers times three yaw angles) simulations calculated with Eq. (5.1):

$$\text{APE}[\%] = \left| \frac{P_{\text{av}} - P_{\text{av,ref}}}{P_{\text{av,ref}}} \right| \cdot 100, \quad (5.1)$$

in which  $P_{\text{av}} = P/C_P = 0.5\rho AU_{\text{eq}}$  with  $\rho$  the air density (assumed to be constant),  $A$  the rotor area and  $U_{\text{eq}}$  the rotor-equivalent wind speed. The bar “all” on the far left in Fig. 5.2 indicates the reconstruction of the wake based on the original LES data, hence the error introduced by the composition method. Further, one, three, five, seven and nine PPI scans were tested, where the middle scans always targeted hub height and the outermost scans upper and lower tip height at  $4D$ . Trajectories with an even number of PPI scans were not tested, as this would remove the scan at hub height that was needed for another study. Additionally, it is desirable to measure the largest wake deficit, which is expected to develop around hub height. Figure 5.2 shows that five PPI scans typically hold the highest accuracy. Using fewer PPI scans results in inaccurate estimations of the wake deficit distribution in the vertical, while using more PPI scans results in long cycles and consequently



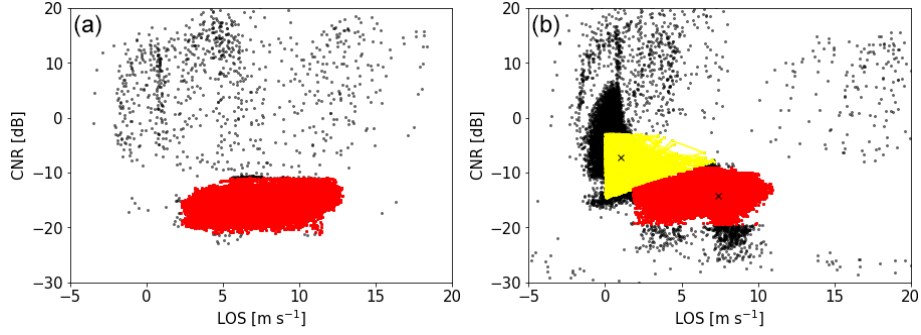


Figure 5.3: Examples of multiple PPI scan filtering in LOS–CNR diagrams in which black markers indicate original data and red markers data kept after filtering. (a) A textbook case with few outliers that indicate hard targets and (b) a more problematic case in which there are many corrupted measurements. Here yellow markers indicate a second cluster from which all measurements were omitted. Black crosses indicate the two cluster centers.

fewer measurements per observation point. The angular speed  $\omega_{\text{lidar}}$  seems to have little effect, except for when seven PPI scans are used. This is attributed to chance, as too few cases are studied for the statistics to converge. Generating more LES results with a wider range of atmospheric conditions and turbine yaw angles was not possible due to computational restrictions. While these results are not statistically significant and it can therefore not be claimed that an “optimal” scanning strategy has been found, this exercise allows for making an informed decision.

It was decided to implement the trajectory showing the lowest error, hence consisting of five PPI scans with  $\omega_{\text{lidar}} = 14^\circ \text{ s}^{-1}$ . The elevation angles of these scans were  $\phi_{\text{PPI}} = \{-7.0, -3.5, 0.0, 3.5, 7.0^\circ\}$ , and the accumulation time used was 0.1 s. With an opening angle of  $70^\circ$ , the duration of one PPI scan is 5 s. Changing elevation angles takes 1.3 s, and resetting to the start of the cycle takes 3.5 s, adding to 34 s to complete one full cycle. The range gate length was set to 25 m, corresponding to a pulse duration of 100 ns. Range gates were defined between 50 and 1340 m with 5 m spacing. However, in the processing phase only data up to 820 m were used to avoid the influence of the ground in the PPI scan with the lowest elevation angle.

### 5.2.3.2 Data processing

Since the performed PPI scans were quite fast with a relatively coarse resolution, all PPI scans with the same elevation angle in a 10 min window (see Sect. 5.2.8) were grouped together to get a better estimate of the measurement distribution.

Simple filtering based on the carrier-to-noise ratio (CNR) and line-of-sight velocity (LOS) was performed, where only realistic data with  $\text{CNR} < 0 \text{ dB}$  and  $0 \text{ m s}^{-1} < \text{LOS} < 20 \text{ m s}^{-1}$  were kept. On the remainder, a Gaussian filter was used, retaining only measurements within 3 standard deviations of the median CNR and LOS (99% confidence interval). This removed outliers due to hard targets, as illustrated in Fig. 5.3a.

However, some PPI scans exhibited a LOS–CNR diagram as illustrated in Fig. 5.3b, containing many measurements with high CNR and low LOS values. To filter out these erroneous measurements, a mean shift clustering algorithm (Fukunaga and Hostetler, 1975) was employed, as was for instance used in Wang et al. (2022) as part of data cleaning for power curve tuning. The algorithm identified clusters in

the LOS–CNR space and allocated all measurements to any of the clusters based on the Euclidean distance to the cluster center. Clusters were then either considered or eliminated based on whether the location of their center was physically feasible. In the example in Fig. 5.3b, the yellow cluster was omitted, since many points outside the main cluster with high CNR and low LOS values indicate erroneous measurements. Lastly, the Gaussian filter based on the 99% confidence interval was repeated, as removing one cluster drastically affected the outcome of this filter.

After filtering, all PPI scans were interpolated to a standard grid with a resolution of  $1.4^\circ$  (corresponding to the original resolution) to account for the slightly different azimuth angles between scans as a result of the lidar’s inability to measure the exact same location each time. Next, the PPI scans were temporally averaged as long as not more than two data points within a 10 min window were missing. When more than 25% of the measurements were filtered out, as is the case with Fig. 5.3b, the averaged PPI scan was removed from the 10 min window, resulting in fewer than five PPI scans. If fewer than four averaged PPI scans remained after filtering, the case was eliminated.

Lastly, the PPI scans’ azimuth and elevation angles were corrected with the nacelle’s 10 min averaged tilt angle and misalignment (see Sect. 5.2.7). The horizontal wind speed was subsequently computed by correcting the LOS with these azimuth and elevation angles.

#### 5.2.4 Ground-based lidar (VAD)

As shown in Fig. 5.1, the ground-based lidar was situated  $1.85D$  upstream of the lidar-equipped turbine for  $\delta = 281^\circ$  to measure profiles of wind speed and direction. The ground-based lidar performs continuous velocity–azimuth display (VAD) scans at an elevation angle of  $\phi_{\text{VAD}} = 75^\circ$  with an accumulation time of 0.5 s and an angular speed of  $30^\circ \text{ s}^{-1}$ . Also for this lidar, the range gate length was set to 25 m, corresponding to a pulse duration of 100 ns. Range gates were defined between 50 and 840 m with 5 m spacing.

Filtering was done based on the 2D histogram method introduced by Beck and Kühn (2017), which assumes a normal distribution of LOS and CNR values. The measured data points were binned by their LOS and CNR values, and the number of data points in each bin were counted. Bins having a count below 10% of the bin with the highest count were omitted.

Next, the azimuth angle ( $\theta_{\text{VAD}}$ ) was corrected by means of a hard-target analysis, such that  $\theta_{\text{VAD}} = 0^\circ$  faces north. To obtain the wind speed components ( $u$ ,  $v$ ,  $w$ ) and consequently the horizontal wind speed and direction, the measurements of each range gate were fitted with the following sinusoid:

$$\text{LOS} = u \cos(\theta_{\text{VAD}}) \sin\left(\frac{\pi}{2} - \phi_{\text{VAD}}\right) + v \sin(\theta_{\text{VAD}}) \sin\left(\frac{\pi}{2} - \phi_{\text{VAD}}\right) + w \cos\left(\frac{\pi}{2} - \phi_{\text{VAD}}\right) \quad (5.2)$$

Lastly, only when at least 75% of the data points remained after filtering and the fitted sinusoid achieved a correlation coefficient of at least 0.8 (determined empirically), the wind speed components of a vertical level were retained.

### 5.2.5 Met mast

A meteorological (met) mast was positioned  $2.7D$  upstream of T1 at  $\delta = 350^\circ$  (Fig. 5.1). This mast was equipped with cup anemometers at 116.3 m (hub height,  $U_h$ ) and 54.2 m (lower tip height,  $U_{lt}$ ) to measure wind speed and shear. Wind vanes were located at 112.2 m (approximately hub height,  $\delta_h$ ) and 54.5 m (lower tip height,  $\delta_{lt}$ ). The highest cup anemometer was located on the top of the met mast for undisturbed flow from all directions, whereas the other cup anemometer and wind vanes had orientations of  $315$  and  $135^\circ$ , respectively. A flow distortion due to the tower structure affecting the measurements occurs for wind directions between approximately  $310$  and  $320^\circ$ , which is not considered in this study (see Sect. 5.2.1). The wind directions analyzed here are assumed to be undisturbed. The cup anemometers and vanes had an accuracy of  $0.2 \text{ m s}^{-1}$  and  $1.5^\circ$ , respectively. All sensors operated at a sampling frequency of 50 Hz.

### 5.2.6 Wind turbine operational data

SCADA data were collected at the turbine at a frequency of 50 Hz. These data contain measurements from the nacelle's wind vane  $\delta_s$  and cup anemometer  $U_s$ , as well as power  $P$ , rotor speed  $\omega$  and turbine status, the latter indicating whether the turbine was operating normally. A standard nacelle transfer function was used by the operator to correct wind speed measurements for the influence of the rotor.

### 5.2.7 GPS

All above-mentioned systems were equipped with a Global Positioning System (GPS) sensor used for time synchronization. Additionally, the nacelle of T1 was equipped with a three-antenna global navigation satellite system (GNSS) to measure orientation, roll and tilt. This system was operated at a sampling frequency of 10 Hz, and its measurements have a root mean square error of less than  $0.1^\circ$ . This results in a spatial error of less than 1 m at  $4D$  downstream.

Orientation measurements, averaged to 10 min values to smooth out high-frequency vibrations, were used to compute the yaw misalignment  $\phi$  of the turbine relative to the wind direction  $\delta_h$  measured at the met mast. These measurements were then used to correct the PPI scans' azimuth angles. Likewise, 10 min averaged nacelle tilt angles were used to correct the PPI scans' elevation angles, but the scans were not corrected for roll as it was expected to only have a small influence on the results.

### 5.2.8 Selection of data for model evaluation

The measurements were averaged over 10 min as is commonly done in the wind energy industry. Case selection was done using the following steps:

1. Within a 10 min window, no yaw maneuver should take place. A preselection of cases was therefore done purely based on GPS data. A case was considered when the orientation did not change for at least 12 min, of which the first 2 min was not considered for analysis because the wake needed time to reach  $4D$  downstream. In the case that the orientation did not change for more than 22 min, the first 2 min was omitted and the remainder was split into two 10 min windows as far apart as possible.

2. The 10 min averaged  $U_h$  needed to be between cut-in and rated wind speed.  $\delta_h$  needed to be in the defined sector (Sect. 5.2.1) and approximately normally distributed. This eliminated situations where there is a clear trend in the wind direction signal.
3. The inflow measured at the met mast should reasonably compare to the measurements at the turbine’s nacelle. The met mast measurements were temporally corrected to match the nacelle signal using Taylor’s hypothesis of frozen turbulence. Next, the two signals were compared, where the 10 min averaged wind speed  $|U_h - U_S| < 1 \text{ m s}^{-1}$  and direction  $|\delta_h - \delta_S| < 5^\circ$ .
4. The profiles from the VAD lidar were used to check whether the wind speed profiles were approximately logarithmic, as the effect of low-level jets on the downstream wake characteristics is currently not captured by the wake models and considered out of the scope of this study.
5. If all checks were passed, all completed cycles within the defined 10 min window were averaged as described in Sect. 5.2.3. After averaging, the PPI scans were interpolated to a vertical plane at  $4D$  downstream of the turbine. The wake deficit ( $U_{\text{def}}$ ) was calculated by subtracting the wake measurements with the inflow profile obtained from the met mast measurements and normalized by dividing by the hub height wind speed  $U_h$ .
6. Lastly, the 10 min averaged cases were evaluated by the multiple 1D Gaussian method (see Sect. 5.3.1). Since the opening angle of the PPI scans is  $70^\circ$ , it can be expected that wakes from other turbines are also visible in the measurements. To prevent using an incorrect wake, the scans are sliced around the expected location of the considered wake. Boundaries of these slices are determined by the maximum wind speeds between the scan’s center, corrected for yaw misalignment, and 150 m left and right of this center. Furthermore, the correlation coefficient ( $R$ ) of the Gaussian fit with the wake deficit observations needed to be higher than 0.85 (empirically determined) to be considered, removing cases that do not fulfill the model assumptions of a Gaussian wake deficit.

This selection procedure resulted in 382 individual 10 min averaged cases to be used for analysis. Figure 5.4 displays the distribution of measured yaw angles during the campaign. Most measurements were done without yaw misalignment, since during a part of the campaign the implemented controller had issues and turbine control reverted back to standard operation. The difference between the number of positive and negative yaw angles is due to a more dominant wind direction in the sector containing positive yaw angles.

The solid vertical lines indicate the median yaw angles per target angle. For greedy control, the median shows a small bias of  $\phi = -0.94^\circ$ , suggesting a calibration error of the nacelle’s wind vane. For a target angle  $\phi_t = +15^\circ$ , the median achieved  $\phi = +11.14^\circ$ , whereas for  $\phi_t = -15^\circ$ ,  $\phi = -13.19^\circ$  is achieved. These angles are smaller than the targeted angles, which is due to the wind vane error under yaw misalignment (Kragh and Fleming, 2012; Simley et al., 2021a). Figure 5.5 displays an overview of the inflow conditions measured during these 382 cases. The shear  $\alpha$  with a mean of 0.3 is slightly larger than expected, and the veer  $\delta\alpha$  is smaller than

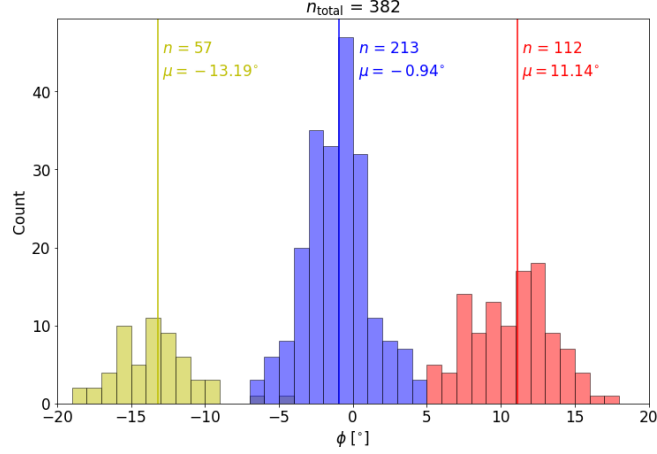


Figure 5.4: Data availability of the 10 min averaged cases as a function of achieved yaw angle ( $\phi$ ). Colors indicate the targeted  $\phi_t = -15^\circ$  (yellow),  $\phi_t = 0^\circ$  (blue) and  $\phi_t = +15^\circ$  (red). Solid vertical lines and accompanying text mark the median of the achieved yaw angles.

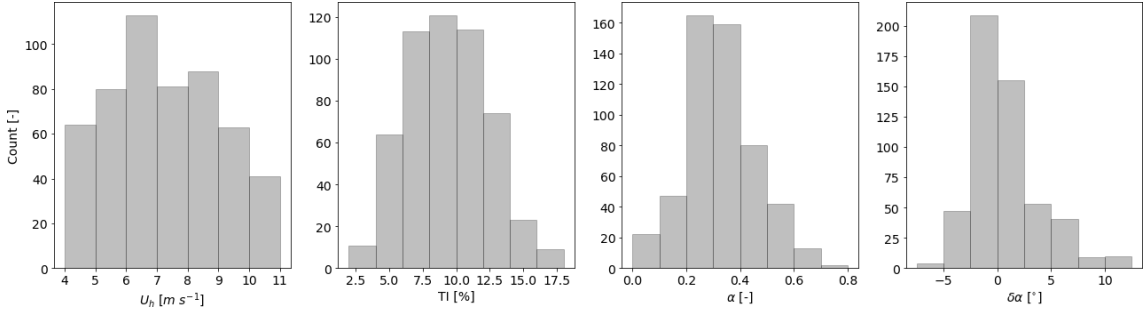


Figure 5.5: Distribution of 10 min averaged inflow variables measured at the met mast for all 382 cases: hub height wind speed ( $U_h$ ), turbulence intensity (TI), shear ( $\alpha$ ) and veer ( $\delta\alpha$ ).

expected, showing a high occurrence of negative values. Regardless, all variables show a range of values that are physically reasonable.

## 5.3 Methods

This section introduces the modeling aspects of this study. First, Sect. 5.3.1 summarizes the multiple 1D Gaussian method used to obtain quantifiable wake characteristics. Section 5.3.2 discusses what information is used as a reference, and Sect. 5.3.3 describes the splitting of the data set into training and testing subsets. Then, Sect. 5.3.4 introduces the data-driven model and Sect. 5.3.5 briefly introduces the analytical model used in this study.

### 5.3.1 Multiple 1D Gaussian method

The multiple 1D Gaussian method (Sengers et al., 2020) is utilized to obtain quantifiable wake characteristics, listed in Table 5.1. This method fits a 1D Gaussian through the wake deficit data normalized by the wind speed at hub height ( $U_{\text{def}}/U_h$ ) in the horizontal plane for every height level, in the current study obtained from five consecutive PPI scans. This results in a set of local wake deficits (amplitude), center positions (location) and widths (standard deviation) for each height. By

Table 5.1: Dimensionless variables describing the wake characteristics obtained with the multiple 1D Gaussian method. Reused from Sengers et al. (2022) with permission.

| Scalar parameter                  | Symbol     |
|-----------------------------------|------------|
| Amplitude normalized wake deficit | $A_z$      |
| Lateral wake center displacement  | $\mu_y$    |
| Vertical wake center displacement | $\mu_z$    |
| Width wake center height          | $\sigma_y$ |
| Vertical extent                   | $\sigma_z$ |
| Curl                              | curl       |
| Tilt                              | tilt       |
| Quadratic wake width parameter    | $s_a$      |
| Linear wake width parameter       | $s_b$      |

fitting another 1D Gaussian through the set of local deficits in the vertical, the vertical deficit profile can be determined. The position of the maximum deficit in this profile is then considered the vertical position of the wake center. The horizontal position of the wake center is determined by interpolating the set of local center positions to this height. A second-order polynomial is fit through the set of local wake center positions to find the wake curl and tilt. The same method is applied for the wake widths to find their profile as a function of height.

The reverse of this method, hereafter called the composition method, can be used to obtain a vertical cross-section of the wake from a set of wake characteristics. For more details on the multiple 1D Gaussian method and the composition method, the reader is referred to Sengers et al. (2020, 2022).

### 5.3.2 Reference power

The wind speed measured by the nacelle lidar is used to obtain the available power at  $4D$  downstream. Since the spatial resolution is relatively coarse and the two outermost PPI scans target the tip heights, the 10 min averaged wind speeds are interpolated using a cubic spline function to a resolution of  $\Delta = 5$  m. This inherently fills gaps when data are not available. The spatially interpolated data are consequently used to determine a rotor-equivalent wind speed ( $U_{eq}$ ) and an available power  $P_{av,ref}$  used as a reference in the remainder of this study.

### 5.3.3 Training and testing data

The data set is split into a training part (80% of total size) and a testing part (remaining 20%). This has been done in a stratified random manner, meaning the data set was first split up into three subsets according to their target yaw angle  $\phi_t = \{-15, 0, 15^\circ\}$ , after which from each subset 20% of data were randomly selected to be testing data. This way, it is ensured that both testing and training data contain cases with a yaw misalignment.

To not base the results on only a single testing data set, this random splitting of the data set (resampling) has been repeated 96 times (hereafter: resamples). The choice of 96 resamples is pragmatic, as it was convenient for parallel computing (multiple of 24 nodes per core). Error statistics appear to be normally distributed, which was not the case with 24, 48 or 72 resamples. Although more resamples are desirable (e.g., bootstrapping is typically done over several thousands), this was not

possible due to computational limitations as the training of the models can be quite expensive as discussed in Sect. 5.3.4.4 and 5.3.5.

### 5.3.4 Data-driven wAke steeRing surrogaTe model (DART)

This subsection introduces DART, starting with a summary from previous work in Sect. 5.3.4.1 and changes made to the model since this work in Sect. 5.3.4.2. This is followed by information on the input variables (Sect. 5.3.4.3). Lastly, the feature selection of the three versions of the model considered in this study is discussed in Sect. 5.3.4.4.

#### 5.3.4.1 Model description

DART was introduced in an LES study by Sengers et al. (2022). It estimates wake characteristics (Table 5.1) obtained from the multiple 1D Gaussian method (Sect. 5.3.1) with a linear regression model from standard input parameters (e.g., yaw misalignment, shear, thrust coefficient). These wake characteristics ( $\vec{Y}$ ) are estimated from input parameters ( $\mathbf{X}$ ) using a simple linear model:

$$\vec{Y}_{(n)} = \mathbf{X}_{(n \times p)} \times \vec{B}_{(p)}, \quad (5.3)$$

in which  $\vec{B}$  denotes the model coefficients. The matrix dimensions are indicated by the sample size  $n$  and the number of input parameters  $p$ , containing the input variables, their second-order and interaction terms, and intercepts. The model coefficients are fitted with the lasso method (Tibshirani, 1996), using the following cost function:

$$\operatorname{argmin}_B \sum_n (y_n - \sum_p x_{np} \vec{B}_p)^2 + \lambda \sum_p |\vec{B}_p|. \quad (5.4)$$

This method remains close to ordinary least squares but adds a regularization parameter  $\lambda$  to its cost function, effectively penalizing adding more parameters. This ensures shrinkage of the input parameters and eliminates the issue of multicollinearity as only one of the highly correlated input parameters is chosen. The notations presented here deviate slightly from those in Sengers et al. (2022), as in the current study only one distance downstream is considered, simplifying the equations.

To include nonlinear relations between input parameters and wake characteristics, the original variables can be transformed with, e.g., a square root or exponential transformation. In the training stage (Sect. 5.3.4.4), it is determined what set of input variables and transformations yields the most accurate results.

Lastly, the estimated wake characteristics are used in a composition method (Sect. 5.3.1) to generate a vertical cross-section of the wake deficit and wind field. For a more detailed description of DART, the reader is referred to Sengers et al. (2022).

#### 5.3.4.2 Modifications to the model

A few changes have been made to DART since its first description in Sengers et al. (2022). Most notably, the feature selection procedure has been changed. Before estimating the wake characteristics with a linear model, inflow variables

(e.g.,  $\phi, \alpha, \omega$ ) undergo transformations. In addition to the non-transformed variable, the square root, exponent, natural logarithm and reciprocal transformation are considered for all input variables, resulting in five options for each variable and many possible sets of input parameters (e.g.,  $\phi, \alpha^{-1}, \ln(\omega)$ ). In Sengers et al. (2022), all these possibilities were tested, the available power of a virtual turbine was estimated and compared to the original data, and the set of input parameters that had the smallest error was chosen. This selection procedure not only was very computationally expensive but also does not necessarily give the most accurate solution for all wake characteristics. Hypothetically, the wake center position could be best explained by the non-transformed yaw angle, whereas the wake curl could be best explained by the exponent of the yaw angle. In the current work, the determination of the best set of transformations is tested for each wake steering variable individually. The best transformation is then chosen as the one that has the smallest mean absolute error in the training data. This not only allows for more accurate estimates but also speeds up the training process.

Secondly, square root and natural logarithm transformations do not allow for negative input values. A sign function is used to include these values rather than omitting them, as was done in the previous work.

Lastly, in the testing phase, extrapolation is prevented by using the maximum (or minimum) value found in the training data when an input variables exceeds this range. Although this does not allow DART to give accurate estimations in new situations, it eliminates erroneous estimates due to extrapolation.

#### 5.3.4.3 Input variables

As argued in Sengers et al. (2022), highly correlated input variables are interchangeable as they provide similar information. However, as long as they are not perfectly correlated, including all variables can lead to a higher accuracy as some new information is added. Due to the use of the lasso regression method, multicollinearity is not an issue.

Because of DART's flexibility, training with different sets of input variables is possible, allowing for an analysis of the model's accuracy as a function of chosen input variables. An overview of the available input variables is displayed in a correlation matrix (using the Pearson correlation coefficient) in Fig. 5.6. Other variables such as the wind direction variability and TI at lower tip height could have been included but were omitted for brevity. As opposed to what was seen in LES in Sengers et al. (2022), the inflow variables  $\delta\alpha$ ,  $\alpha$  and TI are weakly correlated in this field experiment. Secondly,  $\omega$  and  $P$  are highly correlated with  $U_h$ .

#### 5.3.4.4 Feature selection

In this study, multiple versions of the DART model were considered, each having a different set of input variables. Adding more input variables might increase the accuracy but will increase the training time of the model significantly. In Sengers et al. (2022) it was hypothesized that DART can achieve reasonable accuracy as long as each of the following clusters is represented: yaw ( $\phi$ ), atmospheric inflow ( $\delta\alpha$ ,  $\alpha$ , TI) and turbine ( $\omega$ ,  $P$ ,  $U_h$ ). Due to its high correlation with the turbine variables,  $U_h$  is here considered a turbine variable rather than an inflow variable. Following this logic, the first version of DART uses three input variables.



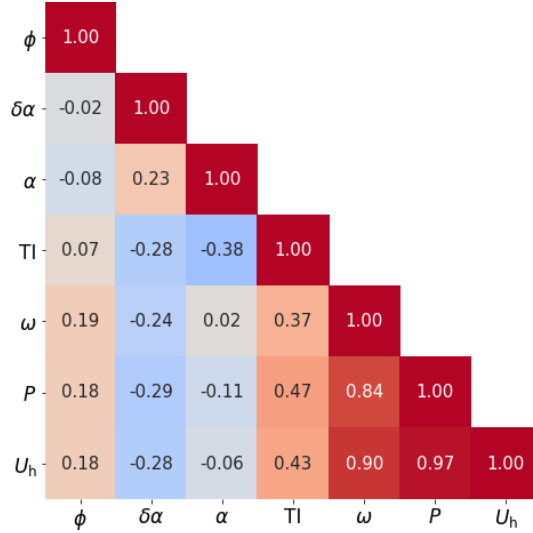


Figure 5.6: Correlation matrix of available input variables. In addition to the inflow variables shown in Fig. 5.5, yaw misalignment  $\phi$ , rotor speed  $\omega$  and power  $P$  are considered input variables.

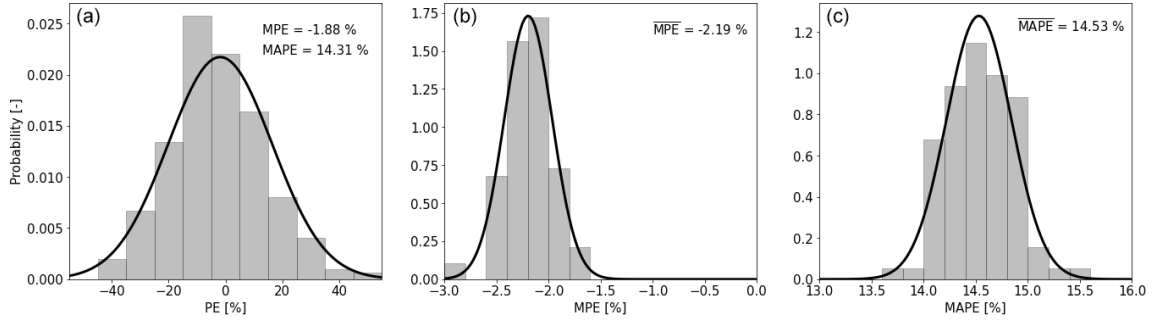


Figure 5.7: Performance of DART-3 on the training data. The set of input variables is  $\{\phi, \alpha, P\}$ . (a) Histogram of PE of  $P_{av}$  for one resample. Fitted normal distributions are indicated with solid lines, and MPE and MAPE are given in the top right. Histograms of MPEs (b) and MAPEs (c) over all 96 resamples.

### DART-3

To determine the most accurate solution using only three variables, all possible sets of input variables and their respective transformations (Sect. 5.3.4.2) are tested during the training stage and their accuracy to reproduce the training data set is investigated. By means of an example, Fig. 5.7a displays the error distribution of one resample. The error metric used here is the percentage error (PE) of  $P_{av}$  (calculated analogously to Eq. 5.1 but without absolute values) at  $4D$  downstream. From these values, a mean percentage error (MPE) and mean absolute percentage error (MAPE) can be computed, as indicated in the top right of the figure.

Repeating this for all 96 resamples, one can obtain a histogram of MPEs and MAPEs as displayed in Fig. 5.7b and c. Finally, the mean over 96 MPEs ( $\overline{\text{MPE}}$ ) and MAPEs ( $\overline{\text{MAPE}}$ ) can be calculated; see top right of the figures. The  $\overline{\text{MPE}} = -2.19\%$  illustrates a negative systematic bias, meaning DART underestimates  $P_{av}$ .

To determine the most accurate set of input variables,  $\overline{\text{MAPE}}$  is considered. The results for all considered combinations of input variables are displayed in Table 5.2, showing that the set  $\{\phi, \alpha, P\}$  provides the most accurate result (lowest  $\overline{\text{MAPE}}$ ) and is therefore used in the remainder of the study, denoted as DART-3. The

Table 5.2: Overview of all possible combinations of input variables in DART-3 and their respective  $\overline{\text{MAPE}}$  values. Boldface indicates the combination resulting in the lowest error.

| Variable 1               | Variable 2                 | Variable 3            | MAPE [%]     |
|--------------------------|----------------------------|-----------------------|--------------|
| $\phi$                   | $\delta\alpha$             | $\omega$              | 18.24        |
| $\phi$                   | $\delta\alpha$             | $P$                   | 16.70        |
| $\phi$                   | $\delta\alpha$             | $U_h$                 | 17.17        |
| $\phi$                   | $\alpha$                   | $\omega$              | 15.11        |
| <b><math>\phi</math></b> | <b><math>\alpha</math></b> | <b><math>P</math></b> | <b>14.53</b> |
| $\phi$                   | $\alpha$                   | $U_h$                 | 15.08        |
| $\phi$                   | TI                         | $\omega$              | 15.66        |
| $\phi$                   | TI                         | $P$                   | 14.77        |
| $\phi$                   | TI                         | $U_h$                 | 14.81        |

training time for each set of input variables with DART-3 is on the order of 10 min; hence the total computation time to determine the best set of input variables is approximately 1.5 h.

#### DART-4

Because the training of DART-3 is fast, an additional variable can be included to improve the accuracy of the model. The first three variables are chosen similarly to DART-3 (one from each cluster), while the fourth variable can be any input variable not yet selected. Repeating the analysis of computing a MAPE for each resample and consequently a  $\overline{\text{MAPE}}$  for each set of input variables, generating a table corresponding to Table 5.2 (not shown here for brevity), reveals that  $\{\phi, \alpha, P, U_h\}$  is the most accurate combination with  $\overline{\text{MAPE}} = 12.69\%$ , hereafter called DART-4. Its training time for each combination is approximately 1 h; hence with 18 possible sets of input variables, the total computation time needed for training is 18 h.

#### DART-7

Lastly, all available variables are used as input in DART-7, demonstrating the maximum achievable accuracy of the data-driven model during this experiment. DART-7's accuracy on the training data was indeed the highest with  $\overline{\text{MAPE}} = 10.31\%$ . The computation time needed to train DART-7 is approximately 1 month if not parallelized.

### 5.3.5 Analytical wake model

The state-of-the-art GCH model (King et al., 2021) as available in version 3.0rc4 of the FLORIS framework (NREL, 2022) acts as a reference model in this study. The GCH model incorporates the spanwise and vertical velocity components (Martínez-Tossas et al., 2019) due to the present vortices into the Gaussian wake model (Bastankhah and Porté-Agel, 2014, 2016; Niayifar and Porté-Agel, 2016).

Since presently only the wake at a distance of  $4D$  behind the upstream turbine is studied, the GCH model could have benefited from including a near-wake model (e.g., Blondel and Cathelain, 2020), but this coupling was not available in this version of FLORIS. The  $C_T$  curve of the eno126 turbine is obtained from the Bladed model for which the aerodynamic properties of the turbine were provided by the operator and is used in these calculations.

Inflow information is taken from the 10 min averaged met mast data. The model tuning parameters ( $\alpha_{\text{GCH}}$ ;  $\beta_{\text{GCH}}$  for the far-wake onset; and  $k_{a,\text{GCH}}$ ,  $k_{b,\text{GCH}}$  for the wake growth rate) are determined by minimizing the MAPE of available power over the training data, analogously to the training of DART described in Sect. 5.3.4.4. The tuning takes about 3 h, and the model has an error of  $\overline{\text{MAPE}} = 18.13\%$ .

## 5.4 Results

This section presents the results of this study. Section 5.4.1 describes the characteristics of the wake observed in the field, after which in Sect. 5.4.2 the performance of the wake models in reproducing these wake characteristics is discussed.

### 5.4.1 Observed wake characteristics

In Sect. 5.4.1.1 an assessment of the characteristics of the observed wake listed in Table 5.1 is performed, which is deemed a necessary first step before investigating the accuracy of wake models. The observed wake characteristics are linked to the inflow variables to examine whether the measurements are physically feasible. In Sect. 5.4.1.2, two wake characteristics that are deemed important for wake steering are further investigated.

#### 5.4.1.1 Correlation with inflow variables

The multiple 1D Gaussian method (Sect. 5.3.1) is used to describe the wake in quantifiable characteristics. Figure 5.8 displays how the nine wake characteristics correlate with the input variables.

The wake center deficit normalized with the hub height wind speed, denoted  $A_z$ , is highly correlated with shear  $\alpha$  and turbulence intensity TI and shows a moderate correlation with veer  $\delta\alpha$ , corresponding to the correlations found in previous studies (e.g., Bastankhah and Porté-Agel, 2016; Schottler et al., 2017).  $A_z$  has a weak correlation with the hub height wind speed  $U_h$  as it has already been used to normalize the deficit.

The lateral wake center displacement  $\mu_y$  has a relatively high correlation with the yaw misalignment  $\phi$ , confirming that the wake is deflected when the turbine is operated with a yaw misalignment. Moderate correlations with  $\alpha$  and  $\delta\alpha$  are found, corresponding to previous findings (e.g., Fleming et al., 2015; Sengers et al., 2022) that found that wake deflection is affected by atmospheric conditions. The vertical wake center displacement  $\mu_z$ , a relatively unexplored wake characteristic, appears to be positively correlated with  $\alpha$ . It is hypothesized that this is due to a larger wind speed gradient at lower tip height, increasing the mixing compared to that at upper tip height, effectively moving the wake center upwards. Further analysis (results not shown here) suggests that the vertical wake center displacement, and with that its correlation with input variables, is independent of wind direction. This excludes the influence of topography on these results.

The curl only correlates with  $\phi$ , whereas the wake tilt is highly correlated with  $\delta\alpha$ , corresponding to Abkar et al. (2018). Lastly, variables related to wake size ( $\sigma_y$ ,  $\sigma_z$ ,

|            |        |       |       |          |                |
|------------|--------|-------|-------|----------|----------------|
| $A_z$      | 0.14   | 0.19  | 0.65  | -0.68    | -0.15          |
| $\mu_y$    | -0.56  | 0.01  | -0.06 | 0.35     | 0.28           |
| $\mu_z$    | 0.05   | 0.28  | -0.12 | 0.47     | 0.17           |
| curl       | 0.53   | 0.21  | -0.02 | -0.01    | -0.26          |
| tilt       | -0.11  | -0.20 | -0.27 | 0.27     | 0.75           |
| $\sigma_y$ | 0.01   | 0.04  | 0.05  | -0.06    | -0.05          |
| $\sigma_z$ | 0.16   | 0.25  | 0.21  | -0.24    | -0.02          |
| $s_a$      | -0.05  | -0.14 | -0.00 | 0.05     | -0.12          |
| $s_b$      | 0.23   | 0.01  | -0.03 | 0.11     | 0.05           |
|            | $\phi$ | $U_h$ | TI    | $\alpha$ | $\delta\alpha$ |

Figure 5.8: Correlation matrix of the input variables and wake characteristics.  $A_z$  is the amplitude of the wake deficit normalized by  $U_h$ ,  $\mu_y$  and  $\mu_z$  the lateral and vertical wake center displacement, “curl” and “tilt” the wake curl and tilt,  $\sigma_y$  and  $\sigma_z$  the width and height of the wake, and  $s_a$  and  $s_b$  the quadratic and linear wake width parameter.

$s_a$ ,  $s_b$ ) have very weak correlations with the input variables, which could be due to the spatial resolution of the lidar PPI scans.

#### 5.4.1.2 Lateral wake center displacement and wake curl

Two wake characteristics,  $\mu_y$  and curl, are investigated as a function of  $\phi$  as these are deemed important for wake steering. Figure 5.9a demonstrates that  $|\mu_y|$  typically increases with  $|\phi|$ ; hence the wake deflection is larger for larger yaw misalignment angles, although there is a lot of scatter in the field measurements as also indicated by the correlation coefficient  $R$ . Three clusters can be identified, corresponding to the distribution of yaw angles shown in Fig. 5.4.

To check whether  $\mu_y$ 's order of magnitude is reasonable, field measurements are compared with LES results. Differently than in Sect. 5.2.3, the turbine simulated here represents turbine T1 in the field, for which the aerodynamic properties were provided by the operator in the Bladed model and translated into FAST. Because of computational restrictions, only three yaw settings  $\{-15^\circ, 0^\circ, 15^\circ\}$  with each of the four inflow conditions were simulated, which will represent only a small part of the full range of conditions observed in the field. The simulations have  $U_h \approx 8 \text{ m s}^{-1}$ , and the inflow variables are  $0.11 < \alpha < 0.26$ ;  $1.1^\circ < \delta\alpha < 2.6^\circ$  and  $6.0\% < \text{TI} < 8.4\%$ . The LES results show an initial deflection for  $\phi = 0^\circ$  (Gebraad et al., 2016), which is not clearly observed in the field. Otherwise, the observed magnitude of deflection is comparable between LES and the field.

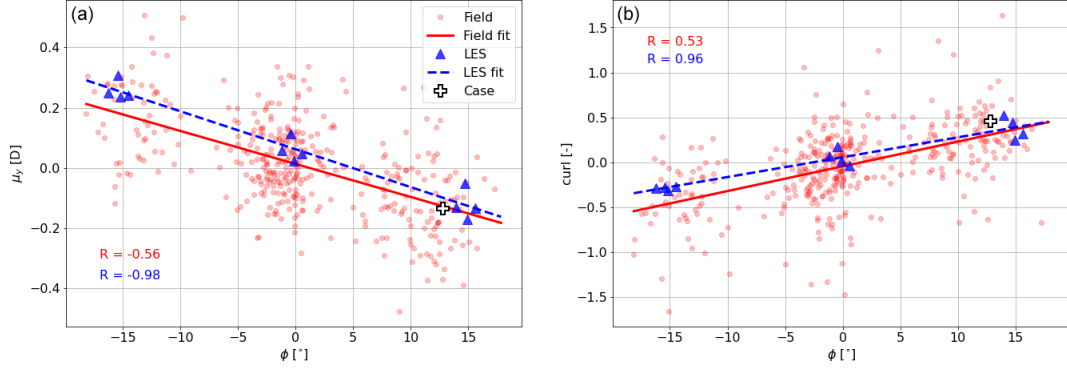


Figure 5.9: Scatterplot of (a)  $\mu_y$  and (b) curl as a function of yaw angle  $\phi$ . Red markers indicate field measurements, and blue triangles indicate LES data. Fitted linear functions are indicated with lines. The quality of these fits is indicated by the correlation coefficient  $R$ , corresponding to Fig. 5.8. White plus signs indicate the case studied in Fig. 5.10.

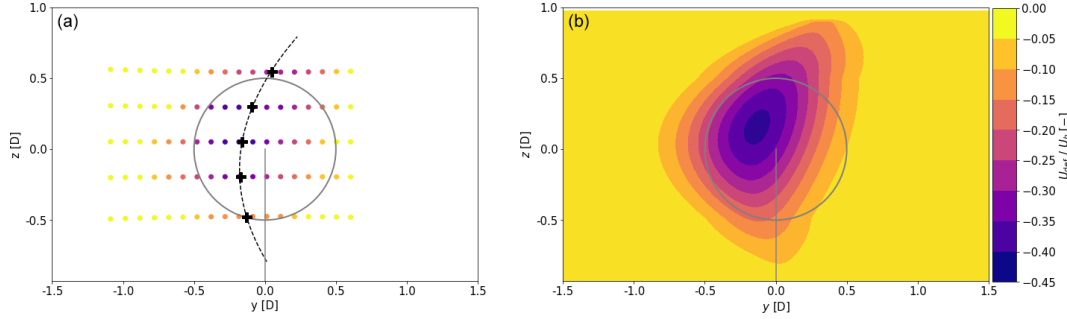


Figure 5.10: Exemplary case illustrating the wake curl generated by a misaligned turbine ( $\phi = 12.8^\circ$ ,  $U_h = 9.4 \text{ m s}^{-1}$ ,  $\alpha = 0.33$ ,  $\delta\alpha = -0.8^\circ$ ,  $\text{TI} = 10.4\%$ ). (a) The wake deficit of the 10 min averaged lidar data of 17 consecutive PPI scans (colors) and local wake center positions (black plus signs) with corresponding fitted polynomial (dashed black line) indicating the wake curl. (b) The wake reconstructed by utilizing the composition method. The color bar applies to both figures.

Figure 5.9b displays curl as a function of  $\phi$ . Similarly to  $\mu_y$ , the field measurements have a larger spread than the LES results, expressed by the lower quality of the linear fit (correlation coefficient  $R$ ). However, the fitted lines are similar, indicating that the wake curl does indeed occur in the field, something that until now had not conclusively been shown in the literature.

One case is selected (indicated with a white plus sign in Fig. 5.9) to illustrate what a wake with curl  $\approx 0.5$  looks like. Figure 5.10a presents the observed deficit measurements ( $U_{\text{def}}$ ) normalized by  $U_h$ , in which the wake's curl is indicated by the dashed black line. The curl is indeed relatively small and could be missed when operating the long-range lidar with a different scanning strategy. Figure 5.10b represents a reconstructed wake using the composition method (Sect. 5.3.1), which clearly shows that the wake center has moved to the left and up.

Even though the curling observed in this study is relatively small, Fig. 5.9b does confirm that the wake curls as expected from numerical and wind tunnel experiments. Field experiments are often restricted to yaw misalignments smaller than  $20^\circ$ , whereas numerical and wind tunnel studies allow for larger misalignments. As suggested in Brugger et al. (2020), this is the reason for the lack of observations of fully curled (or kidney-shaped) wakes in the field.

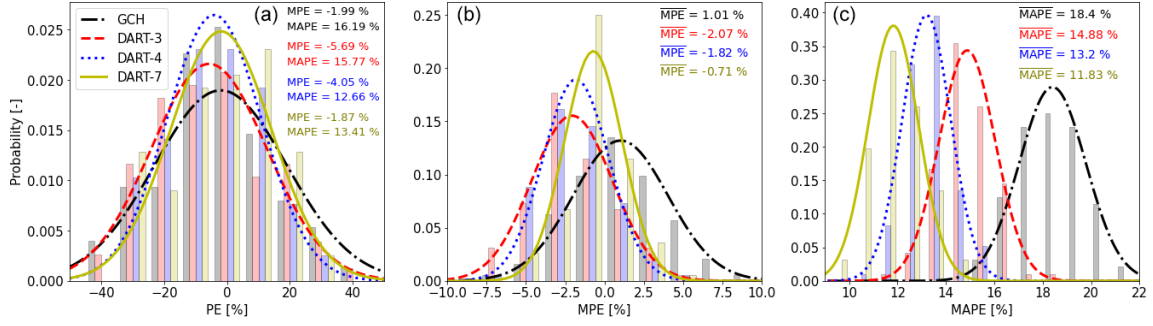


Figure 5.11: Like Fig. 5.7 but for the testing data for GCH (black/grey), DART-3 (red), DART-4 (blue) and DART-7 (yellow). Histogram (a) for one resample and (b) for MPEs and (c) for MAPEs of all 96 resamples. Fitted normal distributions are indicated with lines, and statistics are given in the top right.

## 5.4.2 Performance of wake models

This subsection presents the performance of the DART and GCH wake models in reproducing the wake characteristics observed in the field. Section 5.4.2.1 presents how well the models can reproduce the available power measured by the lidar. Following this general result, Sect. 5.4.2.2 zooms in on how well the models perform under different conditions and Sect. 5.4.2.3 displays how well the models can reproduce a selection of wake characteristics. Section 5.4.2.4 discusses how sensitive the models are to the number of training data. Lastly, Sect. 5.4.2.5 evaluates how well DART performs when only using SCADA data as input.

### 5.4.2.1 Comparison of DART and GCH

This subsection discusses the performance of DART and GCH in a comparison with the wake observed in the field. The models were trained (DART, Sect. 5.3.4.4) or tuned (GCH, Sect. 5.3.5) on 80% of the data and are now tested on the remaining 20% of the data. Figure 5.11a displays the model accuracy on one resample, using the percentage error (PE) of available power ( $P_{av}$ ) as a performance metric, analogously to Fig. 5.7. All models seem to have negative bias ( $\overline{MPE} < 0\%$ ), indicating that the rotor-equivalent wind speed  $U_{eq}$  is overestimated. DART's bias reduces with an increasing number of input variables, as is evident from the smaller error in DART-7 compared to DART-3 and DART-4. DART-7's bias is comparable to that of GCH. GCH's spread is however larger than DART's, resulting in a larger MAPE despite having a lower MPE.

When repeating this for all 96 resamples, a distribution of MPE and MAPE values can be found (Fig. 5.11b–c). Also here DART shows a small negative bias ( $\overline{MPE} < 0\%$ ), hence underestimating  $U_{eq}$ . GCH has a small positive bias, therefore overestimating  $U_{eq}$ , and a much wider distribution.

The distribution of MAPE values indicates that with just three input variables, DART-3 is able to outperform GCH, showing a reduction in  $\overline{MAPE}$  of 19%. Moreover, both its  $\overline{MPE}$  and  $\overline{MAPE}$  are very similar to those of the training data (Fig. 5.7), indicating that the model is able to generalize well to unseen or independent data. Adding more variables further improves DART's accuracy, reducing  $\overline{MAPE}$  with 28% and 36% for DART-4 and DART-7 compared to GCH. Moreover, the fitted normal distributions of  $\overline{MAPE}$  for GCH and DART-4 or DART-

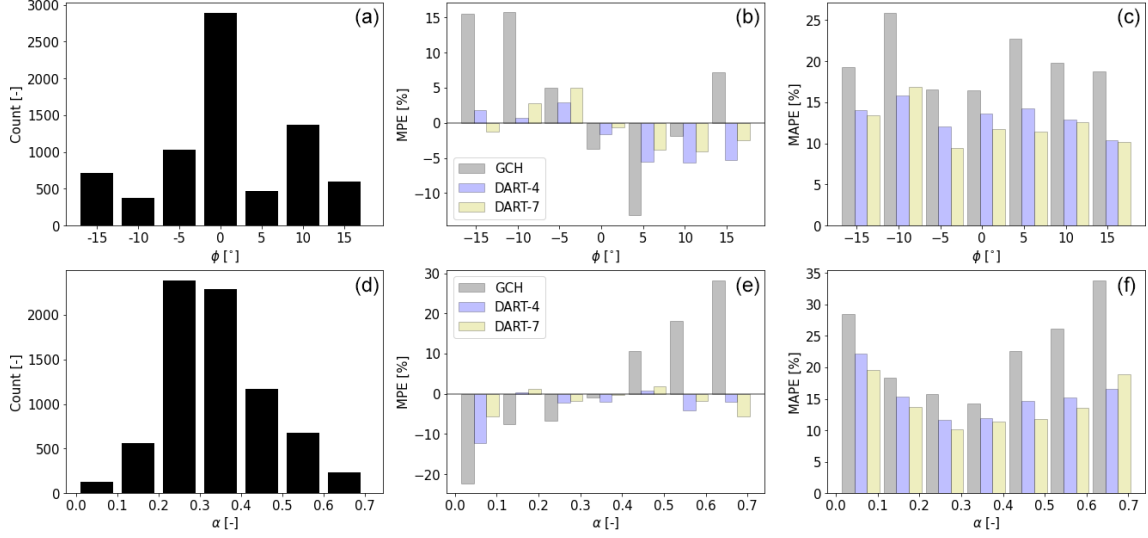


Figure 5.12: Performance of GCH (grey), DART-4 (blue) and DART-7 (yellow) as a function of  $\phi$  (a–c) and  $\alpha$  (d–f). Histogram of data availability per bin (a, d) and corresponding MPE (b, e) and MAPE (c, f) per bin.

7 hardly overlap, indicating that DART significantly outperforms GCH when trained with at least four variables.

These results show the potential of a data-driven model: more of the variability in wakes observed in the field can be explained by using only four input parameters in a data-driven model than with an industry-standard analytical model.

#### 5.4.2.2 Model accuracy under different conditions

To gain a better understanding of these results, under what conditions the models' performances differ considerably is investigated. DART-3 is here omitted for brevity. First, the models' errors are investigated in relation to the yaw angle  $\phi$ . Figure 5.12a displays a histogram of data availability per  $\phi$  bin of  $5^\circ$  over all 96 resamples, while Fig. 5.12b and c show the MPE and MAPE of  $P_{av}$  per bin. The GCH model has  $MPE > 0\%$  for  $\phi < -7.5^\circ$  and  $MPE < 0\%$  for  $2.5^\circ < \phi < 7.5^\circ$ . This is likely due to low data availability. DART demonstrates a more uniform trend over all yaw angles. When looking at MAPE (Fig. 5.12c), it can be seen that especially under yawed conditions (both positive and negative), DART seems to outperform GCH. It is hypothesized that this is due to a more accurate estimation of the wake center position in DART.

Figure 5.12d–f display a similar analysis as a function of shear  $\alpha$ . GCH shows an almost linear trend as a function of  $\alpha$ , with  $MPE < 0\%$  for small  $\alpha$  and  $MPE > 0\%$  for large  $\alpha$ . This indicates that the modeled wake recovery is too slow under low shear and too fast under high shear inflow, which could be due to the turbulence model not explicitly including  $\alpha$  as an input parameter. In contrast, DART explicitly uses  $\alpha$  to estimate wake characteristics. It therefore produces more uniform results and outperforms GCH, especially when  $\alpha > 0.4$  (see Fig. 5.12c). Over the whole range of  $\phi$  and  $\alpha$ , DART-7 is marginally more accurate than DART-4.

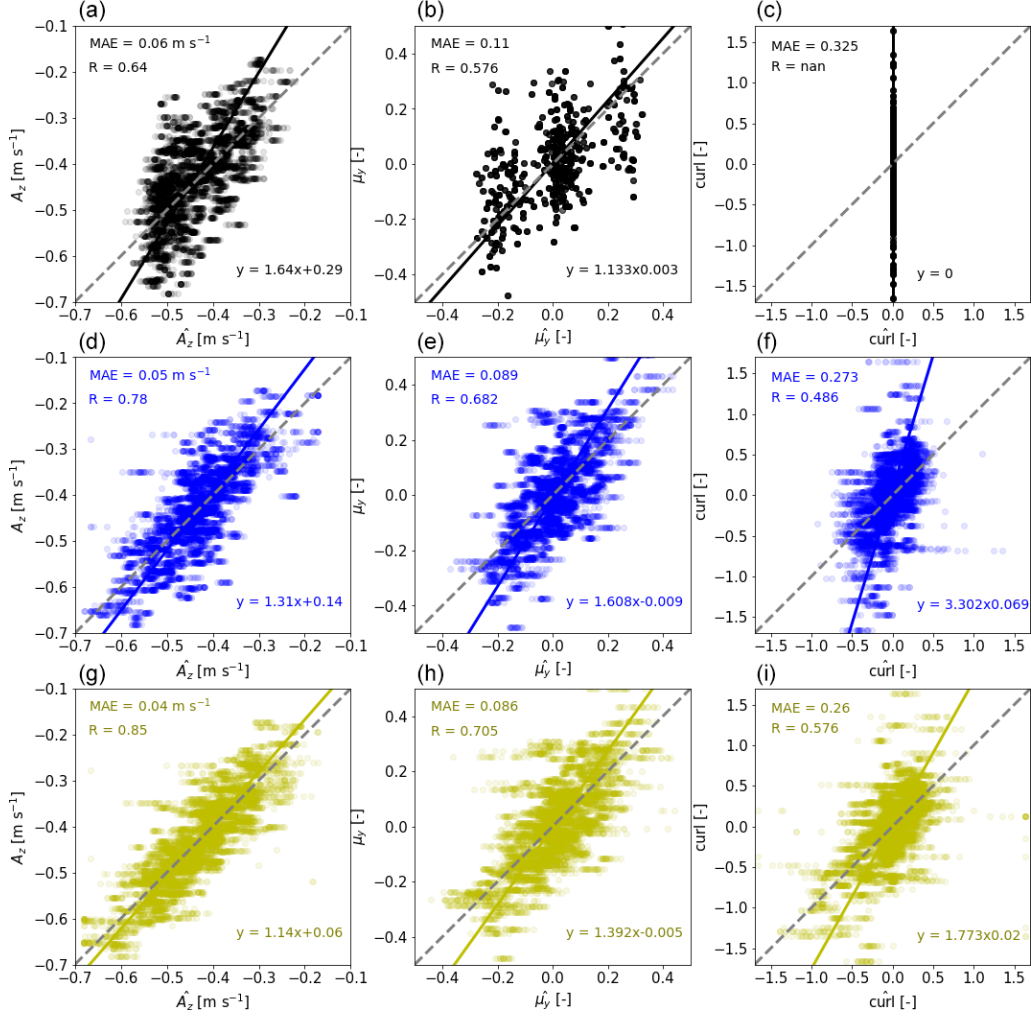


Figure 5.13: Accuracy of GCH (a–c), DART-4 (d–f) and DART-7 (g–i) in estimating wake characteristics  $A_z$  (a, d, f),  $\mu_y$  (b, e, h) and curl (c, f, i). The models’ estimates are given on the  $x$  axis and the observations on the  $y$  axis. Solid lines indicate linear orthogonal distance regression fits and dashed lines the identity lines.

#### 5.4.2.3 Estimating wake characteristics

Finally, the accuracy of GCH and DART in estimating the wake characteristics  $A_z$ ,  $\mu_y$  and curl is investigated. The left column of Fig. 5.13 displays the observed  $A_z$  as a function of the model-estimated  $\hat{A}_z$ . As clearly indicated by the fitted line, the GCH model overestimates small deficits and underestimates large deficits. This could be resolved by giving more weight to outliers when tuning the parameters, although that could lead to the undesirable decrease in accuracy in frequently occurring conditions. The fitted line to the DART-4 results appears to be closer to the unity line, while for DART-7 an even better agreement is found. Additionally, the mean absolute error (MAE) and Pearson correlation coefficient ( $R$ ) displayed in the top left indicate a more accurate modeling of  $A_z$  using DART.

The center column displays a similar analysis for  $\mu_y$ . The fitted lines imply a higher accuracy for GCH than for DART, while the statistical metrics suggest the opposite. GCH’s estimates for  $\mu_y$  seem to be clustered, which is not true for DART or the measurements. As noted in Sengers et al. (2022), the effect of inflow conditions



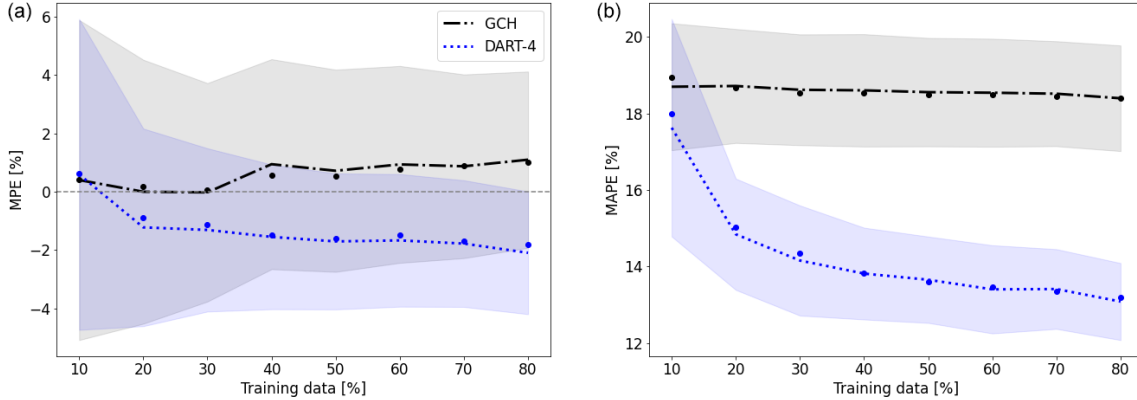


Figure 5.14: MPE (a) and MAPE (b) as a function of training data set size. Markers indicate the means ( $\overline{\text{MPE}}$  and  $\overline{\text{MAPE}}$ ), lines indicate the median and shaded areas indicate the standard deviation, corresponding to the fitted normal distributions in Fig. 5.11.

(e.g.,  $\alpha$ ) on the wake deflection is not well described in GCH. Consequently, the wake deflection is only a function of the yaw angle and the observed clusters can directly be related to the distribution of yaw misalignment angles shown in Fig. 5.4. Additionally, while in Fig. 5.13e and h transparent markers can be observed, the markers in Fig. 5.13b appear to be opaque. Here, many transparent markers overlay each other, indicating that GCH estimates the same wake center location in all resamples and that these estimates are not affected by the model’s tuning parameters.

Lastly, the right column displays the results for curl. GCH does not model any curl, whereas DART is able to capture some of the observed variability. DART-7 performs better than DART-4 as more variables that are (weakly) correlated with curl (see Fig. 5.8) are considered. Although the variability found in the field is not fully captured by either model, it is clear that the wake curl is better reproduced by DART than by GCH.

#### 5.4.2.4 Dependency of performance on data set size

An important aspect of data-driven models is understanding how the number of training data affects the model’s accuracy. This is especially relevant as one of the most commonly named drawbacks of data-driven models is their high need for data. This subsection studies the sensitivity of the accuracy of DART-4 to the number of training data. DART-7 is not considered due to its long training time. Additionally, GCH is included in the analysis as it contains tuning parameters which could benefit from being tuned to a larger data set. All models are trained with a part of the full data set, ranging from 10% to 80%, and tested on the remaining 20%, analogously to the procedure described in Sect. 5.3.3. Regardless of the number of training data, the testing data are always 20% of the original data set and consist of the same cases for fair comparison. When using, e.g., 40% of the data for training and 20% for testing, the remaining 40% are not used at all.

Figure 5.14 displays the accuracy of the models as a function of the size of the training data set. The metrics used for this analysis are again the distribution of MPE and MAPE values of the 96 resamples, corresponding to the normal distributions shown in Fig. 5.11. Figure 5.14a again reveals that DART-4 has a

negative bias ( $\text{MPE} < 0\%$ ), which is present regardless of the number of training data, whereas GCH typically has a small positive bias ( $\text{MPE} > 0\%$ ). The uncertainty bands, representing 1 standard deviation indicated by the shaded area, are larger for GCH than for DART-4, while for both models the uncertainty is reduced when trained with more data.

Figure 5.14b displays the distribution of MAPE values of the 96 resamples as a function of the data set size. GCH and DART-4 have a similar accuracy when few data are available, but DART-4 already outperforms GCH when as little as 20% of the data set ( $\approx 75$  cases or 13h) is used for training. Note that this does not indicate 13h of consecutive measurements but rather 75 cases covering a range of meteorological conditions representative of the variability experienced by the turbine. Additionally, the accuracy of DART-4 seems to continue to improve when adding more data, albeit at a slower rate, whereas GCH hardly shows any improvement with higher data availability.

#### 5.4.2.5 Performance with SCADA data as input

In this subsection, DART-4 is trained using only data routinely available to the operator (SCADA data) as input variables, called DART-4S. However, it still uses the measurements from the nacelle-mounted lidar to obtain the wake characteristics. Input variables includes power  $P$ , rotor speed  $\omega$ , wind speed  $U_S$  and turbulence intensity  $\text{TI}_S$  estimated from the cup anemometer and yaw misalignment  $\phi_S$  extracted from the wind vane. As discussed, according to Fig. 5.4, this signal contains a systematic bias (Fleming et al., 2021) and is disturbed by the turbine yaw misalignment (Kragh and Fleming, 2012; Simley et al., 2021a), resulting in misalignments being overestimated by the nacelle vane. No correction was applied here, as data-driven models can compensate for any systematic biases. A similar reasoning can be applied to the use of  $\text{TI}_S$ : although turbulence intensity estimates from a nacelle cup anemometer are affected by the rotor (e.g., Barthelmie et al., 2007), biases can be handled by data-driven models and are therefore acceptable. Additionally, data-driven models are better able to deal with noise than analytical models, which assume that the inflow information is undisturbed or need error terms inserted in the model equations (Schreiber et al., 2020).

The main issue of only using SCADA data is that there is no reliable estimate for the vertical wind speed profile. In this study, the shear  $\alpha$  measured at the met mast is estimated from  $\text{TI}_S$  using the fitted linear relation:  $\hat{\alpha} = 0.625 - 0.023 \text{TI}_S$ . Because  $\alpha$  and  $\text{TI}_S$  are quite weakly correlated ( $R = -0.47$ ), this simple approach introduces uncertainty. However, developing a more sophisticated solution was deemed out of the scope of this work and this approach is deemed sufficient for the current purpose. An alternative approach could be to use strain measurements from the turbine’s blades to estimate shear, as demonstrated in Bertelè et al. (2017, 2021), although this would also involve additional sensors.

Figure 5.15 displays the results of DART-4S, using  $\{\phi_S, \text{TI}_S, U_S, P\}$  as input, in a comparison with GCH and DART-4, both trained with met mast data. The accuracy of DART-4S is very similar to DART-4, showing a larger negative  $\overline{\text{MPE}}$  but an almost identical  $\overline{\text{MAPE}}$ . This indicates that using an arguably lower quality data set hardly affects the accuracy of the wake estimates. It is hypothesized that this is because the SCADA data better capture the atmospheric conditions at the

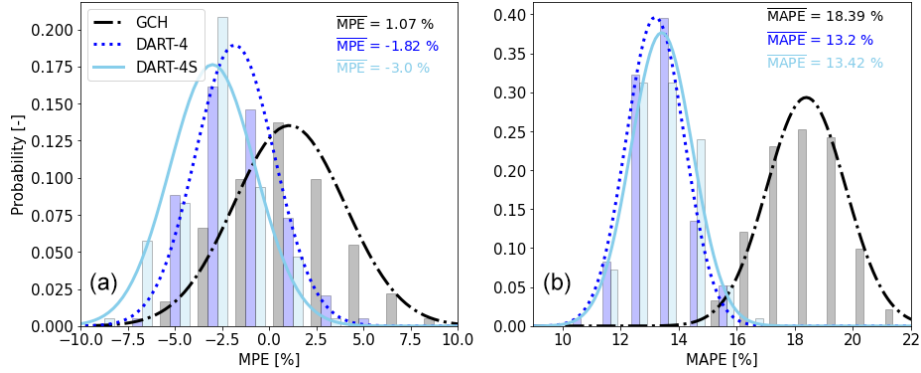


Figure 5.15: Same as Fig. 5.11b–c but with DART-4S (light blue).

turbine, whereas met mast data are subject to heterogeneity between met mast and turbine. This would counter the lower quality of the data, leading to only a slight decrease in the model accuracy. Interestingly, DART-4S is significantly more accurate than GCH, even though the latter needs undisturbed measurements as input.

## 5.5 Discussion

Section 5.5.1 discusses the measurement campaign and its accuracy. In Sect. 5.5.2 the limitations of the data-driven model are reviewed. Finally, Sect. 5.5.3 focuses on the implication of this study’s results for future work.

### 5.5.1 Campaign

This subsection discusses some key takeaways for future campaigns (Sect. 5.5.1.1) and an uncertainty analysis considering measurement errors (Sect. 5.5.1.2).

#### 5.5.1.1 Lessons learned

Several considerations regarding the experimental campaign are noteworthy. First, the nacelle-mounted lidar’s scanning strategy was based on Brugger et al. (2019, 2020) and evaluated systematically using large-eddy simulation results and a lidar simulator. However, during this analysis, data losses were not considered. Subsequently, in the field data occasionally all information at one height was filtered out, leaving only information at four heights for the analysis (Sect. 5.2.3), which could lead to interpolation errors. A more robust approach would have been to perform seven instead of five consecutive PPI scans, although the accuracy of the wake reconstruction method is slightly lower (see Fig. 5.2). Lastly, in this study only one distance of  $4D$  was targeted, but for other purposes it could be desirable to target multiple positions at once. This would likely require more PPI scans with a larger range of elevation angles, as used in Brugger et al. (2020). Large elevation angles are needed to capture the wake close to the turbine, whereas small elevation angles capture the wake further downstream.

Further, no systematic hard-target analysis was performed with the nacelle-based lidar. The horizontal offset relative to the turbine’s center axis could be estimated

from a set of coarser PPI scans, but no vertical offset could be estimated. Although this is not expected to have a large influence on the results presented here, as is also discussed in Sect. 5.5.1.2, it is recommended to always carry out a hard-target analysis in future measurement campaigns to reduce the uncertainty in the measurements.

### 5.5.1.2 Measurement uncertainty

Although the measurement data after filtering have been considered the “ground truth” in this study, a few aspects affecting the data quality should be considered. Homogeneity of the background flow is assumed, as well as a vertical wind profile that can be described with the power law, which is not always satisfied. This refers specifically to the trees in the wind direction sector around  $\delta = 350^\circ$  that are assumed not to affect met mast data, as mentioned in Sect. 5.2.1. Besides, turbines T3 (induction zone) and T4 (wake) are assumed to not affect the wake, although this cannot be ruled out entirely. Lastly, the lidar measurements are inherently subject to probe volume averaging, and a different filtering method than the one described in Sect. 5.2.3 will retain other information and therefore result in slightly different wake characteristics.

Additional analyses were carried out to investigate the effect of measurement uncertainty in the results presented in Sect. 5.4, specifically those in Fig. 5.11. An overview of these tests is displayed in Table 5.3. First, the influence of the missing hard-target analysis (Sect. 5.5.1.1) is investigated. In the original measurements, an upward vertical displacement of the wake center of  $0.15D$  was observed, averaged over all 382 cases. Although displacements of this magnitude have been observed in numerical simulations (Sengers et al., 2020), it is here assumed that this is purely the consequence of an installation error of the lidar. Such a displacement at  $4D$  downstream would come from a downward angle of  $\tan^{-1}(0.15/4) = -2.18^\circ$ . In test 1, the elevation angles of all lidar scans were adjusted with this value, resulting in an average vertical wake center displacement of zero. Since vertical wake center displacements have been observed in other studies (e.g., Bastankhah and Porté-Agel, 2016; Sengers et al., 2020), the previous test was not deemed completely realistic. Additional tests (2 and 3) with half the correction value, as well as a positive correction value, were carried out. The next set of tests varies the wind speed and direction measured at the met mast. As noted in Sect. 5.2.5, the accuracy of the anemometer is  $0.2 \text{ m s}^{-1}$  and the accuracy of the vane is  $1.5^\circ$ . These values are used in tests 4–7, varying the measurements at hub height (subscript h) and lower tip height (lt) in opposite directions, investigating the maximum influence of these uncertainties. Note that this affects the shear and veer as well.

In all tests, DART-4 (DART-3, DART-7 and DART-4S omitted for brevity) and GCH are trained on the adjusted data for all 96 resembles. Their accuracy on the testing data is evaluated using  $\overline{\text{MPE}}$  and  $\overline{\text{MAPE}}$  and shown in Fig. 5.16. Compared to the original (Test 0) of Fig. 5.11, Test 1 shows a slightly poorer performance of DART-4 (larger  $\overline{\text{MPE}}$  and  $\overline{\text{MAPE}}$ ). It is hypothesized that this is due to the fact that now the five PPI scans do not fully target the rotor area anymore, resulting in less relevant information about the wake to estimate the available power. GCH, on the other hand, seems to perform better (smaller  $\overline{\text{MPE}}$  and  $\overline{\text{MAPE}}$ ) than the original. Since no vertical displacement is estimated with GCH, these new data more closely

Table 5.3: Overview of all tests carried out for the uncertainty analysis.

| Test | Description                                                             |
|------|-------------------------------------------------------------------------|
| 0    | Original; Fig. 11                                                       |
| 1    | $\phi_{\text{PPI}} - 2.18^\circ$                                        |
| 2    | $\phi_{\text{PPI}} - 1.09^\circ$                                        |
| 3    | $\phi_{\text{PPI}} + 1.09^\circ$                                        |
| 4    | $U_h + 0.2 \text{ m s}^{-1}$ and $U_{\text{lt}} - 0.2 \text{ m s}^{-1}$ |
| 5    | $U_h - 0.2 \text{ m s}^{-1}$ and $U_{\text{lt}} + 0.2 \text{ m s}^{-1}$ |
| 6    | $\delta_h + 1.5^\circ$ and $\delta_{\text{lt}} - 1.5^\circ$             |
| 7    | $\delta_h - 1.5^\circ$ and $\delta_{\text{lt}} + 1.5^\circ$             |

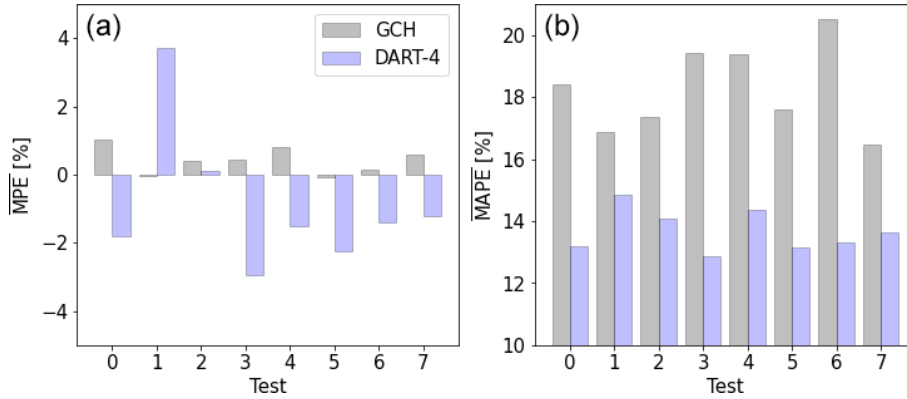


Figure 5.16: Results of the tests of Table 5.3.  $\overline{\text{MPE}}$  and  $\overline{\text{MAPE}}$  of Test 0 correspond to the values found in Fig. 5.11.

resemble the model’s assumptions. Tests 2 and 3 confirm this, as GCH’s  $\overline{\text{MAPE}}$  increases with the magnitude of the vertical wake center displacement.

Tests 4 and 5 illustrate that both models perform better when the shear is decreased (Test 5) compared to when the shear is increased (Test 4), which relates to the fact that more uniform conditions are easier to reproduce. Lastly, GCH performs worse in Test 6 and better in Test 7 compared to the original, but no satisfying explanation was found.

In general, these tests demonstrate that the more closely a data set resembles the model assumptions, the better the model performs. DART-4 typically shows a higher  $\overline{\text{MPE}}$  and a lower  $\overline{\text{MAPE}}$  compared to GCH, which is similar to the results presented in Sect. 5.4. This uncertainty analysis is believed to demonstrate that the results presented in this study are robust and not very sensitive to measurement uncertainty.

### 5.5.2 Data-driven model

DART’s quantitative results presented in this study are not fully generalizable. The fitted coefficients in Eq. (5.3) are only valid for the scenario considered in this study, and it is unknown how the model’s accuracy transfers to different scenarios, such as other turbine types and downstream distances. Besides, while the range of achieved yaw misalignments is typical of field experiments nowadays (e.g., Fleming et al., 2020, 2021; Doekemeijer et al., 2021), future campaigns could see larger misalignments such as those currently considered in numerical studies (e.g., Howland et al., 2016; Martínez-Tossas et al., 2019; Bastankhah et al., 2022). Further

lidar measurements would be needed in new scenarios to guarantee accurate model estimates, and although it needs relatively few data for retraining in new situations (Sect. 5.4.2.4), this limits the potential for application of data-driven models in wake steering control.

To overcome this, future work should attempt to generalize the model’s coefficients. Alternatively, model equations using coefficients determined with previous numerical or experimental data could still be used at new locations to generate a first estimate of the wake characteristics. Assuming that the wake position and shape are sufficiently accurately modeled, coefficients for the wake deficit could be retrained using SCADA data by deducing a rotor-equivalent wind speed.

Lastly, other data-driven models could be used. Currently, to the best of our knowledge DART is the only data-driven wake model available that does not make use of complex black-box models such as neural networks. Although it would be interesting to compare different data-driven models, more complex models typically need more data. For instance, Asmuth and Korb (2022) proposed a neural network and showed they need at least 800 cases to train the model for non-yawed cases only. Although their results are extremely promising, extending this to include wake steering would likely require a substantially longer measurement campaign.

### 5.5.3 Implications for future work

As noted in the Introduction, the industry appears to be hesitant to adopt the wake steering strategy due to large uncertainties. To overcome this, yaw controllers need to become more sophisticated, for instance by using closed-loop controllers (Doekemeijer et al., 2020; Howland et al., 2020) or using preview information (Simley et al., 2021b). On the other hand, the low-fidelity wake models that are utilized to determine the yaw misalignment set points used by the yaw controller need to become more accurate.

This study contributes to the latter by showing that both DART and GCH perform well on average (small systematic bias) but that DART can capture a higher degree of variability observed in the field. Besides more accurate estimations of the wake deficit, which historically has been the main focus of wake models, this extends to other wake characteristics like wake curl and wake center location. The latter is especially important for wake steering, as erroneous steering can steer the wake into a downstream turbine.

Since DART shows a higher accuracy than GCH in estimating wake characteristics, it can be hypothesized that when using DART to determine yaw misalignment set points used by the yaw controller, the wake steering strategy can be applied more successfully. This can consist of achieving higher power gains when wake steering is performed successfully or reducing power losses due to erroneous steering. However, an extensive campaign would be needed to investigate this, which was considered out of the scope of the current work.

On a more general level, this study shows that data-driven models are a viable alternative to analytical models. Whereas data-driven models have often been criticized for their complex nature, this study has demonstrated that accurate estimations can also be obtained with a very simple linear model.

While the current model focuses on estimated wind speed and consequently power, a similar methodology could be developed to estimate turbulence and consequently

turbine loads. Alternatively, it would be interesting to combine analytical and data-driven models in hybrid models. Such models could initially benefit from the robustness of analytical models but exploit the higher accuracy of data-driven models when more data become available.

## 5.6 Conclusions

This study uses nacelle-based lidar measurements of the wake of a commercial turbine with a fixed intentional yaw misalignment. Performing a trajectory of five consecutive plan position indicator (PPI) scans with different elevation angles, a vertical wake cross-section at four rotor diameters downstream is reconstructed. Utilizing the multiple 1D Gaussian method, wake characteristics are obtained. The lateral wake center displacement and wake curl observed in the field compare well with large-eddy simulation results. The results from the lidar measurements demonstrate the occurrence of the wake curl in the field, which had not conclusively been shown in the literature before. This is due to small curling observed for yaw misalignments below  $20^\circ$ , which could be missed when using a different scanning trajectory.

The field measurements are subsequently used to train and validate the DART model and compare the accuracy of the trained data-driven model to the accuracy of the GCH model. When estimating the observed wake characteristics with both wake models, it is demonstrated that DART systematically outperforms GCH. Depending on the number of input variables used for DART, the error is reduced by between 19% and 36% compared to GCH. The metric used here is the mean absolute percentage error of the available power of a virtual downstream turbine, averaged over 96 resampled testing data sets. Especially when the turbine is misaligned or high vertical shear is observed, DART outperforms GCH. Besides, DART requires a relatively small number of training data (about 75 cases at specific set points) to outperform GCH. Further analysis suggests that DART's accuracy is hardly affected when only considering SCADA data as input in comparison to using undisturbed measurements from a met mast.

DART shows a high accuracy in the current study, targeting a downstream distance of four rotor diameters and using a range of yaw misalignments commonly used in field experiments. However, these results cannot directly be generalized and further lidar measurements are needed to retrain DART for new scenarios, limiting its applicability. Regardless, this study's results are believed to demonstrate the potential of data-driven wake models and the role they can play in the further deployment of wake steering control strategies.

## Chapter 6

# Increased power gains from wake steering control using preview wind direction information

The content of this chapter is identical to the following journal article:

Sengers, B. A. M., Rott, A., Simley, E., Sinner, M., Steinfeld, G., and Kühn, M.: Increased power gains from wake steering control using preview wind direction information, *Wind Energy Science*, 8, 1693–1710, <https://doi.org/10.5194/wes-8-1693-2023>, 2023.

©Author(s) 2023. This work is distributed under the Creative Commons Attribution 4.0 License. Reprinted with permission.

**Abstract** Yaw controllers typically rely on measurements taken at the wind turbine, resulting in a slow reaction to wind direction changes and subsequent power losses due to misalignments. Delayed yaw action is especially problematic in wake steering operation because it can result in power losses when the yaw misalignment angle deviates from the intended one due to a changing wind direction. This study explores the use of preview wind direction information for wake steering control in a two-turbine setup with a wind speed in the partial load range. For these conditions and a simple yaw controller, results from an engineering model identify an optimum preview time of 90 s. These results are validated by forcing wind direction changes in a large-eddy simulation model. For a set of six simulations with large wind direction changes, the average power gain from wake steering increases from only 0.44 % to 1.32 %. For a second set of six simulations with smaller wind direction changes, the average power gain from wake steering increases from 1.24 % to 1.85 %. Low-frequency fluctuations are shown to have a larger impact on the performance of wake steering and the effectiveness of preview control, in particular, than high-frequency fluctuations. From these results, it is concluded that the benefit of preview wind direction control for wake steering is substantial, making it a topic worth pursuing in future work.



## 6.1 Introduction

To support the energy transition, it is important to maximize the value of the renewable energy portfolio. On the one hand, this includes minimizing the costs of installation and maintenance; on the other hand, this means maximizing the power yield. Focusing on wind energy, wind farm control to mitigate wake effects has received considerable attention in recent years (Meyers et al., 2022). Additionally, short-term forecasting of the wind speed and direction can be used to adapt the turbine for approaching changes; hereafter, this is called preview control (PC), as opposed to traditional standard control (SC) using measurements at the turbine. PC can be used to reduce the occurrence of suboptimal blade pitch angles and turbine misalignment, two aspects that result in power losses and increased loads (Scholbrock et al., 2016). Furthermore, operators can use the forecasts to support grid stability and reduce curtailment (Bird et al., 2016). Downstream turbines can use information from turbines further upstream (Rott et al., 2020), or remote sensing techniques (lidar-assisted control) can be used (e.g., Theuer et al., 2020; Würth et al., 2019). Many studies have investigated the application of preview wind speed information in turbine control, a few of which are discussed in the following. Torque control to improve its aerodynamic efficiency is observed to achieve very small power gains, but it drastically increases the turbine’s loads (Schlipf et al., 2011; Wang et al., 2013). However, pitch control significantly reduces the loads with a minimum change in generated power (Dunne et al., 2011; Bossanyi et al., 2014). Combinations of the two have shown promising results in terms of both reducing the loads and increasing the power (Schlipf et al., 2013; Schlipf and Cheng, 2014). On the contrary, remote sensing techniques to improve the turbine’s yaw control are relatively rare and are usually only done to help calibrate the nacelle’s wind vane (e.g., Fleming et al., 2014b; Scholbrock et al., 2015). This is interesting, as some studies have reported potential power gains from reduced yaw misalignment when using preview information. Spencer et al. (2011) modeled perfect wind direction prediction to reduce the yaw misalignment of a single turbine, resulting in a power gain of 0.5% and a reduction in fatigue loads. Using a weighted average of wind direction measurements from upstream turbines, Bossanyi (2019) found a 0.2% power increase and a 24% reduction in yaw travel for a wind farm in a 30 min simulation. Similarly, Sinner et al. (2021) averaged wind direction signals of neighboring turbines to obtain a smoother wind direction signal. They demonstrated that this results in power gains and yaw travel reductions for both greedy and wake steering operations, but using preview information did not yield significant results. In light of the controller lag observed in a wake steering experiment reported in Fleming et al. (2019), Simley et al. (2021b) employed the FLOW Redirection and Induction in Steady State (FLORIS) simulation tool (NREL, 2022) to compare preview control using wind direction information to standard control for a turbine pair in wake steering operation. Using an optimal preview time of 90 s, their results demonstrate that the power gain of 5.8% achieved with SC wake steering increases to 8.9% when PC is enabled. However, this analysis uses perfect preview information, and no improvement was found with realistic measurement accuracy. Howland et al. (2022) simulated a diurnal cycle with time-varying wind speed, wind direction, and atmospheric stability in a large-eddy simulation (LES) model. Using a simple forecasting method based on linear regression of past data, they demonstrated that

in wake steering operation, PC’s power production is slightly increased compared to that of SC.

Although it intuitively makes sense that PC turbines anticipating an approaching wind direction change yield more power than SC turbines, it is a relatively unexplored topic. PC is expected to be especially beneficial in wake steering operation because it could limit erroneous wake steering, which is when wake steering results in power losses compared to greedy control (e.g., Doekemeijer et al., 2021). The magnitude of potential power gains is unknown, but they should be substantial to make preview control worth pursuing in future work.

The objective of this paper is to demonstrate the benefit of using preview wind direction observations for wake steering purposes to further increase power production. Preview information is obtained from a virtual met mast located upstream, as developing a more sophisticated wind direction forecasting technique was considered out of scope. This objective comprises three components: (1) to develop a simple engineering model to obtain estimates of the expected power gain and optimal preview time; (2) to validate the findings of the engineering model with results from large-eddy simulations; and (3) to identify the characteristics of the wind direction signal that benefit from preview control the most.

## 6.2 Turbine yaw controller

This section describes the turbine yaw controller used in this study. It covers how the controller functions in greedy and wake steering operations, as well as how preview control is handled. The turbine pair simulated in this study consisted of two NREL 5 MW turbines with a hub height of 90 m and a rotor diameter  $D = 126$  m (Jonkman et al., 2009). While the upstream turbine could operate in greedy or wake steering control, the downstream turbine always operated in greedy yaw control.

### 6.2.1 Greedy

The turbine controller used a 60 s moving average of wind direction observations  $\bar{\delta}$  and turbine orientation  $\gamma$  to determine the yaw misalignment angle  $\bar{\phi}$  of the turbine with the inflow wind direction:

$$\bar{\phi} = \gamma - \bar{\delta}. \quad (6.1)$$

Once  $|\bar{\phi}|$  exceeded a preset limit of  $7.5^\circ$ , the turbine corrected its orientation at  $0.3^\circ \text{ s}^{-1}$ , as is standard for the NREL 5 MW turbine, until  $|\bar{\phi}| \leq 0.15^\circ$  was reached. This check was performed every second, except during and the first minute after a yaw maneuver, to eliminate measurements disturbed due to the rotating nacelle.

### 6.2.2 Wake steering

To implement wake steering, existing controllers are typically adapted to include an intended target yaw misalignment  $\phi_t$ . In this study, a positive misalignment was defined as a clockwise rotation of the turbine when looking from above. Because of the intentional misalignment, an effective yaw angle  $\bar{\phi}_e$  was determined:

$$\bar{\phi}_e = \gamma - \bar{\delta} - \phi_t, \quad (6.2)$$

which triggered a yaw maneuver when  $|\overline{\phi_e}|$  exceeded  $7.5^\circ$ .  $\phi_t$  was determined using a lookup table (LUT) that contained the power-maximizing yaw misalignment angles as a function of inflow conditions. The LUT was developed based on the Data-driven wAKE steeRING surrogate model (DART) introduced in Sengers et al. (2022). This wake model uses a set of only linear equations ( $\mathbf{Y} = \mathbf{X} \times \mathbf{B}$ ) to estimate wake characteristics  $\mathbf{Y}$  (e.g., deficit, center position) from the input variables  $\mathbf{X}$  (e.g., yaw angle, shear exponent, thrust coefficient). The model coefficients  $\mathbf{B}$  are found by a regression analysis with reference data. The wake characteristics can consequently be used to generate a vertical cross-section of the streamwise wind speed component to estimate the available power at a virtual wind turbine at a downstream position. Based on the results described in Sengers et al. (2022), the set of  $(\phi_t, \overline{\delta\alpha}$  and  $C_T)$ , in which  $\overline{\delta\alpha}$  is the 60 s moving-averaged vertical wind veer over the rotor area, were used as input variables. The thrust coefficient  $C_T$  was estimated as a function of  $\phi_t$ :

$$C_T = C_{T,\phi_0} \cos^{1.28}(\phi_t), \quad (6.3)$$

in which  $C_{T,\phi_0}$  is the turbine's thrust coefficient at  $\phi = 0^\circ$ . This is analogous to how the power coefficient is typically corrected for the yaw angle in wake modeling; see also Eq. (6.5). The exponent 1.28 was determined using LES data from Sengers et al. (2022). The same LES results were used for training to obtain the model coefficients  $\mathbf{B}$ .

Uncertainty is typically included in the form of adding discretized wind direction variability bins to the LUT (Rott et al., 2018; Simley et al., 2020). Rather than for the mean wind direction only, the optimal yaw misalignment is computed for a distribution of wind directions – typically a Gaussian distribution with standard deviation  $\sigma_\delta$  around a mean  $\bar{\delta}$ . This uncertainty parameter  $\sigma_\delta$  is affected by the wind direction variability as well as the accuracy of the measurement devices, although the latter is not considered in the current work. This results in a more conservative controller setting when the uncertainty is high, mitigating erroneous steering but also resulting in a lower achievable power gain. On average, however, this results in a higher gain than if a more aggressive controller setting was used. In the current study, the target yaw angle was therefore determined from the LUT as a function  $\phi_t(\bar{\delta}, \overline{\delta\alpha}, \sigma_\delta)$ . For clarity, however, this notation is omitted in the remainder of the present work. Referring back to Eq. (6.2), this indicates that not only could a change in  $\bar{\delta}$  cause  $|\phi_e|$  to exceed  $7.5^\circ$  but also that a change in  $\overline{\delta\alpha}$  or  $\sigma_\delta$  could initiate a yaw maneuver.

Figure 6.1 illustrates the  $\phi_t$  suggested by the LUT as a function of  $\bar{\delta}$ . Figure 6.1a shows that with increasing uncertainty (higher  $\sigma_\delta$ ), the controller setting becomes more conservative: for  $\sigma_\delta = 2^\circ$ , the maximum  $\phi_t$  is  $22^\circ$ , whereas, when  $\sigma_\delta = 10^\circ$ , the controller settings have a maximum of  $\phi_t$  of  $8^\circ$ , corresponding to the logic discussed before. Figure 6.1b illustrates that the aggressiveness of the controller setting does not really depend on  $\overline{\delta\alpha}$ , but the controller switches from positive to negative  $\phi_t$  at a different  $\bar{\delta}$ . Wind veer inherently deflects the wake due to a crosswise force pointing toward the right above hub height and to the left below hub height (when looking downstream). Since the wind speed is higher above hub height, the rotor equivalent wake deficit is deflected to the right. With increasing veer, this effect becomes stronger and the wind direction under which a full wake situation occurs (typically the crossover point in the LUT) moves to the left (a more negative  $\bar{\delta}$ ).

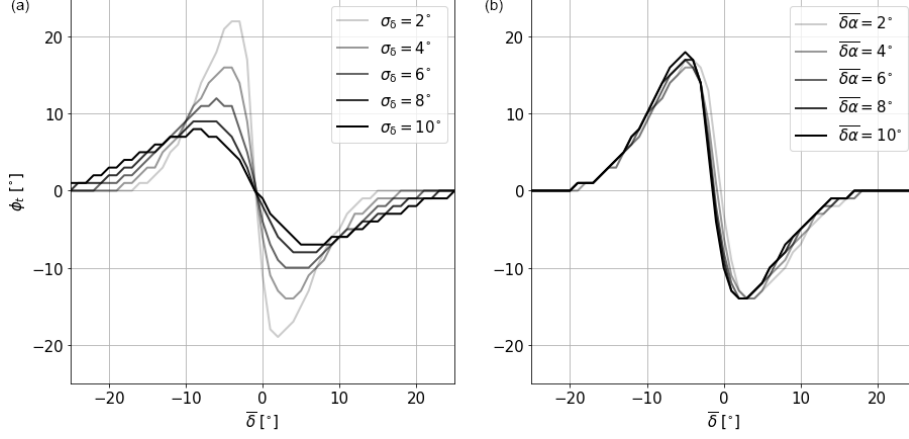


Figure 6.1: Target yaw misalignment  $\phi_t$  as a function of the 60 s averaged wind direction  $\bar{\delta}$  for a changing wind direction standard deviation of  $\sigma_\delta$  with a wind veer  $\bar{\delta\alpha} = 4^\circ$  (a) and for a changing  $\bar{\delta\alpha}$  with  $\sigma_\delta = 4^\circ$  (b). A turbine spacing of 6D is assumed and  $\bar{\delta} = 0^\circ$  indicates the wind direction where the turbine pair is aligned.

## 6.3 Simulation environment

### 6.3.1 Engineering model

A simple engineering model is developed to estimate the power gain and optimal preview time for a given time series of the wind direction. Assuming a constant wind speed, it computes the power yield of a turbine pair as a function of the wind direction only.

The instantaneous power is computed with

$$P = 0.5\rho C_P \pi R^2 U_{\text{eq}}^3, \quad (6.4)$$

in which  $\rho$  is the air density,  $R$  is the turbine radius and  $U_{\text{eq}}$  is the rotor equivalent wind speed.  $C_P$  is the turbine's power coefficient corrected for the yaw misalignment  $\phi$ :

$$C_P = C_{P,\phi_0} \cos^{1.89}(\phi), \quad (6.5)$$

which is analogous to Eq. (6.3). The exponent 1.89 (referred to as  $P_p$  in the literature; e.g., Howland et al. (2020)) is again based on LES data from Sengers et al. (2022). A low-pass filter is applied to the wind direction time series using a cutoff frequency of 0.0037 Hz, as proposed in Simley et al. (2020). For each point in the low-pass-filtered wind direction time series  $\delta_{\text{lp}}(t)$ , the power generated by the upstream turbine can be estimated as described in the following:

1. Calculate the yaw misalignment  $\phi_{\text{up}}$  from the current turbine orientation  $\gamma$  and the low-pass-filtered wind direction at time  $t$ :  $\phi_{\text{up}} = \gamma_{\text{up}} - \delta_{\text{lp}}(t)$ .
2. Calculate  $C_{P,\text{up}}$  according to Eq. (6.5) using  $\phi_{\text{up}}$ .
3. Calculate  $P_{\text{up}}$  using Eq. (6.4) with  $C_{P,\text{up}}$  and a constant  $U_{\text{eq,up}}$ .

To estimate the power of the downstream turbine, a wake model needs to be employed. In this study, again, DART with  $\phi$ ,  $\bar{\delta\alpha}$  and  $C_T$  as input variables is used to make these estimations. A constant veer of  $\bar{\delta\alpha}$  (see Sect. 6.3.2.1) is assumed.

4. Calculate  $\phi_{\text{dn}} = \gamma_{\text{dn}} - \delta_{\text{lp}}(t - \Delta T)$ . Here,  $\delta_{\text{lp}}(t)$  is time-shifted by  $\Delta T = x/U_{\text{h}}$ , where  $x$  is the turbine spacing and  $U_{\text{h}}$  is the wind speed at hub height.
5. Calculate  $C_{\text{T,up}}$  of the upstream turbine with Eq. (6.3) using  $\phi_{\text{up}}$ .
6. Model wake characteristics with DART, using  $(\phi_{\text{up}}, \bar{\delta\alpha}$  and  $C_{\text{T,up}})$  as input parameters.
7. Move the wake position by  $\Delta y = \sin(\delta_{\text{lp}}(t - \Delta T)) \cdot x$ , in which  $\delta_{\text{lp}}(t - \Delta T)$  is the time-shifted low-pass-filtered wind direction and  $x$  is the turbine spacing.
8. Calculate  $U_{\text{eq,dn}}$  of the downstream turbine from the modeled wake characteristics.
9. Estimate  $C_{\text{P},\phi_0}$  from the turbine power curve and subsequently calculate  $C_{\text{P,dn}}$  with Eq. (6.5) using  $\phi_{\text{dn}}$ .
10. Calculate  $P_{\text{dn}}$  using Eq. (6.4) with  $C_{\text{P,dn}}$  and  $U_{\text{eq,dn}}$ .
11. Calculate the total power as the sum of  $P_{\text{up}}$  and  $P_{\text{dn}}$ .

Besides the power calculation, the yaw controller described in Sect. 6.2 is implemented in the engineering model. It utilizes the original wind direction signal  $\delta(t)$ , not the low-pass-filtered signal, to compute the 60s moving average  $\bar{\delta}$  and the corresponding standard deviation  $\sigma_{\delta}$  of the wind direction. It uses this information and the wind veer to decide upon the next target yaw misalignment angle  $\phi_{\text{t}}$  from the LUT (upstream turbine only) and whether a yaw maneuver should be initiated. Preview wind direction signals are considered in the engineering model by simply shifting the wind direction time series provided to the controller forward in time, resembling a perfect forecast. Preview times (temporal shifts) of between 10 and 300 s in 10 s increments are tested, resulting in an estimated power gain over SC as a function of preview time. Smooth wind direction time series with a constant change rate can be fed to the model, but a turbulent signal is added to get more reasonable results. To get realistic turbulent signals, data are extracted from LES results of a neutral boundary layer (see Sect. 6.3.2.1) without a wind direction change. Using a systematic sampling technique with equidistant points, 50 samples are taken from a domain with a size of approximately 5 km by 2.5 km. These turbulent signals are added to the smooth time series and fed to the engineering model. This allows not only the study of the influence of turbulence on the turbine's behavior but also the quantification of uncertainty by determining a confidence interval around a mean value.

### 6.3.1.1 Example

Figure 6.2a illustrates an example displaying the wind direction signal (gray) and the orientation of the upstream turbine for four different yaw controllers. The smooth wind direction change experienced by the turbine is trailed by yaw actuator movement under traditional greedy SC (black). In its optimization, the engineering model tests for the preview time at which the highest power gain can be achieved; the corresponding result is shown in yellow. It is evident that the turbine yaws to the same new orientation but does so earlier, such that the wind direction reaches the orientation of the preview-controlled turbine right in between two consecutive

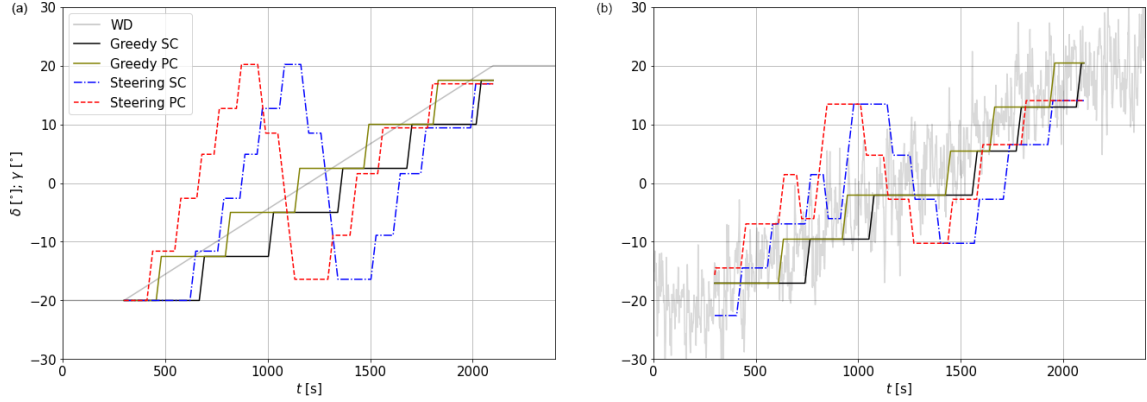


Figure 6.2: Examples of the engineering model’s results for a wind direction change rate of  $\theta = 80^\circ \text{ h}^{-1}$ . Gray lines indicate the wind direction of an (a) smooth and (b) turbulent time series. Black and yellow indicate greedy SC and PC; blue and red indicate wake steering SC and PC, respectively. A turbine spacing of  $6D$  is assumed, and  $\bar{\delta} = 0^\circ$  indicates the wind direction in which the turbine pair is aligned.

actuator movements. This intuitively makes sense, as the optimum solution aims to limit misalignment. When adding turbulence (Fig. 6.2b), this is still true, although it is not as clearly visible. When applying the wake steering control (blue (SC) and red (PC) in Fig. 6.2a), a clear misalignment of the turbine with the wind direction can be observed. The misalignment increases as the wind direction approaches  $0^\circ$  until it crosses over from a positive to a negative misalignment. When turbulence is introduced (Fig. 6.2b), the controllers become more conservative (smaller intentional misalignments), which is a direct consequence of the included uncertainty parameter, as discussed in Sect. 6.2.2.

### 6.3.2 Large-eddy simulations

This study uses revision 3475 of the PArallelized Large-eddy simulation Model (PALM, Maronga et al. (2020)). PALM uses a non-hydrostatic incompressible Boussinesq approximation of the Navier–Stokes equations. The exchange between the surface and the lowest grid cell in the vertical is handled following Monin–Obukhov similarity theory. Time integration is done by a third-order Runge–Kutta scheme, advection of momentum is performed by a fifth-order Wicker–Skamarock scheme, and subgrid-scale turbulence is modeled by applying Deardorff’s 1.5-order turbulence closure parameterization. The Coriolis parameter is computed for a latitude of  $55^\circ \text{ N}$ . The grid has a regular spacing of  $\Delta = 5 \text{ m}$  on a right-handed Cartesian coordinate system, but to save computational costs, the vertical grid size increases by 8% per cell above the boundary layer height.

The simulation chain consists of three simulations: first, a precursor simulation to generate realistic inflow conditions; second, a simulation in which the wind direction in the domain is changed; and third, a main simulation that contains two turbines.

#### 6.3.2.1 Precursor simulation

In the precursor simulation, a realistic turbulent flow is generated by adding random perturbations to an initially laminar flow. The chaotic behavior of the modeled boundary layer generates turbulent structures at a range of scales until a stationary

state is reached after several hours of simulation time. This study only considers one atmospheric condition, a conventionally neutral boundary layer with a hub height (90 m) wind speed of  $8.3 \text{ m s}^{-1}$ . The hub height turbulence intensity in this boundary layer is 10.3 %, while the power law wind shear exponent and vertical wind veer between lower and upper tip height are  $0.17$  and  $2.0^\circ$ , respectively. Although the effect of atmospheric conditions (wind speed, stability) on the effectiveness of preview control is deemed interesting, investigating this was considered out of the scope of the current study. A short discussion is included in Sect. 6.5.2.

### 6.3.2.2 Simulation of wind direction changes

In this study, the wind direction is changed by applying the methodology developed by Stieren et al. (2021), in which the momentum equations are modified by adding an artificial Coriolis force  $F_\theta$ :

$$F_\theta = -\theta(t)u_j\epsilon_{ij3} , \quad (6.6)$$

in which  $\theta(t)$  is the forced wind direction change rate,  $u_j$  are the wind speed components, and  $\epsilon$  is the Levi–Civita symbol. This is an engineering approach in which the centrifugal and Euler force are neglected. Although not physical, Stieren et al. (2021) demonstrated that the observed wind direction compares well with the forced signal. This methodology allows for changing the wind direction at a constant rate ( $\theta(t) = \theta_0$ ) as well as more realistic wind direction changes as observed in the field.

The code employed in Stieren et al. (2021) used a concurrent precursor inflow method with a fringe region, ensuring undisturbed inflow in the cyclic boundary conditions that are required for the implementation of this method to change the wind direction. PALM does not have this feature implemented, so, for this reason, an intermediate simulation is carried out. An empty domain (no turbines) with cyclic horizontal boundary conditions is initialized with the turbulent flow generated by the precursor simulation. A predetermined  $\theta(t)$  forces the wind direction to change in the whole model domain simultaneously, and a slice in the  $yz$  plane (crosswise and vertical dimensions) is saved to use as the inflow in the main run. This information comprises the three wind speed components as well as the potential temperature and the subgrid-scale kinetic energy.

### 6.3.2.3 Main simulation

In the main simulation, two NREL 5 MW turbines are simulated using an actuator disk model with rotation (ADMR) similar to Wu and Porté-Agel (2011) as described in Dörenkämper et al. (2015). The turbine pair has a spacing of 6 D and is aligned for a wind direction of  $\delta = 270^\circ$ . In a domain with non-cyclic boundary conditions in the streamwise direction, the  $yz$  plane saved from the simulation discussed in the previous section is used as the inflow 25 D upstream of the first turbine. As a result, a transient wind direction change propagates through the domain with a time-varying wind speed (fluctuations around the mean) and direction (fluctuations around the mean on top of the forced signal) rather than collectively in the whole domain, as was the case in Stieren et al. (2021). This is important for this study, as an incoming wind direction change needs to be detected before it reaches the turbines in order for PC to be beneficial. Additionally, a time delay between the

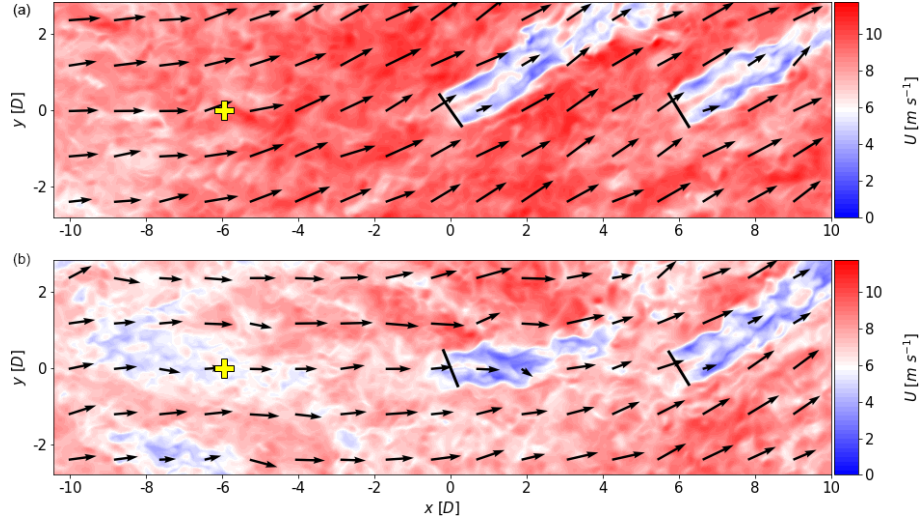


Figure 6.3: Examples of wind fields illustrating a wind direction change propagating through the domain. Wind field (b) is taken 140s after wind field (a). The background color indicates the wind speed and the arrows indicate the wind direction. The solid black lines indicate the turbines, both of which are operating in greedy control without preview information. The yellow markers indicate the location of the virtual met mast.

upstream turbine and the downstream turbine experiencing a wind direction change is likely more realistic. Figure 6.3 displays examples of the flow field with the two turbines that illustrate a wind direction change propagating through the domain. Besides the wind direction change, large turbulent structures with different wind speeds can be observed. Additionally, the misalignment of the upstream turbine indicates the controller lag.

Since the boundary conditions in the streamwise direction are non-cyclic, the introduced wind direction change results in a gradient of the horizontal wind speed components in the streamwise direction ( $\partial\bar{u}/\partial x$ ). This needs to be compensated for in either the crosswise or vertical direction to obey the conservation of mass. Because of the cyclic boundary conditions in the crosswise direction, this gradient cannot be compensated for with  $\partial\bar{v}/\partial y$ . Therefore, the gradient  $\partial\bar{u}/\partial x$  is compensated for by  $\partial\bar{w}/\partial z$ , introducing a vertical velocity that alters the wind speed and direction profiles over time. Since all experiments with different controllers experienced the same effect, it is not considered detrimental to the outcome of this study.

*Standard control.* The input for SC consists of information at the position of two grid cells (10 m) upstream of the turbine. A point in front of the turbine was chosen to mimic a nacelle wind vane that is not disturbed by the rotor. This allows for a fairer comparison of the model results, as the preview control wind vane (see below) is not disturbed by any rotor.

*Preview control.* PC is implemented in the form of a virtual wind vane at hub height on a meteorological (met) mast. The virtual met mast is located at a fixed position upstream of the first turbine for  $\delta = 0^\circ$ , the wind direction in which the turbine pair are aligned. In Sect. 6.4.1, the optimum preview time is estimated with the engineering model before being converted to a preview distance considering a hub height wind speed of  $8.3 \text{ m s}^{-1}$ . The position of the vertical met mast is indicated in



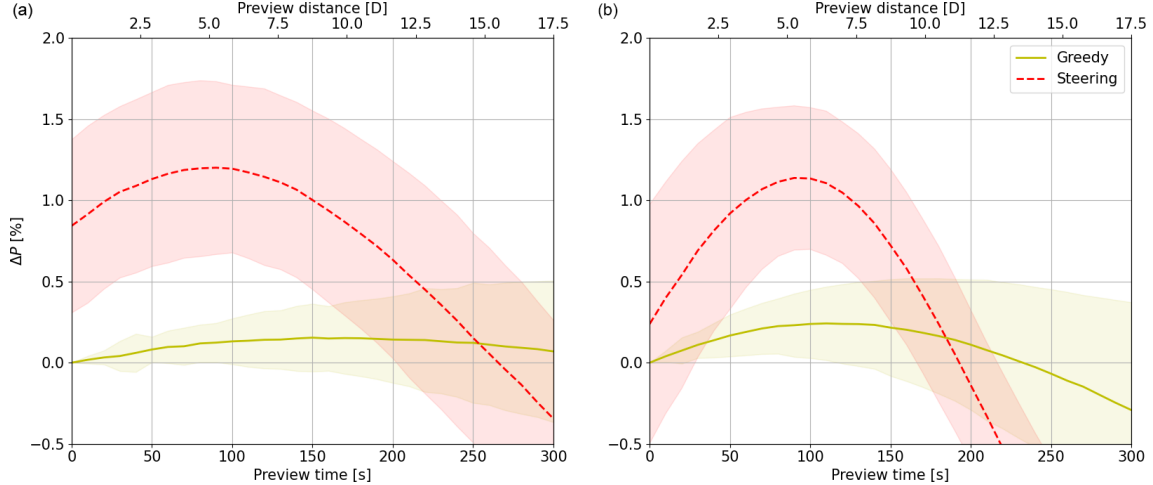


Figure 6.4: Turbine pair power gain  $\Delta P$  of greedy control (yellow) and wake steering control (red) with PC relative to greedy SC as a function of preview time for wind direction change rates of  $\theta = 80^\circ \text{ h}^{-1}$  (a) and  $\theta = 160^\circ \text{ h}^{-1}$  (b). Lines indicate the mean and shaded areas indicate the 95% confidence interval over 50 turbulent time series.

yellow in Fig. 6.3. Although the relative position of a measurement point upstream of the rotor changes with wind direction, a fixed position of the virtual vane is deemed sufficient, as wake steering is limited to  $|\bar{\delta}| < 20^\circ$  (Sect. 6.2.2). The wind direction signal is directly passed to the controller assuming Taylor’s hypothesis of frozen turbulence, meaning that no wind evolution is considered, although it is deemed important, as pointed out in Laks et al. (2010). As the signal is subject to advection and heterogeneity, this method does not resemble a perfect forecast.

## 6.4 Results

### 6.4.1 Engineering model

#### 6.4.1.1 Theoretical linear wind direction changes

In this section, a wind direction change of  $40^\circ$  is simulated with different change rates  $\theta$  using the engineering model. Starting from a constant  $\delta = -20^\circ$  for the first 300 s (spin-up, not used for analysis), the direction changes linearly to  $\delta = +20^\circ$ , where it remains for the last 300 s (spin-down, not used for analysis). As described in Sect. 6.3.1, 50 different seeds of turbulent noise are added on top of this linear wind direction change to statistically analyze the impact of turbulence. Values for the wind speed ( $U_h = 8.30 \text{ m s}^{-1}$ ), wind shear and veer over the rotor area ( $\alpha = 0.17$ ,  $\delta\alpha = 2^\circ$ ) and, consequently, the rotor equivalent wind speed ( $U_{\text{eq,up}} = 8.25 \text{ m s}^{-1}$ ) are taken from LES (Sect. 6.3.2.1).

Figure 6.4 displays the turbine pair power gain of PC relative to SC as a function of preview time for two wind direction change rates:  $\theta = 80^\circ \text{ h}^{-1}$  (Fig. 6.4a) and  $\theta = 160^\circ \text{ h}^{-1}$  (Fig. 6.4b). First focusing on greedy control, the maximum power gain from PC is higher for a larger  $\theta$ , whereas the optimal preview time is smaller. With a faster wind direction change, the misalignment of the SC turbine is larger, resulting in higher power losses. As a result, the benefit of PC is greater. When the turbine yaws too early it also loses power, explaining the decreasing gains for longer

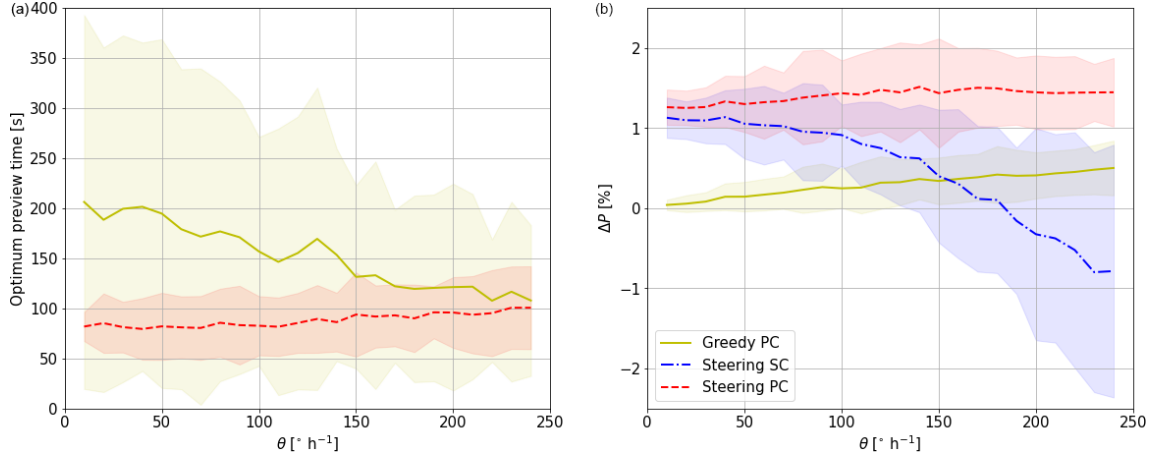


Figure 6.5: Optimal preview time **(a)** and corresponding power gain relative to greedy SC **(b)** as a function of  $\theta$ . Yellow indicates greedy PC, blue indicates wake steering SC, and red indicates wake steering PC. Lines indicate the mean and shaded areas indicate the 95 % confidence interval over 50 turbulent time series.

preview times and the shorter optimal preview time for a larger  $\theta$ . Although an optimum is found, PC seems relatively insensitive to the preview time, as indicated by a relatively flat curve. Lastly, the uncertainty increases with larger preview times, as illustrated by the 95 % confidence interval.

Now, focusing on the wake steering controller, it can be seen that wake steering with SC (preview time = 0s) is estimated to achieve a power gain of 0.8 % (for  $\theta = 8^\circ \text{h}^{-1}$ ), whereas PC with optimum preview time results in a power gain of 1.2 %. This difference exceeds the power gain achieved by PC in the greedy control of 0.2 %, which suggests that wake steering can benefit more from PC than greedy control. This is strengthened by the findings from the  $\theta = 160^\circ \text{h}^{-1}$  case, where wake steering with SC only achieves a power gain of 0.25 %, with the 95 % confidence interval also displaying power losses. PC with the optimum preview time gives a power gain of 1.3 %, again far exceeding the 0.3 % gain expected from greedy control. Figure 6.5 represents the optimal preview time and corresponding power gain as a function of  $\theta$ . Focusing first on the optimal preview time for greedy control in Fig. 6.5a, the mean over the turbulent simulations indicates decreasing optimal preview times for increasing  $\theta$ , corresponding to the findings in Fig. 6.4. The uncertainty decreases with increasing  $\theta$ , as dynamic changes become more dominant, preventing the yaw controller from chasing turbulence. As for wake steering, the optimal preview time seems to be relatively insensitive to  $\theta$ , showing an almost constant value between 80 and 100s. This value likely depends on the updating frequency of the yaw controller, but it is an interesting finding that would make the implementation of PC in the field easier.

The maximum achievable power gain with an optimal preview time (Fig. 6.5b) appears to increase linearly with  $\theta$  for greedy control. The mean ranges from 0.1 % for slow wind direction changes to almost 0.8 % for extreme events, while the uncertainty slightly increases with  $\theta$ . This is similar to PC in wake steering, which shows power gains ranging from 1.3 % to 1.7 %. Steering SC shows power gains very similar to PC for small  $\theta$ , but for larger  $\theta$  the gains rapidly decrease and turn into losses (erroneous steering). Especially under these fast-changing conditions, wake

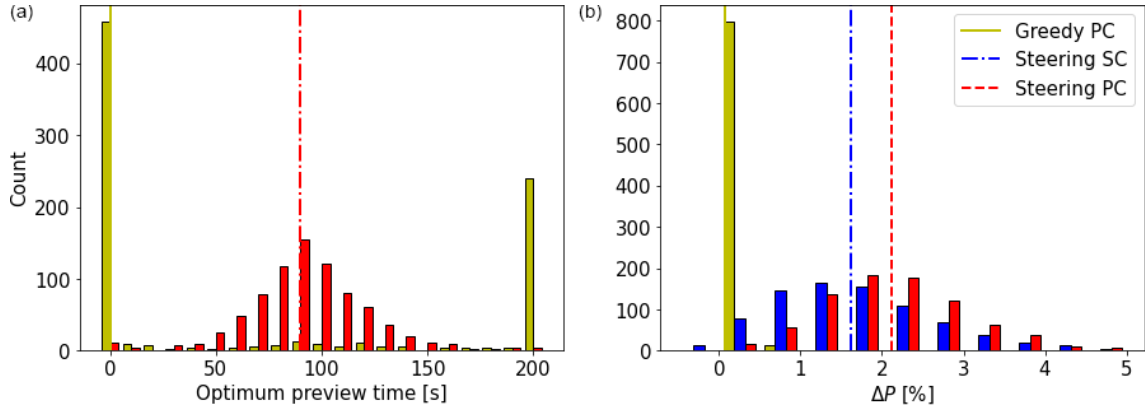


Figure 6.6: Histogram of optimum preview time (a) and corresponding power gain (b) when using wind direction measurements from a met mast. Lines indicate the median optimum preview time (a) and corresponding mean power gain (b). Colors correspond to those used in Fig. 6.5.

steering can benefit the most from PC, as it provides consistent power gains.

#### 6.4.1.2 Wind direction time series from met mast measurements

In addition to the linear wind direction changes considered in the previous section, more realistic wind direction changes are studied here using the engineering model. Wind vane and anemometer measurements at hub height (116 m) from an experimental campaign are used. This campaign was carried out between February and April 2021 at a slightly hilly onshore site in northeastern Germany located approximately 13.5 km from the Baltic Sea. For more details, the reader is referred to Sengers et al. (2023b). The data are split into 1 h subsets, where again the first and last 300 s are disregarded as spin-up and spin-down times. Because this study limits its analysis to wind speeds around  $8 \text{ m s}^{-1}$ , only subsets with an average wind speed between  $6$  and  $10 \text{ m s}^{-1}$  are considered, resulting in a total of 815 subsets. Other atmospheric characteristics (e.g., turbulence intensity, shear, stability) are not considered. For each subset, the average wind direction is assumed to coincide with the alignment of the turbine pair. The turbines are initialized with an orientation corresponding to the low-pass-filtered signal at the start of the hour. As preview times larger than 200 s do not seem to be relevant according to Fig. 6.5, the maximum preview time considered here is 200 s. Figure 6.6 displays the findings of this analysis in two histograms. The optimum preview time (Fig. 6.6a) for greedy control shows that the extreme values of 0 and 200 s often occur. These represent cases in which there was hardly any wind direction change within the hour. In these cases, either no yawing takes place and PC and SC estimate the same power, displayed here as a preview time of 0 s, or one yaw maneuver takes place, which is most beneficial when done as early as possible. Excluding these events, the results show a very flat distribution of optimal preview times. For wake steering, on the other hand, an approximately normal distribution with a median of 90 s is found, corresponding well to the results of Fig. 6.5.

The maximum power gain, displayed in (Fig. 6.6b), indicates that PC under greedy operation is not very beneficial. With a mean gain of 0.06 %, much lower power gains are expected from realistic wind direction data than from previous tests with a linear wind direction change. Wake steering with SC shows an approximately

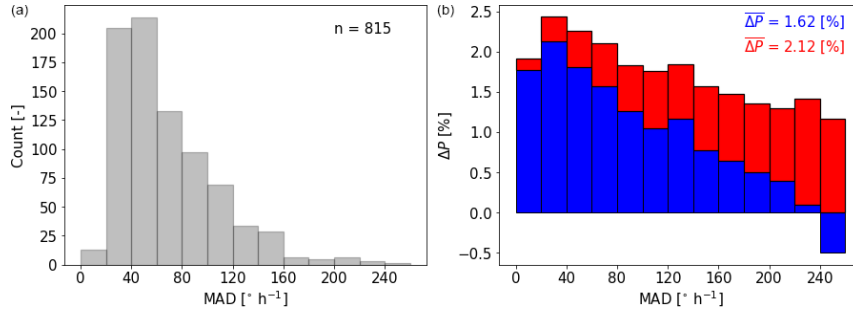


Figure 6.7: (a) Histogram of met mast data binned in mean of absolute differences (MAD). (b) Power gain of steering SC relative to greedy SC (blue) and power gain of steering PC relative to greedy SC (red). Power gains averaged over all 815 cases are noted in the top right corner.

normal distribution of power gains with a mean of 1.62%, whereas PC increases this to 2.12%, again suggesting that PC is especially beneficial when applying wake steering.

To investigate under what conditions steering SC and PC are most beneficial, the power gains are studied as a function of the characteristics of the wind direction signal. For this, the mean of absolute differences (MAD) is calculated as

$$\text{MAD} = \frac{1}{T} \sum_{t=2}^T |\delta_{lp,t} - \delta_{lp,t-1}|, \quad (6.7)$$

which computes the mean of the absolute differences in wind directions of consecutive time steps. Here,  $\delta_{lp}$  is again the low-pass-filtered time series obtained using a cutoff frequency of 0.0037 Hz. Because the signal is already low-pass filtered, MAD does not relate to the small-scale turbulence, but rather to larger-scale wind direction fluctuations. The unit of MAD  $^{\circ}\text{s}^{-1}$ , which, for interpretability, is converted to  $^{\circ}\text{s}^{-1}$ . The histogram in Fig. 6.7a displays that the majority of the cases represent steady conditions with only a wind direction change. However, several cases with large dynamic changes are observed. Figure 6.7b shows in blue the average power gain of steering SC compared to greedy SC as a function of MAD. The largest gains are found for small wind direction changes, as this approaches a steady state for which the controller was developed. However, power losses are found for large values of MAD. Despite their rare occurrence, these cases undermine confidence in the wake steering strategy. It is especially under these conditions that PC has a large added benefit. Steering PC shows a more consistent power gain relative to greedy SC (red) regardless of the characteristics of the wind direction time series; hence, a power gain using wake steering seems guaranteed. The difference between the blue and red bars illustrates that when the signal is relatively steady, PC only has a small benefit. However, the more the signal fluctuates (increasing MAD), the larger the benefit of PC, as the yaw controller is now able to anticipate incoming wind direction changes.

#### 6.4.2 Large-eddy simulations

In this section, LES results are used to validate the findings of the previous section and, with that, demonstrate the benefit of preview control. For this purpose, wind direction time series observed in the field are reproduced in LES. First, two examples

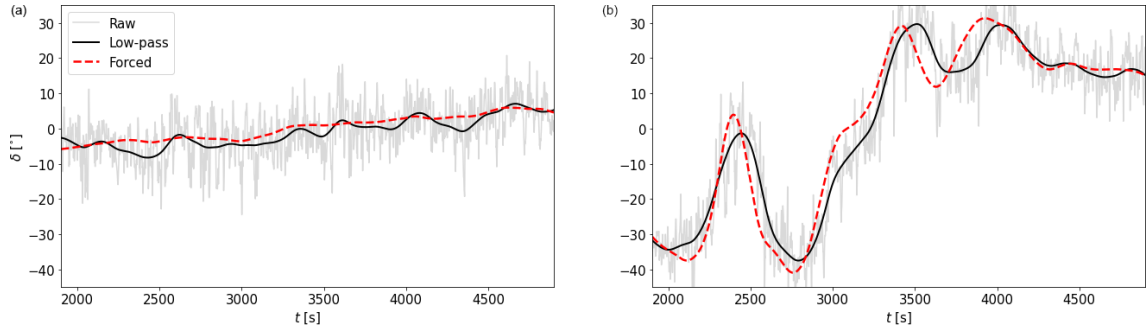


Figure 6.8: Simulated wind direction cases. Raw (gray) and low-pass-filtered (black) signals at the upstream turbine are shown, as well as the forced (dashed red) signal. **(a)** Case 1: a slowly varying wind direction change. **(b)** Case 2: a fast-varying wind direction change.

are simulated (Sects. 6.4.2.1 and 6.4.2.2), one with a low and one with a high large-scale wind direction variability. Second, to approach statistical significance, multiple cases with similar characteristics are simulated. As LES is too expensive to use to obtain fully statistically significant results, only six seeds are performed, following the standard used in fatigue load estimation studies. To investigate the sensitivity of the preview controller performance, changes in both low-frequency (Sect. 6.4.2.3) and high-frequency fluctuations (Sect. 6.4.2.4) are considered to better understand the performance of the preview controller.

#### 6.4.2.1 Case selection

Figure 6.8 illustrates the two simulated examples, in which the obtained wind direction signal at the upstream turbine is indicated in gray (raw) and black (low-pass filtered) and the forced signal (Sect. 6.3.2.2) in red. This forced signal is the low-pass-filtered wind direction measured at the met mast using the same cutoff frequency of 0.0037 Hz. It should be noted that besides the mean wind speed, no other meteorological conditions (e.g., shear, veer, stability) are evaluated on how well they match the simulated boundary layer characteristics.

Comparing the signals reveals that the main characteristics of the forced signal are reproduced. Differences are due to advection, as the wind direction signal is forced at the domain inflow boundary 25D upstream of the turbine. Case 1 (Fig. 6.8a) represents a scenario in which wake steering with standard control is expected to obtain a large power gain. This case is considered to demonstrate that preview control is not detrimental to the power gain achieved with wake steering SC. Case 2 (Fig. 6.8b) illustrates an event in which wake steering with standard control is expected to see a power loss due to rapidly changing conditions, a scenario in which wake steering is expected to benefit greatly from preview control. A third case, which is of interest but may be less common, is provided in Appendix A. It represents a situation with strong fluctuations around  $\delta = 0^\circ$ .

The first 600 s of the simulation are used to move from  $\delta = 0^\circ$  to the initial  $\delta$ , the start of the low-pass-filtered time series. At 600 s, both turbines are turned on and are given an additional 600 s to spin up while the mean wind direction remains constant. Corresponding to Sect. 6.4.1, the first 300 s of the field time series are omitted. After 1500 s, the wind direction signal used for analysis enters the domain, but it takes 400 s for this information to flow from the inflow boundary to the upstream turbine.

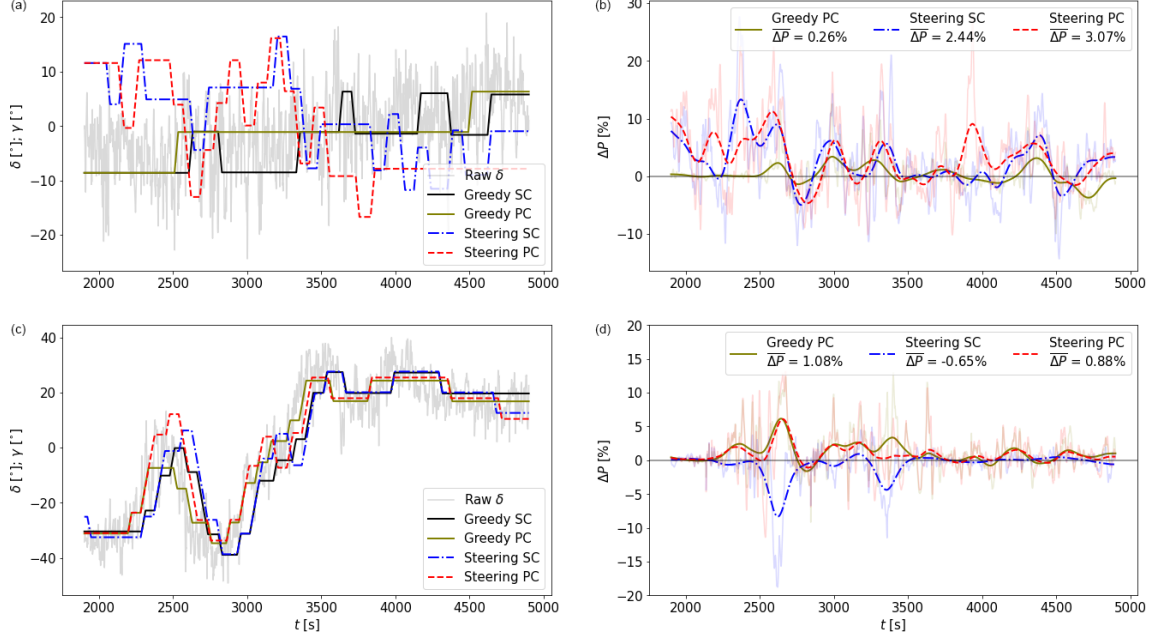


Figure 6.9: LES results for Case 1 (a–b) and Case 2 (c–d). The left column shows the wind direction  $\delta$  (gray, see Fig. 6.8) and orientations of the upstream turbine  $\gamma$  (colors). The right column shows the raw (transparent) and low-pass-filtered (opaque) power gain  $\Delta P$  relative to greedy SC. The gain averaged over the simulation  $\overline{\Delta P}$  is indicated in the legend.

Altogether, the first 1900 s of the simulation are omitted, whereas the following 3000 s are used for analysis. Corresponding to the findings in Sect. 6.4.1.2, the preview time was chosen as 90 s, equivalent to a preview distance of 750 m or 6 D for an average hub height wind speed of  $8.3 \text{ m s}^{-1}$ .

#### 6.4.2.2 Performance of the controllers for selected cases

Figure 6.9 shows the wind direction ( $\delta$ ) and yaw angle ( $\phi$ ) of the upstream turbine (left column) and the corresponding power gain relative to greedy SC (right column). Since the raw power gain signal (transparent) is rather noisy, the low-pass-filtered (also using a cutoff frequency of 0.0037 Hz) signal is also included and is shown by opaque lines. In Case 1 (Fig. 6.9a–b), the turbine orientation of greedy SC illustrates that small-scale turbulence has a large influence on the controller actions, as is evident from the maneuvers in the direction opposing the large-scale wind direction change (e.g., at 2800 s). Enabling PC eliminates this behavior, although this is likely a coincidence rather than an effect of PC. A textbook-like situation can be seen at around 2500 s, where the PC turbine yaws earlier than the SC turbine, resulting in a small power gain due to a better orientation. This is directly followed by a power loss, as the wake reaching the downstream turbine is slightly stronger. Averaged over the whole simulation, greedy PC achieves a small power gain of  $\overline{\Delta P} = 0.26\%$ . Wake steering results in more yaw maneuvers than greedy control. For the first half of the simulation, the misalignment is characterized by positive angles, whereas the second half is characterized by negative angles. The orientation of the SC and PC turbines deviates from a temporally shifted signal due to the heterogeneity between the two locations from which information is acquired. Wake steering with SC results in  $\overline{\Delta P} = 2.44\%$ , which is increased to  $\overline{\Delta P} = 3.07\%$  when

PC is enabled. This suggests that PC is not detrimental to the power gain achieved with steering SC and can increase this gain even further.

In Case 2 (Fig. 6.9c–d), wake steering with SC results in a power loss of  $\overline{\Delta P} = -0.65\%$ . This is mainly due to two events that produce a significant power loss for several minutes. Both events are characterized by the upstream turbine yawing to a certain orientation exactly when the wind direction quickly rotates in the other direction, resulting in a large misalignment and a corresponding power loss. Enabling PC converts this power loss into a gain of  $\overline{\Delta P} = 0.88\%$ , mainly achieved by eliminating these events. This suggests that PC could be used to avoid erroneous steering. It is noteworthy that in this case, greedy PC actually achieves the largest power gain ( $\overline{\Delta P} = 1.08\%$ ). This is partially due to the wind direction being only in the region where wake steering is deemed useful ( $|\delta| < 20^\circ$ ) during a small part of the simulation.

#### 6.4.2.3 Variation of low-frequency fluctuations

As mentioned before, an analysis with six seeds is performed to approach statistical significance. In this section, the variation of low-frequency fluctuations is considered. Besides Case 1 from the previous section, five more cases are randomly selected from all met mast data with a low variability ( $\text{MAD} < 40^\circ \text{h}^{-1}$ , Fig. 6.7). Figure 6.10a displays these results; the six seeds are displayed (Seed 1 indicates Case 1), as are their means on the far right. The benefit of PC in greedy operation is negligible, as the power gains of the upstream turbine due to a better alignment do not outweigh the power losses observed for the downstream turbine due to a stronger wake. It is, however, expected that greedy PC outperforms greedy SC in scenarios where the downstream turbine is not heavily waked. Steering SC achieves a power gain of  $1.24\%$  on average, which is increased to  $1.85\%$  when PC is enabled. The differences between the seeds are substantial, which can be directly linked to the characteristics of the wind direction signal. For instance, in Seeds 1 and 6, a partial wake situation occurs for a substantial part of the simulation. However, the other simulations display a full wake situation for almost the whole simulation, resulting in lower power gains. The effectiveness of PC can also be directly linked to the nature of the wind direction signal, as a very steady, non-changing wind direction will not benefit from PC. Lastly, these results are subject to small-scale turbulence, as pointed out in Sect. 6.4.1, as well as the controller design. It is therefore deemed important to look at the statistics (here, the mean), rather than the individual seeds.

Due to a lower occurrence of cases with a very high variability corresponding to Case 2, five randomly drawn cases with a  $\text{MAD} > 140^\circ \text{h}^{-1}$  make up the remaining seeds. Note that the variability between these seeds is larger than between the six low-variability seeds discussed in Fig. 6.10a. It can be seen that Case 2, indicated as Seed 1 in Fig. 6.10b, was actually the only time series that resulted in a power loss for steering SC. On average, the power gain achieved with steering SC is still relatively small ( $\overline{\Delta P} = 0.44\%$ ). PC is able to increase this gain to  $1.32\%$ , which is a larger benefit than observed for the low-variability seeds. Also, greedy control benefits more from PC in cases with a high variability. Large differences between the seeds can be observed, the most striking being the slight power loss observed for steering PC relative to steering SC in Seed 6. Like before, this is attributed to the chaotic nature of the simulations and is expected to be subject to small-scale



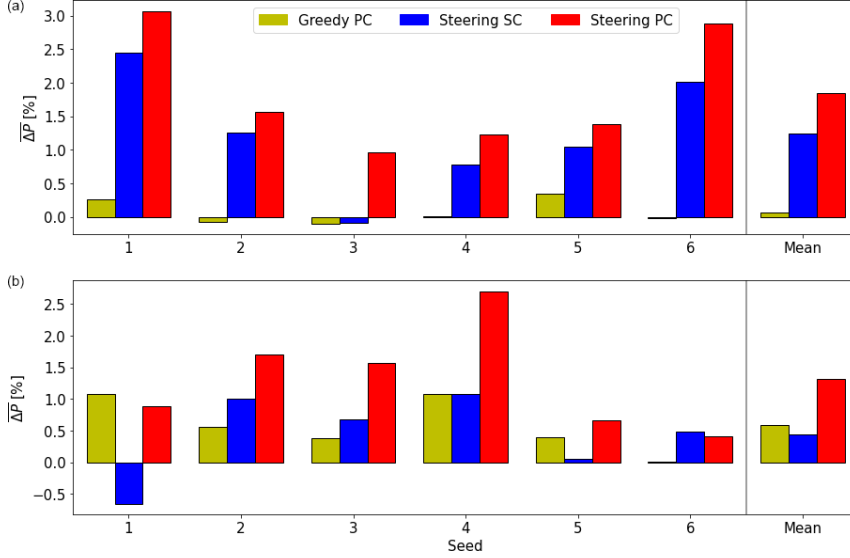


Figure 6.10: Seed analysis of low-frequency fluctuations. Averaged power gains  $\overline{\Delta P}$  of six seeds for slowly varying  $\text{MAD} < 40^\circ \text{h}^{-1}$  (a) and fast-varying  $\text{MAD} > 140^\circ \text{h}^{-1}$  (b) wind direction changes. The average of all seeds is indicated on the far right.

turbulence and controller design. Nevertheless, these results are believed to make a convincing case for the use of preview wind direction information, especially in wake steering operation.

#### 6.4.2.4 Variation of high-frequency fluctuations

As already illustrated in Sect. 6.4.1, high-frequency turbulence has a significant effect on the power yield and therefore on the benefit of PC. In addition to the seed analysis performed in Sect. 6.4.2.3 by varying the low-frequency characteristics of the wind direction signal, a similar analysis is performed by varying the high-frequency characteristics. Focusing again on Cases 1 and 2, the simulations are forced by the same low-frequency signal, but both turbines are shifted laterally in the domain in increments of  $2.5D$  to induce a different high-frequency wind direction component. Figure 6.11a displays that for Case 1, greedy PC results in a small power gain in four out of six seeds but losses in the remaining two, resulting in a very small gain when averaged over all seeds. Steering SC shows  $\overline{\Delta P} > 2\%$  for all seeds, averaging a gain of 2.74%. With PC enabled, this increases to 3.26%, with a substantial spread between the seeds. For instance, PC's benefit in Seed 4 is negligible, but PC adds almost a full percentage point of power gain in Seed 6.

Figure 6.11b shows the same analysis for Case 2. Steering SC results in a power loss in all seeds, with a mean power loss of  $\overline{\Delta P} = -0.58\%$ . This loss is converted into a gain of 0.93% when PC is enabled, clearly demonstrating that PC is able to prevent erroneous yawing. Greedy PC achieves the highest gain,  $\overline{\Delta P} = 0.94\%$ , corresponding to the results discussed in Sect. 6.4.2.2.

The results from all cases and seeds sketch the clear picture that wake steering benefits substantially from preview control. Since the differences between seeds in Fig. 6.10 are larger than those in Fig. 6.11, it is concluded that the magnitude of this benefit mainly depends on the low-frequency wind direction variability (Sect. 6.4.2.3). The high-frequency variability (turbulence) plays a secondary role,



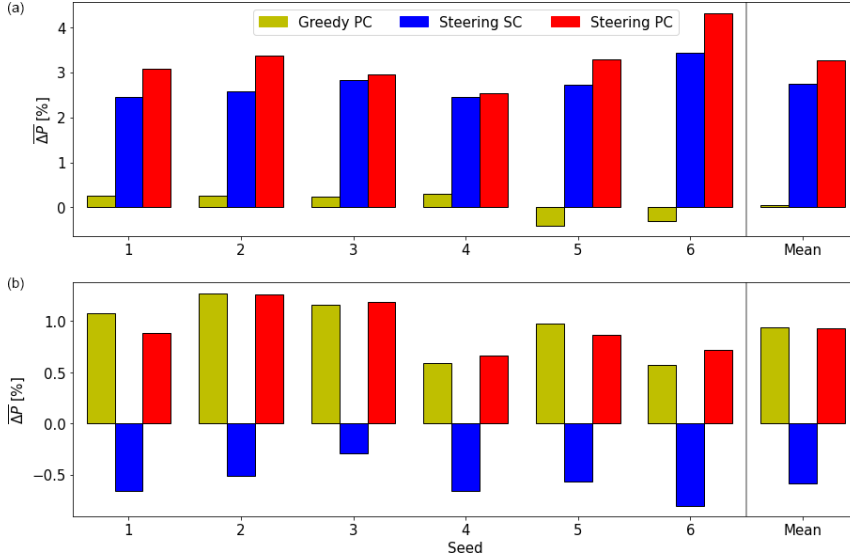


Figure 6.11: Same as Fig. 6.10, but for the seed analysis of high-frequency fluctuations.

as these fluctuations have a smaller effect on the moving average of wind direction used by the yaw controller to decide when to initiate a yaw maneuver.

### 6.4.3 Comparison of large-eddy simulation and engineering model results

In this section, the power gains computed with the engineering model are compared to those obtained with LES. While acknowledging that models are inherently imperfect, the LES results are considered the truth here. The wind direction signal at the turbine of the greedy SC LES run is passed to the engineering model. It should be noted that in LES, the time series of wind directions at the turbine differ slightly between the simulations since the turbines do not exert the same thrust force on the incoming flow due to their different orientations. The analysis is restricted to the 12 low-frequency varying simulations discussed in Sect. 6.4.2.3.

Figure 6.12a shows that the engineering model has a mean absolute error  $\text{MAE} = 0.49\%$  and a correlation coefficient  $R = 0.83$ . The fitted linear relation indicates that large gains are typically overestimated with the engineering model. Splitting the data by control strategy (Fig. 6.12b) reveals that this systematic bias is mainly caused by steering SC. Lastly, splitting the data into low ( $\text{MAD} < 40^\circ$ ) and high ( $\text{MAD} > 140^\circ$ ) variability in Fig. 6.12c illustrates that the engineering model struggles in the low-variability cases. This is likely due to the relatively long period of the full wake situation, which emphasizes any inaccuracies of the wake model.

Considering the assumptions made in the engineering model (e.g., a constant wind speed) and the difference in computational costs ( $\approx 1500$  CPU hours for LES and  $\approx 0.1$  CPU hours for the engineering model), the accuracy of the engineering model is considered acceptable. This gives some credibility to the results discussed in Sect. 6.4.1. The next steps to improve the engineering model could be to include the time-varying wind speed and veer, which are currently assumed to be constant. This would likely result in an increased accuracy at the cost of slowing down the model. Additionally, as the engineering model is subject to the underlying DART

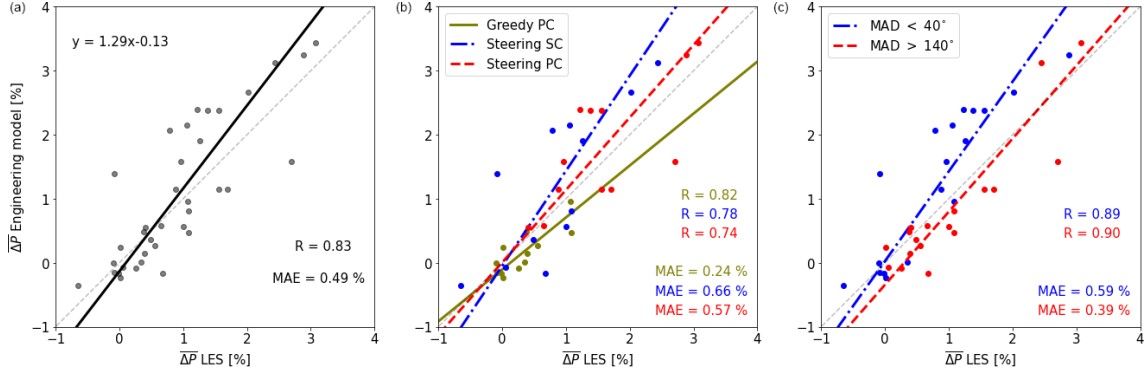


Figure 6.12: Comparison of the engineering model and LES in estimating the power gain  $\overline{\Delta P}$ . The Pearson correlation coefficient ( $R$ ), mean absolute error (MAE) and orthogonal distance regression fit are indicated. (a) All results, (b) the results split by control strategy and (c) the results split by variability of the wind direction signal.

wake model, improvements there will likely also result in a more accurate engineering model.

## 6.5 Discussion

The results presented in this study demonstrate the benefit of preview wind direction control. However, the authors are aware that many assumptions were made to show this proof of concept. These, as well as their implications for future work, are described in this section.

### 6.5.1 Comparison to existing literature

The body of existing literature on the topic of preview wind direction control for wake steering purposes is small. However, some interesting points can be noted when comparing the current results to those in Simley et al. (2021b). Both studies use an engineering model with a similar controller logic and consider wind speed. Interestingly, an identical optimal preview time of 90 s was identified in both works. Using this optimum preview time and assuming perfect preview measurements, Simley et al. (2021b) reported a power gain ranging from 5.8% for wake steering with standard control to 8.9% when preview control was enabled, representing an increase of 55%. Performing a similar exercise, the current study found an increase of 31%: from 1.62% for standard to 2.12% for preview wake steering control. These differences are subject to the different engineering models used, the size of the data set, the turbine spacing, and assumptions about the average wind direction. Regardless, both studies show a significant increase in power gain when using perfect preview information.

Lastly, Simley et al. (2021b) did not find any benefit of preview control in wake steering operation when feeding realistic wind direction information to the engineering model. By contrast, in the even more realistic environment of large-eddy simulations, this study demonstrated a significant power gain when using imperfect preview information. It should be noted that measurement errors due to device imperfections are not considered here. Regardless, this is an important result

that demonstrates that the concept of wake steering using preview wind direction information is worth pursuing in future work.

### 6.5.2 Generalizability

This study was restricted to studying a very limited range of conditions. Only one wind speed in the partial load range was considered, as well as only a single stratification and turbine layout. For this reason, the results presented in this work cannot be directly generalized.

Since the wake steering effectiveness is influenced by the atmospheric stratification (Vollmer et al., 2016; Simley et al., 2022), it is reasonable to assume that the benefit of preview control is also subject to stability. With similar reasoning, the wind speed is also expected to impact the benefit of preview control, as it was demonstrated to affect the effectiveness of wake steering (Simley et al., 2021a). Furthermore, the preview distance is directly subject to the wind speed, and fluctuations will add another layer of complexity in the forecasting of the incoming wind direction changes.

Besides atmospheric conditions, the benefit of preview control is likely also subject to the yaw controller logic. The controller logic not only affects the timing to initiate a yaw maneuver but could also have implications for the optimum preview time identified in this work.

A logical next step for future work would therefore be to assess the effectiveness of the preview control strategy for a wider range of atmospheric conditions, as well as its dependence on yaw controller logic. Additionally, simulations containing full wind farms with different layouts should be carried out to see how the benefit of preview control changes with scale. This increases the complexity of the problem, as it is for instance unclear where the preview information for downstream turbines should be obtained. This is further discussed in Sect. 6.5.4.

### 6.5.3 Large-eddy simulation considerations

As mentioned in Sect. 6.3.2.3, the use of non-cyclic boundary conditions introduces a vertical gradient  $\partial w/\partial z$ , which alters the wind speed and direction profiles over time. Although this is not considered to affect the outcome of this study as all controllers experience the same effect, it is deemed important for future work to quantify the effect of this behavior and possibly use a different simulation setup to prevent it.

More generally, it should be noted that in LES, the wind direction changes always propagate through the domain, allowing an incoming change to be detected at the preview measurement location before it reaches the turbine. In reality, there may be scenarios when changes occur at the preview measurement and turbine locations at the same time. This would reduce the benefit of preview wind direction control.

### 6.5.4 Forecasting wind direction changes

Arguably the most important task is creating a feasible method to forecast the incoming wind direction. This study assumes the presence of a wind vane on a met mast  $6D$  upstream of the first turbine, corresponding to an optimal preview time of  $90\text{ s}$  for a wind speed of  $8.3\text{ m s}^{-1}$ . Not only is it unfeasible to erect met

masts upstream of each turbine pair, but it is also impossible to adapt the met mast location to varying wind speeds and directions. More feasible would be to use SCADA data from surrounding turbines, as explored in Rott et al. (2020). A disadvantage of this is that it would only provide information further downstream in the wind farm and not for the first row of turbines, which may be the most crucial for wake steering. Alternatively, the use of long-range lidars should be explored. It is difficult to obtain accurate wind direction estimates with lidars, as they only measure a line-of-sight velocity (LOS). The measured LOS can be affected by both wind speed and direction changes, as illustrated in Held and Mann (2019) for a two-beam lidar. When operating the lidar with plan position indicator (PPI) scans, a sinusoid can possibly be fitted to the LOS measurements, as done in Theuer et al. (2020). This would, however, result in a relatively low update frequency and spatial averaging over a large area. Alternatively, multiple (at least two) lidars targeting the same points upstream can be installed at opposite sides of the wind farm; these can be used to reconstruct two wind speed components and consequently the wind direction (van Dooren et al., 2016). Lastly, lidar-based and SCADA-based forecasts can be combined, as done for wind speed in Theuer et al. (2022).

Regardless of what forecasting method is used, the smoothing of raw signals can be done with wind field estimation approaches using surrogate models (e.g., Doekemeijer et al., 2018; Sinner et al., 2020). The forecasting method’s measurement error should be quantified, and how this error affects the effectiveness of preview control should be investigated. As the preview quality of these new methods is likely lower than that of a virtual met mast, power gains from preview control could be lower than illustrated in this work. However, given the substantiality of the gains demonstrated here, preview control using lower-quality wind direction signals still has the potential to provide significant power gains.

### 6.5.5 Yaw controller

In this study, a very simple controller was used that bases its yawing decisions on whether the turbine misalignment exceeds a preset limit of  $7.5^\circ$ , after which it blindly yaws to its next orientation. As discussed in Sect. 6.5.2, the yaw controller logic is expected to affect the effectiveness of preview control. Aggressive controllers are better able to follow wind direction changes, resulting in higher power production at the cost of more yaw maneuvers; therefore, the added value of preview control might be small. Likewise, conservative controllers likely benefit more (i.e., have a higher power gain compared to SC) from the use of preview information.

However, upon utilizing preview information, more intelligent controllers could be developed that, for instance, schedule the next maneuver. This could be used to mitigate frequent yawing, especially switching from positive to negative misalignments and vice versa, as seen in the extra case shown in Appendix A. A strong candidate is model predictive control (e.g., Spencer et al., 2011), which has been well researched for wind turbine blade pitch and generator torque control but has only recently been considered for yaw control. For instance, Song et al. (2019) formulated a model predictive controller that uses wind direction preview and realistic yaw dynamics for the greedy control of a single wind turbine. Model predictive control for wake steering remains a topic to be explored in future research.

### 6.5.6 Effect of preview control on yawing action and loads

As can be seen in Figs. 6.2 and 6.9, the number of yaw maneuvers in wake steering is much higher than in greedy control, which is well described in the literature (e.g., Bossanyi, 2019; Kanev, 2020). However, preview control does not seem to affect the number of yaw maneuvers, at least not as long as the same yaw controller is used. A detailed analysis of how preview control affects turbine loads was considered out of the scope of the current work. The effect of wake steering on loads is complicated and heavily discussed in the literature (Houck, 2021, and references therein). It can be hypothesized that preview control reduces the loads on the upstream turbine since extreme misalignments are avoided (e.g., Fig. 6.9c). Since the wake will be more successfully steered away from the downstream turbine, the loads on this turbine are also expected to be lower.

## 6.6 Conclusions

This study has explored the use of preview wind direction information for wake steering control. An engineering model based on the Data-driven wAke steerIng surrogaTe model (DART) used wind direction time series to estimate power yields with perfect preview information. For this purpose, a turbine pair with a spacing of six rotor diameters was considered in a turbulent flow with a constant wind speed in the partial load range. Based on theoretical linear wind direction changes and later on field measurement data, the results of the engineering model identify an optimum preview time of 90 s for the considered controller, atmospheric conditions, and farm characteristics. Preview control results in an overall power gain, with the highest benefit obtained when the wind direction changes rapidly.

These results were validated by employing a large-eddy simulation model. Wind direction changes were forced in a neutral boundary layer containing the turbine pair. Preview information was taken from a virtual wind vane six rotor diameters upstream of the first turbine, corresponding to the previously determined optimum preview time of 90 s. A six-seed analysis of 3000 s simulations demonstrated that under large, low-frequency wind direction changes, wake steering with standard control results in only small power gains of 0.44 % on average and, occasionally, a power loss due to erroneous steering. In contrast, preview control achieves higher power gains of 1.32 % on average. In a second six-seed analysis with small low-frequency wind direction changes, wake steering with standard control achieved an average power gain of 1.24 %, which further increased to 1.85 % when enabling preview control. Fluctuations in the low-frequency region were shown to have a dominant effect on the performance of wake steering, particularly the effectiveness of preview control. High-frequency fluctuations (turbulence) are less important, as their impact on the yaw controller decision is smaller. Contrary to Simley et al. (2021b), who found no benefit of preview control with realistic wind direction information in wake steering operation, this study has demonstrated a significant power gain using realistic large-eddy simulation results.

This study has introduced many new research questions, such as how to feasibly obtain preview information, how the quality of these forecasts affects the effectiveness, and how to use this information in more intelligent controllers. However, the results demonstrate that wake steering can benefit considerably from

preview wind direction control, making it a topic worth pursuing in future work.

## A6.1 Case with strong fluctuations around $\delta = 0^\circ$

Large-eddy simulation (LES) runs forced by an additional wind direction signal were performed, but these results were excluded from the main text for brevity. However, the results of this case might be of interest to some readers and have therefore been included in this appendix. The case represents a situation where  $\delta = 0^\circ$  is crossed several times. The sign of the intentional misalignment switches several times, resulting in many and large yaw maneuvers, as can be seen in Fig. 6.13a. Although this case is typically viewed as detrimental for wake steering, here, steering standard control (SC) still obtains a power gain of  $\overline{\Delta P} = 0.86\%$  (Fig. 6.13b), which is almost doubled when enabling preview control (PC). Greedy PC actually results in a power loss (a negative  $\overline{\Delta P}$ ), which is likely due to a stronger wake reaching the downstream turbine as a consequence of a better alignment of the upstream turbine. Figure 6.14 shows the six-seed analysis with varying high-frequency fluctuations (see Sect. 6.4.2.4). Greedy PC has, on average, a very small power loss. Steering SC shows consistent power gains, averaging to  $\overline{\Delta P} = 1.21\%$ , which is increased to  $1.83\%$  when PC is enabled. Moreover, five out of six seeds show a substantial power gain for PC over SC. These results indicate that wake steering also benefits from preview wind direction control in this scenario.

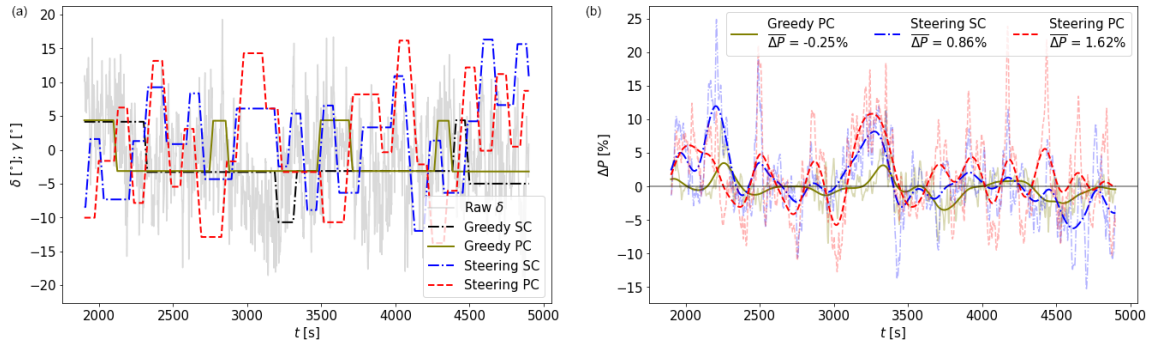


Figure 6.13: Same as Fig. 6.9, but for a case where  $\delta = 0^\circ$  is crossed several times.

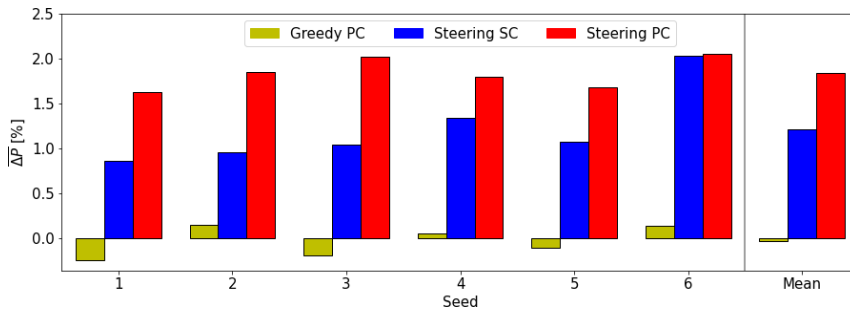


Figure 6.14: Same as Fig. 6.11, but for a case where  $\delta = 0^\circ$  is crossed several times.

# Chapter 7

## Conclusions and outlook

### 7.1 Conclusions

Wake steering is a promising wind farm control strategy that has received an increasing amount of attention in academia and industry in recent years. This thesis builds on the advancements made in recent years and demonstrates that emerging technologies from the field of computer science can be exploited for wake steering purposes. In particular, this thesis shows that interpretable data-driven approaches can be used to benefit wake steering applications. The characteristics of the (redirected) wake in a steady state can be more accurately estimated with a data-driven wake model than with current analytical models, even when only using routinely available measurements as input data. Furthermore, in scenarios challenging for wake steering due to rapid wind direction changes, appropriate preview wind direction information can be used to consistently achieve power gains compared to greedy control. The results from this thesis are discussed in more detail following the research questions proposed in Chapter 1.

1. How can characteristics of a steady state wake be described with a set of quantifiable parameters?
  - The strengths of two traditional wake tracking algorithms are combined in a new Multiple 1D Gaussian method. It includes the simplicity of the 1D Gaussian method and the ability of the 2D Gaussian method to obtain information of the wake extension in both the horizontal and vertical. This method describes traditional characteristics like wake center deficit and position, but also introduces new parameters describing the wake shape in terms of curl and tilt.
  - These wake parameters can be used to study the effect of inflow conditions on wake characteristics. For example, it was shown that a wake in a stable atmosphere deflects more to the right and has a larger curl than a wake in a neutral boundary layer.
2. How can these wake parameters be estimated from inflow and turbine variables?
  - The wake parameters (output parameters) can be estimated from inflow and turbine variables (input parameters) by employing the Data-driven wAKE steering surrogate model (DART), which consists of linear equations only.

The models' coefficients are obtained using a Lasso regression algorithm which isolates relevant from irrelevant parameters, effectively shrinking the number of variables and avoiding multicollinearity.

- Due to its simplicity, DART is highly interpretable, meaning it is clear how input parameters affect output parameters. An example illustrates that to estimate the lateral wake center displacement, the most important variable is the yaw angle, followed by the thrust and wind veer.
- Highly correlated input variables are interchangeable in DART as they provide much of the same information. However, as long as they are not perfectly correlated, adding both variables can increase the model's accuracy, but at the cost of increased model training time.
- Compared to two analytical wake models in a large-eddy simulation study, DART provides more accurate estimates of the available power at downstream locations under all tested conditions, but especially in a stably stratified atmospheric boundary layer. DART reproduces the wake shape and center position under the influence of high wind veer more accurately, leading to a better representation of the wake in stable conditions.

3. What variables and how much data need to be obtained in the field to estimate these wake parameters?

- Also in a field experiment, DART is demonstrated to outperform an analytical model. This is mainly due to a decreased spread, as the systematic bias is comparable. DART demonstrates an error reduction between 19 and 36 %, depending on the used number of input variables.
- DART is especially more accurate than the analytical model when the upstream turbine is misaligned or when the wind shear is large. The latter relates to the higher accuracy in stable conditions as found in the large-eddy simulation study. This indicates that it outperforms the analytical model particularly when performing wake steering and in conditions in which wake steering is deemed most beneficial.
- DART's accuracy increases with the used number of input variables, as it has more information available to explain the variability observed in the field. Increasing the number of input variables both lowers the systematic bias and reduces the spread, but increases the model's training time.
- While analytical models rely on data not affected by the rotor, typically obtained at a nearby met mast, DART is able to handle disturbed data, such as routinely available SCADA data. When only considering SCADA data as input, DART achieves an accuracy very similar to when using undisturbed met mast data. The systematic bias slightly increases, but the spread remains identical. This suggests that no met mast is needed to accurately estimate the wake characteristics after successfully training the model.
- While one of the main drawbacks of data-driven models is their high data need, DART is shown to be able to outperform the analytical model with limited training data, in this particular study about 75 cases at specific set points.



Besides, using more data further increases DART’s accuracy, while the error of the analytical model remains constant.

4. What conditions are detrimental for wake steering and can these be mitigated by using preview wind direction information?

- Unexpected wind direction changes lead to larger yaw misalignments than intended. This results in substantial power losses of the upstream turbine, which are not compensated for by gains at the downstream turbine. This erroneous wake steering, referring to a power loss compared to greedy control, mainly occurs when wind direction changes rapidly.
- An engineering model developed based on DART illustrates that the turbine controller can use preview wind direction information to eliminate erroneous wake steering events.
- The engineering model suggests an optimal preview time of 90 s. It appears to be constant regardless of the variability of the wind direction signal and is likely only dependent on the yaw controller logic. The corresponding preview distance is then a function of the wind speed.
- Large-eddy simulations confirm that the use of preview wind direction information is beneficial when wake steering is applied. Especially when the wind direction changes rapidly, power losses are converted into power gains or small power gains are further increased. However, also when the wind direction changes are slower, preview control further increases the power gain achieved with wake steering.
- The low-frequency wind direction variability (dynamic changes) are dominant in explaining the effectiveness of wake steering and the added benefit of preview control. High-frequency variations (turbulence) play a secondary role, as these have a smaller effect on decisions made by the yaw controller.

## 7.2 Outlook

Since the start of the work for this thesis in 2019, data-driven methods have gained immense popularity in the wind energy research community. Besides a growing number of papers using data-driven techniques (Zehtabiyani-Rezaie et al., 2022), conferences now have designated time slots for these kind of studies. Additionally, even a "Symposium on data-driven modeling and optimization in fluid mechanics" was organized in 2022 (Aarhus University, 2022). When writing the manuscript for Sengers et al. (2022) (Chapter 4) in mid 2020, hardly any references for existing data-driven wake models could be found, whereas there was an abundance of options when writing the manuscript for Sengers et al. (2023b) (Chapter 5) in mid 2022. Most work with data-driven techniques is highly complex and a computer scientist or machine learning expert might be needed to create and operate such models, which deteriorates many end-users from adopting these. This thesis has demonstrated that also simple, interpretable data-driven techniques can be beneficial for wake steering applications.

Specifically for the DART model developed in this work, further developments

constitute of a near wake representation, for instance using a super-Gaussian description, and the ability to simulate more than two turbines. The latter includes superpositioning the wakes of multiple turbines, but also generating accurate results for disturbed inflow when a downstream turbine operates in the full or partial wake. This would likely involve many high-fidelity simulations or an extensive measurement campaign.

Although this work focused on wind speed and consequently power estimation, a methodology similar to DART could be developed to predict the turbulent wind field and consequently estimate turbine loads. The wind tunnel experiments from Bartl et al. (2018b) illustrate a turbulent "ring of fire" of which the shape and amplitude could be quantified and consequently be estimated with for instance the Lasso algorithm. In fact, Peters et al. (2022) recently attempted to predict loads using a reduced order model inspired by the work presented in Chapter 4.

More generally, further advancements in the field of machine learning will allow for the development of more accurate wake models that will outperform DART as proposed in this work. However, these models will have similar issues with generalizability as this is an inherent shortcoming of data-driven models, which limits their application to other locations. Section 5.4.2.4 showed that DART needs relatively few data representing specific set points to generate accurate results. It is deemed an important task for future research to define these set points, and possibly to design a guide describing the campaign setup and measurement matrix needed to retrain data-driven models at new locations. Alternatively, yet more challenging, a methodology could be developed to generalize the models' coefficients, directly making the model applicable to other sites.

Perhaps utilizing the best of both worlds is to develop a hybrid model that is initially trained with (high-fidelity) numerical data or measurement data from other sites, which are gradually replaced by measurements collected at the new site. Alternative to installing measurement equipment at every new site, it could be assumed that the wake position and shape are sufficiently accurately described by the old data, so that only the coefficients related to the wake deficit would need retraining. This could for instance be done using SCADA data by deducing rotor equivalent wind speeds.

With the demonstrated benefit of preview wind direction information for wake steering control, Chapter 6 opened up a wide range of research questions for future work. This includes developing a feasible methodology to forecast wind direction changes before they reach the turbine, either utilizing already available information from other turbines or met mast, or with the deployment of remote sensing devices such as lidars. Besides, wake steering experiments are currently pushing the boundaries of standard yaw controllers developed for greedy control. Various studies have shown that power gains can be achieved when using more intelligent yaw controllers such as closed-loop controllers (e.g., Doekemeijer et al., 2020; Howland et al., 2020). It is hypothesized that more intelligent controllers enhance the benefit of preview information provided by wind direction forecasts as well.

# Bibliography

- Aarhus University: IUTAM Symposium on Data-driven modeling and optimization in fluid mechanics Web Page, URL <https://conferences.au.dk/iutam>, last accessed October 7th, 2022, 2022.
- Abkar, M. and Porté-Agel, F.: Influence of atmospheric stability on wind-turbine wakes: A large-eddy simulation study, *Physics of Fluids*, 27, 35 104, <https://doi.org/10.1063/1.4913695>, 2015.
- Abkar, M., Sørensen, J. N., and Porté-Agel, F.: An Analytical Model for the Effect of Vertical Wind Veer on Wind Turbine Wakes, *Energies*, 11, 1838, <https://doi.org/10.3390/en11071838>, 2018.
- Abolude, A. T., Zhou, W., and Leung, Y. T.: Regional Impact Assessment of Monsoon Variability on Wind Power Availability and Optimization in Asias, *Atmosphere*, 8, 219, <https://doi.org/10.3390/atmos8110219>, 2017.
- Adaramola, M. S. and Krogstad, P.-A.: Experimental investigation of wake effects on wind turbine performances, *Renewable Energy*, 36, 2078–2086, <https://doi.org/10.1016/j.renene.2011.01.024>, 2011.
- Agarwal, H. and Agarwal, R.: First Industrial Revolution and Second Industrial Revolution: Technological Differences and the Differences in Banking and Financing of the Firms, *Saudi Journal of Humanities and Social Sciences*, 2, 1062–1066, <https://doi.org/10.21276/sjhss.2017.2.11.7>, 2017.
- Ahmad, T., Basit, A., Ahsan, M., Coupiac, O., Girard, N., Kazemtabrizi, B., and Matthews, P. C.: Implementation and Analyses of Yaw Based Coordinated Control of Wind Farms, *Energies*, 12, 1266, <https://doi.org/10.3390/en12071266>, 2019.
- Ainslie, J. F.: Calculating the flowfield in the wake of wind turbines, *Journal of Wind Engineering and Industrial Aerodynamics*, 27, 213–224, <https://doi.org/10.3390/en12071266>, 1988.
- Annoni, J., Gebraad, P. M. O., Scholbrock, A. K., Fleming, P., and van Wingerden, J.-W.: Analysis of axial-induction-based wind plant control using an engineering and a high-order wind plant model, *Wind Energy*, 19, 1135–1150, <https://doi.org/10.1002/we.1891>, 2016.
- Annoni, J., Fleming, P., Scholbrock, A., Roadman, J., Dana, S., Adcock, C., Porté-Agel, F., Raach, S., Haizmann, F., and Schlipf, D.: Analysis of control-oriented wake modeling tools using lidar field results, *Wind Energy Science*, 3, 819–831, <https://doi.org/10.5194/wes-3-819-2018>, 2018.

- Archer, C. L. and Vassel-Be-Hagh, A.: Wake steering via yaw control in multi-turbine wind farms: Recommendations based on large-eddy simulation, *Sustainable Energy Technologies and Assessments*, 33, 34–43, <https://doi.org/10.1016/j.seta.2019.03.002>, 2019.
- Arrhenius, S.: On the Influence of Carbonic Acid in the Air upon the Temperature of the Ground, *Philosophical Magazine and Journal of Science*, 41, 237–276, <https://doi.org/10.1080/14786449608620846>, 1896.
- Asmuth, H. and Korb, H.: WakeNet 0.1 - A Simple Three-dimensional Wake Model Based on Convolutional Neural Networks, *Journal of Physics: Conference Series*, 2265, 022 066, <https://doi.org/10.1088/1742-6596/2265/2/022066>, 2022.
- Barrie, D. B. and Kirk-Davidoff, D. B.: Weather response to a large wind turbine array, *Atmospheric Chemistry and Physics*, 10, 769–775, <https://doi.org/10.5194/acp-10-769-2010>, 2010.
- Barthelmie, R. J., Frandsen, S. T., Nielsen, M. N., Pryor, S. C., Rethore, P.-E., and Jørgensen, H. E.: Modelling and measurements of power losses and turbulence intensity in wind turbine wakes at Middelgrunden offshore wind farm, *Wind Energy*, 10, 517–528, <https://doi.org/10.1002/we.238>, 2007.
- Bartl, J., Mühle, F., and Saetran, L.: Wind tunnel study on power output and yaw moments for two yaw-controlled model wind turbines, *Wind Energy Science*, 3, 489–502, <https://doi.org/10.5194/wes-3-489-2018>, 2018a.
- Bartl, J., Mühle, F., Schottler, J., Saetran, L., Peinke, J., Adaramola, M., and Hölling, M.: Wind tunnel experiments on wind turbine wakes in yaw: effects of inflow turbulence and shear, *Wind Energy Science*, 3, 329–343, <https://doi.org/10.5194/wes-3-329-2018>, 2018b.
- Bastankhah, M. and Porté-Agel, F.: A new analytical model for wind-turbine wakes, *Renewable Energy*, 70, 116–123, <https://doi.org/10.1016/j.renene.2014.01.002>, 2014.
- Bastankhah, M. and Porté-Agel, F.: Experimental and theoretical study of wind turbine wakes in yawed conditions, *Journal of Fluid Mechanics*, 806, 506–541, <https://doi.org/10.1017/jfm.2016.595>, 2016.
- Bastankhah, M. and Porté-Agel, F.: Wind farm power optimization via yaw angle control: A wind tunnel study, *Journal of Renewable and Sustainable Energy*, 11, 023 301, <https://doi.org/10.1063/1.5077038>, 2019.
- Bastankhah, M., Shapiro, C. R., Shamsoddin, S., Gayme, D. F., and Meneveau, C.: A vortex sheet based analytical model of the curled wake behind yawed wind turbines, *Journal of Fluid Mechanics*, 933, A2, <https://doi.org/10.1017/jfm.2021.1010>, 2022.
- Basu, S., Holtslag, A. A. M., Van De Wiel, B. J. H., Moene, A. F., and Steeneveld, G.-J.: An inconvenient "truth" about using sensible heat flux as a surface boundary condition in models under stably stratified regimes, *Acta Geophysica*, 56, 88–99, <https://doi.org/10.2478/s11600-007-0038-y>, 2008.

- Bay, C. J., Fleming, P., Doekemeijer, B., King, J., Churchfield, M., and Mudafort, R.: Addressing deep array effects and impacts to wake steering with the cumulative-curl wake model, *Wind Energy Science*, 8, 401–419, <https://doi.org/10.5194/wes-8-401-2023>, 2023.
- Beare, R. J. and Macvean, M. K.: Resolution sensitivity and scaling of large-eddy simulations of the stable boundary layer, *Boundary-Layer Meteorology*, 112, 257–281, <https://doi.org/10.1023/B:BOUN.0000027910.57913.4d>, 2004.
- Beck, H. and Kühn, M.: Dynamic Data Filtering of Long-Range Doppler LiDAR Wind Speed Measurements, *Remote Sensing*, 9, 561, <https://doi.org/10.3390/rs9060561>, 2017.
- Beck, H. and Kühn, M.: Temporal Up-Sampling of Planar Long-Range Doppler LiDAR Wind Speed Measurements Using Space-Time Conversion, *Remote Sensing*, 11, 867, <https://doi.org/10.3390/rs11070867>, 2019.
- Bertelè, M., Bottasso, C. L., Cacciola, S., Adegas, F. D., and Delport, S.: Wind inflow observation from load harmonics, *Wind Energy Science*, 2, 615–640, <https://doi.org/10.5194/wes-2-615-2017>, 2017.
- Bertelè, M., Bottasso, C. L., and Schreiber, J.: Wind inflow observation from load harmonics: initial steps towards a field validation, *Wind Energy Science*, 6, 759–775, <https://doi.org/10.5194/wes-6-759-2021>, 2021.
- Bird, L., Lew, D., Milligan, M., Carlini, E. M., Estanqueiro, A., Flynn, D., Gomez-Lazaro, E., Holttinen, H., Menemenlis, N., Orth, A., Eriksen, P. B., Smith, J. C., Soder, L., Sorensen, P., Altiparmakis, A., Yasuda, Y., and Miller, J.: Wind and solar energy curtailment: A review of international experience, *Renewable and Sustainable Energy Reviews*, 65, 577–586, <https://doi.org/10.1016/j.rser.2016.06.082>, 2016.
- Blondel, F. and Cathelain, M.: An alternative form of the super-Gaussian wind turbine wake model, *Wind Energy Science*, 5, 1225–1236, <https://doi.org/10.5194/wes-5-1225-2020>, 2020.
- Boccolini, M., Bossanyi, E., Bourne, S., Dombrowski, A., Ferraro, G., Harman, K., Harrison, M., Hille, N., Landberg, L., Levick, T., Manjock, A., Mercer, T., Neubert, A., Ruisi, R., and Skeen, N.: Wind Farm Control: The Route to Bankability, Tech. rep., DNV, URL <https://www.dnv.com/Publications/wind-farm-control-198162>, 2021.
- Bossanyi, E.: Optimising yaw control at wind farm level, *Journal of Physics: Conference Series*, 1222, 012023, <https://doi.org/10.1088/1742-6596/1222/1/012023>, 2019.
- Bossanyi, E. A., Kumar, A., and Hugues-Salas, O.: Wind turbine control applications of turbine-mounted LIDAR, *Journal of Physics: Conference Series*, 555, 012011, <https://doi.org/10.1088/1742-6596/555/1/012011>, 2014.
- Bottasso, C. L., Cacciola, S., and Schreiber, J.: Local wind speed estimation, with application to wake impingement detection, *Renewable Energy*, 116, 155–168, <https://doi.org/10.1016/j.renene.2017.09.044>, 2018.

- BP: Statistical Review of World Energy, Tech. rep., BP, URL <https://www.bp.com/en/global/corporate/energy-economics/statistical-review-of-world-energy.html>, last accessed September 5th, 2022, 2022.
- Bromm, M., Rott, A., Beck, H., Vollmer, L., Steinfeld, G., and Kühn, M.: Field investigation on the influence of yaw misalignment on the propagation of wind turbine wakes, *Wind Energy*, 21, 1011–1028, <https://doi.org/10.1002/we.2210>, 2018.
- Brugger, P., Carbajo Fuertes, F., Vahidzadeh, M., and Markfort, C D Porté-Agel, F.: Characterization of Wind Turbine Wakes with Nacelle-Mounted Doppler LiDARs and Model Validation in the Presence of Wind Veer, *Remote Sensing*, 11, 2247, <https://doi.org/10.3390/rs11192247>, 2019.
- Brugger, P., Debnath, M., Scholbrock, A., Fleming, P., Moriarty, P., Simley, E., Jager, D., Roadman, J., Murphy, M., Zong, H., and Porté-Agel, F.: Lidar measurements of yawed-wind-turbine wakes: characterization and validation of analytical models, *Wind Energy Science*, 5, 1253–1272, <https://doi.org/10.5194/wes-5-1253-2020>, 2020.
- Brunton, S., Proctor, J., and Kutz, J.: Discovering governing equations from data by sparse identification of nonlinear dynamical systems, *Proceedings of the National Academy of Sciences*, 113, 3932–3937, <https://doi.org/10.1073/pnas.1517384113>, 2016.
- Brunton, S., Noack, B. R., and Koumoutsakos, P.: Machine Learning for Fluid Mechanics, *Annual Review of Fluid Mechanics*, 52, 477–508, <https://doi.org/10.1146/annurev-fluid-010719-060214>, 2020.
- Calaf, M., Meneveau, C., and Meyers, J.: Large eddy simulation study of fully developed wind-turbine array boundary layers, *Physics of Fluids*, 22, 015 110, <https://doi.org/10.1063/1.3291077>, 2010.
- Callendar, G. S.: The artificial production of carbon dioxide and its influence on temperature, *Quarterly Journal of the Royal Meteorological Society*, 64, 223–240, <https://doi.org/10.1002/qj.49706427503>, 1938.
- Campagnolo, F., Petrovic, V., Schreiber, J., Nanos, E., Croce, A., and Botasso, C.: Wind tunnel testing of a closed-loop wake deflection controller for wind farm power maximization Recent citations, *Journal of Physics: Conference Series*, 753, 032 006, <https://doi.org/10.1088/1742-6596/753/3/032006>, 2016.
- Carbajo Fuertes, F. and Porté-Agel, F.: Using a Virtual Lidar Approach to Assess the Accuracy of the Volumetric Reconstruction of a Wind Turbine Wake, *Remote Sensing*, 10, 721, <https://doi.org/10.3390/rs10050721>, 2018.
- Churchfield, M. J., Schreck, S., Martínez-Tossas, L. A., Meneveau, C., and Spalart, P. R.: An Advanced Actuator Line Method for Wind Energy Applications and Beyond, in: *AIAA SciTech Forum*, 09-13 January, Grapevine, Texas, USA, <https://doi.org/10.2514/6.2017-1998>, 2017.
- Clifton, A., Clive, P., Gottschall, J., Schlipf, D., Simley, E., Simmons, L., Stein, D., Trabucchi, D., Vasiljevic, N., and Würth, I.: IEA Wind Task 32: Wind

- Lidar Identifying and Mitigating Barriers to the Adoption of Wind Lidar, Remote Sensing, 10, 406, <https://doi.org/10.3390/rs10030406>, 2018.
- Corten, G. and Schaak, P.: Heat and Flux: Increase of Wind Farm Production by Reduction of the Axial Induction, in: EWEC 2003, 16-19 June, Madrid, Spain, 2003.
- Dahlberg, J. and Medici, D.: Potential improvement of wind turbine array efficiency by active wake control (AWC), in: EWEC 2003, 16-19 June, Madrid, Spain, 2003.
- Deardorff, J. W.: Stratocumulus-capped mixed layers derived from a three-dimensional model, Boundary-Layer Meteorology, 18, 495–527, <https://doi.org/10.1007/BF00119502>, 1980.
- Department Of Energy: Solar Futures study, URL <https://www.energy.gov/sites/default/files/2021-09/Solar%20Futures%20Study.pdf>, last accessed September 7th, 2022, 2021.
- Devine Jr., W. D.: From Shafts to Wires: Historical Perspective on Electrification, Journal of Economic History, 43, 347–372, 1983.
- Digital Science: Dimensions [Software], URL <https://app.dimensions.ai>, last accessed May 19th, 2023, under licence agreement, 2018-.
- Doekemeijer, B. M., Boersma, S., Pao, L. Y., Knudsen, T., and van Wingerden, J.-W.: Online model calibration for a simplified LES model in pursuit of real-time closed-loop wind farm control, Wind Energy Science, 3, 749–765, <https://doi.org/10.5194/wes-3-749-2018>, 2018.
- Doekemeijer, B. M., van der Hoek, D., and van Wingerden, J.-W.: Closed-loop model-based wind farm control using FLORIS under time-varying inflow conditions, Renewable Energy, 156, 719–730, <https://doi.org/10.1016/j.renene.2020.04.007>, 2020.
- Doekemeijer, B. M., Kern, S., Maturu, S., Kanev, S., Salbert, B., Schreiber, J., Campagnolo, F., Bottasso, C. L., Schuler, S., Wilts, F., Neumann, T., Potenza, G., Calabretta, F., Fioretti, F., and van Wingerden, J.-W.: Field experiment for open-loop yaw-based wake steering at a commercial onshore wind farm in Italy, Wind Energy Science, 6, 159–176, <https://doi.org/10.5194/wes-6-159-2021>, 2021.
- Dörenkämper, M., Witha, B., Steinfeld, G., Heinemann, D., and Kühn, M.: The impact of stable atmospheric boundary layers on wind-turbine wakes within offshore wind farms, Journal of Wind Engineering and Industrial Aerodynamics, 144, 146–153, <https://doi.org/10.1016/j.jweia.2014.12.011>, 2015.
- Doubrawa, P., Barthelmie, R. J., Wang, H., Pryor, S. C., and Churchfield, M. J.: Wind Turbine Wake Characterization from Temporally Disjunct 3-D Measurements, Journal of Wind Engineering and Industrial Aerodynamics, 8, 939, <https://doi.org/10.3390/rs8110939>, 2016.
- Dunne, F., Pao, L. Y., Wright, A. D., Jonkman, B., and Kelley, N.: Adding feedforward blade pitch control to standard feedback controllers for load mitigation in wind turbines, Mechatronics, 21, 682–690, <https://doi.org/10.1016/j.mechatronics.2011.02.011>, 2011.

- European Commission: Questions and answers - The European Green Deal Investment Plan and Just Transition Mechanism explained, URL [https://ec.europa.eu/commission/presscorner/detail/en/qanda\\_20\\_24](https://ec.europa.eu/commission/presscorner/detail/en/qanda_20_24), last accessed September 7th, 2022, 2020a.
- European Commission: Commission notice: Guidance document on wind energy developments and EU nature legislation, URL [https://ec.europa.eu/environment/nature/natura2000/management/docs/\wind\\_farms\\_en.pdf](https://ec.europa.eu/environment/nature/natura2000/management/docs/\wind_farms_en.pdf), last accessed September 7th, 2022, 2020b.
- European Commission: COMMUNICATION FROM THE COMMISSION TO THE EUROPEAN PARLIAMENT, THE COUNCIL, THE EUROPEAN ECONOMIC AND SOCIAL COMMITTEE AND THE COMMITTEE OF THE REGIONS: An EU Strategy to harness the potential of offshore renewable energy for a climate neutral future, URL [https://ec.europa.eu/energy/sites/ener/files/offshore\\_renewable\\_ener\gy\\_strategy.pdf](https://ec.europa.eu/energy/sites/ener/files/offshore_renewable_ener\gy_strategy.pdf), last accessed September 7th, 2022, 2020c.
- European Commission: Press release - European Green Deal: Commission proposes transformation of EU economy and society to meet climate ambitions, URL [https://ec.europa.eu/commission/presscorner/detail/en/IP\\_21\\_3541](https://ec.europa.eu/commission/presscorner/detail/en/IP_21_3541), last accessed September 7th, 2022, 2021.
- European Commission: COMMUNICATION FROM THE COMMISSION TO THE EUROPEAN PARLIAMENT, THE EUROPEAN COUNCIL, THE COUNCIL, THE EUROPEAN ECONOMIC AND SOCIAL COMMITTEE AND THE COMMITTEE OF THE REGIONS: REPowerEU Plan, URL [https://eur-lex.europa.eu/resource.html?uri=cellar:fc930f14-d7ae-11\ec-a95f-01aa75ed71a1.0001.02/DOC\\_1&format=PDF](https://eur-lex.europa.eu/resource.html?uri=cellar:fc930f14-d7ae-11\ec-a95f-01aa75ed71a1.0001.02/DOC_1&format=PDF), last accessed September 7th, 2022, 2022.
- Fleming, P., Gebraad, P. M. O., Lee, S., van Wingerden, J.-W., Johnson, K., Churchfield, M., Michalakes, J., Spalart, P., and Moriarty, P.: Simulation comparison of wake mitigation control strategies for a two-turbine case, *Wind Energy*, 18, 2135–2143, <https://doi.org/10.1002/we.1810>, 2015.
- Fleming, P., Annoni, J., Scholbrock, A., Quon, E., Dana, S., Schreck, S., Raach, S., Haizmann, F., and Schlipf, D.: Full-Scale Field Test of Wake Steering, *Journal of Physics: Conference Series*, 854, 012013, <https://doi.org/10.1088/1742-6596/854/1/012013>, 2017a.
- Fleming, P., Annoni, J., Shah, J. J., Wang, L., Ananthan, S., Zhang, Z., Hutchings, K., Wang, P., Chen, W., and Chen, L.: Field test of wake steering at an offshore wind farm, *Wind Energy Science*, 2, 229–239, <https://doi.org/10.5194/wes-2-229-2017>, 2017b.
- Fleming, P., Annoni, J., Churchfield, M., Martinez-Tossas, L. A., Gruchalla, K., Lawson, M., and Moriarty, P.: A simulation study demonstrating the importance of large-scale trailing vortices in wake steering, *Wind Energy Science*, 3, 243–255, <https://doi.org/10.5194/wes-3-243-2018>, 2018.



- Fleming, P., King, J., Dykes, K., Simley, E., Roadman, J., Scholbrock, A., Murphy, P., Lundquist, J. K., Moriarty, P., Fleming, K., Van Dam, J., Bay, C., Mudafort, R., Lopez, H., Skopek, J., Scott, M., Ryan, B., Guernsey, C., and Brake, D.: Initial Results From a Field Campaign of Wake Steering Applied at a Commercial Wind Farm: Part 1, *Wind Energy Science*, 4, 273–285, <https://doi.org/10.5194/wes-4-273-2019>, 2019.
- Fleming, P., King, J., Dykes, K., Simley, E., Roadman, J., Scholbrock, A., Murphy, P., Lundquist, J. K., Moriarty, P., Fleming, K., van Dam, J., Bay, C., Mudafort, R., Lopez, H., Skopek, J., Scott, M., Ryan, B., Guernsey, C., and Brake, D.: Continued Results from a Field Campaign of Wake Steering Applied at a Commercial Wind Farm: Part 2, *Wind Energy Science*, 4, 945–958, <https://doi.org/10.5194/wes-5-945-2020>, 2020.
- Fleming, P., Sinner, M., Young, T., Lannic, M., King, J., Simley, E., and Doekemeijer, B.: Experimental results of wake steering using fixed angles, *Wind Energy Science*, 6, 1521–1531, <https://doi.org/10.5194/wes-6-1521-2021>, 2021.
- Fleming, P. A., Gebraad, P. M., Lee, S., van Wingerden, J.-W., Johnson, K., Churchfield, M., Michalakes, J., Spalart, P., and Moriarty, P.: Evaluating techniques for redirecting turbine wakes using SOWFA, *Renewable Energy*, 70, 211–218, <https://doi.org/10.1016/j.renene.2014.02.015>, 2014a.
- Fleming, P. A., Scholbrock, A. K., Jehu, A., Davoust, S., Osler, E., Wright, A. D., and Clifton, A.: Field-test results using a nacelle-mounted lidar for improving wind turbine power capture by reducing yaw misalignment, *Journal of Physics: Conference Series*, 524, <https://doi.org/10.1088/1742-6596/524/1/012002>, 2014b.
- Fraunhofer IWES: Press release - New European Wind Atlas published, URL <https://www.iwes.fraunhofer.de/en/press/archive-2019/new-european-wind-atlas-published.html>, last accessed September 29th, 2022, 2019.
- Fukunaga, K. and Hostetler, L.: The estimation of the gradient of a density function, with applications in pattern recognition, *IEEE Transactions on Information Theory*, 21, 32–40, <https://doi.org/10.1109/TIT.1975.1055330>, 1975.
- Gebraad, P., Fleming, P., and Wingerden: Wind turbine wake estimation and control using FLORIDyn, a control-oriented dynamic wind plant model, *IEEE American Control Conference (ACC)*, pp. 1702–1708, <https://doi.org/10.1109/ACC.2015.7170978>, 2015.
- Gebraad, P., Teeuwisse, F., Wingerden, J. v., Fleming, P., Ruben, S., Marden, J., and Pao, L.: Wind plant power optimization through yaw control using a parametric model for wake effects—a CFD simulation study, *Wind Energy*, 19, 95–114, <https://doi.org/10.1002/we.1822>, 2016.
- Gebraad, P., Thomas, J., Ning, A., Fleming, P., and Dykes, K.: Maximization of the annual energy production of wind power plants by optimization of layout and yaw-based wake control, *Wind Energy*, 20, 97–107, <https://doi.org/10.1002/we.1993>, 2017.

- Göçmen, T. and Giebel, G.: Data-driven Wake Modelling for Reduced Uncertainties in short-term Possible Power Estimation, *Journal of Physics: Conference Series*, 1037, 072 002, <https://doi.org/10.1088/1742-6596/1037/7/072002>, 2018.
- Grassi, S., Junghans, S., and Raubal, M.: Assessment of the wake effect on the energy production of onshore wind farms using GIS, *Applied Energy*, 136, 827–837, <https://doi.org/10.1016/j.apenergy.2014.05.066>, 2014.
- Gryning, S.-E., Batchvarova, E., Brümmner, B., Jørgensen, H., and Larsen, S.: On the extension of the wind profile over homogeneous terrain beyond the surface boundary layer, *Boundary-Layer Meteorology*, 124, 251–268, <https://doi.org/10.1007/s10546-007-9166-9>, 2007.
- Hargadon, A. B. and Douglas, Y.: When Innovations Meet Institutions: Edison and the Design of the Electric Light, *Administrative Science Quarterly*, 46, 476–501, <https://doi.org/10.2307/3094872>, 2001.
- Harris, D. C.: Charles David Keeling and the Story of Atmospheric CO<sub>2</sub> Measurements, *Analytical Chemistry*, 82, 7865–7870, <https://doi.org/10.1021/ac1001492>, 2010.
- Harrison, M. R.: The Media and Public Perceptions of Climatic Change, *Bulletin of the American Meteorological Society*, 63, 730–738, [https://doi.org/10.1175/1520-0477\(1982\)063<0730:TMAPPO>2.0.CO;2](https://doi.org/10.1175/1520-0477(1982)063<0730:TMAPPO>2.0.CO;2), 1982.
- Hastie, T., Tibshirani, R., and Friedman, J.: *The elements of statistical learning: data mining, inference, and prediction*, Springer Science & Business Media, 2nd edn., 2009.
- Held, D. P. and Mann, J.: Detection of wakes in the inflow of turbines using nacelle lidars, *Wind Energy Science*, 4, 407–420, <https://doi.org/10.5194/wes-4-407-2019>, 2019.
- Herges, T., Maniaci, D., Naughton, B., Mikkelsen, T., and Sjöholm, M.: High resolution wind turbine wake measurements with a scanning lidar, *Journal of Physics: Conference Series*, 854, 012 021, <https://doi.org/10.1088/1742-6596/854/1/012021>, 2017.
- Houck, D.: Review of wake management techniques for wind turbines, *Wind Energy*, 25, 195–220, <https://doi.org/10.1002/we.2668>, 2021.
- Howland, M. F., Bossuyt, J., Martínez-Tossas, L. A., Meyers, J., and Meneveau, C.: Wake structure in actuator disk models of wind turbines in yaw under uniform inflow conditions, *Journal of Renewable and Sustainable Energy*, 8, 043 301, <https://doi.org/10.1063/1.4955091>, 2016.
- Howland, M. F., Lele, S. K., and Dabiri, J. O.: Wind farm power optimization through wake steering, *Proceedings of the National Academy of Sciences*, 116, 14 495–14 500, <https://doi.org/10.1073/pnas.1903680116>, 2019.
- Howland, M. F., Ghate, A. S., Lele, S. K., and Dabiri, J. O.: Optimal closed-loop wake steering - Part 1: Conventionally neutral atmospheric boundary layer conditions, *Wind Energy Science*, 5, 1315–1338, <https://doi.org/10.5194/wes-5-1315-2020>, 2020.

- Howland, M. F., Ghate, A. S., Quesada, J. B., Pena Martínez, J. J., Zhong, W., Larrañaga, F. P., Lele, S. K., and Dabiri, J. O.: Optimal closed-loop wake steering - Part 2: Diurnal cycle atmospheric boundary layer conditions, *Wind Energy Science*, 7, 345–365, <https://doi.org/10.5194/wes-7-345-2022>, 2022.
- Hulsman, P., Juhl Andersen, S., and Göçmen, T.: Optimizing Wind Farm Control through Wake Steering using Surrogate Models based on High Fidelity Simulations, *Wind Energy Science*, 5, 309–329, <https://doi.org/10.5194/wes-5-309-2020>, 2020.
- Hulsman, P., Sucameli, C., Petrović, V., Rott, A., Gerds, A., and Kühn, M.: Turbine power loss during yaw-misaligned free field tests at different atmospheric conditions, *Journal of Physics: Conference Series*, 2265, 032 074, <https://doi.org/10.1088/1742-6596/2265/3/032074>, 2022a.
- Hulsman, P., Wosnik, M., Petrović, V., and Kühn, M.: Development of a curled wake of a yawed wind turbine under turbulent and sheared inflow, *Wind Energy Science*, 7, 237–257, <https://doi.org/10.5194/wes-7-237-2022>, 2022b.
- IMUK: PALM Seminar, Institut für Meteorologie und Klimatologie, Leibniz Universität Hannover, URL [https://palm.muk.uni-hannover.de/trac/attach\ment/wiki/doc/tut/palm/L-3.2\\_Noncyclic\\_boundary\\_conditions.pdf](https://palm.muk.uni-hannover.de/trac/attach\ment/wiki/doc/tut/palm/L-3.2_Noncyclic_boundary_conditions.pdf), last accessed October 21st, 2022, 2022.
- IPCC: Intergovernmental Panel on Climate Change Web Page, URL <https://www.ipcc.ch>, last accessed August 31st, 2022, 2022.
- Jensen, N. O.: A note on wind generator interaction, Tech. Rep. Risø-M No. 2411, Risø National Laboratory, 1983.
- Jimenez, A., Crespo, A., and Migoya, E.: Application of a LES technique to characterize the wake deflection of a wind turbine in yaw, *Wind Energy*, 13, 559–572, <https://doi.org/10.1002/we.380>, 2010.
- Jonkman, J., Butterfield, S., Musial, W., and Scott, G.: Definition of a 5-MW Reference Wind Turbine for Offshore System Development, Tech. Rep. TP-500-38060, National Renewable Energy Laboratory, <https://doi.org/10.2172/947422>, 2009.
- Jonkman, J. M. and Buhl Jr., M. L.: FAST User’s Guide, Tech. Rep. EL-500-38230, National Renewable Energy Laboratory, 2005.
- Kanev, S.: Dynamic wake steering and its impact on wind farm power production and yaw actuator duty, *Renewable Energy*, 146, 9–15, <https://doi.org/10.1016/j.renene.2019.06.122>, 2020.
- Karad, S. and Thakur, R.: Efficient monitoring and control of wind energy conversion systems using Internet of things (IoT): a comprehensive review, *Environment, Development and Sustainability*, 23, 14 197–14 214, <https://doi.org/10.1007/s10668-021-01267-6>, 2021.
- Kataoka, H. and Mizuno, M.: Numerical flow computation around aeroelastic 3D square cylinder using inflow turbulence, *Wind and Structures*, 5, 379–392, <https://doi.org/10.12989/was.2002.5.2\3\4.379>, 2002.

- Kheirabadi, A. and Nagamune, R.: A quantitative review of wind farm control with the objective of wind farm power maximization, *Journal of Wind Engineering and Industrial Aerodynamics*, 192, 45–73, <https://doi.org/10.1016/j.jweia.2019.06.015>, 2019.
- Kidambi Sekar, A. P., van Dooren, M. F., Rott, A., and Kühn, M.: Lower Order Description and Reconstruction of Sparse Scanning Lidar Measurements of Wind Turbine Inflow Using Proper Orthogonal Decomposition, *Remote Sensing*, 14, 2681, <https://doi.org/10.3390/rs14112681>, 2022.
- Kim, H., Kim, K., Bottasso, C. L., Campagnolo, F., and Paek, I.: Wind Turbine Wake Characterization for Improvement of the Ainslie Eddy Viscosity Wake Model, *energies*, 11, 2823, <https://doi.org/10.3390/en11102823>, 2018.
- Kim, K.-J. and Tagkopoulos, I.: Application of machine learning in rheumatic disease research, *The Korean Journal of Internal Medicine*, 34, 708–722, <https://doi.org/10.3904/kjim.2018.349>, 2019.
- King, J., Fleming, P., King, R., Martínez-Tossas, L., Bay, C., Mudafort, R., and Simley, E.: Controls-Oriented Model for Secondary Effects of Wake Steering, *Wind Energy Science*, 6, 701–714, <https://doi.org/10.5194/wes-6-701-2021>, 2021.
- Kragh, K. A. and Fleming, P. A.: Rotor Speed Dependent Yaw Control of Wind Turbines Based on Empirical Data, in: 50th AIAA Aerospace Sciences Meeting, 09-12 January, Nashville, Tennessee, USA, <https://doi.org/10.2514/6.2012-1018>, 2012.
- Krüger, S., Steinfeld, G., Kraft, M., and Lukassen, L. J.: Validation of a coupled atmospheric–aeroelastic model system for wind turbine power and load calculations, *Wind Energy Science*, 7, 323–344, <https://doi.org/10.5194/wes-7-323-2022>, 2022.
- Lacerda, M., Couto, A., and Estanqueiro, A.: Wind Power Ramps Driven by Windstorms and Cyclones, *Energies*, 10, 1474, <https://doi.org/10.3390/en10101475>, 2017.
- Laks, J., Pao, L. Y., Wright, A., Kelley, N., and Jonkman, B.: Blade pitch control with preview wind measurements, in: 48th AIAA Aerospace Sciences Meeting Including the New Horizons Forum and Aerospace Exposition, 4-7 January, Orlando, Florida, USA, <https://doi.org/10.2514/6.2010-251>, 2010.
- Larsen, G. C., Madsen, H. A., Thomsen, K., and Larsen, T. J.: Wake meandering: A pragmatic approach, *Wind Energy*, 11, 377–395, <https://doi.org/10.1002/we.267>, 2008.
- Lissaman, P. B. S.: Energy Effectiveness of Arbitrary Arrays of Wind Turbines, *Journal of Energy*, 3, 323–328, <https://doi.org/10.2514/3.62441>, 1979.
- Lucas Jr., R. E.: The industrial revolution: past and future, *Economic Education Bulletin*, 44, 1–8, 2004.
- Lund, T. S., Wu, X., and Squires, K. D.: Generation of Turbulent Inflow Data for Spatially-Developing Boundary Layer Simulations, *Journal of Computational Physics*, 140, 233–258, <https://doi.org/10.1006/jcph.1998.5882>, 1998.

- Marčiukaitis, M., Žutautaitė, I., Martišauskas, L., Jokšas, B., Gecevičius, G., and Sfetsos, A.: Non-linear regression model for wind turbine power curve, *Renewable Energy*, 113, 732–741, <https://doi.org/10.1016/j.renene.2017.06.039>, 2017.
- Maronga, B., Banzhaf, S., Burmeister, C., Esch, T., Forkel, R., Fröhlich, D., Fuka, V., Gehrke, K. F., Geletič, J., Giersch, S., Gronemeier, T., Groß, G., Heldens, W., Hellsten, A., Hoffmann, F., Inagaki, A., Kadasch, E., Kanani-Sühring, F., Ketelsen, K., Khan, A., Knigge, C., Knoop, H., Krč, P., Kurppa, M., Maamari, H., Matzarakis, A., Mauder, M., Pallasch, M., Pavlik, D., Pfafferoth, J., Resler, J., Rissmann, S., Russo, E., Salim, M., Schrempf, M., Schwenkel, J., Seckmeyer, G., Schubert, S., Sühring, M., Von Tils, R., Vollmer, L., Ward, S., Witha, B., Wurps, H., Zeidler, J., and Raasch, S.: Overview of the PALM model system 6.0, *Geoscientific Model Development*, 13, 1335–1372, <https://doi.org/10.5194/gmd-13-1335-2020>, 2020.
- Martínez-Tossas, L. A., Annoni, J., Fleming, P. A., and Churchfield, M. J.: The aerodynamics of the curled wake: a simplified model in view of flow control, *Wind Energy Science*, 4, 127–138, <https://doi.org/10.5194/wes-4-127-2019>, 2019.
- Marugán, A. P., Márquez, F. P. G., Perez, J. M. P., and Ruiz-Hernández, D.: A survey of artificial neural network in wind energy systems, *Applied Energy*, 228, 1822–1836, <https://doi.org/10.1016/j.apenergy.2018.07.084>, 2018.
- Medici, D., Ivanell, S., Dahlberg, J., and Alfredsson, P.: The upstream flow of a wind turbine: blockage effect, *Wind Energy*, 14, 691–697, <https://doi.org/10.1002/we.451>, 2011.
- Messner, J. W. and Pinson, P.: Online adaptive lasso estimation in vector autoregressive models for high dimensional wind power forecasting, *International Journal of Forecasting*, 35, 1485–1498, <https://doi.org/10.1016/j.ijforecast.2018.02.001>, 2019.
- Meyers, J., Bottasso, C., Dykes, K., Fleming, P., Gebraad, P., Giebel, G., Göçmen, T., and van Wingerden, J.-W.: Wind farm flow control: prospects and challenges, *Wind Energy Science*, 7, 2271–2306, <https://doi.org/10.5194/wes-7-2271-2022>, 2022.
- Miraftebzadeh, S. M., Foadelli, F., Longo, M., and Pasetti, M.: A Survey of Machine Learning Applications for Power System Analytics, *IEEE International Conference on Environment and Electrical Engineering and IEEE Industrial and Commercial Power Systems Europe (EEEIC / I&CPS Europe)*, <https://doi.org/10.1109/EEEIC.2019.8783340>, 2019.
- Mirocha, J., Kosović, B., and Kirkil, G.: Resolved Turbulence Characteristics in Large-Eddy Simulations Nested within Mesoscale Simulations Using the Weather Research and Forecasting Model, *Monthly Weather Review*, 142, 806–831, <https://doi.org/10.1175/MWR-D-13-00064.1>, 2013.
- Moeng, C.-H. and Wyngaard, J. C.: Spectral Analysis of Large-Eddy Simulations of the Convective Boundary Layer, *Journal of the Atmospheric Sciences*, 45, 3573–3587, [https://doi.org/10.1175/1520-0469\(1988\)045<3573:SAOLES>2.0.CO;2](https://doi.org/10.1175/1520-0469(1988)045<3573:SAOLES>2.0.CO;2), 1988.

- Mohammadi, K. and Goudarzi, N.: Study of inter-correlations of solar radiation, wind speed and precipitation under the influence of El Nino Southern Oscillation (ENSO) in California, *Renewable Energy*, 120, 190–200, <https://doi.org/10.1016/j.renene.2017.12.069>, 2018.
- Moore, G. E.: Cramming more components onto integrated circuits, *Electronics*, 38, 114–117, 1965.
- Moore, G. E.: Progress in digital integrated electronics, *IEEE Solid-State Circuits Society Newsletter*, 11, 36–37, <https://doi.org/10.1109/N-SSC.2006.4804410>, 1975.
- Munters, W., Meneveau, C., and Meyers, J.: Shifted periodic boundary conditions for simulations of wall-bounded turbulent flows, *Physics of Fluids*, 28, 025 112, <https://doi.org/10.1063/1.4941912>, 2016a.
- Munters, W., Meneveau, C., and Meyers, J.: Turbulent Inflow Precursor Method with Time-Varying Direction for Large-Eddy Simulations and Applications to Wind Farms, *Boundary-Layer Meteorology*, 159, 305–328, <https://doi.org/10.1007/s10546-016-0127-z>, 2016b.
- Niyayifar, A. and Porté-Agel, F.: Analytical modeling of wind farms: A new approach for power prediction, *Energies*, 9, 741, <https://doi.org/10.3390/en9090741>, 2016.
- Nilsson, K., Ivanell, S., Hansen, K. S., Mikkelsen, R., Sørensen, J. N., Breton, S.-P., and Henningson, D.: Large-eddy simulations of the Lillgrund wind farm, *Wind Energy*, 18, 449–467, <https://doi.org/10.1002/we.1707>, 2014.
- NREL: FLORIS. Version 2.2.2 GitHub [code], last access: 26 November 2020, 2020.
- NREL: FLORIS. Version 3.0rc4 GitHub [code], URL <https://github.com/NREL/floris>, last access: 6 April 2022, 2022.
- NREL: FLORIS. Version 3.2.1, URL <https://github.com/NREL/floris>, last accessed November 28th, 2022, 2022.
- Nyenah, E., Sterl, S., and Thiery, W.: Pieces of a puzzle: solar-wind power synergies on seasonal and diurnal timescales tend to be excellent worldwide, *Environmental Research Communications*, 4, 055 011, <https://doi.org/10.1088/2515-7620/ac71fb>, 2022.
- Obozinski, G., Taskar, B., and Jordan, M.: Multi-task feature selection, Tech. Rep., Statistics Department, UC Berkeley, 2006.
- Ortensi, M., Theuer, F., and Kühn, M.: Analysis of the effects of scanning trajectory parameters on minute-scale lidar forecasting , *Journal of Physics: Conference Series*, 2265, 022 002, <https://doi.org/10.1088/1742-6596/2265/2/022002>, 2022.
- Peña, A., Hasager, C., Lange, J., Anker, J., Badger, M., Fingöl, F., Bischoff, O., Carrieu, J.-P., Dunne, F., Emeis, S., Harris, M., Hoffsäss, M., Karagali, J., Laks, J., Larsen, S. E., Mann, J., Mikkelsen, T., Pao, L. Y., Pitter, M., Rettenmeier, A., Sathe, A., Scanzani, F., Schlipf, D., Simley, E., Slinger, C., Wagner, R., and Würth, I.: Remote Sensing for Wind Energy, Tech. Rep. DTU Wind Energy E; No. 0029(EN)), DTU Wind Energy, 2013.

- Pedregosa, F., Varoquaux, G., Gramfort, A., Michel, V., Thirion, B., Grisel, O., Blondel, M., Prettenhofer, P., Weiss, R., Dubourg, V., Vanderplas, J., Passos, A., Cournapeau, D., Brucher, M., Perrot, M., and Duchesnay, E.: Scikit-learn: Machine Learning in Python, *Journal of Machine Learning Research*, 12, 2825–2830, 2011.
- Peters, N., Silva, C., and Ekaterinaris, J.: A Data-Driven Reduced Order Model for Rotor Optimization, *Wind Energy Science Discussions*, <https://doi.org/10.5194/wes-2022-95>, 2022.
- Phillips, H. A.: Pollution of the Atmosphere, *Nature*, 27, 127, 1882.
- Plass, G. N.: The Carbon Dioxide Theory of Climatic Change, *Tellus*, 8, 140–154, 1956.
- Pryor, S. C. and Barthelmie, R. J.: Climate change impacts on wind energy: A review, *Renewable and Sustainable Energy Reviews*, 14, 430–437, <https://doi.org/10.1016/j.rser.2009.07.028>, 2010.
- Pryor, S. C., Barthelmie, R. J., Clausen, N. E., MacKellar, N., and Kjellström, E.: Analyses of possible changes in intense and extreme wind speeds over northern Europe under climate change scenarios, *Climate Dynamics*, 38, 189–208, <https://doi.org/10.1007/s00382-010-0955-3>, 2012.
- Purohit, S., Ng, E. Y. K., and Kabir, I. F. S. A.: Evaluation of three potential machine learning algorithms for predicting the velocity and turbulence intensity of a wind turbine wake, *Renewable Energy*, 184, 405–420, <https://doi.org/10.1016/j.renene.2021.11.097>, 2022.
- Renganathan, S. A., Maulik, R., Letizia, S., and Iungo, G. V.: Data-driven wind turbine wake modeling via probabilistic machine learning, *Neural Computing and Applications*, 34, 6171–6186, <https://doi.org/10.1007/s00521-021-06799-6>, 2022.
- Revelle, R., Broecker, W., Craig, H., Keeling, C. D., and Smagorinsky, J.: Restoring the Quality of our Environment: Report of the Environmental Pollution Panel, President’s Science Advisory Committee, The White House, Washington, DC, USA, pp. 111–133, 1965.
- Ritchie, H., Roser, M., and Rosado, P.: Our World in Data - Energy Mix, URL <https://ourworldindata.org/grapher/energy-consumption-by-source-and-country>, last accessed September 5th, 2022, 2022.
- Rodriguez, S.: LES and DNS Turbulence Modeling, in: *Applied Computational Fluid Dynamics and Turbulence Modeling*, chap. 5, pp. 197–223, Springer, Cham, [https://doi.org/10.1007/978-3-030-28691-0\\_5](https://doi.org/10.1007/978-3-030-28691-0_5), 2019.
- Rose, K.: The internet of things: An overview, *The internet society (ISOC)*, 2015.
- Rott, A., Doekemeijer, B., Seifert, J. K., Van Wingerden, J.-W., and Kühn, M.: Robust active wake control in consideration of wind direction variability and uncertainty, *Wind Energy Science*, 3, 869–882, <https://doi.org/10.5194/wes-3-869-2018>, 2018.

- Rott, A., Petrović, V., and Kühn, M.: Wind farm flow reconstruction and prediction from high frequency SCADA Data, *Journal of Physics: Conference Series*, 1618, 062067, <https://doi.org/10.1088/1742-6596/1618/6/062067>, 2020.
- Saiki, E. M., Moeng, C.-H., and Sullivan, P. P.: Large-Eddy Simulation Of The Stably Stratified Planetary Boundary Layer, *Boundary-Layer Meteorology*, 95, 1–30, <https://doi.org/10.1023/A:1002428223156>, 2000.
- Sathe, A. and Mann, J.: A review of turbulence measurements using ground-based wind lidars, *Atmospheric Measurement Techniques*, 6, 3147–3167, <https://doi.org/10.5194/amt-6-3147-2013>, 2013.
- Schlipf, D. and Cheng, P. W.: Flatness-based feedforward control of wind turbines using lidar, *IFAC Proceedings Volumes*, 19, 5820–5825, <https://doi.org/10.3182/20140824-6-ZA-1003.00443>, 2014.
- Schlipf, D., Kapp, S., Anger, J., Bischoff, O., Hofsäß, M., Rettenmeier, A., and Kühn, M.: Prospects of Optimization of Energy Production by LIDAR Assisted Control of Wind Turbines, in: *EWEA 2011, 14-17 March, Brussels, Belgium, 2011*.
- Schlipf, D., Schlipf, D., and Kuhn, M.: Nonlinear model predictive control of wind turbines using LIDAR, *Wind Energy*, 16, 1107–1129, <https://doi.org/10.1002/we.1533>, 2013.
- Scholbrock, A., Flemingy, P., Wright, A., Slinger, C., Medley, J., and Harris, M.: Field test results from lidar measured yaw control for improved yaw alignment with the NREL controls advanced research turbine, in: *33rd Wind Energy Symposium, 5-9 January, Kissimmee, Florida, USA, https://doi.org/10.2514/6.2015-1209, 2015*.
- Scholbrock, A., Fleming, P., Schlipf, D., Wright, A., Johnson, K., and Wang, N.: Lidar-Enhanced Wind Turbine Control: Past, Present, and Future, in: *IEEE American Control Conference (ACC), 6-8 July, Boston, Massachusetts, USA, pp. 1399–1406, https://doi.org/10.1109/ACC.2016.7525113, 2016*.
- Schot, S. H.: Eighty years of Sommerfeld’s radiation condition, *Historia Mathematica*, 19, 385–401, [https://doi.org/10.1016/0315-0860\(92\)90004-U](https://doi.org/10.1016/0315-0860(92)90004-U), 1992.
- Schottler, J., Hölling, A., Peinke, J., and Hölling, M.: Brief Communication: On the influence of vertical velocity profiles on the combined power output of two model wind turbines in yaw, *Wind Energy Science*, 2, 439–442, <https://doi.org/10.5194/wes-2-439-2017>, 2017.
- Schreiber, J., Bottasso, C. L., Salbert, B., and Campagnolo, F.: Improving wind farm flow models by learning from operational data, *Wind Energy Science*, 5, 647–673, <https://doi.org/10.5194/wes-5-647-2020>, 2020.
- Schumann, U.: Subgrid scale model for finite difference simulations of turbulent flows in plane channels and annuli, *Journal of Computational Physics*, 18, 376–404, [https://doi.org/10.1016/0021-9991\(75\)90093-5](https://doi.org/10.1016/0021-9991(75)90093-5), 1975.
- Schwab, K.: *The fourth industrial revolution*, World Economic Forum, 1st edn., 2016.



- scikit-learn: Choosing the right estimator, URL [https://scikit-learn.org/stable/tutorial/machine\\_learning\\_map/index.html](https://scikit-learn.org/stable/tutorial/machine_learning_map/index.html), last accessed October 12th, 2022, 2022.
- Sengers, B. A. M., Steinfeld, G., Heinemann, D., and Kühn, M.: A new method to characterize the curled wake shape under yaw misalignment, *Journal of Physics: Conference Series*, 1618, 062050, <https://doi.org/10.1088/1742-6596/1618/6/062050>, 2020.
- Sengers, B. A. M., Zech, M., Jacobs, P., Steinfeld, G., and Kühn, M.: A physically interpretable data-driven surrogate model for wake steering, *Wind Energy Science*, 7, 1455–1470, <https://doi.org/10.5194/wes-7-1455-2022>, 2022.
- Sengers, B. A. M., Rott, A., Steinfeld, G., Simley, E., Sinner, M., and Kühn, M.: Increased power gains from wake steering control using preview wind direction information, *Wind Energy Science*, *Submitted*, 2023a.
- Sengers, B. A. M., Steinfeld, G., Hulsman, P., and Kühn, M.: Validation of an interpretable data-driven wake model using lidar measurements from a field wake steering experiment, *Wind Energy Science*, 8, 747–770, <https://doi.org/10.5194/wes-8-747-2023>, 2023b.
- Shapiro, C. R., Starke, G., Meneveau, C., and Gayme, D.: A wake modeling paradigm for wind farm design and control, *Energies*, 12, 2956, <https://doi.org/10.3390/en12152956>, 2019.
- Simley, E., Fleming, P., and King, J.: Design and analysis of a wake steering controller with wind direction variability, *Wind Energy Science*, 5, 451–468, <https://doi.org/10.5194/wes-5-451-2020>, 2020.
- Simley, E., Fleming, P., Girard, N., Alloin, L., Godefroy, E., and Duc, T.: Results from a wake-steering experiment at a commercial wind plant: investigating the wind speed dependence of wake-steering performance, *Wind Energy Science*, 6, 1427–1453, <https://doi.org/10.5194/wes-6-1427-2021>, 2021a.
- Simley, E., Fleming, P., King, J., and Sinner, M.: Wake Steering Wind Farm Control with Preview Wind Direction Information, *IEEE American Control Conference (ACC)*, pp. 1783–1789, <https://doi.org/10.23919/ACC50511.2021.9483008>, 2021b.
- Simley, E., Debnath, M., and Fleming, P.: Investigating the impact of atmospheric conditions on wake-steering performance at a commercial wind plant, *Journal of Physics: Conference Series*, 2265, 032097, <https://doi.org/10.1088/1742-6596/2265/3/032097>, 2022.
- Sinner, M., Pao, L. Y., and King, J.: Estimation of Large-Scale Wind Field Characteristics using Supervisory Control and Data Acquisition Measurements, *IEEE American Control Conference (ACC)*, pp. 2357–2362, <https://doi.org/10.23919/ACC45564.2020.9147859>, 2020.
- Sinner, M., Simley, E., King, J., Fleming, P., and Pao, L. Y.: Power increases using wind direction spatial filtering for wind farm control: Evaluation using FLORIS, modified for dynamic settings, *Journal of Renewable and Sustainable Energy*, 13, 023310, <https://doi.org/10.1063/5.0039899>, 2021.

- Sok, C. and Adams, M. D.: Visually aided feature extraction from 3D range data, IEEE International Conference on Robotics and Automation, <https://doi.org/10.1109/ROBOT.2010.5509308>, 2010.
- Song, D. R., Li, Q. A., Cai, Z., Li, L., Yang, J., Su, M., and Joo, Y. H.: Model Predictive Control Using Multi-Step Prediction Model for Electrical Yaw System of Horizontal-Axis Wind Turbines, IEEE Transactions on Sustainable Energy, 10, 2084–2093, <https://doi.org/10.1109/TSTE.2018.2878624>, 2019.
- Spencer, M., Stol, K., and Cater, J.: Predictive Yaw Control of a 5MW Wind Turbine Model, in: 51th AIAA Aerospace Sciences Meeting Including the New Horizons Forum and Aerospace Exposition, 9-12 January, Nashville, Tennessee, USA, <https://doi.org/10.2514/6.2012-1020>, 2011.
- Stathopoulos, C., Kaperoni, A., Galanis, G., and Kallos, G.: Wind power prediction based on numerical and statistical models, Journal of Wind Engineering and Industrial Aerodynamics, 112, 25–38, <https://doi.org/10.1016/j.jweia.2012.09.004>, 2013.
- Steinbuch, M., de Boer, W. W., Bosgra, O. H., Peters, S. A. W. M., and Ploeg, J.: Optimal control of wind power plants, Journal of Wind Engineering and Industrial Aerodynamics, 27, 237–246, [https://doi.org/10.1016/0167-6105\(88\)90039-6](https://doi.org/10.1016/0167-6105(88)90039-6), 1988.
- Steinfeld, G., Tambke, J., Peinke, J., and Heinemann, D.: Development of a tool for the study of flow conditions and turbulent loads in offshore wind farms, Proceedings of EWEC 2010, 20, 23.04, 2010.
- Stieren, A., Gadde, S. N., and Stevens, R. J.: Modeling dynamic wind direction changes in large eddy simulations of wind farms, Renewable Energy, 170, 1342–1352, <https://doi.org/10.1016/j.renene.2021.02.018>, 2021.
- Stull, R. B.: An Introduction to Boundary Layer Meteorology, vol. 13, Springer Science & Business Media, 1988.
- The White House: Executive Order on Catalyzing Clean Energy Industries and Jobs Through Federal Sustainability, URL <https://www.whitehouse.gov/briefing-room/presidential-actions/2021/12/08/executive-order-on-catalyzing-clean-energy-industries-and-jobs-through-federal-sustainability/>, last accessed September 7th, 2022, 2021a.
- The White House: FACT SHEET: Biden Administration Launches New Federal-State Offshore Wind Partnership to Grow American-Made Clean Energy, URL <https://www.whitehouse.gov/briefing-room/statements-releases/2021/03/29/fact-sheet-biden-administration-jumpstarts-offshore-wind-energy-projects-to-create-jobs/>, last accessed September 7th, 2022, 2021b.
- Theuer, F., van Dooren, M. F., von Bremen, L., and Kühn, M.: Minute-scale power forecast of offshore wind turbines using long-range single-Doppler lidar measurements, Wind Energy Science, 5, 1449–1468, <https://doi.org/10.5194/wes-5-1449-2020>, 2020.

- Theuer, F., Rott, A., Schneeman, J., von Bremen, L., and Kühn, M.: Observer-based power forecast of individual and aggregated offshore wind turbines, *Wind Energy Science*, 7, 2099–2116, <https://doi.org/10.5194/wes-7-2099-20221>, 2022.
- Ti, Z., Deng, X. W., and Yang, H.: Wake modeling of wind turbines using machine learning, *Applied Energy*, 257, 114025, <https://doi.org/10.1016/j.apenergy.2019.114025>, 2020.
- Tibshirani, R.: Regression Shrinkage and Selection Via the Lasso, *Journal of the Royal Statistical Society. Series B (Methodological)*, 58, 267–288, <https://doi.org/10.1111/j.2517-6161.1996.tb02080.x>, 1996.
- Tobin, I., Jerez, S., Vautard, R., Thais, F., van Meijgaard, E., Prein, A., Déqué, M., Kotlarski, S., Maule, C. F., and Nikulin, G.: Climate change impacts on the power generation potential of a European mid-century wind farms scenario, *Environmental Research Letters*, 11, 034013, <https://doi.org/10.1088/1748-9326/11/3/034013>, 2016.
- topographic-map.com: Topographic map, URL <http://topographic-map.com>, last accessed: 1 August 2022, 2022.
- Trabucchi, D.: Lidar Measurements and Engineering Modelling of Wind Turbine Wakes, Dissertation, University of Oldenburg, URL [http://oops.uni-oldenburg.de/4671/1/PhD\\_Thesis\\_Trabucchi\\_2019\\_to\\_prin\t\\_v2.pdf](http://oops.uni-oldenburg.de/4671/1/PhD_Thesis_Trabucchi_2019_to_prin\t_v2.pdf), 2019.
- Trujillo, J. J., Seifert, J. K., Würth, I., Schlipf, D., and Kühn, M.: Full-field assessment of wind turbine near-wake deviation in relation to yaw misalignment, *Wind Energy Science*, 1, 41–53, <https://doi.org/10.5194/wes-1-41-2016>, 2016.
- Udina, M., Montornès, A., Casso, P., Kosović, and Bech, J.: WRF-LES Simulation of the Boundary Layer Turbulent Processes during the BLLAST Campaign, *Atmosphere*, 11, 1149, <https://doi.org/10.3390/atmos11111149>, 2020.
- United Nations: United Nations Treaty Collection - Chapter XXVII: Environment, URL [https://treaties.un.org/Pages/Treaties.aspx?id=27&subid=A&clang=\\_en](https://treaties.un.org/Pages/Treaties.aspx?id=27&subid=A&clang=_en), last accessed August 31st, 2022, 2022.
- U.S. Energy Information Administration: Wind generation seasonal patterns vary across the United States, URL <https://www.eia.gov/todayinenergy/detail.php?id=20112#>, last accessed September 21st, 2022, 2015.
- Vali, M., van Wingerden, J.-W., Boersma, S., Petrović, V., and Kühn, M.: A predictive control framework for optimal energy extraction of wind farms, *Journal of Physics: Conference Series*, 753, 052013, <https://doi.org/10.1088/1742-6596/753/5/052013>, 2016.
- Valdecabres, L., von Bremen, L., and Kühn, M.: Minute-scale detection and probabilistic prediction of offshore wind turbine power ramps using dual-Doppler radar, *Wind Energy*, 23, 2202–2224, <https://doi.org/10.1002/we.2553>, 2020.
- van der Hoek, D., Kanev, S., Allin, J., Bieniek, D., and Mittelmeier, N.: Effects of axial induction control on wind farm energy production - A field test, *Renewable Energy*, 140, 994–1003, <https://doi.org/10.1016/j.renene.2019.03.117>, 2019.

- van der Hoek, D., Sinner, M., Simley, E., Pao, L., and van Wingerden, J.-W.: Estimation of the Ambient Wind Field From Wind Turbine Measurements Using Gaussian Process Regression, *IEEE American Control Conference (ACC)*, pp. 558–563, <https://doi.org/10.23919/ACC50511.2021.9483088>, 2021.
- van der Laan, M. P., Andersen, S. J., Réthoré, P.-E., Baungaard, M., Sørensen, J. N., and Troldborg, N.: Faster wind farm AEP calculations with CFD using a generalized wind turbine model, *Journal of Physics: Conference Series*, p. 022030, <https://doi.org/10.1088/1742-6596/2265/2/022030>, 2022.
- van Dooren, M. F., Trabucchi, D., and Kühn, M.: A Methodology for the Reconstruction of 2D Horizontal Wind Fields of Wind Turbine Wakes Based on Dual-Doppler Lidar Measurements, *Remote Sensing*, 8, 809, <https://doi.org/10.3390/rs8100809>, 2016.
- van Wingerden, J.-W., Fleming, P. A., Göçmen, T., Eguinoa, I., M, D. B., Dykes, K., Lawson, M., Simley, E., King, J., and Astrain, D.: Expert Elicitation on Wind Farm Control, *Journal of Physics: Conference Series*, 1618, 022 025, <https://doi.org/10.1088/1742-6596/1618/2/022025>, 2020.
- Veers, P., Dykes, K., Lantz, E., Barth, S., Bottasso, C. L., Carlson, O., Clifton, A., Green, J., Green, P., Holttinen, H., Laird, D., Lehtomäki, V., Lundquist, J. K., Manwell, J., Marquis, M., Meneveau, C., Moriarty, P., Munduate, X., Muskulus, M., Naughton, J., Pao, L., Paquette, J., Peinke, J., Robertson, A., Rodrigo, J. S., Sempreviva, A. M., Smith, J. C., Tuohy, A., and Wiser, R.: Grand challenges in the science of wind energy, *Science*, 366, <https://doi.org/10.1126/science.aau2027>, 2019.
- Vollmer, L., Steinfeld, G., Heinemann, D., and Kühn, M.: Estimating the wake deflection downstream of a wind turbine in different atmospheric stabilities: an LES study, *Wind Energy Science*, 1, 129–141, <https://doi.org/10.5194/wes-1-129-2016>, 2016.
- Wagenaar, J., Machielse, L., and Schepers, J.: Controlling Wind in ECN’s Scaled Wind Farm, in: *Proceeding of the EWEA Annual Meeting*, 16-19 April, Copenhagen, Denmark, 2012.
- Wang, J., Bottasso, C., and Campagnolo, F.: Wake redirection: comparison of analytical, numerical and experimental models, *Journal of Physics: Conference Series*, 753, 032 064, <https://doi.org/10.1088/1742-6596/753/3/032064>, 2016.
- Wang, N., Johnson, K. E., and Wright, A. D.: Comparison of strategies for enhancing energy capture and reducing loads using LIDAR and feedforward control, *IEEE Transactions on Control Systems Technology*, 21, 1129–1142, <https://doi.org/10.1109/TCST.2013.2258670>, 2013.
- Wang, W., Yang, S., and Yang, Y.: An Improved Data-Efficiency Algorithm Based on Combining Isolation Forest and Mean Shift for Anomaly Data Filtering in Wind Power Curve, *energies*, 15, 4918, <https://doi.org/10.3390/en15134918>, 2022.
- Watts, D., Durán, P., and Flores, Y.: How does El Niño Southern Oscillation impact the wind resource in Chile? A techno-economical assessment of the influence

- of El Niño and La Niña on the wind power, *Renewable Energy*, 103, 128–142, <https://doi.org/10.1016/j.renene.2016.10.031>, 2016.
- Werner, C.: Doppler Wind Lidar, in: *Lidar: Range-Resolved Optical Remote Sensing of the Atmosphere*, chap. 12, pp. 325–354, Springer New York, New York, NY, 2005.
- Wicker, L. J. and Skamarock, W. C.: Time-Splitting Methods for Elastic Models Using Forward Time Schemes, *Monthly Weather Review*, 130, 2088–2097, [https://doi.org/10.1175/1520-0493\(2002\)130<2088:TSMFEM>2.0.CO;2](https://doi.org/10.1175/1520-0493(2002)130<2088:TSMFEM>2.0.CO;2), 2002.
- Williamson, J. H.: Low-storage Runge-Kutta schemes, *Journal of Computational Physics*, 35, 48–56, [https://doi.org/10.1016/0021-9991\(80\)90033-9](https://doi.org/10.1016/0021-9991(80)90033-9), 1980.
- Witha, B., Steinfeld, G., and Heinemann, D.: Advanced turbine parameterizations in offshore LES wake simulations, *Proceedings of the 6th International Symposium on Computational Wind Engineering*, Hamburg, Germany, pp. 8–13, 2014.
- Wu, Y.-T. and Porté-Agel, F.: Large-Eddy Simulation of Wind-Turbine Wakes: Evaluation of Turbine Parametrisations, *Boundary-Layer Meteorology*, 138, 345–366, <https://doi.org/10.1007/s10546-010-9569-x>, 2011.
- Würth, I., Valldecabres, L., Simon, E., Möhrlen, C., Uzunoglu, B., Gilbert, C., Giebel, G., Schlipf, D., and Kaifel, A.: Minute-scale forecasting of wind power—results from the collaborative workshop of IEA Wind task 32 and 36, *Energies*, 12, <https://doi.org/10.3390/en12040712>, 2019.
- You, L., Jiang, H., Hu, J., Chang, H., Chen, L., Cui, X., and Zhao, M.: GPU-accelerated Faster Mean Shift with euclidean distance metrics, *IEEE 46th Annual Computers, Software, and Applications Conference (COMPSAC)*, <https://doi.org/10.1109/COMPSAC54236.2022.00037>, 2022.
- Zahle, F. and Sørensen, N. N.: Overset grid flow simulation on a modern wind turbine, in: *AIAA 26th Applied Aerodynamic Conference*, 18-21 August, Honolulu, Hawaii, USA, <https://doi.org/10.2514/6.2008-6727>, 2008.
- Zehtabiyani-Rezaie, N., Iosifidis, A., and Abkar, M.: Data-driven fluid mechanics of wind farms: A review, *Journal of Renewable and Sustainable Energy*, 14, 032 703, <https://doi.org/10.1063/5.0091980>, 2022.
- Zha, J., Shen, C., Li, Z., Wu, J., Zhao, D., Fan, W., Sun, M., Azorin-Molina, C., , and Deng, K.: Projected changes in global terrestrial near-surface wind speed in 1.5 °C–4.0 °C global warming levels, *Environmental Research Letters*, 16, 114 016, <https://doi.org/10.1088/1748-9326/ac2fdd>, 2021.

# Publication list

## Publications on which this thesis is based

### Peer-reviewed journal articles

Sengers, B. A. M., Zech, M., Jacobs, P., Steinfeld, G., and Kühn, M.: A physically interpretable data-driven surrogate model for wake steering, *Wind Energy Science*, 7, 1455-1470, <https://doi.org/10.5194/wes-7-1455-2022>, 2022.

BAMS developed the surrogate model, performed the simulations, generated the results, and wrote and edited the manuscript. MZ developed the regression model and contributed to writing Sect. 3.3 and Appendix A. PJ tested various tuning strategies for the benchmark models and provided a general understanding of these models. GS provided intensive consultation on the development of the model and the scientific analyses. MK provided general consultation and had a supervisory function. All coauthors reviewed the manuscript.

This publication serves as Chapter 4 in the dissertation.

Sengers, B. A. M., Steinfeld, G., Hulsman, P., and Kühn, M.: Validation of an interpretable data-driven wake model using lidar measurements from a field wake steering experiment, *Wind Energy Science*, 8, 747-770, <https://doi.org/10.5194/wes-8-747-2023>, 2023.

BAMS designed the experiment, processed the data, generated the results, and wrote and edited the manuscript. GS provided intensive consultation on the experimental design and generation of the results. PH was heavily involved in organizing the campaign and contributed to the processing of the raw data, as well as translated the aerodynamic properties of the turbine provided by the operator in Bladed into FAST. MK provided general consultation and had a supervisory function. All co-authors reviewed the manuscript.

This publication serves as Chapter 5 in the dissertation.

Sengers, B. A. M., Rott, A., Simley, E., Sinner, M., Steinfeld, G., and Kühn, M.: Increased power gains from wake steering control using preview wind direction information, *Wind Energy Science*, 8, 1693–1710, <https://doi.org/10.5194/wes-8-1693-2023>, 2023.

BAMS designed the experiment, developed the engineering model, implemented the LES setup, generated the results, and wrote and edited the manuscript. AR conceptualized the experiment. AR, ES and MS provided intensive consultation, helped design the experiment and critically evaluated the results. GS provided help implementing the LES setup. MK had a supervisory function. All coauthors reviewed the manuscript.

This publication serves as Chapter 6 in the dissertation.

## Peer-reviewed conference proceedings

Sengers, B. A. M., Steinfeld, G., Heinemann, D., and Kühn, M.: A new method to characterize the curled wake shape under yaw misalignment, *Journal of Physics: Conference Series*, 1618, 062050, <https://doi.org/10.1088/1742-6596/1618/6/062050>, 2020.

BAMS developed the methodology, performed the simulations, analyzed the results and wrote and edited the manuscript. GS provided intensive consultation on the development of the method and analysis of the results. DH and MK had supervising functions. All authors reviewed the manuscript.

This publication serves as Chapter 3 in the dissertation.

## Further publications

### Conference presentations

Schmidt, J., Mellish, B., Sengers, B. A. M., Vollmer, L., and Dörenkämper, M.: Wind farm and wake modelling with FOXES, *Wind Energy Science Conference*, Glasgow, United Kingdom, May 2023 (Oral presentation).

Sengers, B. A. M., Steinfeld, G., Heinemann, D., and Kühn, M.: A new method to characterize the curled wake shape under yaw misalignment, *Science of making Torque from Wind*, web conference, Delft, The Netherlands, September 2020 (Poster presentation).

Sengers, B. A. M., Zech, M., Jacobs, P., Steinfeld, G., and Kühn, M.: Framework for a statistical wake steering model, 16th EAWC PhD Seminar, web conference, Porto, Portugal, December 2020 (Oral presentation).

Sengers, B. A. M., Steinfeld, G., van Dooren, M. F., Heinemann, D., and Kühn, M.: Optimal Lidar Scanning Pattern for Wake Composition under Yaw Misalignment, Wind Energy Science Conference, web conference, Hannover, Germany, May 2021 (Oral presentation).

Vollmer, L., Dörenkämper, M., and Sengers, B. A. M.: Large scale wake effects of the German offshore wind expansion plans, Wind Energy Science Conference, Glasgow, United Kingdom, May 2023 (Oral presentation).



# Acknowledgments

I would like to thank my supervisor, Prof. Dr. Martin Kühn for his support during the last years. I thank Dr. Mahdi Abkar of Aarhus University for accepting to review my thesis and to be part of the examination committee.

The work presented in this thesis has been carried out within the national research project CompactWind II (FKZ 0325492H), funded by the Federal Ministry for Economic Affairs and Energy (BMWi) on the basis of a decision by the German Bundestag. The work was partially funded by the Ministry for Science and Culture of Lower Saxony through the funding initiative “Niedersächsisches Vorab”. Computer resources have been provided by the national research project “Heterogener Hochleistungsrechner für windenergierelevante Meteorologie- und Strömungsberechnungen (WIMS-Cluster)” (FKZ 0324005), funded by the Federal Ministry for Economic Affairs and Energy (BMWi) on the basis of a decision by the German Bundestag. I thank the eno energy for granting access a commercial turbine to perform my experiments.

I greatly appreciate all the help and support I have received from Dr. Gerald Steinfeld. Apart from sharing his expertise on LES modeling and helping me design the experimental setup of this work, his unwavering support when I was insecure or overwhelmed helped me get through the rough stages of the PhD journey.

I would like to thank Dr. Paul van der Laan and colleagues from the Department of Wind and Energy Systems at the Technical University of Denmark for giving me the opportunity for a lab visit. Due to COVID regulations we had to cut the stay short, but it was amazing to experience the environment at DTU.

Furthermore I would like to thank all students that have contributed to my PhD: Pim Jacobs, Maike Schröder, Freerk Schütt, Surangi Wanninayaka and Paul Wißmann. A great thanks goes out to all my colleagues at ForWind Oldenburg for creating an comfortable environment, in particular Dagmar Battermann, Frauke Haunhorst, Irene Meints, Janka Heits and Agnes Seeger. I want to thank the following colleagues for all the help and discussions the last years: Detlev Heinemann, Sonja Steinbrück, Renko Buhr, Wilke Trei, Hauke Beck, Hauke Wurps, Marijn van Dooren, Anantha Kidambi, Paul Hulsman, Frauke Theuer, David Bastine, Stephan Stone, Vlaho Petrovic, Andreas Rott and Priscila Orozco.

Lastly, I would like to thank my parents for their unwavering support. Although they don't understand a think I'm doing, their enthusiasm for every piece of work I created was important to stay motivated. An enormous appreciating goes out to my girlfriend, who stood by my side throughout the last years. She would always make time to listen to my complaints and actively tried to help when I was feeling demotivated.

I am grateful for everyone that has made this possible. Thank you.

# Curriculum Vitae

## Personal Information

Name: Balthazar Arnoldus Maria (Luuk) Sengers  
Date of Birth: 08.01.1995  
Place of Birth: 's-Hertogenbosch, the Netherlands

## Education

Sep 2016 - Feb 2019 MSc Earth and Environment  
Specialization Meteorology and Air Quality  
Wageningen University & Research

Sep 2013 - Aug 2016 BSc Soil, Water, Atmosphere  
Wageningen University & Research

Sep 2007 - Aug 2013 High School  
Stedelijk Gymnasium van 's-Hertogenbosch

## Scientific Experience

Jan 2023 - now Research Associate  
Institute for Wind Energy Systems  
Fraunhofer-Gesellschaft, Germany

Apr 2019 - Dec 2022 Scientific Researcher  
Institute of Physics, ForWind - Carl von Ossietzky  
University of Oldenburg, Germany

Feb 2022 Visiting Researcher  
Department of Wind and Energy Systems  
Technical University of Denmark (DTU), Denmark

Sep 2018 - Feb 2019 Master Internship  
Eneco & Royal Netherlands Meteorological  
Institute (KNMI), Netherlands

Jan - Jul 2018 Master Thesis  
Research Applications Laboratory  
National Center for Atmospheric Research (NCAR), USA